CERN – European Organization for Nuclear Research

European Laboratory for Particle Physics

CTF3 Note 047
CERN/PS 2002-008 (RF)
LNF-02/008 (IR)

(CTF Design Report))

CTF3 DESIGN REPORT

Edited by G. Geschonke (CERN) and A. Ghigo (INFN Frascati)

Abstract

The design of CLIC is based on a two-beam scheme, where short pulses of high power 30 GHz RF are extracted from a drive beam running parallel to the main beam. The 3rd generation CLIC Test Facility (CTF3) will demonstrate the generation of the drive beam with the appropriate time structure, the extraction of 30 GHz RF power from this beam, as well as acceleration of a probe beam with 30 GHz RF cavities. The project makes maximum use of existing equipment and infrastructure of the LPI complex, which became available after the closure of LEP.

Geneva, Switzerland
31 May 2002

25 April 2002

CTF3 Design Report

Abstract

The design of CLIC is based on a two-beam scheme, where short pulses of high power 30 GHz RF are extracted from a drive beam running parallel to the main beam. The 3rd generation CLIC Test Facility (CTF3) will demonstrate the generation of the drive beam with the appropriate time structure, the extraction of 30 GHz RF power from this beam, as well as acceleration of a probe beam with 30 GHz RF cavities The project makes maximum use of existing equipment and infrastructure of the LPI complex, which became available after the closure of LEP.

Contributors:

R. Bossart, H. Braun, P. Brown, G. Carron, V. Chohan, R. Corsini, E. D'Amico, S. Deghaye, J.P. Delahaye, F. Di Maio, S. Doebert, B. Dupuy, G. Geschonke, L. Gröning, G. Guignard, H. Hellgren, S. Hutchins, J.H. Lewis, E. Jensen, G.McMonagle, A. Millich, J. Monteiro, J.P. Delahaye, T. Otto, P. Pearce, E. Peschardt, R. Pittin, M. Poehler, J.P. Potier, L. Rinolfi, T. Risselada, G. Rossat, P. Royer, D. Schulte, J. Sladen, G. Suberlucq, I. Syratchev, F. Tecker, H. Trautner, L.Thorndahl, I. Wilson, W. Wünsch
CERN

R. Koontz, R. Miller, R. Ruth, A. Yeremian,
SLAC

D. Alesini, C. Biscari, R. Boni, A. Clozza, G. Di Pirro, A. Drago, A. Gallo, A. Ghigo, F. Marcellini, C. Milardi, M.A. Preger, C. Sanelli, F. Sannibale, M. Serio, F. Sgamma, A. Stecchi, A. Stella, M. Zobov.
INFN Laboratori Nazionali di Frascati

I.N. Ross
Central Laser Facility, RAL, Didcot, U.K.

E. Bente, G. Valentine
University of Strathclyde, Institute of Photonics, Glasgow, U.K.

G. Bienvenu, M. Bernard, M. Omeich, R. Roux, T. Garvey
LAL Orsay

Edited by

G. Geschonke/CERN and A. Ghigo/INFN Frascati

CTF3 DESIGN REPORT

TABLE OF CONTENTS

1. INTRODUCTION

The CLIC design aims for a maximum energy of 3 to 5 TeV (centre of mass) to be reached by acceleration with high gradients of 150 MV/m at 30 GHz with a RF pulse length of 130 ns. The RF power requirement is 460 MW per metre of linac length. Therefore a very efficient and reliable source of RF power is required. The scheme is based on a drive beam running parallel to the main beam, whose bunch structure carries a 30 GHz component. The RF power is extracted from the drive beam in Power Extraction and Transfer Structures (PETS) and transferred to the main beam.

A novel scheme for the drive beam generation has been proposed, in which a long bunch train with low bunch repetition frequency is accelerated with low RF frequency. Subsequent packets of this bunch train are interleaved in isochronous rings thereby increasing the bunch repetition frequency and shortening the bunch train with a corresponding increase in peak RF power.

The main goals of CTF3 are to test this new RF power generation scheme and to produce 30 GHz RF power at the nominal peak power and pulse length, such that all 30 GHz components for CLIC can be tested at nominal parameters.

The facility will be built in the existing infrastructure of the LPI complex and make maximum use of equipment which became available after the end of LEP operation. The existing RF power plant from LIL at 3 GHz will be used. The project is based in the PS Division with collaboration from many other Divisions at CERN, as well as from INFN Frascati, SLAC, IN2P3/LAL at Orsay, Rutherford Appleton Laboratory (RAL) and the University of Uppsala.

Power efficiency is of utmost importance for CLIC, therefore the drive beam with high peak current is accelerated in fully beam-loaded cavities, such that the 3 GHz power is completely converted to beam energy. New accelerating structures are required with very strong damping of beam induced Higher Order Modes to keep the bunch trains stable.

Since these new cavities will not be available before 2003, a proof of principle experiment of the bunch frequency multiplication scheme is planned for 2001/2002, using the present accelerating structures from LIL as well as the existing EPA ring with several modifications. This first phase of CTF3 is known as the "Preliminary Phase".

From the end of 2002 onwards the "Nominal" phase of CTF3 will be built, which is described in this report. For this programme the existing LPI installation will be substantially modified: a newly developed triode gun will be installed, the present LIL cavities will be replaced by the new damped structures, a Delay Loop and a Combiner Ring will be installed, allowing a multiplication of the bunch repetition frequency by a factor of 10. This beam is used to provide 30 GHz power at the nominal CLIC values of peak power and pulse length, which can be used to test CLIC components in a new test area. A "probe beam" simulating the CLIC main beam will be available in this test area, to demonstrate acceleration with the 30 GHz equipment at the CLIC design accelerating gradient.

An intermediate test station is foreseen immediately after the linac for power-testing CLIC components at longer pulse length than presently available at CTF2 at the earliest possible moment.

The whole system is an important step to demonstrate the technical feasibility of the key concepts of CLIC.

2. LAYOUT OF CLIC

The next generation of high energy e^+ e^- machines after LEP will be linear colliders. CLIC has the potential to achieve a collision energy as high as 3 – 5 TeV. A special feature of CLIC as compared to other schemes presently being studied is the high frequency of the accelerating cavities of 30 GHz, and the high accelerating gradient of 150 MV/m.

CLIC is based on a two beam scheme, where the required RF power is provided through a drive beam running parallel to the main linac. The whole system is schematically shown in Figure 2.1. A detailed description of CLIC can be found in [1]

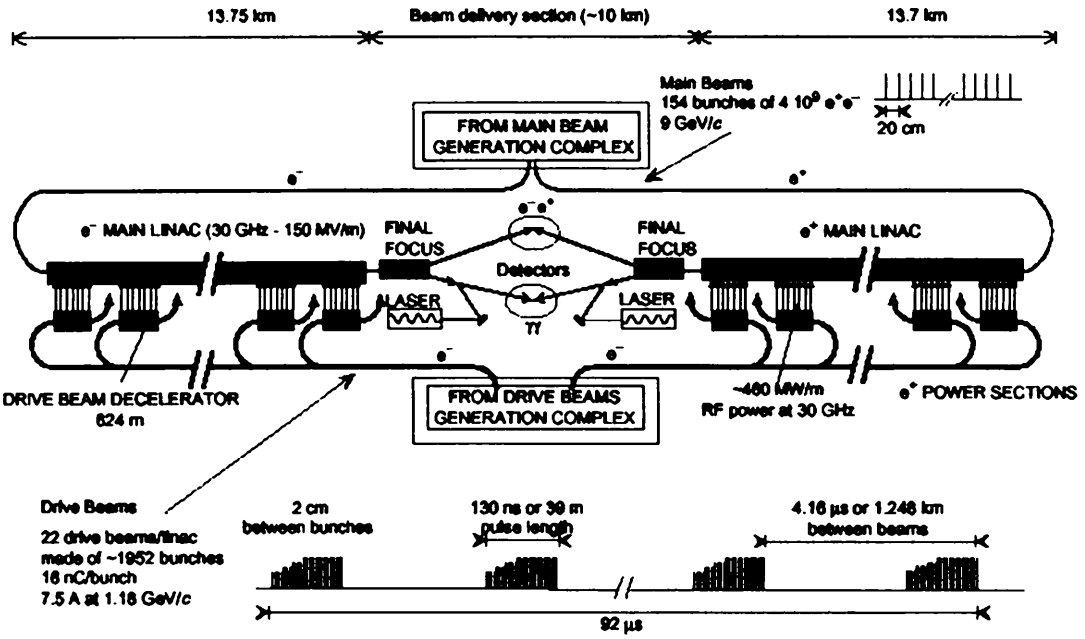

Figure 2.1 Generic Layout of CLIC

The drive beam running parallel to the main linac consists of bunch trains of 130 ns length and very high current of 240 A, spaced by about 4 μs. This bunch structure is produced by a novel technique of bunch combination, which converts a long bunch train with large bunch spacing of 64 cm into a sequence of short trains with a bunch spacing of only 2 cm, which is used for 30 GHz power production. The principle is shown in Figure 2.2. The bunch manipulation is done in three rings, using RF deflectors, giving a multiplication of the bunch repetition frequency by factors of two in the first one, and four in each of the two others. The principle of this technique is described in chapters 3.3.1 and 3.3.2 for the CTF3 parameters.

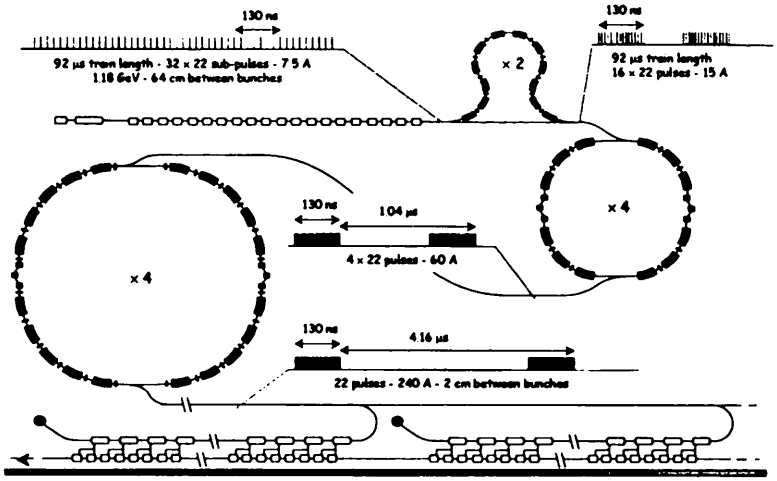

Figure 2.2 Drive beam structure of CLIC

2.1 References

[1] R.W.Assmann, et. al., "A 3 TeV e^+e^- Linear Collider Based on CLIC Technology", CERN Publication CERN 2000 – 008, July 28,

3. DESCRIPTION AND MAIN GOALS OF CTF3

CTF3 is an important test and demonstration facility for many vital components of CLIC. Its main aim is to prove the feasibility of the RF power source design and to produce 30 GHz power at nominal CLIC parameters. For cost reasons, maximum use will be made of existing equipment, in particular of the LPI complex which has become available after the closure of LEP. The conceptual layout of CTF3 is shown in Figure 3.1.

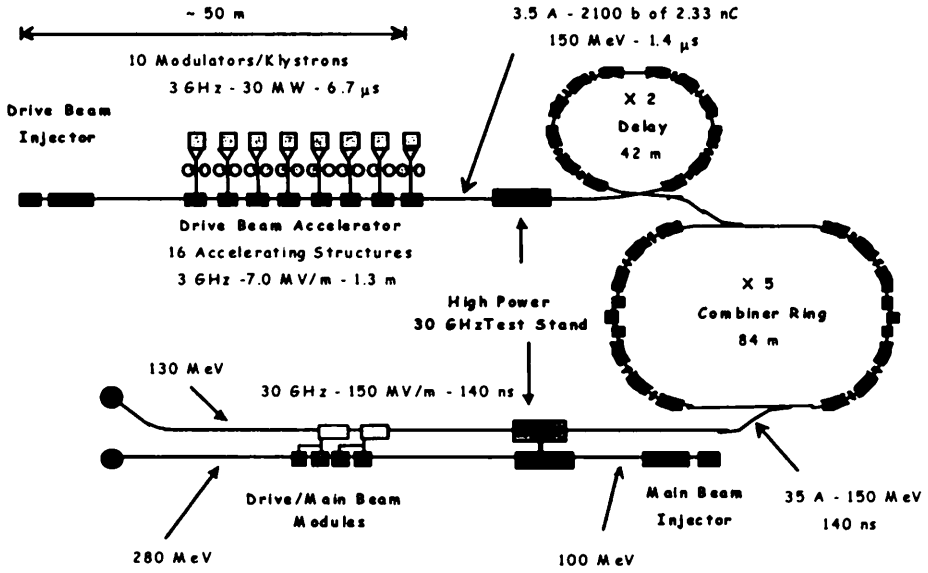

Figure 3.1 Conceptual layout of CTF3

The 1.6 μs long drive beam pulse is generated by a 140 kV, 9 A thermionic triode gun (chapter 7). The time structure of the pulse is obtained in a bunching system composed of three 1.5 GHz sub-harmonic bunchers, a 3 GHz pre-buncher and a 3 GHz tapered phase velocity travelling wave buncher. The phase of the sub-harmonic bunching cavities is switched rapidly by 180° every 140 ns, as needed for the phase coding operation described in chapter 3.3.1 .

The bunches thus obtained are spaced by 20 cm (two 3 GHz buckets) and have a charge of 2.3 nC per bunch, corresponding to an average current of 3.5 A.

The drive beam injector is completed by two 3 GHz fully-loaded travelling wave structures (see Section 9.2), bringing the beam energy up to 20 MeV. Solenoidal focusing is used all along the injector. A magnetic chicane with collimators downstream of the injector will be used to eliminate low energy beam tails produced during the bunching process. The chicane region will also be instrumented to perform emittance and energy spectra measurements on the drive beam.

An alternative option to the thermionic injector scheme described above, based on the use of an RF photo-injector, is also under study as a potential later upgrade for CTF3 (see section 8). The advantages of such a solution are smaller beam emittances in all three phase space planes, absence of low charge parasite bunches in every second 3 GHz bucket and easier tailoring of the 180° phase switching. A feasibility study made by RAL/UK on the laser needed in such a scheme, gave promising results. Experimental tests are now under way at RAL. The feasibility of photo-cathodes with the required performance in terms of average current has recently been experimentally demonstrated at CERN.

The beam is then accelerated in a linac with newly developed accelerating structures up to about 150 MeV. These new cavities allow to accelerate the very high beam current with near to 100 % beam loading. Efficient damping of beam induced higher order modes is of particular importance. For the linac optics, triplet focusing has been chosen since it provides superior beam stability compared to other lattices using FODO focusing.

The linac is followed by two rings, which multiply the bunch repetition frequency by a factor of two and five respectively, at the same time compressing the length of the pulse by a factor of 10 to 140 ns. The beam current of 35 A is then used to power a high RF power test stand for component development, and testing CLIC accelerating modules at the nominal gradient of 150 MV/m. A probe beam, generated in a photo cathode RF gun or a classical thermionic gun will be accelerated up to 150 MeV. This will be used to demonstrate the two beam scheme at nominal CLIC parameters.

Because of the use of existing equipment and infrastructure, some parameters of CTF3 are different from the final CLIC design. The comparison of CTF3 and CLIC parameters is shown in Table 3.1.

Table 3.1 Comparison CTF3 - CLIC

		CTF3	CLIC (3 TeV)
Drive beam			
Acceleration frequency	MHz	2 998.55	937.047
repetition rate	Hz	5	100
energy	MeV	150	1180
Number of accelerating structures		16 + 2	91 x 2
average current after linac	A	3.5	7.5
Number of klystrons		10	182 x 2
Number of RF pulse compressors		9	0
Beam pulse length	μs	1.4	92
Bunch spacing before compression	cm	20	64
Delay Loop length	m	42	39
Combiner Ring length	m	84	78
Average beam current after compression	A	35	240
Bunch spacing after compression	cm	2	2
Drive beam energy per pulse	kJ	0.735	812
average beam power	kW	3.675	81 000
Main beam			
Number of accelerating structures		max 8	22 x 976
RF Pulse length	ns	140	130
Acceleration Frequency	GHz	30	30
Acceleration Gradient	MV/m	150	150

The CLIC parameters used in this table are taken from ref [1] in chapter 2.1.

In the following sections the main objectives of CTF3 are presented.

3.1 Two beam scheme

The acceleration in CLIC at 30 GHz is based on a two-beam scheme where the 30 GHz RF power is extracted from the drive beam running parallel to the main beam, via Power Extraction and Transfer Structures (PETS). The basic principle of extracting 30 GHz power from a beam and powering 30 GHz accelerating structures has been successfully demonstrated in CTF1 and CTF2. Power levels of up to 150 MW have been produced, at RF pulse lengths from 2 to 16 ns instead of the nominal 130 ns. CTF2 is presently the only RF power source at 30 GHz, where CLIC components can be tested with such high RF peak power. In order to fully qualify CLIC RF components, a power source with the full pulse length is necessary.

CTF3 will provide 30 GHz RF power of nominal CLIC parameters of 240 MW as well as 130 ns pulse length. This can be used to power up to four CLIC accelerating modules.

This would allow to accelerate a probe beam from 100 MeV to 280 MeV. The parameters of this facility are still under discussion.

The bunch current is smaller than in CLIC, therefore in order to reach the nominal power level the impedance of the PETS structure will be different from CLIC.

3.2 Fully Loaded Linac Operation

The conversion efficiency of mains power to 30 GHz power is of prime importance for CLIC. Therefore an important feature of the scheme is the fully beam-loaded operation of the travelling wave sections of the Drive Beam Accelerator (DBA). This means that almost all RF power travelling down the structure is converted to beam energy and no power is dissipated in the output loads. This operating scheme is a new feature of CLIC, and operational stability needs to be demonstrated. The beam loading coefficient κ is defined as the ratio of power transferred to the beam (P_b) to the power available for the beam.

$$\kappa = \frac{P_b}{P_{in} - P_{loss}}$$

with P_{in} = power into structure and P_{loss} = power lost into structure walls.
For $\kappa = 1$, the structure is fully loaded, i.e. the forward power at the downstream end of the structure is zero.
The nominal parameters are:

Number of DBA cells/structure: 32 cells + 2 coupler cells
RF power at input of structure: 30 MW
Beam current: 3.5 A
Beam loading coefficient: 97.9 %
RF to beam efficiency: 93 %

For test purposes the beam loading can be varied by changing the beam current or the input RF power. A graph of the variation of the accelerating gradient with input power and beam current is shown in Figure 3.2.

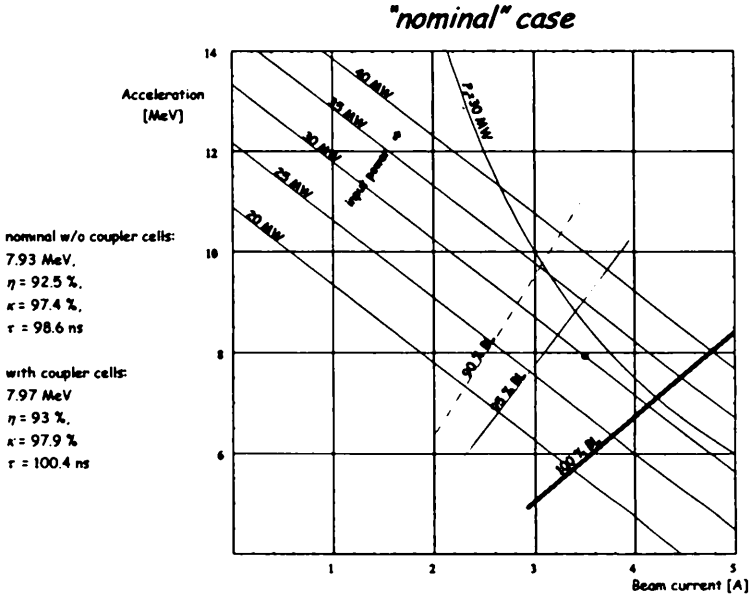

Figure 3.2 Beam Loading as function of RF Power and beam current

The high beam current in the linac requires an effective damping of the beam induced higher order modes (HOMs) in the travelling wave structures. Two structure types have been

developed with different damping schemes. They are described in chapter 9.2. The first design is derived from the 30 GHz Tapered Damped Structure (TDS) developed for the CLIC main beam linac. The damping here is achieved by four waveguides with wide-band Silicon-Carbide (SiC) loads in each accelerating cell. The waveguides act as a high pass band filter, since their cut-off frequency is above the fundamental frequency but below the HOM frequency range. The Q-value of the first dipole is thus reduced to about 18. A further reduction of the long range wake-fields is achieved by a spread of the HOMs frequencies along the structure, obtained by varying the aperture diameter from 34 mm to 26.6 mm. The second approach called SICA, (Slotted Iris Constant Aperture) uses four radial slots in the iris to couple the HOMs to SiC RF loads. In this approach the selection of the modes coupled to the loads is not made by frequency discrimination but is obtained through the field distribution of the modes: therefore all dipole modes are damped. The Q-value of the first dipole is reduced to about 5. In this case a frequency spread of the HOMs is introduced along the structure by nose cones of variable geometry. The aperture can therefore be kept constant at 34 mm, so that a smaller amplitude of the short range wake-fields is obtained.

3.3 Bunch interleaving

One of the most important issues to be tested is the frequency multiplication by the novel bunch interleaving technique. In CTF3 a long train of short bunches with a distance of 20 cm between bunches is converted into a series of short bunch trains, with the individual bunches spaced by 2 cm. This is done in two stages, first by a factor of two in a Delay Loop, then by a factor of 5 in a Combiner Ring. In order to maintain the short bunch length, both rings must be isochronous. The issues to be studied in this context are: injection into the ring using RF deflectors, operation of the isochronous ring, phase extension of the bunches in the deflectors and impedance effects.

3.3.1 Phase coding of bunches and Delay Loop

After the linac, a first stage of electron pulse compression and bunch frequency multiplication of the drive beam is obtained using a transverse RF deflector at 1.5 GHz and a 42 m circumference Delay Loop. The circumference of the loop corresponds to the length of one batch of "even" or "odd" bunches. The process is illustrated in Figure 3.3. The RF deflectors in the Delay Loop deflect every second batch of 210 bunches into the Delay Loop, and after one turn insert this batch between the bunches of the following batch. Therefore the timing of the bunches of subsequent batches is adjusted such that they have a phase difference of 180 ° with respect to the 1.5 GHz RF of the deflector.

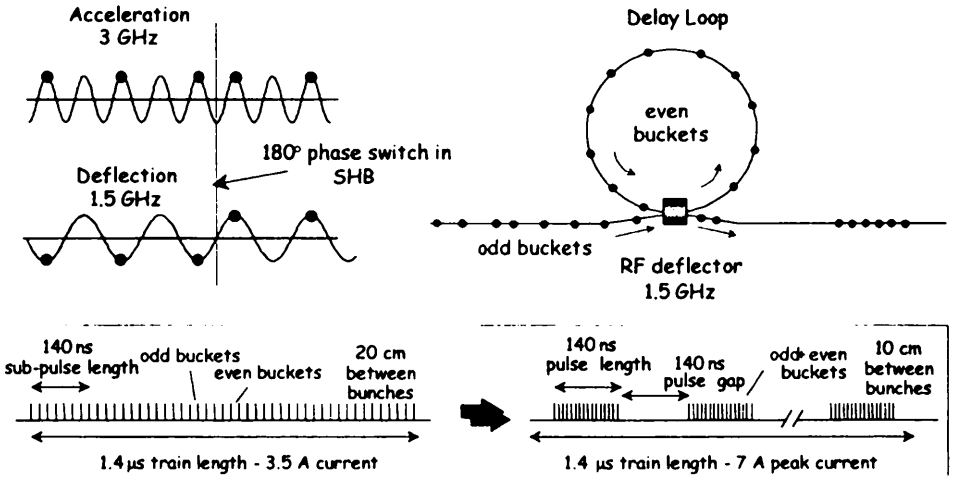

Figure 3.3 Schematic of (x2) bunch frequency multiplication in the Delay Loop.

This timing is controlled by the sub-harmonic bunchers working at 1.5 GHz in the injector. Every 140 ns the phase of the RF is changed by 180 degrees. This requires wide band sub-harmonic buncher structures as well as an RF power source capable of switching phase over a few bunches.

3.3.2 Combiner Ring

An 84 m circumference Combiner Ring is used for a second stage of pulse compression and frequency multiplication by a factor five. This is achieved by two RF deflectors working at 3 GHz, which insert the injected bunches between the already circulating ones, as illustrated in Figure 3.4. After the Combiner Ring the drive beam pulse is 140 ns long and has a current of 35 A with the 2.3 nC bunches spaced by 2 cm.

The short bunch length and the high bunch charge put stringent requirements on the ring impedance budget, where the beam diagnostics elements require particular attention.

For the deflectors, effects of phase extension of the bunches as well as multi-bunch beam loading of the fundamental deflecting mode are of concern.

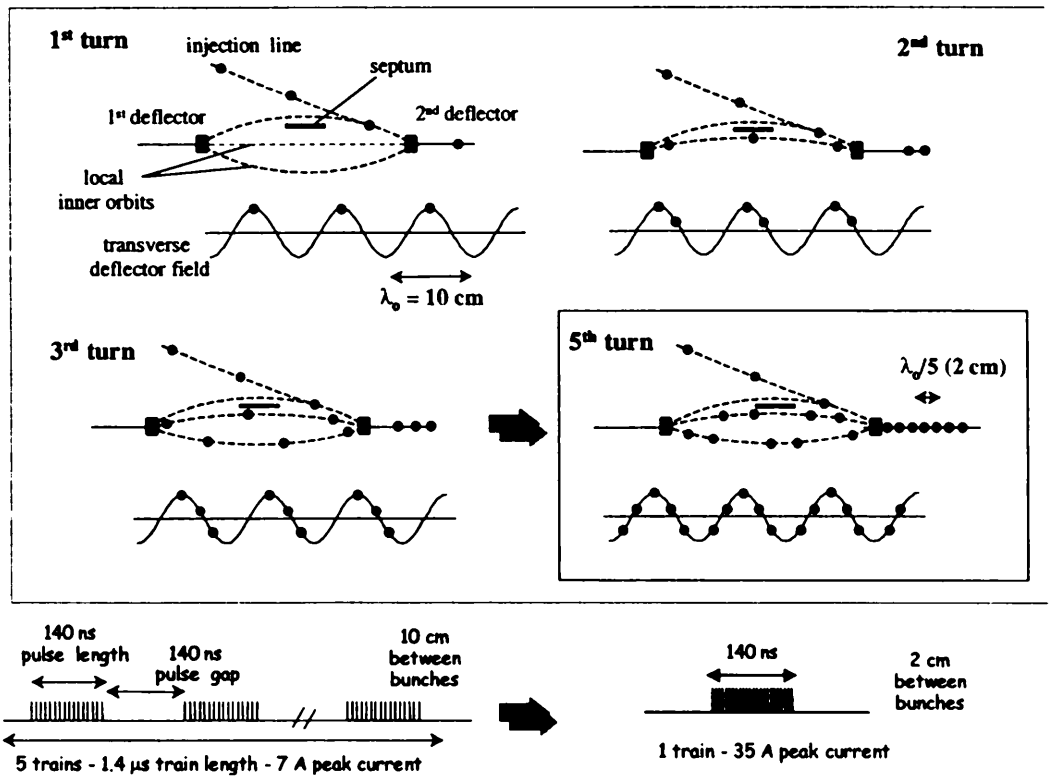

Figure 3.4 Principle of (x5) bunch frequency multiplication

3.4 Bunch length manipulation

A very short bunch length is required after recombination for efficient 30 GHz power production. The rings are isochronous, and the R_{56} of the transfer lines is kept very small.

However for short bunches the impedance of the Combiner Ring, as well as coherent synchrotron radiation effects, become important issues, leading to an energy loss and an increase in energy spread.

In order to minimise these effects, the rms bunch length is increased from its value of 1.5 mm in the linac to a maximum of 2.5 mm in the Delay Loop and Combiner Ring, by a magnetic chicane placed at the end of the linac itself. After combination, for efficient power production, the individual bunches are compressed in length to about 0.5 mm rms in a magnetic bunch compressor.

3.5 RF power generation

A single 30 GHz power extraction structure, optimised for maximum power production, will be used in a high power test stand where CLIC prototype accelerating structures and waveguide components can be tested at nominal power and beyond.

Alternatively the drive beam can be used in a string of PETS to power a representative section of the CLIC main linac and to accelerate a probe beam. The probe beam is generated in a 3 GHz RF photo-injector and pre-accelerated to 100 MeV using standard 3 GHz accelerating structures from LIL. This set-up will allow a realistic simulation of operating conditions for the main building blocks of the CLIC linac.

Since CTF2, the only source for high power 30 GHz RF at CERN, will be stopped at the end of 2002 and the full CTF3 installation will not be available before 2005, the possibility of producing 30 GHz power earlier is being studied. CLIC prototyping ideally requires between 10 and 300 MW of power at a pulse length between 4 and 200 ns. One possibility is to use the beam after the linac. This, however, requires the development of a special PETS, as described in paragraph 21.

4. LAYOUT OF CTF3

The layout of CTF3 in its Nominal phase is shown in Figure 4.1. Maximum use will be made of existing equipment and infrastructure. The parameter list is given in Table 4.1.

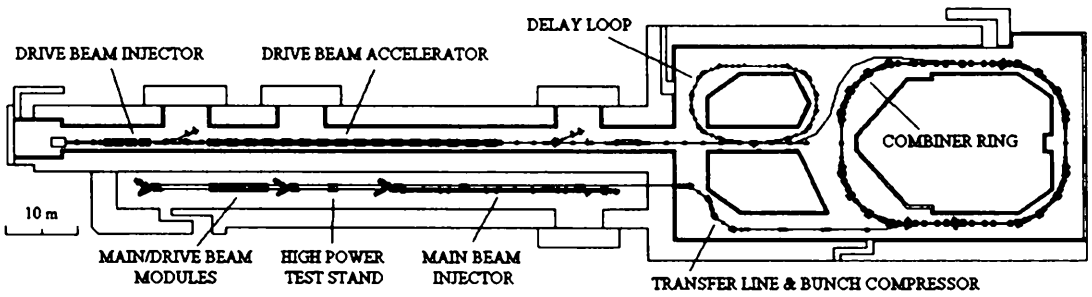

Figure 4.1 Implementation of CTF3 in the existing LPI building.

Table 4.1 Parameters of CTF3

Parameter	Symbol	Value	Unit
Drive Beam (injector exit)			
Energy	E_i	20	MeV
Current	I_i	3.5	A
Pulse duration, total	τ_i	1.54	μs
Bunch charge (flat top)	Q_b	2.33	nC
Number bunches/pulse	N_b	2310	
Bunch separation	Δ_b	0.67	ns
Bunch length, rms	σ_z	≤ 1.3	mm
Energy spread, single bunch rms (10 MeV)	ΔE_{sb}	≤ 0.3 (1)	MV
Energy spread, total on flat top (10 MeV)	ΔE_{ft}	≤ 1	MV
Normalised emittance, rms	ε_N	35	π mm mrad
Drive Beam (Combiner Ring injection)			
Energy	E_a	150 (20 + 130) (2)	MeV
Current	I_a	7	A
Pulse duration, total	τ_a	1.4	μs
Bunch charge (flat top)	Q_b	2.33	nC
Number bunches/pulse	N_b	2100	
Bunch separation	Δ_b	0.33	ns
Bunch length, rms	σ_z	1.5 – 2.5	mm
Energy spread, rms single bunch	$\Delta E/E_{sb}$	~ 1	%
Energy spread, total on flat top	$\Delta E/E_{ft}$	≤ 1	%
Drive Beam (Combiner Ring exit)			
Energy	E_r	150 (20 + 130)	MeV
Current	I_r	35	A
Pulse duration, total	τ_r	140	ns
Bunch charge (flat top)	Q_b	2.33	nC
Number bunches/pulse	N_b	2100	
Bunch separation	Δ_b	0.067	ns
Bunch length, rms, after compression	σ_z	~ 0.5	mm
Energy spread, rms single bunch	$\Delta E/E_{sb}$	~ 1	%
Energy spread, total on flat top	$\Delta E/E_{ft}$	≤ 1	%

RF – 3 GHz			
Number of MDK's	N_{MDK}	10 [3]	
Pulse duration from MDK nominal, (max)	τ_{MDK}	4.5 (6.7)	μs
Power per MDK	P_{MDK}	35 [4]	MW
Pulse compression gain nominal, (max)	G	1.9 (2.2)	
Pulse duration (compressed)	τ_{RF}	1.6	μs
Peak power (compressed)	P_{RF}	66	MW
Drive Beam Injector			
Sub-Harmonic Buncher (SHB) frequency	f_{SHB}	1.499	GHz
SHB power – total	P_{SHB}	400	kW
SHB voltages	$V_{SHB1,2,3}$	15.6, 16, 17	kV
Power for Pre-Buncher(PB), Travelling Wave Buncher (TWB) – total	$P_{PB} + P_{TWB}$	35	MW
PB voltage	V_{PB}	52	kV
Loaded gradient for TWB	$G_{I,TWB}$	10	MV/m
Phase velocity in TWB	β_p	0.71 to 1	
Power for each accelerating structure	P_{S1}, P_{S2}	35	MW
Loaded gradient	$G_{I,S1}, G_{I,S2}$	~ 6	MV/m
Drive Beam Accelerator (DBA)			
Frequency	f	2.99855	GHz
Number of structures	N_S	16	
Power/ structure	P_S	30	MW
Loaded gradient	G_I	6.533	MV/m
Structure length (flange-to-flange)	L_S	1.22	m
Number of cells (regular + couplers)	N_c	32+2	
Phase advance per cell		$2\pi/3$	
Shunt impedance (average)	$r'=R'/Q$	3200	Ω/m (linac)
Quality factor (average)	Q_{acc}	12800	
Group velocity (average)	$\beta_{g,acc}$	3.8 %	
Filling time	τ_{fill}	100.4	ns
Quality factor, first dipole (couplers)	Q_d	≤ 20 (≤ 1000)	
Off-crest operation	ϕ_{RF}	~ 5	degrees
Triplet cell length	$L_{TRIPLET}$	4.5	m
Triplet phase advances (hor. – vert.)	$\mu_{x,y}$	95.2 to 110.8	degrees
Transfer Lines			
Stretcher R_{56} (variable)	$R_{56\text{-}S}$	-0.2 to 0	m
Stretcher length (including matching)	L_S	7.4	m
DL to CR transfer line R_{56}	$R_{56\text{-}DTR}$	-0.16 to 0.16	m
DL-to-CR transfer line length	L_{DTR}	~ 30 m	m
Bunch Compressor R_{56} (tuneable)	$R_{56\text{-}C}$	0. to 0.3	m
Bunch Compressor length	L_C	~ 15 m	m
Delay Line (DL)			
Length	L_D	42	m
Combination factor	FC_D	2	
Momentum acceptance, total	$\Delta E/E_D$	5	%
Isochronicity (absolute value)	$\lvert\alpha_D\rvert$	$\leq 5\ 10^{-4}$	
Path length tuning - nominal (maximum)	ΔL_D	± 0.5 (± 3)	mm

Combiner Ring (CR)			
Circumference	C_R	84	m
Combination factor	FC_R	2 to 5	
Momentum acceptance, total	$\Delta E/E_R$	5	%
Isochronicity	$\lvert\alpha_R\rvert$	$\leq 10^{-4}$	
Path length tuning (for variable FC_R)	$\Delta L_{R,RF}$	± 12.5	mm
Path length tuning – nominal (maximum)	ΔL_R	± 0.5 (± 3)	mm
Vacuum chamber height (in bends)	h	36	mm
RF Deflector – Delay Line (sw)			
Frequency	f	1.499	GHz
Number of Cells	N_C	1	
Cell Length	d	8	cm
Total Length	L	0.08	m
Group Velocity	v_G/c	0	
Filling Time	τ_F	2500	ns
Deflection	ϕ	10	mrad
Input Power (150 MeV – 300 MeV)	P	1.41 to 5.1	MW
RF Deflectors - Ring			
Frequency	f	2.99855	GHz
Number of Cells	N_C	10	
Phase advance per cell		$2\pi/3$	
Aperture	$2a$	4.3	cm
Cell Length	d	3.3	cm
Total Length	L	0.33	m
Group Velocity	v_G/c	- 0.0244	
Filling Time	τ_F	46	ns
Shunt Impedance	R_s	17.35	MΩ / m
Series Impedance	$Z^{1/2}$	1.9	$k\Omega^{1/2}$ / m
Deflection	ϕ	5	mrad
Input Power (150 MeV – 300 MeV)	P	1.5 - 8	MW
Main Beam Injector			
Main beam energy	$E_{main,i}$	150	MeV

(1) Uncorrelated.

(2) Beam energy for the nominal current. The maximum energy for a very low current beam (same RF power, negligible beam loading) is ~ 300 MeV. A possible upgrade with two additional MDKs can bring the nominal beam energy up to ~ 180 MeV.

(3) 2 MDKs in the injector, 8 MDKs in the Drive Beam Accelerator. The last MDK in the accelerator provides also the power to the ring RF deflectors. Possible upgrade with two additional MDKs and four additional accelerator structures to bring the beam energy up to ~ 180 MeV.

(4) For the "standard" 35 MW tubes. Three of the tubes are 45 MW (two used in the injector, one used for the last two accelerating structures + ring RF deflectors). The nominal RF pulse at the MDKs output is 35 MW, 4.5 μs, compressed to 66 MW, 1.6 μs (power gain 1.9), corresponding to a power at the input of each structure of 30 MW (10% max losses in the RF network). A longer pulse from the MDKs, up to 6.7 μs, can possibly be used to further increase the available power.

5. ORGANISATION AND COLLABORATIONS

The project is based in the CERN PS Division, with collaborations from many other Divisions at CERN and the following outside institutes:

SLAC has supplied the triode assembly for the gun, ready for installation. SLAC also does the complete optics design and the detailed layout of the injector.

The two pre-bunchers are designed and manufactured by LAL, Orsay. In addition LAL is responsible for the design and manufacturing of the thermionic gun with all High Voltage equipment, using the triode supplied by SLAC. For the Preliminary Phase of CTF3 LAL has already built and delivered the electron gun.

The collaboration of INFN Frascati focuses mainly on the delay ring, the Combiner Ring and the transfer lines. This includes the optics design, development and supply of the RF deflectors, beam diagnostic and controls interface equipment, fast kicker and all magnetic elements. Wherever possible, existing magnets and power supplies will be used. An active participation in commissioning and exploitation of the facility is envisaged.

For the Photo Injector option the laser development is done in a collaboration with the Central Laser Facility of RAL, Didcot, UK and the Institute of Photonics of the University of Strathclyde, Glasgow, UK.

The Department of Radiation Sciences and the Signal and Systems Group of the Department of Material Sciences, both of the University of Uppsala, are collaborating with CTF3. The development of a microwave detector system has started, for measuring bunch length and longitudinal phase errors of bunches during the interleaving process. In addition active participation in commissioning of the Preliminary Phase of CTF3 is anticipated.

6. SCHEDULE AND CONSTRUCTION PHASES

CTF3 will be built in three phases, as shown in Figure 6.1. Experiments will be done at each phase while waiting for fabrication of the components for the next stage. The present planning is given in chapter 26.

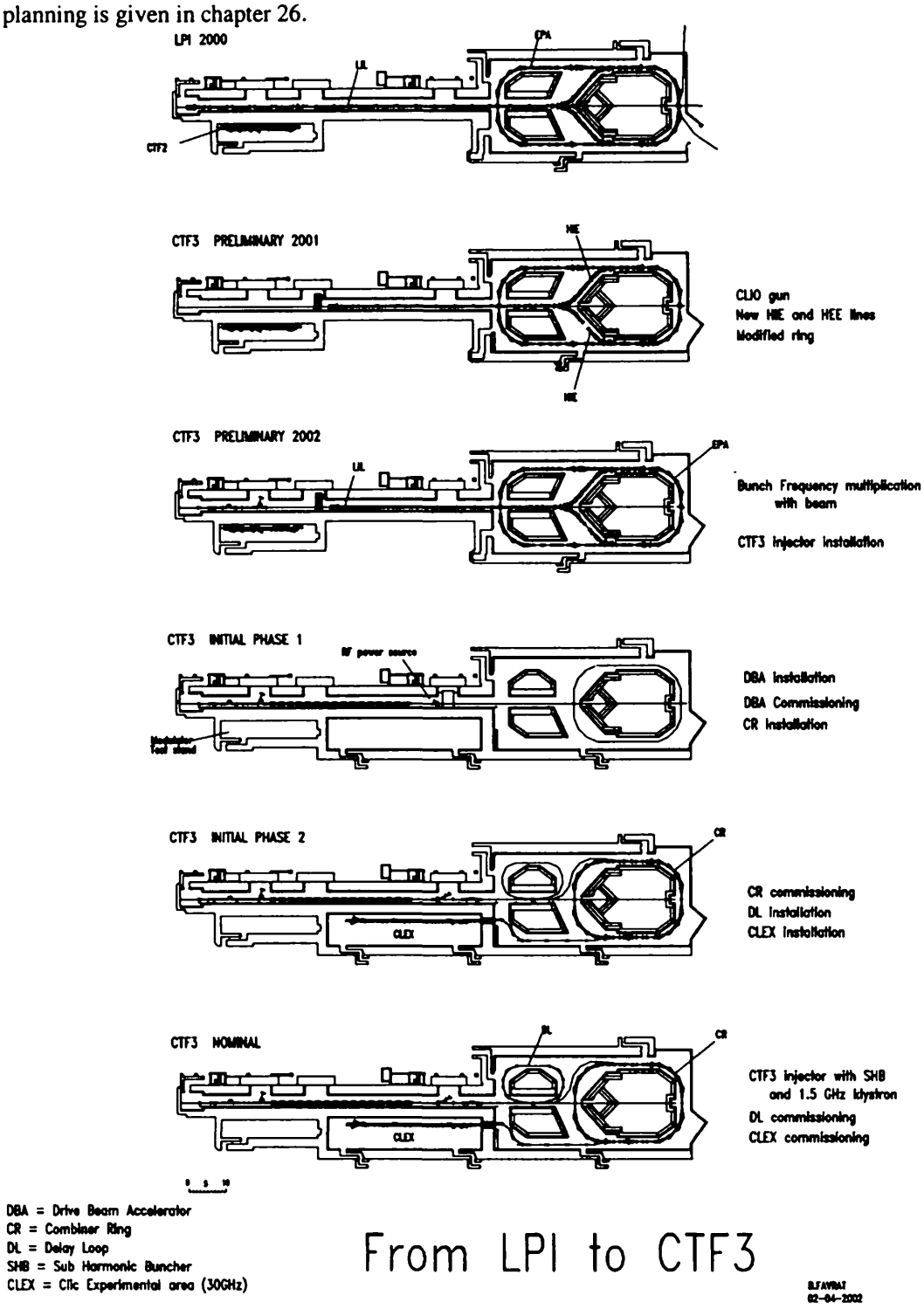

Figure 6.1 CTF3 construction phases from the present LPI to the Nominal phase

6.1 Preliminary Phase

The Preliminary Phase is described in a separate design report [1]. It makes maximum use of the existing LPI equipment. The new accelerating structures capable of handling the nominal beam current are not yet available, therefore only a reduced charge per bunch of 0.1 nC can be used.

The main purpose of the Preliminary Phase is to demonstrate injection into the ring using RF kickers as well as the multiplication of the bunch repetition frequency by a factor of five.

All the redundant LPI equipment for positron handling and the connections to the PS have been removed. The lattice of the Combiner Ring was made isochronous, this required moving some magnetic elements as well as shortening the circumference by 17 mm. The transfer line between linac and ring was also modified to obtain a small R_{56}. RF deflectors will be installed. In order to reduce beam loading, eight of the 16 LIL accelerating structures have been removed. A new thermionic gun was installed, allowing five bunch bursts with a spacing equal to the EPA circumference. A temporary shielding wall was mounted, allowing installation and commissioning of the new injector for the later phases independent of Preliminary Phase operation.

The new thermionic gun produced by LAL under a collaboration agreement was delivered in June 2001.

Commissioning of the Preliminary Phase started in September 2001 and exploitation will last until end 2002.

6.2 Initial Phase

From spring 2003 onwards, the new drive beam accelerating structures will be installed. As soon as the injector and the linac are commissioned, a test stand for 30 GHz power testing will be installed after the linac (see section 21).

The injector will be slightly different from the final configuration, since the three sub-harmonic bunchers will not yet be available.

The Combiner Ring will be installed and tests of bunch combination can be done at reduced bunch charge.

This phase will be exploited until the components of the Nominal Phase become available.

A separate report will describe the details of this phase.

6.3 Nominal Phase

This final configuration of CTF3 is described in this report. The sub-harmonic bunchers and their RF power source will be installed, as well as the Delay Loop with the 1.5 GHz RF deflectors.

The test stand as well as the test beam will be installed after commissioning of this phase.

6.4 References

[1] CTF3 Design Report , Preliminary Phase, CERN/PS 2001-072.

7. CTF3 INJECTOR

CTF3 will be built in stages, with different injector requirements for the Initial and Nominal Phases. In both cases the injector is defined as from the gun through the second accelerator section, with a variety of systems in the sub-relativistic region. Previous work for the injector is published in [1]. The electron beam requirements for both phases are described in Table 7.1.

This report describes the injector for the Nominal Phase, the most difficult stage for CTF3 and the most advanced stage for the proof of principle experiments. The Initial Phase is a derivative of the Nominal Phase and will be described in a later report. In the Nominal Phase the bunch repetition rate is 1.5 GHz and 3.5 A of useable current is required at the end of the second accelerator section. For the "usable current" only the charge of single bunches within 20° of longitudinal phase space is taken into account.. The charge in the satellite bunches one S-band cycle away should be less than 7%.

Table 7.1 Electron beam target parameters at the exit of the Injector for Initial and Nominal Phases of CTF3

Parameters	Initial	Nominal	Unit
Beam Energy	≥20	≥20	MeV
Pulse Length	1.54	1.54	μs
Beam Current	3.5	3.5	A
Charge per pulse	4893	4893	nC
Bunches/pulse	4200	2100	
Charge per bunch	1.17	2.33	nC
Allowed charge in Satellite		<7	%
Bunch Spacing	0.1 0.33	0.2 0.67	m ns
Bunch Length (FWHM)	< 12	< 12	ps
Bunch Length (rms)	< 1.5	< 1.5	mm
Emittance, N, rms	< 100	< 100	mm mrad
Energy spread (single bunch rms)	< 0.5	< 0.5	MeV
Energy spread (total on flat top incl. Beam loading)	< 1	<1	MeV
Charge Variation bunch to bunch (High Frequency)	< 2	< 2	%
Charge Flatness total on flat top (Low Frequency)	< 0.1	< 0.1	%
Beam Repetition Rate	5	5	Hz
RF Repetition Rate	30	30	Hz
RF Fundamental Frequency	2.99855	2.99855	GHz
RF Peak Power into TW Buncher	35	35	MW
RF Peak Power into accelerator	35	35	MW

The injector for the Nominal Phase consists of a thermionic gun, three 1.5 GHz sub-harmonic bunchers (SHB), an S-band prebuncher (PB), a tapered phase velocity travelling wave buncher and two 1 m long accelerating sections, all at 3 GHz. This is schematically shown in Figure 7.1. The transverse beam size is controlled with solenoids and the beam orbit with steering coils. Various beam diagnostics devices are foreseen for tuning and characterising the electron beam from the injector. Figure 7.2 shows the injector block diagram for the Nominal Phase. Simulations of the injector were conducted using EGUN for the gun, SUPERFISH for the buncher and accelerating cavities, and PARMELA for the beam dynamics through the injector.

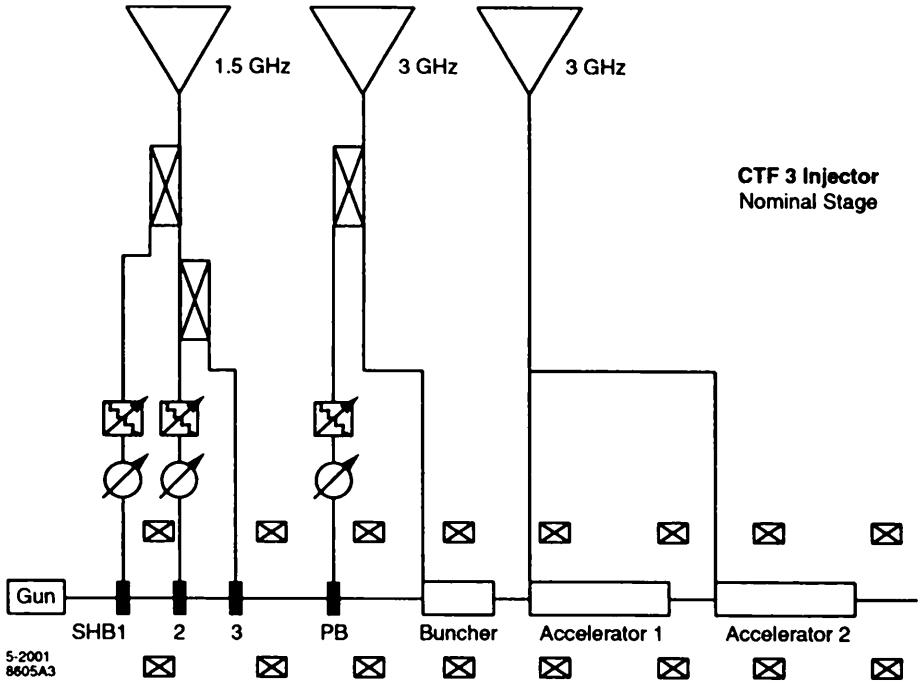

Figure 7.1 Schematic of the thermionic injector layout. SHB: Sub-harmonic buncher, PB: 3 GHz Pre-buncher.

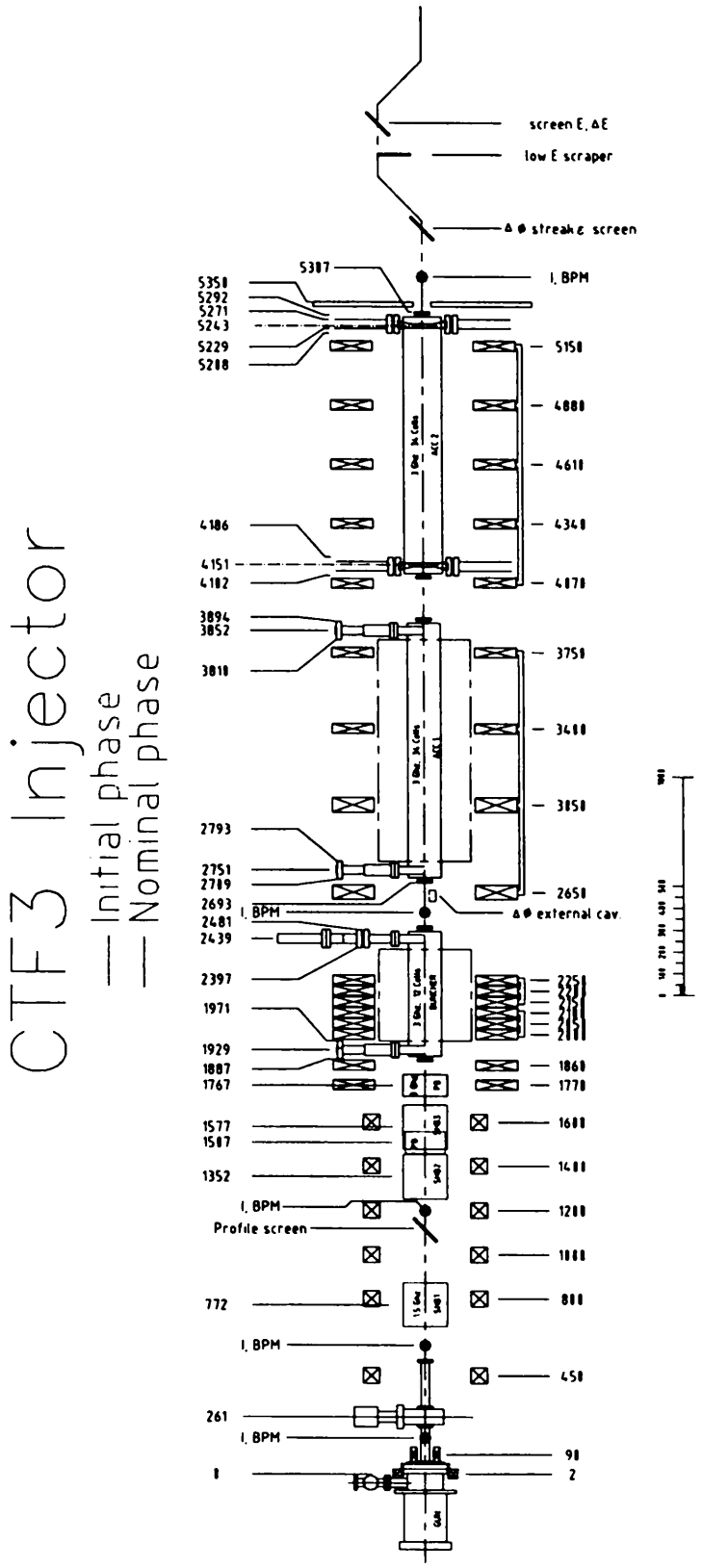

Figure 7.2 CTF3 Nominal Phase Injector block diagram.

7.1 The Electron Gun

A Thermionic electron gun with Pierce type electrodes will be used. The gun was built by Hermosa Electronics and it employs a 2 cm^2 gridded cathode, made by EIMAC. It has been processed up to 160 kV at SLAC and delivered to CERN on a long term loan basis. The gun was designed for 9 A space charge limited current at 140 kV, which may be needed for very high current running conditions in the Initial Phase. However for the Nominal Phase the required current from the gun is 5 A according to the bunching and beam transport simulation results from PARMELA.

The gun electrode geometry and spacing was designed using EGUN. The electron beam parameters for the various conditions of gun operation were calculated using the emittance due to geometry and thermal effects from EGUN simulations plus the emittance due to grid focusing effects when running in grid limited mode at currents lower than 9 A for 140 kV. Figure 7.3 shows the EGUN ray trace for 5 A operation and Table 7.2 lists the electron beam parameters for various types of gun operation.

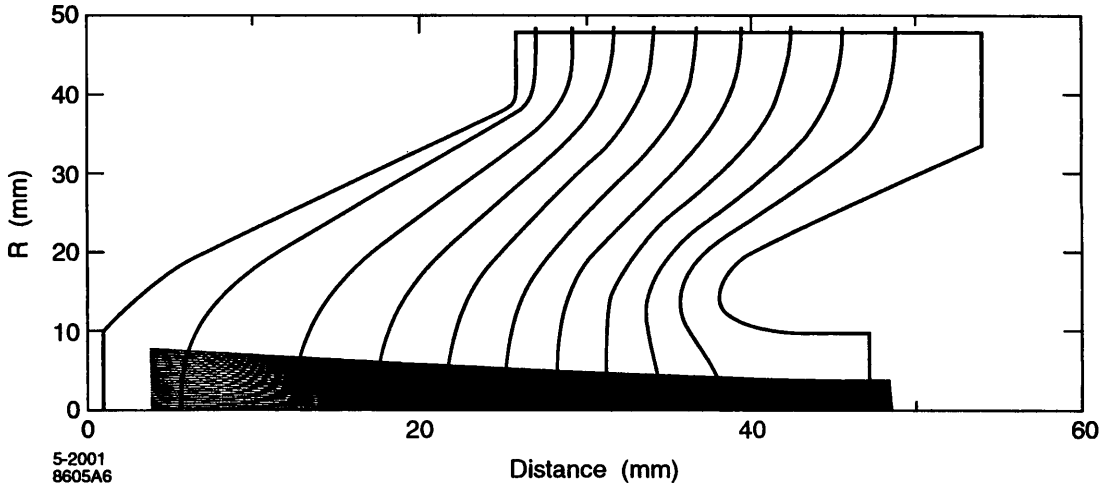

Figure 7.3 CTF3 gun ray trace from EGUN. 5 A, 140 kV grid limited mode.

Table 7.2 Electron Beam characteristics from the CTF3 gun for various electron beam currents I and operating voltages V

I	5	7	9.3	10.4	A
V	140	140	140	150	kV
$\varepsilon_{edge,N}$, includes thermal & grid effects	26	20	13	14	mm mrad

The gun pulser should be able to deliver the train of pulses given in Figure 7.4, Table 7.3 gives the CTF3 gun characteristics.

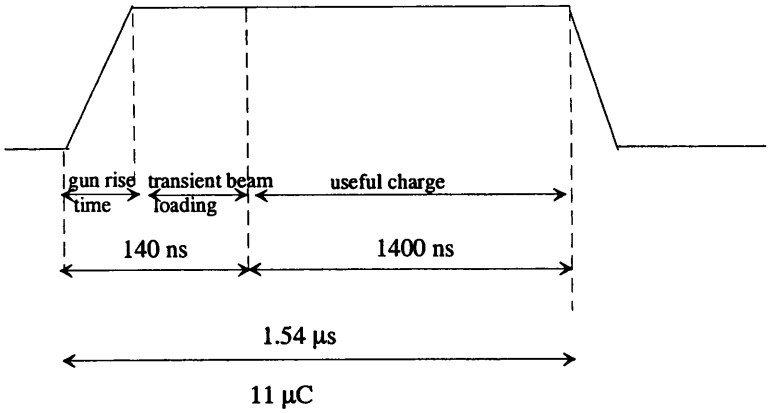

Figure 7.4 Pulse at the CTF3 gun exit

Two scenarios are required:

a) short flat-top 20 – 300 ns

b) long flat-top 200 – 1600 ns.

The nominal characteristics are for the long flat-top and are given in Table 7.3.

Table 7.3 Parameters for the CTF3 gun for the nominal working point

Parameters	Initial and Nominal	Unit
Voltage (Running)	140	kV
Voltage (Conditioning)	160	kV
Pulse flat-top	200 to 1600	ns
Gun current	6	A
Max. mean current	0.5	mA
Rise / Fall time	≤ 20	ns
Current flatness on flat top	≤ 0.1	%
Voltage stability ΔV/V for 200 to 1600 ns (flat-top)	≤ 0.1	%
Repetition rate	5 (*)	Hz

(*) The nominal repetition rate is 5 Hz. The pulser will be able to operate up to 100 Hz. Under these conditions the voltage and current stability are relaxed to ±1%.

The gun electronics includes two power stages to create the electron pulses. The first stage consists of a pulse generator with an output of –850 V and pulse widths between 100 ns to 2 μs. The second stage consists of a power triode whose output is applied to the gun cathode. The advantage of this approach is that the triode tube isolates the upstream solid–state electronics in the event of high voltage breakdown in the gun. Additional pulses can be applied to the triode grid (slope correction, amplitude feed back, current modulation). Operation and monitoring of the gun electronics is performed by fibre-optic connections between the control system and the high voltage deck. A schematic of the gun electronics is shown in Figure 7.5.

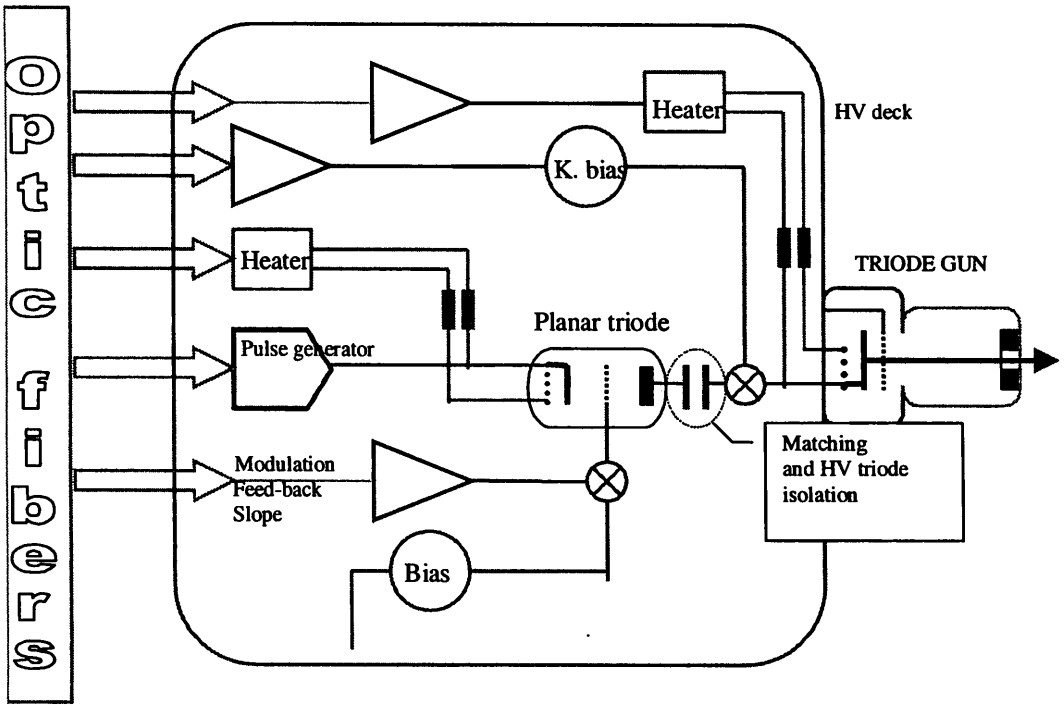

Figure 7.5 Schematic of the electronics for the gun.

7.2 The High Voltage System for the Electron Gun

The specifications shown in Table 7.3 determine the characteristics of the HV system. The electric charge Q in each gun pulse is: $Q = T_{pulse} \cdot I_{peak} = 1.6\,\mu s \cdot 6\,A = 9.6\,\mu C$. This charge Q is supplied to the gun by the HV system during the pulse duration. The same charge has to be accumulated by the HV system during the dead time between 2 pulses (200 ms). The use of a single power supply to obtain this charge is possible but the characteristics of this type of power supply would make it very expensive. Considering that the rise time of the pulse is less than 20 ns and the current during the pulse is 6 A, the power supply would need to be very fast and very large (6 A at 140 kV). Another solution, more classical and less expensive, is to put an HV capacitor between the power supply and the gun for energy storage. This solution allows a power supply of lower current and longer time response. The capacitor supplies the electric charge to the gun which implies a voltage drop ΔV during the pulse. This voltage drop must be less than 1 % of the working voltage of the gun, i.e. 1.4 kV. The charge Q involved during the pulse is $Q = C \cdot \Delta V$ as seen from capacitor side, which must equal 9.6 μC as seen from gun pulse side. Therefore we require a minimum capacity of C = 7 nF. The power supply necessary to charge the capacitor must have a voltage rating higher than the working voltage of the gun. It also has to supply the required charge to the capacitor between successive pulses. This means:

$$Q = I_{supply} \cdot 200\,ms = 9.6\mu C$$

This implies a charging current of ~ 50 μA. Finally, a 160 kV, 1 mA power supply is sufficient for the needs of the CTF3 gun.

Electrical breakdown in guns normally occurs during the first period of commissioning. Little information exists about the energy that can be tolerated by the guns in such discharges.

The experience of people working with pulse discharges in vacuum conditions similar to those of electron guns (10^{-9} mbar) estimate the voltage of such arcs to be about 50 to 100 V. The energy dissipated in these arcs can be minimised by limiting the current by the use of a non-inductive resistor, placed between the capacitor and gun. A resistor of 500 Ω limits the current to 280 A. A voltage drop of 4.5 kV would occur for operation at 9 A gun current. This has to be taken into consideration when fixing the power supply voltage with respect to the gun operating voltage.

The energy of the breakdown depends only upon the arc voltage (gun side). Simulations show that it is about 50 mJ for 140 kV and 280 A and the duration of the breakdown is less than 170 μs.

The rise and fall time of the pulse depends upon the value of the inductance of connections between the different elements of the HV system. Connections to earth are also very important. Simulation of the HV circuit were done to determine the maximum allowed inductances.

The elements of the HV system can be summarised as follows:

(i) A 160 kV, 1 mA DC power supply of negative polarity
(ii) A 7 nF capacitor of 145 kV working voltage and 160 kV maximum voltage. This capacitor is used as an energy storage capacitor, the voltage drop in operation is about 140 V.
(iii) A HV terminal box, of outer dimensions 600 mm x 600 mm x 600 mm to contain the hardware of the gun.
(iv) A HV resistor of 500 Ω / 160 kV, which is non-inductive. It is used to limit the energy dissipation in the gun during breakdown and is placed between the reservoir capacitor and the terminal box of the gun.
(v) A HV resistor of 25 to 30 kΩ /160 kV between the reservoir capacitor and the power supply. This is used to protect the power supply.
(vi) Earthing equipment; a HV relay with a current limiting resistor.
(vii) Equipment for personnel safety against HV hazards.
(viii) An isolation transformer of rating: 230 V / 230 V - 500 VA with the secondary isolated up to 160 kV.

Inductances between all connections are minimised.
A schematic of the HV system is shown in Figure 7.6.

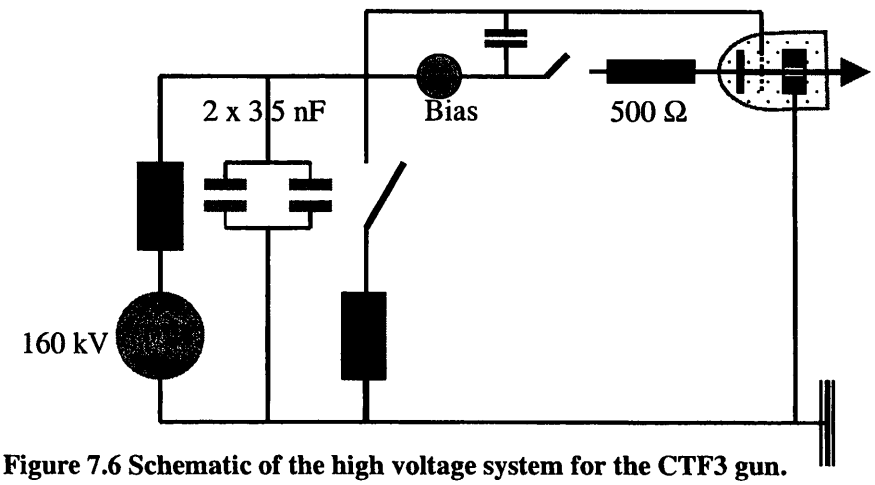

Figure 7.6 Schematic of the high voltage system for the CTF3 gun.

7.3 Standing wave bunchers and travelling wave structures.

The bunching system consisting of three 1.5 GHz sub-harmonic bunchers, one S-band pre-buncher, one 17-cell tapered phase velocity travelling wave buncher, is followed by two travelling wave accelerating sections. The gap voltage in the standing wave bunchers and the gradient in the travelling wave sections were chosen to optimise bunching, keeping in mind the beam loading in these sections as well as the need to minimise the charge in the satellite S-band buckets. SUPERFISH was used to characterise the fields in these cavities, and to calculate space harmonics for the fields to be used in PARMELA.

The design is based on a total available power at 1.5 GHz of 700 kW and a maximum available power for the travelling wave buncher and the accelerator sections of 35 MW. Table 7.4 shows the steady state gap voltage needed for bunching in the standing wave cavities including beam loading compensation. Table 7.5 and Table 7.6 show the gradients in the travelling wave buncher sections and the accelerating structures including beam loading. The accelerating structures will be the prototypes of the TDS and the SICA designs (see paragraph 9.2) built at CERN.

Table 7.4 The gap voltage in the standing wave structures after beam loading compensation for 5 A

Buncher type	**Frequency** (GHz)	**Gap Voltage** Simulated (kV)	**Gap Voltage** Design for (kV)
SHB 1	1.5	20	40
SHB 2	1.5	20	40
SHB 3	1.5	24	40
PB	3	52	60

Table 7.5 The gradient in the 3 GHz tapered phase velocity travelling wave buncher taking into account 5 A beam loading and 35 MW available input power.

Cavity #	Phase Velocity $\beta (v/c)$	Gradient (MV/m)
1	0.71	8.37
2	0.76	9.34
3	0.82	10.06
4	0.88	10.60
5	0.94	11.00
6	1.0	11.25
7	1.0	11.36
8	1.0	11.36
9	1.0	11.30
10	1.0	11.21
11	1.0	11.11
12	1.0	11.01
13	1.0	10.94
14	1.0	10.88
15	1.0	10.84
16	1.0	10.80
17	1.0	10.73

Table 7.6 The gradient in the 3 GHz travelling wave accelerator structures taking into account 4.5 A beam loading and 35 MW available input power.

Cavity #	Gradient (MV/m)
1	11.40
2	11.34
3	11.26
4	11.17
5	11.06
6	10.92
7	10.76
8	10.59
9	10.38
10	10.14
11	9.89
12	9.59
13	9.35
14	8.90
15	8.49
16	8.04
17	7.57

Cavity #	Gradient (MV/m)
18	7.04
19	6.46
20	5.88
21	5.21
22	4.51
23	3.80
24	3.01
25	2.19
26	1.38
27	0.51
28	-0.43
29	-1.32
30	-2.16
31	-3.29
32	-4.28
33	-4.51
34	-6.83

The design of the 3 GHz pre-buncher is based on the experience of the pre-bunchers used in LIL. However, the waveguide coupler is made from full height waveguide rather than the tapered waveguide used in LIL. Consequently the coupling aperture is larger and the cavity therefore had to be slightly re-dimensioned to maintain the 3 GHz resonant frequency. The cavity has been modelled using HFSS (quality factor) and SUPERFISH (shunt impedance). A schematic of the cavity is shown in Figure 7.7 with the dimensions given in Table 7.7. To reduce beam loading effects the cavity is machined from stainless steel. Even so, calculations show that the beam loading at 9 A beam current corresponds to 80 kV which exceeds the generator voltage of 60 kV. To reduce the beam loading the cavity has an external load mounted diametrically opposite to the input coupler.

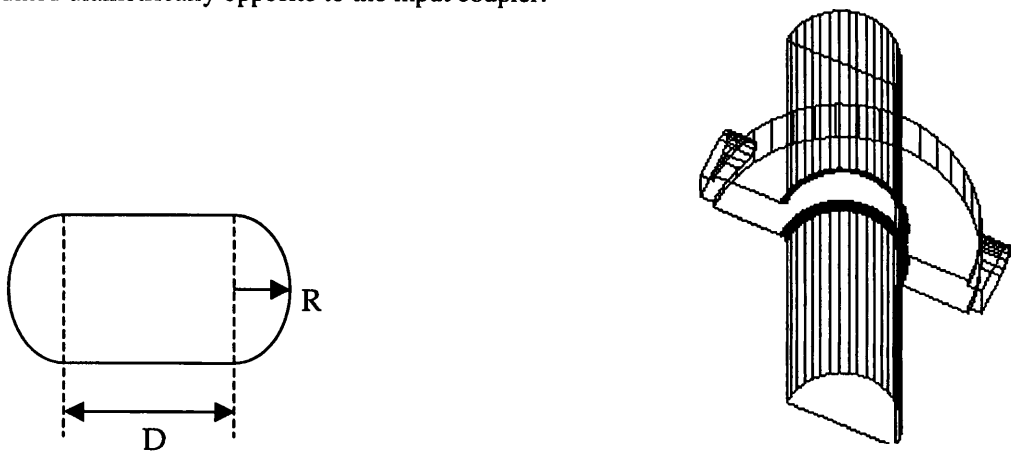

Figure 7.7 Left: form of the coupling aperture: Right: HFSS model of the pre-buncher. The dimensions are summarised in Table 7.7.

Table 7.7 Pre-buncher dimensions

Cavity	Radius (mm)	39.8
	Height (mm)	18
	Cut-off length (mm)	30
	Cut-off diameter (mm)	34
Coupling aperture	R (mm)	6
	D (mm)	26

7.4 Nominal Phase injector beam line simulations

PARMELA was used for calculating the beam dynamics, using the parameters from EGUN and the cavity space harmonics from SUPERFISH as input. Special attention was given to maximising the charge in a 20 degree longitudinal phase space, minimising the charge in the S-band satellites, and minimising the emittance while maintaining the strength of the solenoid field at a reasonable level. It is possible to reduce the charge in the satellite bunches by about a factor of two if a third type of buncher (4.5 GHz) is introduced after the 3 GHz pre-buncher. However, at this stage we have decided to postpone this option to save time and funds in the development of a driver for such a cavity.

The bucking lens at the gun which has a longitudinal magnetic field in the opposite direction from all the other coils, is used to reduce the magnetic field at the cathode to less than 1 Gauss. The longitudinal magnetic field ramps up to about 2 kGauss at the tapered phase velocity buncher as the beam is bunched, focused and accelerated. A 1.7 kGauss longitudinal magnetic field is needed over the downstream portion of the injector to maintain the beam size and emittance. The simulated magnetic field and emittance profile are shown in Figure 7.8. The beam envelope achieved in the injector for the Nominal Phase with this magnetic field profile is shown in Figure 7.9.

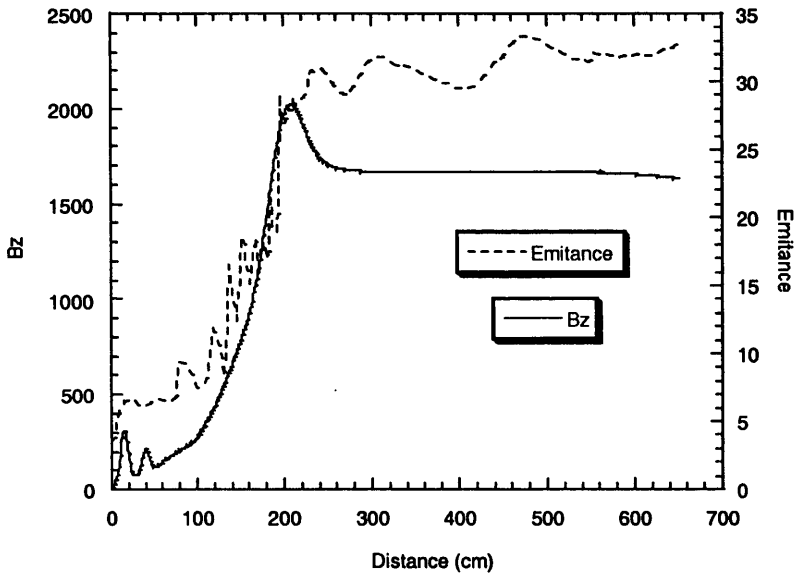

Figure 7.8 The longitudinal magnetic field (in Gauss) and the beam transverse normalised rms emittance in mm mrad along the CTF3 Nominal Phase injector.

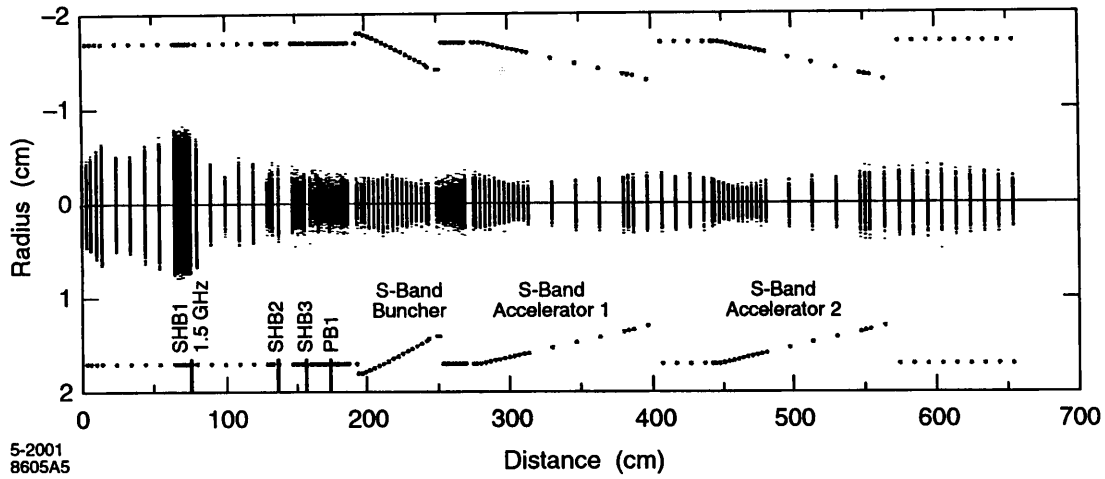

Figure 7.9 Beam envelope in the Nominal Phase injector from PARMELA simulations

Simulations show that with a beam of 5.1 A from the gun it is possible to capture 3.5 A, defined as the charge in 20° of S-band in the main bunch at 17 MeV at the end of the second accelerating structure. The normalised rms emittance at the end of the second accelerator structure is less than 35 mm mrad. The bunch length is 12° FWHM, and the uncorrelated energy spread is about 200 keV, i.e. about 0.1% of the final linac energy. If the beam is accelerated at the crest, the FWHM energy spread due to the 12° FWHM bunch length is 0.5%. The capture into 20° longitudinal phase space is about 72% of the available charge at the end of the second accelerating section, and the charge in 20° of the S-band satellite is about 8% of the charge in 20° of the main bunch. The total current accelerated to the end of the second accelerating section is about 4.9 A based on the simulations which do not take into account any orbit deviations from the centreline. In practice the very low energy particles in the tail are expected to be lost before the end of the travelling wave buncher and the current in the first and second accelerator sections is expected to be about 4.5 A, in which case the current due to the charge in 20° of the main bunch will be about 78% of the total available current. The simulated single bunch characteristics at the end of the injector are shown in Figure 7.10 and tabulated in comparison to the requirements in Table 7.8.

Table 7.8 Simulated single bunch beam characteristics at the end of the second accelerator section in the CTF3 Nominal Phase injector

Parameters	Unit	Nominal Phase Target Parameters	Simulation At end of acc. 2
Beam Energy	MeV	≥ 20	17.2
Beam Current in 20°	A	3.5	3.5
Charge per bunch in 20°	nC	2.33	2.33
Allowed charge in Satellite	%	< 7	8
Bunch Length (FWHM)	ps	< 12	12
Emittance, N, rms	mm mrad	< 100	35
Energy spread (single bunch rms)	MeV	< 0.5	0.5
RF Fundamental Frequency	GHz	2.99855	2.99855
RF Peak Power into TW Buncher	MW	35	35
RF Peak Power into accelerator	MW	35	35

7.5 Steering coils and Diagnostics

In order to tune the injector and to demonstrate the characteristics of the beam it is necessary to equip the injector with steering coils and a variety of diagnostics. To make the solenoid alignment simple, the steering coils should be able to compensate for approximately 4 mrad of solenoid tilt.

The diagnostics in the injector include current monitors, position monitors, profile monitors, bunch length monitors, emittance measurement station, energy and energy spread measurement station and low energy tail scraper. Figure 7.2 shows the layout of this diagnostics.

7.6 Summary

The Nominal Phase injector for the CTF3 has been designed using realistic achievable components. The Initial Phase CTF3 injector is a derivative of the Nominal Phase with the sub-harmonic bunchers missing and an added S-band buncher. The space between the gun and the travelling wave buncher is the same as for the Nominal Phase. The Initial Phase injector will be fully described in a future report.

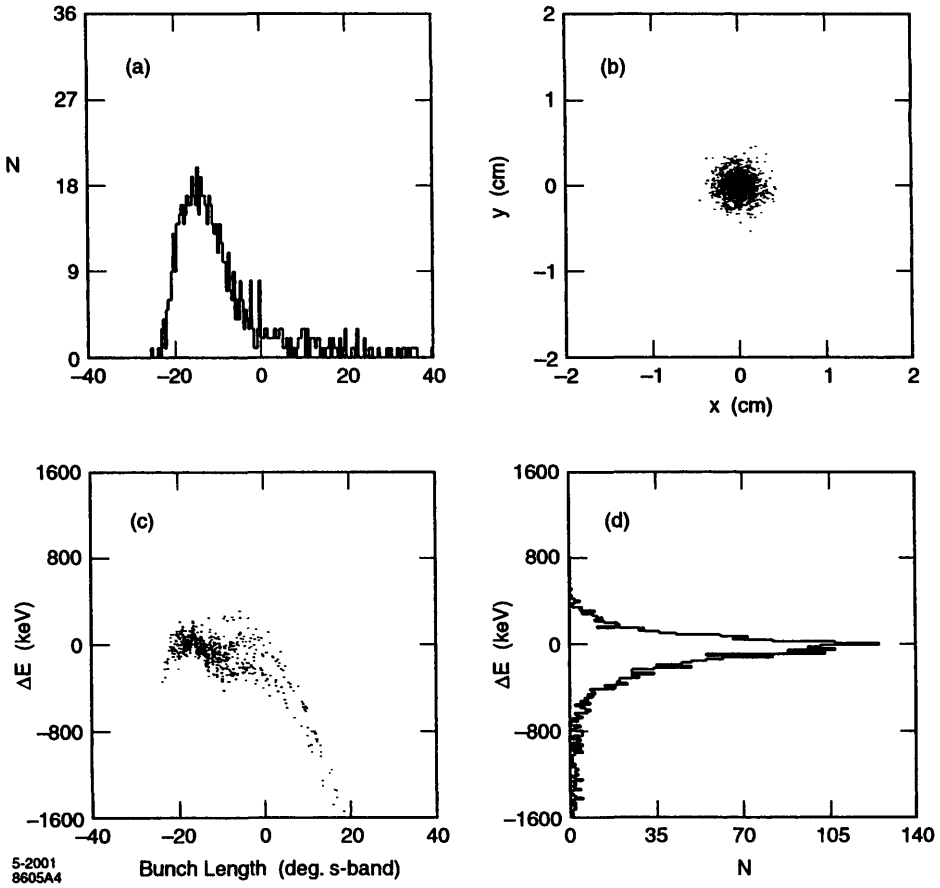

Figure 7.10 The simulated single bunch beam parameters at the end of the second accelerating section for the CTF3 Nominal Phase. a) bunch current profile, b) bunch transverse distribution, c) bunch longitudinal distribution, d) bunch energy spread.

7.7 References

[1] H.Braun et al., "An Injector for the CLIC Test Facility (CTF3)", XX International Linac Conference, , Monterey 2000, CERN/PS 2000-052

8. DRIVE BEAM PHOTO-INJECTOR OPTION

8.1 Motivation for a drive beam photo-injector

Although the reference design of CTF3 and CLIC assumes a thermionic drive-beam injector [1], an option for a photo-injector [2] is kept open because of the following advantages:

- flexibility in manipulating the time structure of the beam because laser beams can be switched faster than electron beams in a thermionic high-voltage gun. This is important for minimising transient beam-loading in the CLIC main beam [3].
- no problems with parasite charges in the supposedly empty RF buckets (in the drive-beam linac only every second bucket is populated, however it is difficult to get zero charge in the "empty" buckets with a conventional bunching system). This unwanted charge can cause considerable radiation problems and efficiency loss.
- smaller transverse and longitudinal emittance and thus easier beam transport and bunch length manipulation.
- smaller longitudinal emittance and therefore easier bunch length manipulation in the downstream systems.
- no low-energy tails at the end of the injector.

8.2 CTF3 Drive Beam Requirements

Table 8.1 shows some of the CTF3 drive beam injector parameters. The main challenges are to build a laser capable of delivering adequate light to the RF gun, and to produce photo-cathodes that are able to produce the required electron beams.

Table 8.1 : CTF3 Drive Beam Parameters

	Unit	CTF3
Pulse charge	nC	2.33
Pulse width (FWHH)	ps	10
Peak current	A	240
Number of pulses	-	2310
Distance between pulses	ns	0.667
Charge stability	%	± 0.1
Train duration	μs	1.54
Train charge	μC	5.4
Repetition rate	Hz	5
Mean current	mA	0.026
Minimum QE at λ_{laser}	%	1.5
Minimum lifetime at QE_{min}	h	100
Shots during lifetime	x 10^9	3.9
Photo cathode produced charge	C	10
Mean Laser power at the cathode	W	0.008

8.3 Past Experiences in CTF2

Laser driven photo-injectors have been used in the CTF2 since its inception. The CTF2 laser system is a Chirped Pulse Amplification system using a 250 MHz mode locked oscillator, one regenerative and two single pass amplifiers optically pumped by flash lamps. The near-infrared light is frequency quadrupled to UV (λ=262 nm) which is then split into 48, 10 ps pulses by an array of semi-reflecting mirrors. These are sent to the cathode of the drive beam RF gun. The residual green light is converted to produce a single UV pulse which illuminates the cathode of the probe beam RF gun [4]. For the CTF2 drive beam, an RF gun with a Cs-Te cathode is routinely used to produce a bunch train with bunch-charges of up to 15 nC. The

field gradient on the cathode surface is 100 MV/m. Cs-Te cathodes offer quantum efficiencies (QE) of over 1.5 % with lifetimes varying from at least some weeks to typically months. Since the production of UV light is relatively simple, this kind of cathode becomes more attractive. The cathodes for CTF2 are produced in a dedicated laboratory, where their QE is measured in a DC gun. They are then brought under ultra-high-vacuum to the accelerator. The cathode for the probe beam is CsI+Ge, which can be transported in air [5].

8.4 CTF3 RF gun design

The design for the RF gun (see Figure 8.1) is based on the existing CTF2 drive beam gun [6]. However, to cope with the heavy beam loading of CTF3 the RF coupling factor β has to be increased. With the parameters given in Table 8.2 this will allow an equilibrium between the power taken by the beam, ohmic losses in the cavity and the input power provided by the klystron.

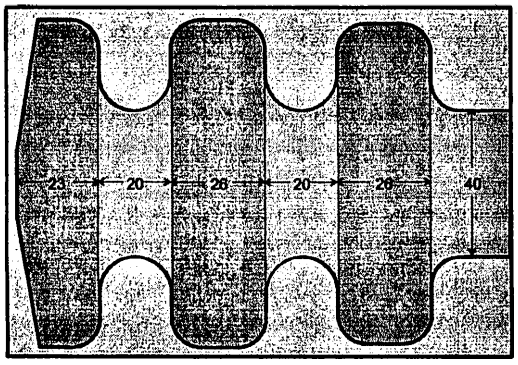

Figure 8.1: The RF gun

RF frequency	2.99855 GHz
RF power	30 MW
Beam energy	5.6 MeV
Beam current	3.5 A
Peak field on cathode	85 MV/m
Unloaded Q	13000
Coupling factor β	2.9
Delay beam /RF	400 ns

Table 8.2 : The RF gun parameters

8.5 The laser

The laser system for the photo-injector has a number of challenging operating parameters. Namely the necessity to produce a 1.54 μs pulse train having high average power, low intensity jitter, synchronisation to the RF to <1 ps, pulse train timing modulation necessary for the RF manipulation of the electron beam in the CLIC scheme [1] and high operational reliability. Other parameters are mentioned in Table 8.1.

A feasibility study [7] concluded that the operating parameters could best be achieved with an all solid-state system consisting of a diode-pumped mode locked oscillator and power amplifier system that operates around 1 μm, which is frequency quadrupled.

Nd:YLF operating at 1047 nm was selected for the laser material as it offers a combination of several important properties. These are the high extraction efficiency, good optical quality in large pieces and low thermal distortion. Tests are underway to improve the IR to UV conversion efficiency of 10 % since this directly affects the diode power needed.

8.5.1 The Oscillator

The laser oscillator will be passively mode locked using a saturable Bragg reflector (SBR) providing a mode locked ps pulse train with the same reliability as a cw laser. The greater the power available from the oscillator system, the less complex the amplifier system can be, therefore work has started on a high-power mode locked oscillator. For the laser oscillator, the following set-up is being prepared for tests (see Figure 8.2).

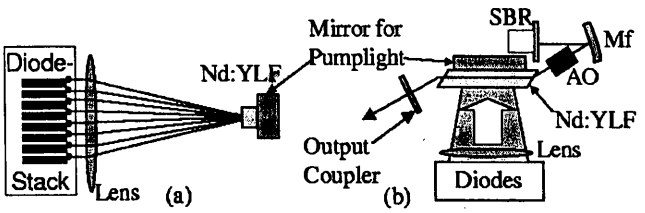

Figure 8.2 Schematic overview of the laser oscillator set-up. (a) Side view of the pump geometry. (b) Top view of the oscillator (Mf - curved folding mirror, AO - acousto-optic modulator).

The laser crystal is a 12 mm long brick with Brewster faces. The crystal is side-pumped by a stack of 8 fast-axis collimated diode arrays that can produce a total power of 300 W. The diode arrays will be operated in a quasi-cw mode for approximately 200 μs. The resonator will be a three-mirror folded cavity with a curved fold mirror to reduce the mode size on the SBR. Since the oscillator cavity length determines the repetition rate of the mode locked train, the laser pulses can be synchronised to an external clock by active control of the cavity length using a piezo-mounted mirror. A faster way of length modulation of the cavity might be required in order to be able to fully operate the mode locked laser in quasi-cw mode. This will be part of the investigation. In this way it is hoped that over 50 W of average output power over the macro-burst can be produced.

8.5.2 The Amplifier Chain

It is planned to install three amplifiers, as shown in Figure 8.3. The first two operate in double pass, the third in a single pass and saturated mode, which efficiently extracts the absorbed pump power. In total 40 kW of diode pump power will be installed [7], assuming a minimum photo-cathode QE of 1.5 %. The basic design of the single amplifier heads is a 5-fold, symmetrically side pumped rod configuration, with a Nd:YLF rod of 1 cm diameter, surrounded by water and a silica tube, which reflects non absorbed pump light back into the rod. This should give an absorption efficiency of 85 %. A test amplifier is currently assembled at RAL. With 5 kW pump power operated in quasi-cw mode, this amplifier head will be used to verify several important aspects of the design [7].

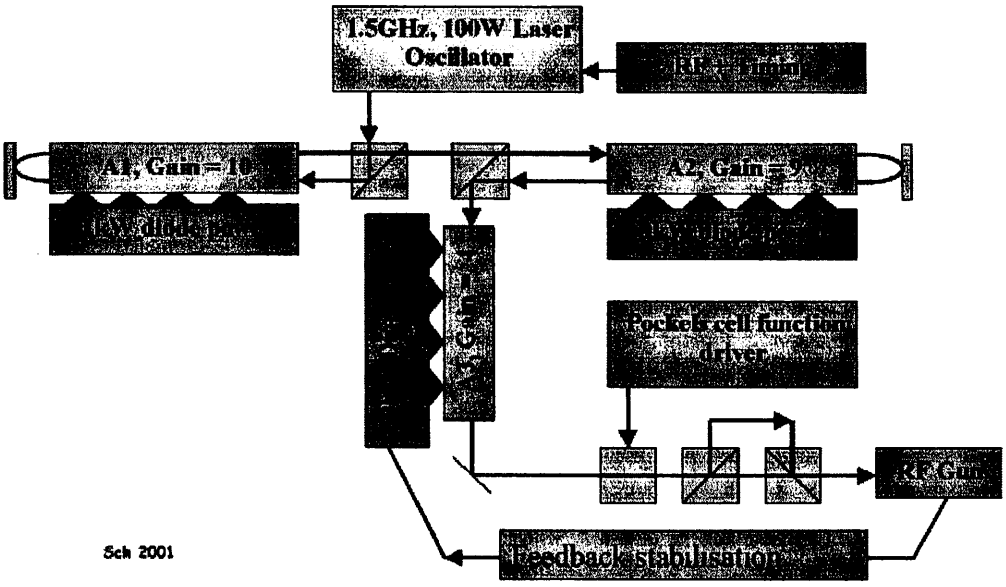

Figure 8.3 CTF3 Laser system

8.6 Photo-cathodes

8.6.1 High average current test

Since the laser for the CLIC drive beam seems feasible, the question remained whether the Cs-Te cathodes would sustain the production of a high-average-current electron beam, under illumination with a high-power-laser beam. Photo-cathode tests in an RF gun would require the laser system that is still currently under development [7], therefore the test was conducted in a DC gun [8]. The laser was an intracavity frequency quadrupled Nd:YLF. Table 8.3 summarises its main parameters and the results of the test. The current delivered by the power supply, the laser power and the vacuum level were measured in real time, the laser spot size on the cathode was controlled at regular intervals. With an increase of laser power, the QE increased slightly. This is a hint that the laser light cleans the cathode from contamination by the rest gas, an assumption which could be verified by the distribution of the QE over the cathode, shown in Figure 8.4. The QE suffered less on the spot the laser hit, with respect to regions that weren't cleaned by the laser and poisoned by the rest gas. We produced a total charge of 1 kC in this configuration at an average current of 751 μA. (750 nC at 1 kHz). The test was stopped after 370 h, during which all CTF3 photo-cathode parameters were demonstrated.

8.6.2 High current density test

The same cathode was then used to conduct a high current density test, during which the laser was focused to a spot size of 3.34 mm^2. The cathode produced 220 C with an average current of 701 μA, delivering an average current density of 21 mA/cm^2. Assuming that this is the maximum current density obtainable for this cathode material, a cathode for CLIC would require a diameter of 2.1 cm, which is feasible for a 469 MHz RF gun.

Table 8.3 Results of the high average current test

	Unit	High Q test
Pulse charge	nC	950
Pulse width	ns	100
Peak current	A	7.5
Repetition rate	Hz	1000
Mean current	mA	0.95
τ_{min} at QE = 1.5 %	h	460
Number of shots during τ_{min}	x 10^9	4
Total produced charge	C	1220
Laser mean power	W	0.3

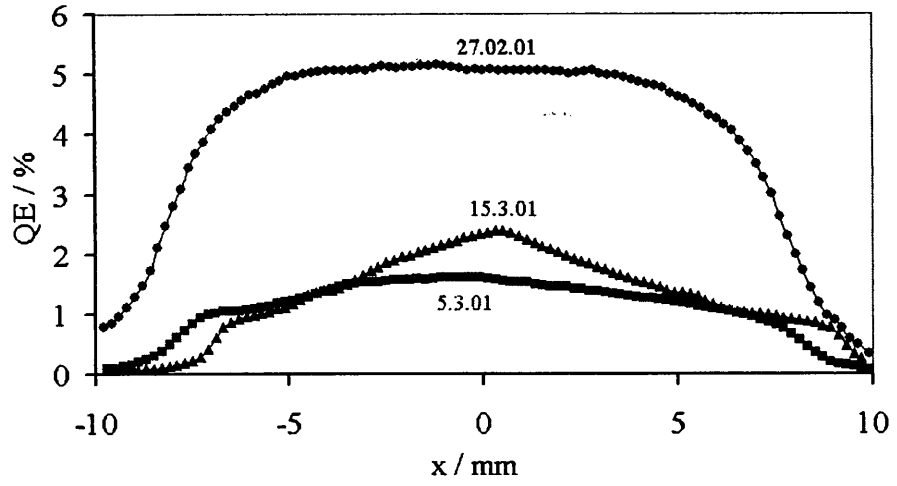

Figure 8.4 : Distribution of QE over the cathode just after evaporation (27.02.01), during use (5.3.01) and after use (15.3.01)

8.7 Recent developments

It has been demonstrated in CTF2 that the infrared to UV conversion efficiency and the UV beam transport could be improved, increasing the total efficiency by 60 %. The long term photo-cathode QE has also been increased by a factor of 3 due to a new photo-cathode fabrication process. If both improvements are operationally confirmed, the laser power should be reduced in the same proportion.

8.8 References

[1] "The CLIC RF power source : a novel scheme of two-beam acceleration for e-/e+ linear colliders", The CLIC Study Team (ed. R. Corsini), CERN yellow report, 99-06

[2] "The photo-injector option for CLIC: past experiments and future developments", E.Bente, H.H.Braun, E.Chevallay, S.Hutchins, P.Legros, I.N.Ross, G.Suberlucq, H.Trautner, CERN/PS 2001-033 (PP), 2001 Particle Accelerator Conference (PAC'2001), Chicago, Illinois, June 18-22, 2001

[3] "Beam Loading Compensation in the main Linac of CLIC", D.Schulte, I.Syratchev, Proc. of XX Int. Linac Conf., Monterey, 2000

[4] "CTF2 Laser and Optical System", S.C.Hutchins, CERN/PS CTF Tech Note 2000-09

[5] "Studies and Production of Photo-cathodes for High Intensity Electron Beams", E.Chevallay, S.Hutchins, P.Legros, G.Suberlucq, H.Trautner, CERN CLIC Note 449

[6] "A 3 GHz Photoelectron Gun for High Beam Intensity", R.Bossart, H.H.Braun, M.Dehler, J.C.Godot, Proc. FEL Conf., New York 1995

[7] "Feasibility Study for the CERN CLIC Photo-Injector Laser System", I.N.Ross, Central Laser Facility, RAL, CLIC note 462

[8] "Production of a high average current electron beam with Cs-Te photo-cathodes", E.Chevallay, G.Suberlucq, H.Trautner, CTF3 Note 20

9. DRIVE BEAM LINAC

9.1 Fully loaded operation

To maximise RF generation efficiency, the Drive Beam Accelerator will be operated at almost 100 % beam loading, i.e. over the length of each accelerating structure, the accelerating gradient will decrease to almost zero. Details are described in chapter 3.2.

9.2 Drive beam accelerating structure

The CTF3 Drive Beam Accelerator (DBA) will consist of 16 accelerating structures, each of 32 cells and a total length of 1.3 m. It will operate in $2\pi/3$ mode and at a moderate accelerating gradient of 7 MV/m.

Two types of structure have been studied: the Tapered Damped Structure (TDS) was originally designed for the CLIC main accelerator and was scaled down in frequency by a factor 10. This structure has, however, the disadvantage of its large size (outer diameter 430 mm). Since some structures in the injector must fit inside focusing solenoids, we have also studied a slotted iris structure with an outer diameter of only 174 mm. This approach is interesting also in view of the scaling to 937 MHz, and has the additional feature of a relatively large constant iris aperture and consequently lower short-range transverse wake fields. We refer to the latter as SICA (Slotted Iris – Constant Aperture).

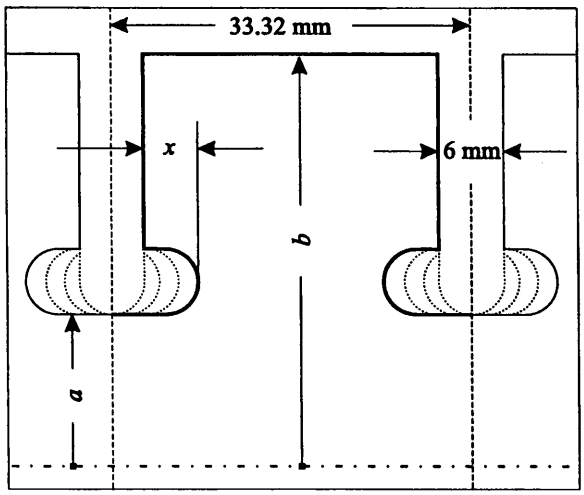

Figure 9.1 Parameters of the cell geometry. The nose-cone size x is zero for the TDS structure. Nose-cone sizes in different SICA cells are shown dotted.

Both the TDS and the SICA structure are based on classical S-band cells. For the generic geometry, see Figure 9.1. Detuning and modulation of the group velocity (from 5 to 2.5 % of c over the length of the structure) are implemented by iris variation in the TDS (keeping the nose-cone size x at zero), and by nose-cone variation in the SICA structure (keeping the dimension "a" constant at 17 mm). In both cases, b is adjusted for the correct phase advance of $\lambda/3$ at the operating frequency. The first cell has the same dimensions in both designs (a = 17 mm, x = 0).

The main difference between the two approaches is the coupling of the higher-order modes (HOMs) to the SiC loads. TDS uses wide openings in the outer cell wall, coupled to 4 waveguides with an axial E-plane, and with a cut-off above the operating frequency serving as high-pass filter for the HOMs. SICA on the other hand relies on geometrical mode-separation by 4 thin radial slots through the iris, coupling dipole modes to a ridged waveguide with its E-plane in the azimuthal direction. In both cases, the SiC absorbers are wedge-shaped for good matching.

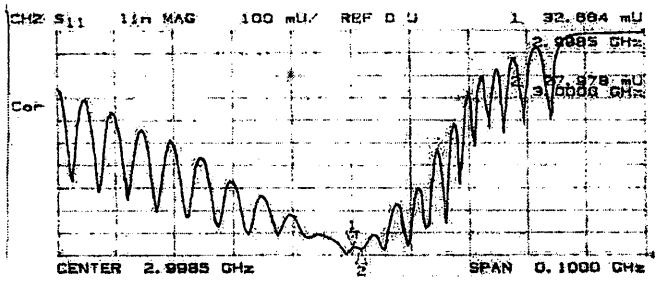

Figure 9.5 Reflection measurement: the input reflection loss is above 30 dB in a usable bandwidth of 10 MHz.

9.2.2 SICA

In the tapered damped structure, the waveguides between the accelerating cells and the SiC loads serve as high-pass filters, below cut-off for the accelerating mode, but transparent for higher-order modes, in particular the first dipole mode (at approximately 4.1 GHz). In order for this filter to work effectively, substantial waveguide length is required. This leads to an outer diameter of the 3 GHz TDS of approximately 430 mm.

As opposed to the "filter" type mode selection of the TDS, the SICA structure uses "geometric" mode selection [1]: a small radial slot in the iris does not intercept radial nor axial surface currents, so it will not perturb the accelerating TM_{01} mode (nor any other TM_{0n} mode). Dipole modes however have azimuthal current components which are intercepted and will thus induce a voltage across the slot. If this slot continues radially, cutting the outer cell wall, it can be considered as a waveguide, the cut-off of which can be made small by using a ridged waveguide. A cutaway view of the SICA cells is shown in Figure 9.6.

Another concern was the short-range transverse wake, the strength of which is dominated by the iris aperture alone and is hardly affected by detuning or damping. So we introduced nose-cones, varying in size from cell to cell to obtain the same linear variation of the group velocity (5 to 2.5 % of c) as in the conventionally detuned structure, keeping the iris aperture constant at Ø 34 mm. The overall detuning of the first dipole mode is slightly smaller than for the TDS, but sufficient. All other HOMs, longitudinal and transverse, show a larger detuning.

The ridged waveguides are machined into the cell, the slots by wire etching, the waveguide by milling. The SiC wedges are fixed with a specially designed clamp, avoiding thermal strains during brazing. Water cooling channels and dimple tuning are provided. The complete structure is brazed vertically and in one pass.

The SICA structure leads to a very compact design and its outer diameter of 174 mm would allow reusing the focusing solenoids from LIL which have a bore of 180 mm.

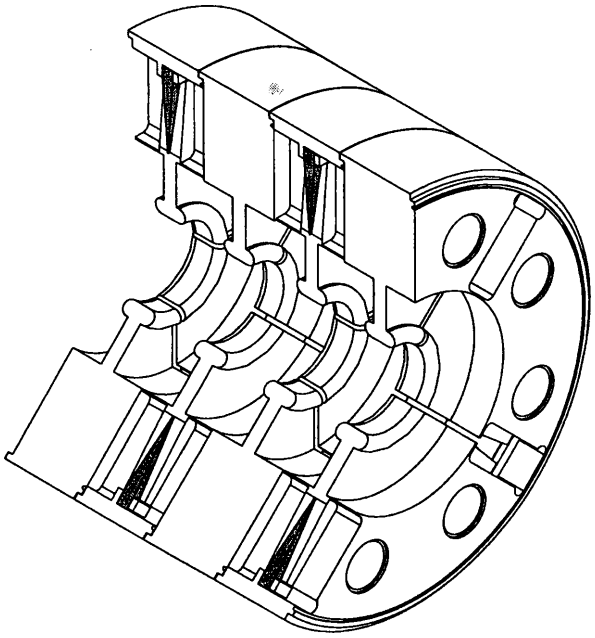

Figure 9.6 Cutaway view of 4 SICA cells. The outer diameter is 174 mm. The round holes are cooling water tubes; dimple tuning is provided (not shown).

A disadvantage of the SICA structure is an increased ratio of surface field to accelerating gradient, about 30 % higher than for the TDS structure at the downstream end. A further 40 % increase of the surface field will occur at the edges of the slots. The edges of the 2 mm wide slots are rounded to a radius of 0.5 mm.

Hhigh power tests of a short SICA prototype (4+2 cells) have indicated its high power capability. During the tests, the maximum power was 34 MW, limited by the klystron. The structure accepted this power level after only 15 h of conditioning. Therefore this structure type was chosen for the linac, and an order for manufacture has been placed in industry.

Figure 9.7 shows a disc of the SICA structure and Figure 9.8 shows the structure being prepared for high power testing.

Both designs allow highly effective dipole mode damping. Figure 9.2 shows the time domain MAFIA simulations of the transverse wake for a Gaussian bunch with a σ of 2.5 mm, assuming the damping waveguides to be matched. These results were confirmed by frequency-domain calculations with HFSS, taking the properties of SiC into account: The first dipole mode of the TDS had a Q of 18, that of the SICA structure had a Q of 5.

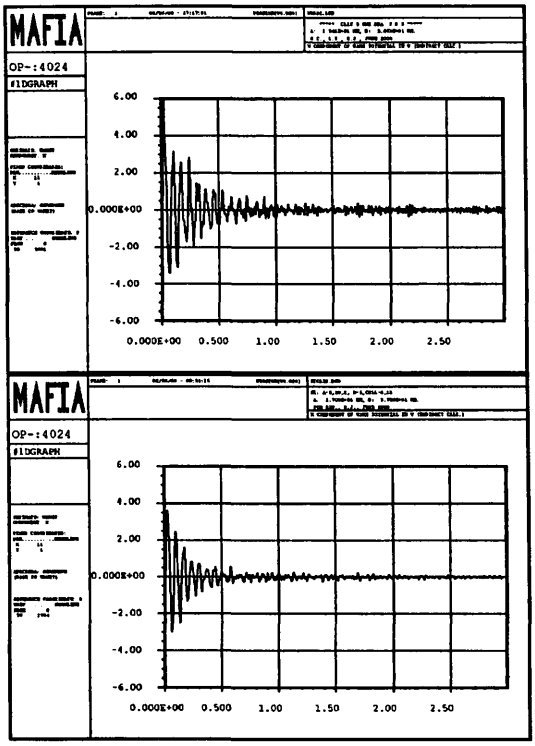

Figure 9.2 MAFIA time domain simulation of the dipole wake in the 32nd cell of TDS (top) and SICA structure (bottom). Abscissa in m behind bunch centre, ordinate in V/(2 pC)/m/mm. Note the smaller short-range wake field in the SICA.

9.2.1 TDS

The cells are fitted with four 32 mm wide damping waveguides to couple transverse and longitudinal beam induced Higher Order Modes (HOM).

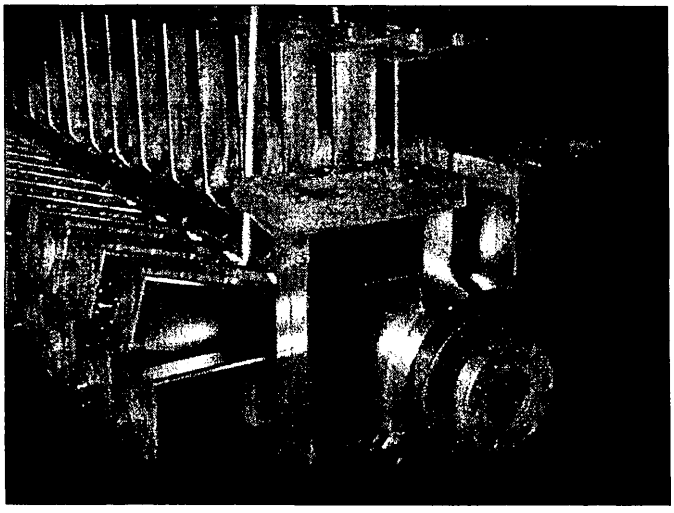

Figure 9.3 Brazed TDS ready for power testing

The cell wall thickness is about 20 mm and the extruded copper waveguides are brazed into openings in the cell wall as shown in Figure 9.3. The extruded waveguides constitute convenient housings at their outer extremities for the SiC absorbers that can be inserted through 16 mm mini-flanges after the final brazing of the structure. The absorbers will then either have been clamped or brazed onto metal holders. By introducing the SiC wedges after the final structure brazing, thermal strains on SiC bonds can be avoided and exchangeability is obtained.

The prototype was brazed in 5 parts in a vertical position (2 couplers and the main body in 3 units). During that operation the damping waveguides with prebrazed end flanges were also bonded with the cells. Finally the 5 parts were brazed horizontally. For future TDSs a single, uncomplicated vertical braze is foreseen at eutectic temperature, joining cells, damping waveguides and couplers. To avoid deformations (during the brazing) of the lowermost cells, the cell wall thickness will be increased to 35 mm, the total structure weight being ~160 kg.

9.2.1 .1 Low-level measurements and power tests

Figure 9.4 and Figure 9.5 give measured low-level results for the brazed 32-cell TDS. Figure 9.4 shows a measurable deviation from the ideal 240 ° phase advance per cell of the reflection coefficient, but even this error would lead to acceptable 1 % loss of accelerating efficiency. The matching of the input and output couplers over a bandwidth of 10 MHz is documented in Figure 9.5. After brazing, the TDS was submitted to RF conditioning and reached the nominal power of 40 MW in less than 1 week, and subsequently 52 MW (the maximum power level available at CERN).

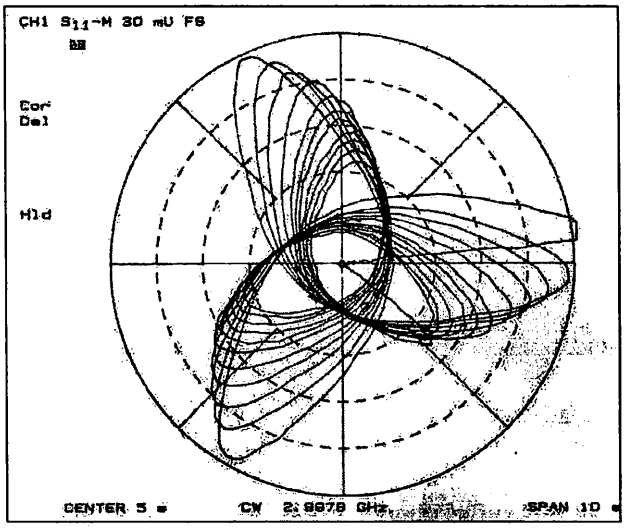

Figure 9.4 Bead-pull measurement: an error of about 40 ° between the 1st and last cell is measured in this reflection diagram, corresponding to a phase slip of ±10 ° between electron and wave over 32 cells. The loss in accelerating efficiency is less than 1 %. The cells are not equipped with dimple tuners.

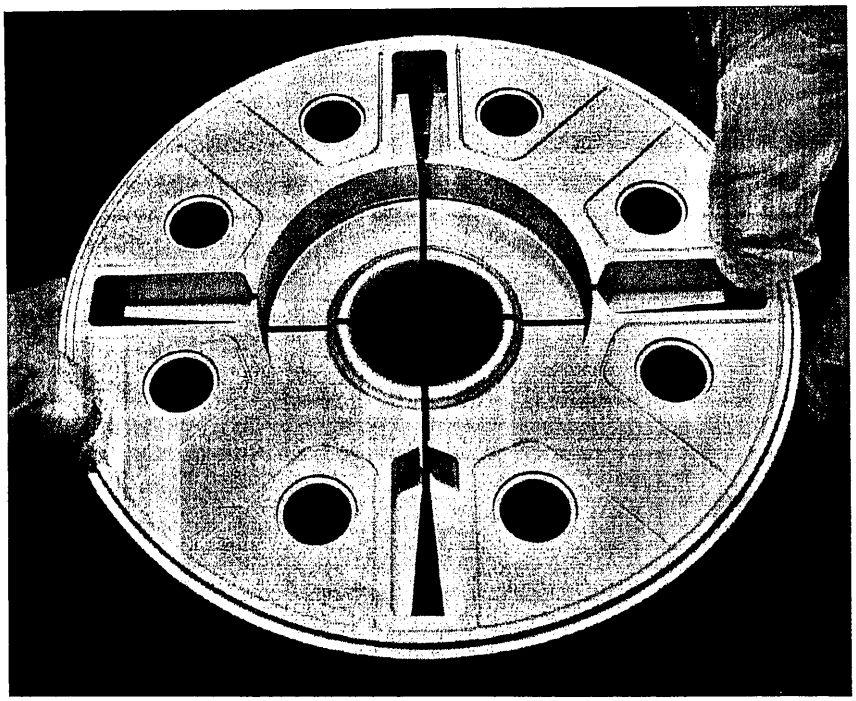

Figure 9.7: Readily machined copper disc for the SICA structure.

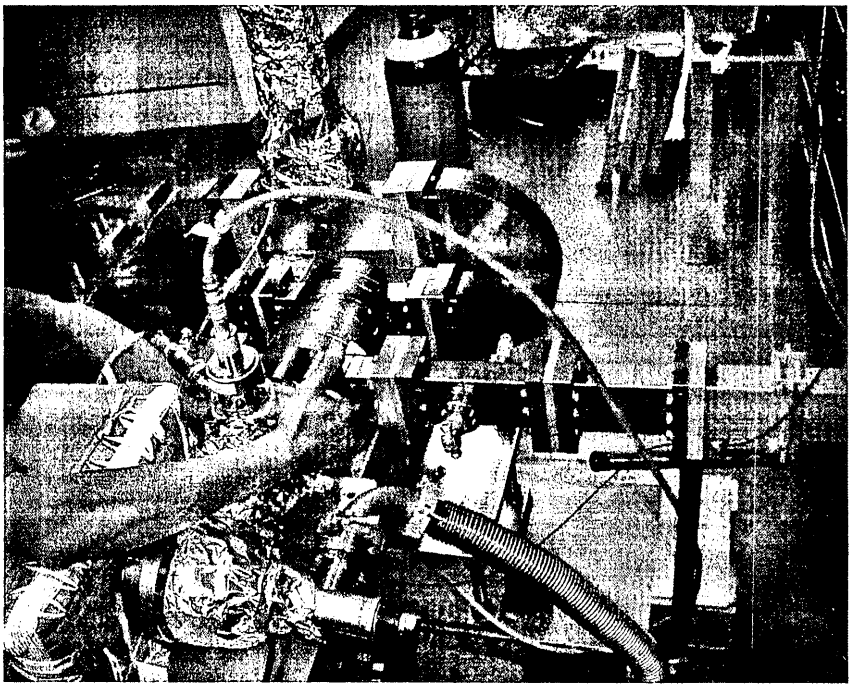

Figure 9.8: Short SICA prototype being prepared for high power tests in the CTF3 tunnel

9.3 References

[1] G.Carron, E.Jensen, M.Luong, A.Millich, E.Rugo, I Syratchev, L.Thorndahl: "Design of a 3 GHz Accelerator Structure for the CLIC Test Facility (CTF 3) Drive Beam", Linac 2000, TUA16

10. DRIVE BEAM LINAC OPTICS

10.1 Introduction

10.1.1 Beam parameters

In the Nominal Phase, the beam pulse consists of ten short trains of about 210 bunches each. The first train fills odd buckets, the immediately following second train fills even buckets; this pattern is then repeated. This method keeps the beam current and subsequently the beam loading constant [1]. Only a very small distortion occurs during switching from one train to the next. If this cannot be done instantaneously, two charge ramps are added to the trains. If the first train fills odd buckets, the charge in these is slowly decreased, while the charge in the even buckets, belonging to the next train, is increased accordingly, keeping the current constant. The trains practically overlap. An RF-deflector at half the linac frequency is used to separate the trains after acceleration.

The initial beam energy is E_0≈24 MeV, the final beam energy E_f≈150 MeV, the bunch charge q=2.33 nC, its length σ_z≈1.5 mm [2] and the transverse normalised emittances are ε_x=ε_y=100 μm.

The RF-phase on which the beam is accelerated is determined by the requirement that the bunches have to be compressed to a very small bunch length after the Combiner Ring. It can therefore not be used to optimise the transverse beam dynamics. In the following calculations a phase of ϕ_{RF}=-6° has been chosen.

10.1.2 Wakefields

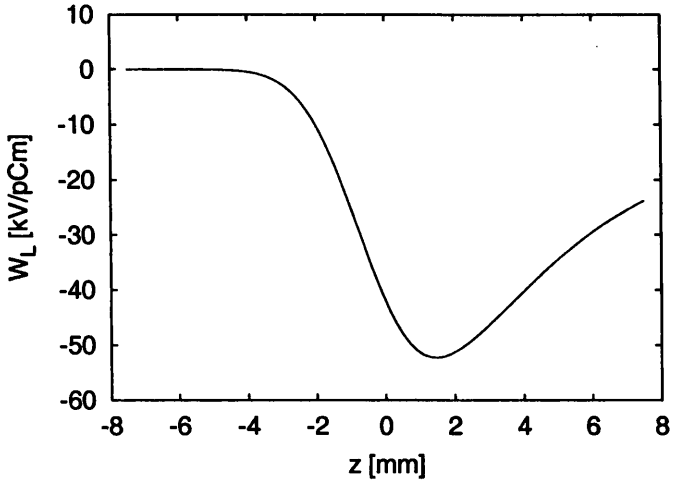

Figure 10.1 The integrated longitudinal single-bunch wakefield of the TDS structure for a bunch length of σ_z=1.5 mm.

Due to the high beam intensity wakefield effects play an important role in the Drive Beam Accelerator of CTF3. Two different structures are considered in the moment namely TDS and SICA as described in chapter 9.2. In the following the SICA structure will be used to determine the lattice behaviour and only some results will be compared to those for the TDS structure.

10.1.2 .1 Wakefields for TDS Structures

The longitudinal short-range wakefield has been calculated with ABCI [3]. Figure 10.1 shows the wakefield along a Gaussian bunch with a length of σ_z=1.5 mm. The transverse short-range delta wakefield has been calculated with MAFIA [4]. The result has been approximated using

$$W_T = 2.57 \frac{\text{kV}}{\text{pCm}^2} \left[1 - e^{-1.29859\sqrt{z/\text{mm}}} (1 + 1.29859\sqrt{z/\text{mm}})\right]$$

Table 10.1 The frequencies and loss factors of the most important transverse modes in three cells of the TDS structure. In the simulation $k_\perp$ and Q were increased by 50 %.

Cell no	f [GHz]	K_{loss} [kV/(pCm^2)]
1	4.0	825
1	6.8	90
1	7.9	95
17	4.2	1095
17	7.0	180
17	8.2	94
32	4.35	1436
32	7.1	326
32	8.25	144

The three most important modes of the long-range transverse wakefield have been calculated for three different cells, assuming no coupling between cells [3], see Table 10.1. The modes for all other cells are determined by linear interpolation. In the simulation the modes are confined to their cells, which allows taking into account the angle of the beam trajectory in the structure. The loss factors are assumed 50% higher than calculated, to account for the uncertainties due to the simplified estimation of the wakefield. The damping of the lowest dipole mode is in the range of Q=11 to Q=19 for perfect loads [5], however, conservative values of Q=30 for the first mode and Q=400 for the other two modes were used in the simulation. It is not possible to damp the first and the last cell of each structure. Therefore Q=1000 is assumed for all modes in each of these cells.

The effect of the long-range longitudinal wakefield is very well compensated by varying the RF phase and amplitude at the head of the train. Due to the beam structure the multi-bunch beam loading is constant. Therefore only a very small variation of the gradient along the train remains.

10.1.2 .2 Wakefields for SICA Structures

For the SICA structure the four to five most important dipole modes have been calculated for five different cells [6], see Table 10.2. Interpolation between these modes is very difficult since the frequencies and loss factors are not monotonous. In the simulations each structure therefore consists of only five different cell types rather than 34. In the simulation the calculated loss factors and Q-values have been increased by 50%. For the two end-cells a damping with Q=1000 has been used for the modes.

The transverse short range wakefield has been determined by scaling the short range wakefields of the TDS with $a^{-2.2}$ which should give pessimistic results for the SICA structure. For the longitudinal short range wakefield the same values as for the TDS were used.

Table 10.2 The long-range transverse wakefield modes in the SICA. In the simulations $k_\perp$ and Q were increased by 50%.

Cell number	f [GHz]	Q	k_{loss} [kV/(pCm^2)]
1	4.11767	8.739	0.457
1	4.34377	8.107	0.664
1	5.19655	71.545	0.171
1	5.48555	3.24486	0.036
9	4.1206	7.253	0.755
9	4.3486	10.201	0.415
9	5.25651	65.365	0.158
9	5.45056	3.26	0.059
9	5.58111	5.04	0.048
17	4.099	6.3	0.451
17	4.262	3.54	0.847
17	5.37084	59.88	0.134
17	5.47245	3.315	0.038
25	4.045	5.77	0.945
25	4.44	17.44	0.119
25	5.47128	5.204	0.104
25	5.47532	3.24	0.119
25	5.52712	56.244	0.063
32	4.0086	5.606	0.994
32	4.471	20.26	0.274
32	5.41693	5.15	0.068
32	5.47233	3.269	0.191

10.2 Lattice Descriptions

10.2.1 Basic Considerations

The lattice has to prevent a significant amplification of any jitter of the incoming beam. It should also have a large energy acceptance and allow easy correction of static errors of the beam line. The first requirement can best be fulfilled using a strongly focusing lattice, while the second requires weaker focusing. The lattice must therefore be a compromise. The final energy of the beam must be very stable since the energy acceptance of the Combiner Ring is limited to a full width of about 5%. In order to achieve the necessary bunch compression after the ring, each bunch almost completely fills this acceptance. The additional energy spread from bunch to bunch should thus be less than about 1%. Since the requirements on the energy spread are so tight a strong lattice is favoured, as long as it does not tighten them further.

Three different lattices have been considered earlier [7]. One is based on FODO cells with one structure between each pair of quadrupoles. The other two are based on triplets, where in one case one structure is placed between two triplets, whilst in the other case two.

The FODO lattice and the triplet lattice with two structures per cell are roughly comparable in cost and length. The other triplet lattice is significantly more expensive and much longer (48 m compared to 36 m). It has been concluded [7], that the triplet lattice with two structures between triplets provides the best compromise between cost and lattice performance. It is therefore considered the reference option in the following. However, some comparison will be made to a FODO and a doublet lattice.

10.2.1 .1 The Triplet Lattice

The lattice consists of equal cells. Each cell contains one triplet followed by a horizontal and a vertical dipole corrector, two structures and a pickup to measure the transverse beam position. The strength of the triplet quadrupoles are scaled along the linac so that the phase advance per cell remains constant for the nominal beam energy.

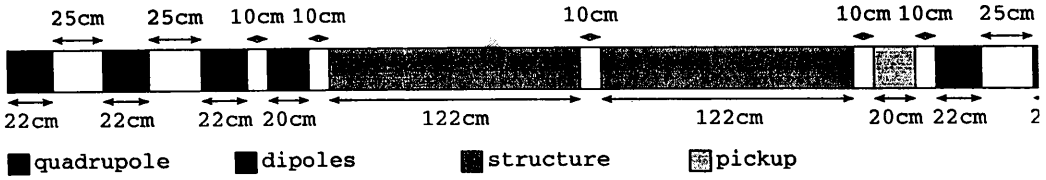

Figure 10.2 Sketch of a single cell in the triplet lattice.

For the calculations the length of the structures is assumed to be 122 cm, the same as the prototype structure, whilst the length of the quadrupoles is assumed to be 22 cm, the same as the existing small aperture LIL quadrupoles. It is assumed that the beam pipe has an aperture of 40 mm in the quadrupoles, although it could be somewhat larger. The length of the two dipole correctors and of the pickups is not known, but about 20 cm has been foreseen for them. This leads to a total cell length of 4.5 m. A schematic sketch is given in Figure 10.2.

The spacing between the quadrupoles in the triplet is 25 cm. Between triplet and dipole corrector as well as between dipole corrector and structure, 10 cm additional space has been foreseen. The same is true between structure and pickup, as well as between pickup and triplet. The two structures are separated by 10 cm to allow the insertion of a bellow.

Currently only eight klystrons are foreseen, which would lead to eight cells, but since it is planned to keep the option of another two klystrons, all simulations are done using ten cells.

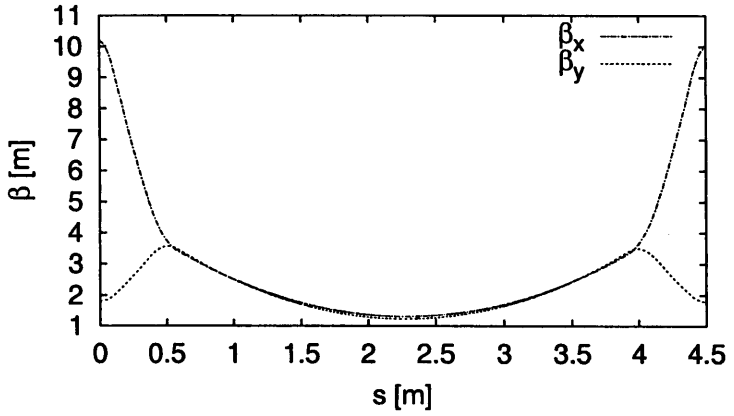

Figure 10.3 The Twiss parameters in a cell of the triplet lattice.

In each triplet the outer two quadrupoles have the same strength, which allows using a single power supply for them. The relative strengths of these quadrupoles with respect to the central one have been determined such that one obtains a round beam in the structures. Five different focusing strengths have been investigated, see Table 10.3. The β-functions in a cell are shown in Figure 10.3 for the parameter set no. 0 from Table 10.3.

In the following the parameter set no 2 will be used unless mentioned otherwise. As shown later it seems to be a good compromise between the benefits and drawbacks of strong focusing.

Table 10.3 The normalised quadrupole strengths and phase advances for different versions of the triplet lattice.

Set no	K_1 [m^{-1}]	K_2 [m^{-1}]	μ_x [°]	μ_y [°]
0	1.96875	-1.18125	113.9	131.0
1	1.859375	-1.09703125	103.8	120.5
2	1.75	-1.015	95.2	110.8
3	1.53125	-0.8575	80.8	92.8
4	1.3125	-0.71203125	68.1	76.5

10.2.1 .2 The FODO Lattice

In the FODO lattice one structure is placed between each pair of quadrupoles. This leads to a cell length of 4.5 m, the same as in the triplet lattice. The layout is sketched in Figure 10.4. The reference strength is set number 1 of Table 10.4.

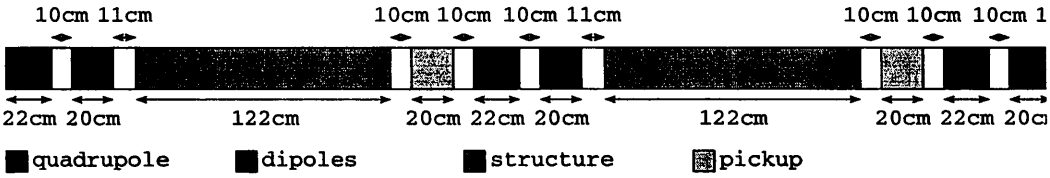

Figure 10.4 Sketch of a single cell in the FODO lattice.

Table 10.4 The normalised quadrupole strengths and phase advances for different versions of the doublet lattice.

Set no	K [m^{-1}]	μ [°]
0	0.9	120.0
1	0.825	105.0
2	0.75	92.4
3	0.675	81.0
4	0.6	70.6
5	0.525	60.7

10.2.2 Doublet Lattice

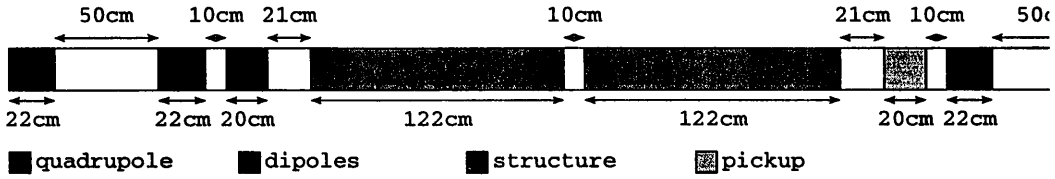

Figure 10.5 Sketch of a single cell in the doublet lattice.

Table 10.5 The normalised quadrupole strengths and phase advances for different versions of the FODO lattice.

Set no	K [m^{-1}]	μ [°]
0	1.4	123
1	1.3	109
2	1.2	98
3	1.1	87
4	1.0	78
5	0.9	69
6	0.8	60

The doublet lattice has a cell length that is equivalent to that of the triplet lattice. In principle, one could slightly reduce it. The layout is illustrated in Figure 10.5 and the different lattice strengths used are given in Table 10.5.

10.3 Lattice Performances

In the following, first the sensitivity of the different lattices to energy errors is investigated. Then the effects of a transverse jitter of the whole pulse and of individual bunches are considered. The two different structures are compared for bunch-to-bunch jitter. Finally beam-based alignment is discussed.

10.3.1 Energy Acceptance

Three different main sources of energy deviation of bunches exist. Bunches can have an initial energy different from the nominal one or they can be accelerated at a gradient different from the nominal one. The gradient could be wrong locally or globally. A global gradient error leads to an energy error of the bunches at the end of the linac. Such an error must be detected and cured since it affects the operation of the Combiner Ring. A local gradient variation that is compensated at some other place is harder to detect. Since it does not necessarily affect the Combiner Ring, the tolerance for the error should also be larger.

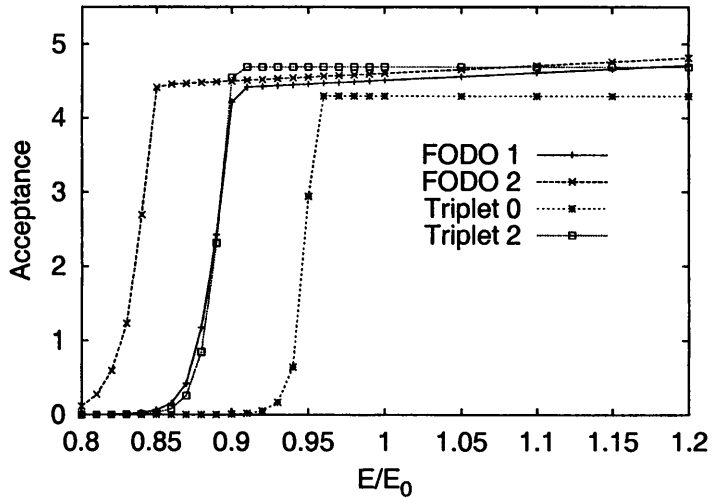

Figure 10.6 The energy acceptance of the FODO lattice and the triplet lattice for different focal strengths.

First the energy acceptance of the lattice is considered assuming a perfectly aligned machine. For the triplet and FODO lattice, Figure 10.6 shows the acceptances A_r as a function of the deviation from the nominal initial energy. It is nevertheless assumed that the

bunches have the nominal Twiss parameters. The acceptance A_r is defined such that any particle with initial positions x_0, x_0', y_0 and y_0' that fulfils

$$\sqrt{\left(\frac{x}{\sigma_x}\right)^2+\left(\frac{x'}{\sigma_{x'}}\right)^2+\left(\frac{y}{\sigma_y}\right)^2+\left(\frac{y'}{\sigma_{y'}}\right)^2} \le A_r$$

will pass through the accelerator.

In a triplet lattice the limitation is dominated by one plane more than by the other, as a result of the different phase advances and maximum beta functions in x- and y-direction.

Also in a FODO lattice the planes are not the same because the first quadrupole is focusing in the horizontal plane. For the nominal beam the smallest aperture is in the first structure just before the second quadrupole.

Both lattices accept energies significantly larger than nominal. However, lower initial energies can not be accepted easily. The strength of the quadrupoles plays an important role. If it is reduced, the energy acceptance improves. A similar behaviour is observed with respect to energy errors: reducing the focal strength improves the acceptance. Therefore it is necessary to consider how much the focusing can be relaxed. One of the main effects that will become worse in a weaker lattice is the amplification of an initial jitter.

10.3.2 Jitter Amplification

The jitter of the incoming beam is unknown. Measurements at LIL show a small transverse pulse-to-pulse jitter of only $\delta_{x,y} \approx 0.04\ \sigma_{x,y}$ at an intensity that is not too different from CTF3 [8]. However, it is not clear if the much longer pulse in CTF3 will have the same stability. Therefore, only the jitter amplification is calculated.

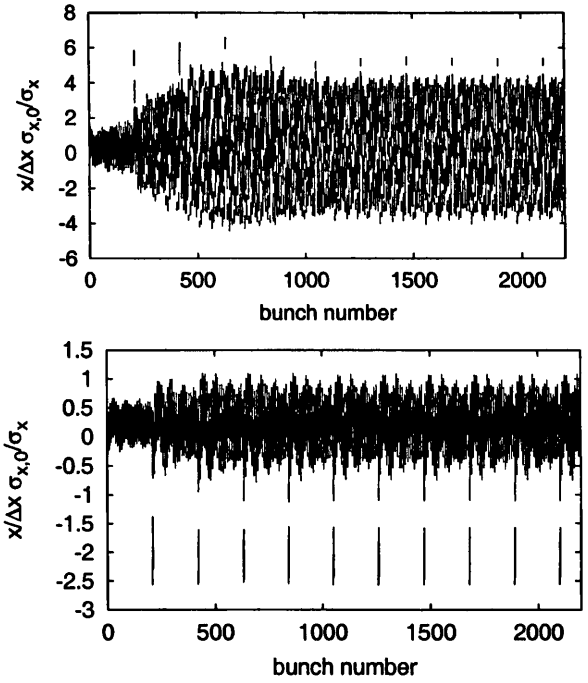

Figure 10.7 The amplification of a transverse jitter of the full pulse. At the positions were one switches from filling odd buckets to filling even buckets and vice versa single bunches are kicked rather hard. The upper plot shows the FODO lattice the lower the triplet lattice.

The effect of a transverse jitter of the initial beam is shown in Figure 10.7. The beam is offset by Δx, Δy at the linac entrance, tracked through the linac and the final offset is plotted.

Due to dispersive and wakefield effects, the beam has widened notably. At regular intervals single bunches have been kicked to rather large offsets. These are the first bunches after one switches from one train to the next. This effect can be reduced by switching more slowly from one train to the next [7].

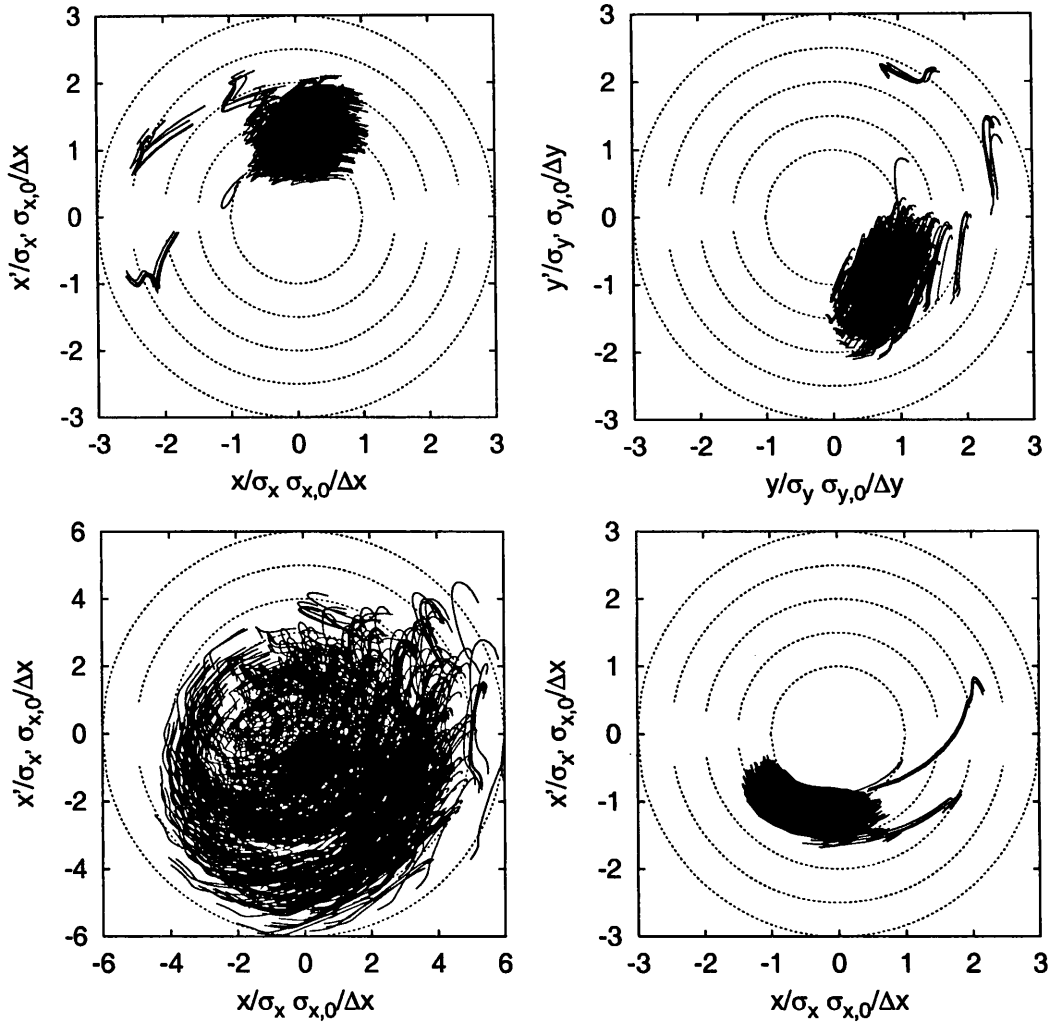

Figure 10.8 The final position of a beam with initial offset. The upper two plots show the horizontal and vertical plane in the triplet lattice. A few bunches at the intersection from one train to the next have significantly larger amplitudes than the rest of the beam. The third plot shows the beam at the end of the FODO lattice in the horizontal plane. The overall beam size has substantially increased. The last plot shows the jitter effect for a beam in the strongest triplet lattice (set number 0).

The plots in Figure 10.8 show the offsets of the beams in phase space at the end of the linac. To quantify the effect, an amplification factor A_x is defined as follows:

$$A_x = \frac{\sigma_x}{\Delta x}\sqrt{\left(\frac{x_f}{\sigma_{x,f}}\right)^2 + \left(\frac{x'}{\sigma_{x',f}}\right)^2}$$

Here, σ_x and $\sigma_{x,f}$ are initial and final beam size, $\sigma_{x'}$ and $\sigma_{x',f}$ are initial and final beam divergence, Δx is the initial beam offset and x_f and x'_f are the final position and angle of the centre of the slice. For a slice with nominal energy and without wakefield effects, A_x=1.

Equivalently one defines A_y. The maximum amplification factor A is the maximum of A_x and A_y over all slices.

The trade-off between jitter amplification and energy acceptance is shown in Figure 10.9. The FODO lattice allows making this trade-off over a large range of quadrupole strengths. The triplet lattice does not work very well if a very large energy acceptance is required. Otherwise, it performs much better than the FODO lattice. The performance of the doublet lattice lies between the other two.

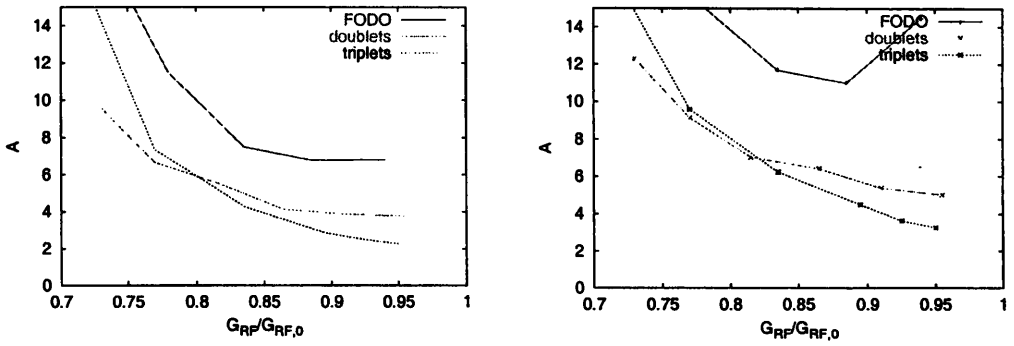

Figure 10.9 Amplification factor and energy acceptance for different quadrupole strengths. The left plot shows the SICA the right one the TDS. There is a noticeable but not an enormous difference between the two structures.

The maximum amplification improves if one switches slowly from one train to the next. The conclusion concerning the relative advantages and drawbacks of the FODO and triplet lattice remain unchanged.

The requirement that the maximum amplification of the beam jitter in the lattice is small ensures that no beam losses occur as a result of this beam jitter. However some losses might be acceptable, in which case the maximum amplification should not be taken as a figure of merit. In that case one wants to determine which amplitudes are reached by a significant fraction of the beam. Therefore a different amplification factor can be used, $A_{0.95}$. This value is defined such, that 95% of the charge of the pulse have an amplification $A_x <= A_{0.95}$ and $A_y <= A_{0.95}$.

Figure 10.10 shows this amplification factor as a function of the possible gradient error in the different lattices. The relative performance of the lattices is the same as for the maximum amplification.

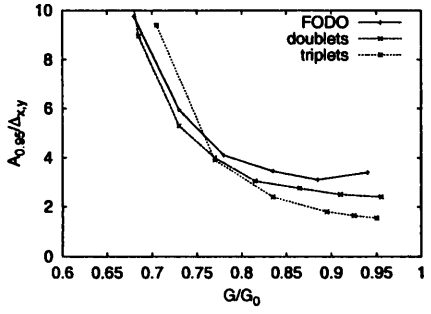

Figure 10.10 The amplification factor $A_{0.95}$ versus the gradient error accepted in the lattices for the SICA.

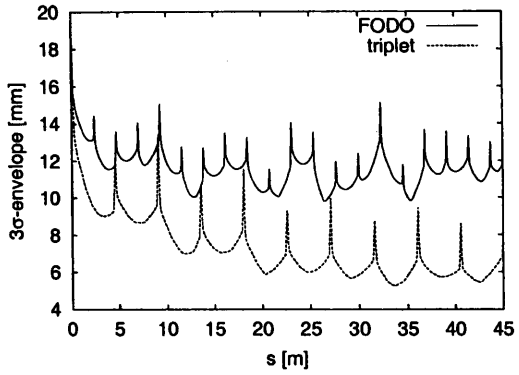

Figure 10.11 The 3-σ envelope of a beam that was injected with an initial offset of $\Delta x=\sigma_x$ and $\Delta y=\sigma$

Beam jitter may not only result in a final beam with bad properties but might also lead to beam loss within the linac. Figure 10.11 shows the envelope of a three sigma beam with an initial offset of one sigma in the horizontal and vertical position. In both lattices one would not have beam loss. A larger offset however would lead to beam loss in both lattices, in the FODO lattice due to the wakefields, in the triplet lattice because the first quadrupole does not provide enough aperture.

10.3.3 Bunch-to-Bunch Jitter

The beam can contain a small transverse position jitter from bunch to bunch. To evaluate this effect, the bunches of the incoming pulse were set to offsets which followed a Gaussian distribution cut at three standard deviations.

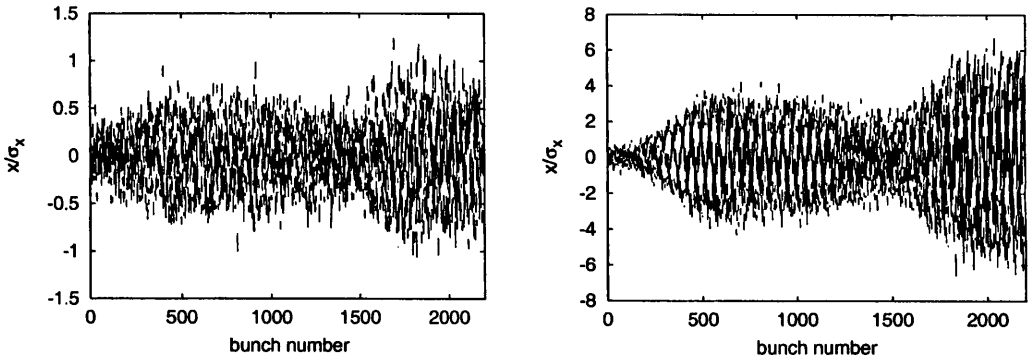

Figure 10.12 The effect of a bunch-to-bunch jitter. The RMS value of the initial transverse jitter is 0.1 σ in all four transverse planes. The left case is the triplet lattice, the right is the FODO lattice

The RMS-width of the distribution is $0.1\sigma_n$ in each direction n. The final offsets of the bunches are shown in Figure 10.12. In the case of the triplet lattice, the effect would be acceptable while in the case of the FODO lattice it is too large.

Figure 10.13 shows the effect more systematically. The $A_{0.95}$ value is plotted versus the allowed gradient error for the FODO and the triplet lattice. The triplet lattice is clearly better here. The difference is even larger than for a coherent offset of the whole pulse.

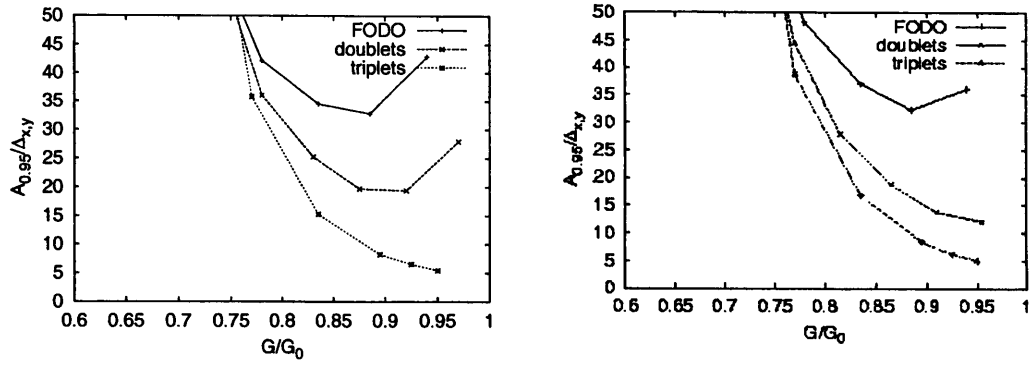

Figure 10.13 The envelope growth as a function of the acceptable gradient error for the different lattices. The left plot is for the TDS, the right one for the SICA.

10.3.4 Comparison of TDS and SICA for a Bunch-To-Bunch Jitter

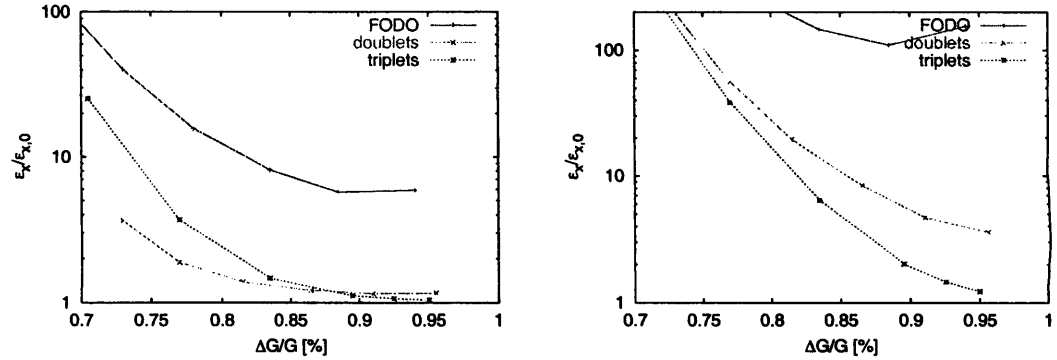

Figure 10.14 The emittance growth for an initial bunch-to-bunch jitter with an RMS offset of 0.1σ. The upper plot shows the SICA the lower one the TDS. The increase of the emittance is very large with the FODO lattice, and still significant with the other two. The SICA performs distinctly better than the TDS.

In order to compare the two different structures we evaluate the emittance growth resulting from a bunch-to-bunch jitter. The initial RMS offsets of the single bunches of 0.1σ in all planes correspond to an emittance growth of 1%. As Figure 10.14 shows, the emittance can reach very large values.

Especially in the FODO lattice one can have more than 500% growth. In order to achieve a growth which is much smaller than the initial emittance of the beam one would have to make sure that the bunch to bunch jitters are limited to an order of magnitude closer to 0.01σ rather 0.1σ.

The TDS structure performs distinctly worse than the SICA. The emittance growth in the doublet lattice is not acceptable and even in the triplet lattice a significant emittance growth can be noticed. The performance for the SICA is shown in detail in Figure 10.15.

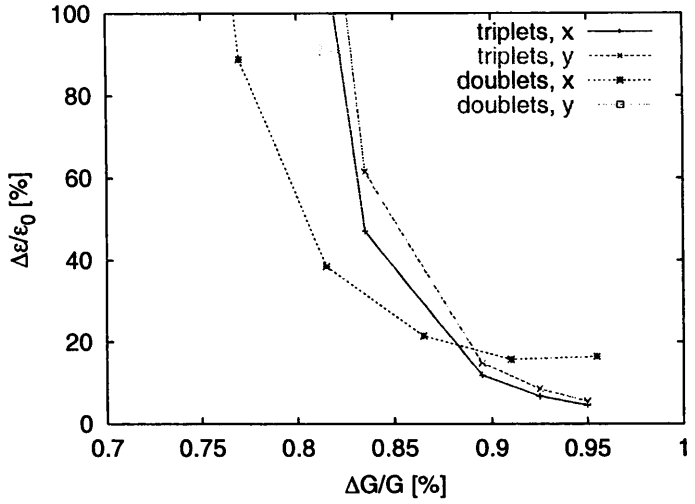

Figure 10.15 The emittance growth in the SICA plotted with a different scale. The FODO lattice leads to an emittance growth of more than 500% so it does not show on the plot. Also the vertical emittance growth in the doublet lattice is too large to be depicted. The nominal triplet lattice leads to a growth of less than 20%.

10.3.5 Chromatic Emittance Growth

Even in a perfectly aligned linac the beam will experience some chromatic emittance growth due to its energy spread. If only the single bunch energy spread is present this effect is quite small in all lattices. However the accelerating gradient may vary along the train. Two models for these variations are used here. A global one in which the gradient of a particle at position s within a train of length L_{train} is given in all structures by $G(s) = G_0(1 + \delta \cdot \sin(2\pi s / L_{train}))$,

and a local one, where the gradient is alternating between

$$G_1(s) = G_0(1 + \delta \cdot \sin(2\pi s / L_{train})) \text{ and } G_2(s) = G_0(1 - \delta \cdot \sin(2\pi s / L_{train}))$$

from one pair of structures (which are fed by one klystron) to the next pair fed by a different klystron.

In the triplet lattice the growth in the horizontal plane is particularly strong. The emittance growth is 3 % in the horizontal and 0.6 % in the vertical plane, for an unacceptable global gradient error δ = 5 %. For an acceptable δ=1 %, the growth is limited to less than 0.5 % in both planes. Also, in the case of a local gradient error of δ=5 % the growth in the horizontal plane is particularly large (6 %). This is due to the phase advance of nearly 90° in this plane. If the gradient does not alternate from one pair of structures to the next but rather from a group of four structures to the next, the resonant effect caused by this phase advance is broken and the emittance growth is significantly reduced, see Figure 10.16. It is not important whether one starts in the middle of a group of four structures or not. In the vertical plane the different configurations have little effect, the growth is about 1 %.

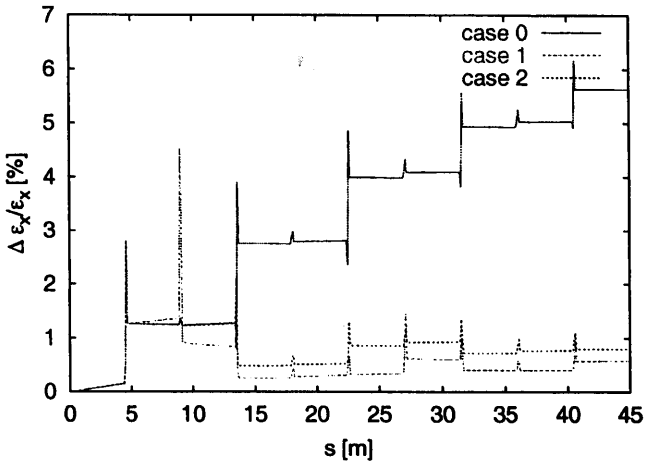

Figure 10.16 Chromatic emittance growth in the horizontal plane of the triplet lattice for a local gradient variation in the bunch train. In case 0, the gradient variation alternates between G_1 and G_2 from one pair of structures to the next. In case 1, groups of four structures have the same gradient variation. Case 2 is the same as case 1, except that the linac starts in the middle of a group of four structures.

10.3.6 Beam-Based Alignment

To keep operation as simple as possible only one-to-one correction is considered. All elements are assumed to be scattered around a straight line following a normal distribution with σ=200 μm. In the FODO-lattice, corrector dipoles are located after each quadrupole and beam position monitors are placed in front of each quadrupole. In the triplet lattices, the corrector dipoles are positioned after the triplets and the BPMs are positioned in front of the triplet. For comparison, cases with one BPM after the triplet but before the dipole and with one BPM before and one after the triplet have also been considered. The correctors are used to bring the average beam position to zero in the BPMs. Figure 10.17 shows the emittance growth along the linac for the FODO and the triplet lattices. For each case 100 different machines are simulated. In all cases the growths are small, but the triplet lattice is the best. If a global gradient variation with an amplitude of δ=0.05 is introduced the emittance growth is increased. While the additional effect is larger in the triplet lattice it is still slightly better than the FODO lattice, see Figure 10.18.

After the beam-based correction has been applied, some residual dispersion and wake field effects will remain. To estimate this effect, the following calculations have been performed. A set of 100 misaligned machines have been corrected with a single bunch at the nominal initial energy and gradient G_0. In each of these machines, a bunch with nominal energy which sees a different gradient G throughout the linac has been injected and the minimum transverse acceptance A_r for a bunch at this energy has been calculated. Figure 10.19 shows the acceptance as a function of the gradient G in the triplet lattice. The initial misalignments reduce the acceptable gradient variation. In the FODO lattice this reduction is somewhat smaller but is still present, see Figure 10.20. However the effect is small enough to be tolerable.

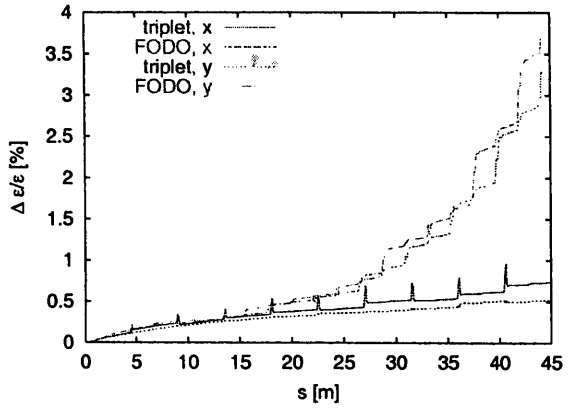

Figure 10.17 The emittance growth along the linac for the FODO and the triplet lattice.

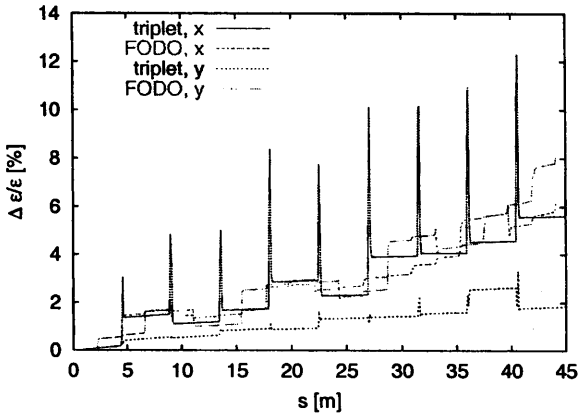

Figure 10.18 The emittance growth along the linac for the FODO and the triplet lattice. A local variation of the gradient with an amplitude of δ=5% is assumed.

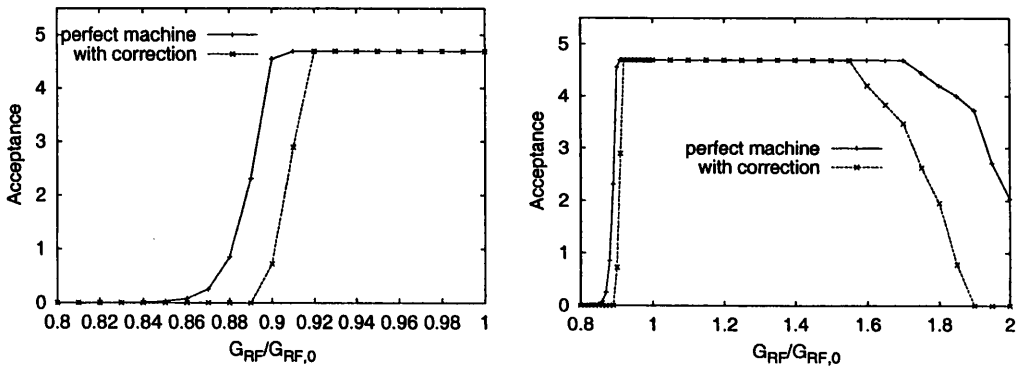

Figure 10.19 The acceptance of the triplet lattice (set number 2) as a function of the gradient error. In one case a perfectly aligned machine is assumed. In the other case the smallest acceptance of 100 different machines is plotted. These machines had initial position errors for all elements and were corrected using one-to-one correction.

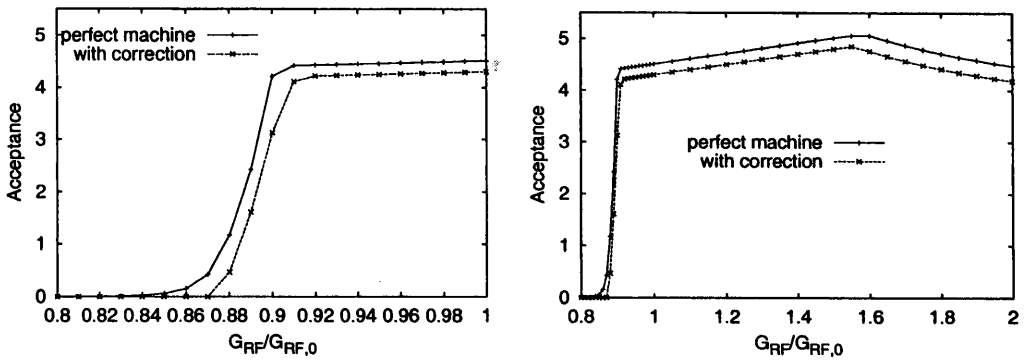

Figure 10.20 The acceptance of the FODO lattice with set 1.

10.3.7 Quadrupole Strength Aberrations

The strengths of the quadrupoles will also have small errors with respect to the nominal value. To simulate this effect the strengths of all quadrupoles are varied according to a Gaussian distribution. Figure 10.21 shows the resulting emittance growths for different error sizes in a perfectly aligned machine. For an error of 1% of the nominal quadrupole strength the emittance growth seems very acceptable. For 2% it will be too large.

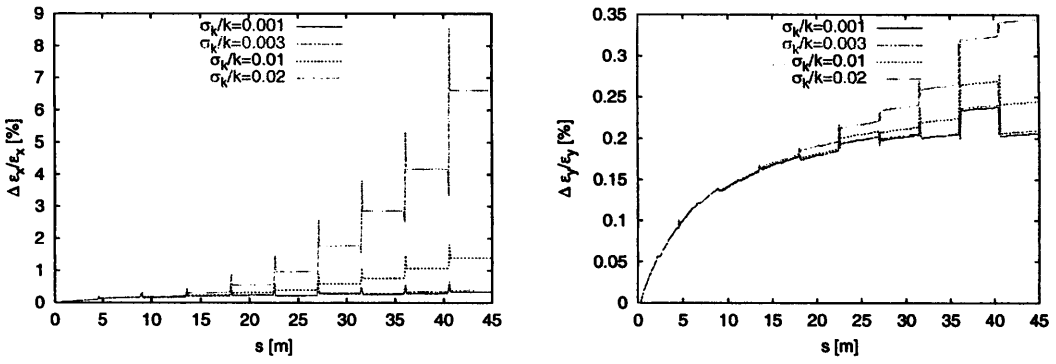

Figure 10.21 The chromatic emittance growth in the triplet lattice for different errors in the quadrupole strengths. The left plot shows the horizontal, the right one the vertical plane.

10.3.8 Dispersion

The initial misalignment of the beam line elements leads to significant energy dispersion, even after beam-based correction in both the triplet lattice and the FODO lattice, see Figure 10.22. This problem can be cured using dispersion free steering. In this method a second beam is used which is accelerated at a different gradient. The correction then tries to minimise the offset of the nominal beam in the beam-position monitors and simultaneously the difference of the trajectories of the two beams. The figure shows the improvement achieved in the triplet lattice.

To estimate the performance of the dispersion free correction the lattice has been corrected using two single bunches at different gradients. The evaluation has then been performed using the full bunch train with a 5% local gradient spread. As can be seen in Figure 10.23 the improvement compared to the simple one-to-one correction is negligible.

In the case of a global gradient error the dispersion free steering is more effective. For $\delta = 5$ %, the horizontal emittance growth can be reduced from 5 % to 4 %. For the acceptable value of $\delta = 1$ % the difference is however again small and the growth remains under 1 %.

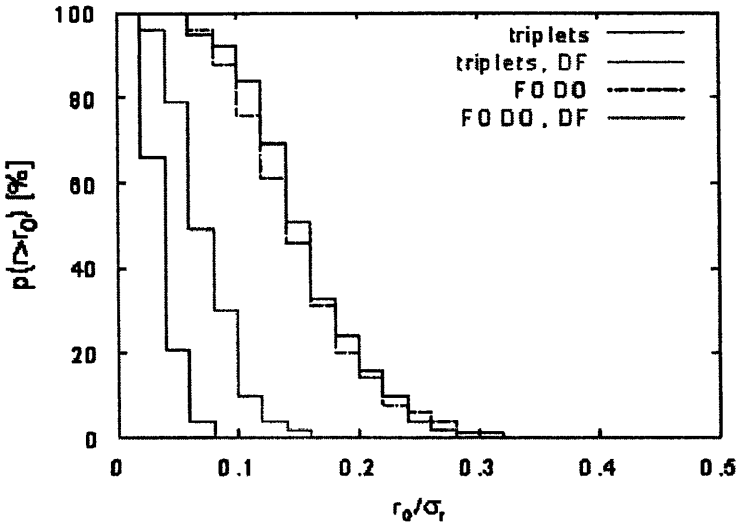

Figure 10.22 Energy dispersion in the FODO lattice and the triplet lattice. A beam was accelerated with a beam loading 10 % smaller than nominal, the relative offset to the nominal beam is plotted normalised to the final beam sizes. The plot shows the result if only one-to-one correction is applied and after the use of dispersion free steering.

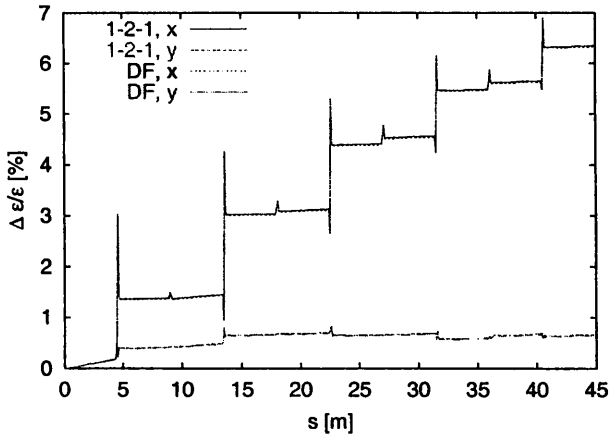

Figure 10.23 The emittance growth for a beam with a local gradient spread of δ=0.05 after dispersion free correction.

10.4 Conclusion

The calculations show that the effects of transverse wakefields in the CTF3 drive-beam accelerator will be significantly smaller if a triplet lattice is used. The higher sensitivity of the triplet lattice to energy errors should not be important since the energy of the beam has to be controlled very accurately to allow operation of the Combiner Ring. The cost of this lattice should not be much higher than for a FODO-cell design. The SICA gives a distinctly better beam stability in the linac than the TDS.

10.5 References

[1] The Drive-Beam Accelerator of CLIC. Proceedings of Linac 1998, Chicago, USA and CERN/PS 98-042 (LP) (1998).

[2] L.Rinolfi. Private communication

[3] L.Thorndahl. Private communication.

[4] A.Millich. Private communication.

[5] M.Luong. Private communication.

[6] E.Jensen. Private communication

[7] D.Schulte. Beam Dynamics Simulations for the CTF3 Drive-Beam Accelerator. CERN/PS 2000-050 (AE) and XX International Linac Conference, 21-25 August 2000, Monterey, California, USA

[8] F.Tecker. Private communication

11. RF POWER

11.1 High Power Generation

11.1.1 General considerations

The basic klystron-modulator layout for the Nominal Phase of CTF3 is shown in Figure 11.1. This will be built up [1] using the existing LIL 3 GHz klystron-modulator high-power RF sources, together with two additional new systems. This will allow the Drive Beam Accelerator to accelerate a beam with 3.5 A current to 150 MeV. The existing modulators were initially designed to operate at 100 Hz with a peak RF power of around 30 MW and a 4.5 μs pulse width. The new klystron-modulators are designed to provide pulsed power for both 35 and 45 MW klystrons, at repetition frequencies up to 25 Hz.

In addition to the 3 GHz systems there are two pulsed RF sources operating at 1.5 GHz. The first, MDK01, is a wide band, low-power klystron-modulator [2] that produces a train of "phase coded" sub-pulses as part of the injector scheme. The second, MDK02 [3], will provide around 20 MW of power for the 1.5 GHz RF deflectors in the Delay Loop.

The RF power for the CTF3 probe beam will be provided by MDK35. This klystron-modulator will also be used as power source for component testing.

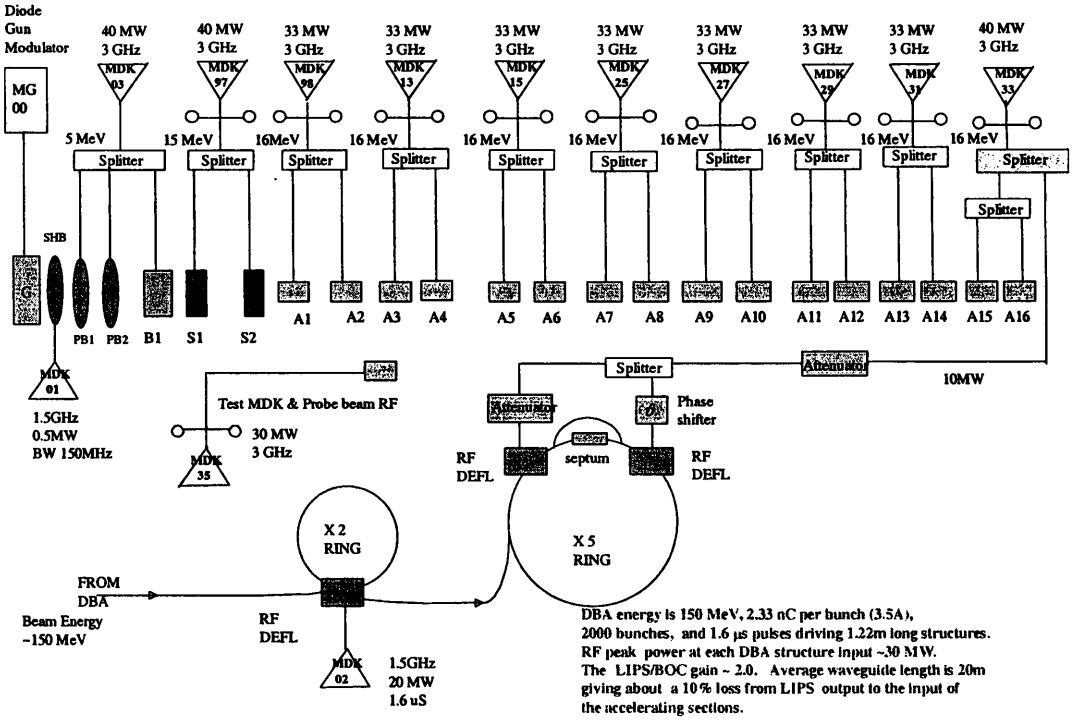

Figure 11.1 Basic klystron-modulator layout

The existing pulsed RF sources can be used at the lower repetition frequency (5 or 10 Hz) of CTF3. They can also provide the same peak output power with the same RF pulse width, but will require a modification to the high-voltage system to maintain the pulse-to-pulse voltage stability at this lower repetition frequency. Alternatively they can operate at 50 Hz without hardware modification, but the RF drive pulses would have to be synchronised and injected into the klystron amplifiers at the desired beam repetition frequency (5 or 10 Hz). A similar method is currently in use with CTF2.

Klystron-modulators MDK13, 15, 25, 27, 29, 31 and 33 are to be used for the Drive Beam Accelerator whilst MDK 03, 97 and 98 will be used for the Drive Beam Injector.

MDK 31 will also be used to provide 3 GHz RF power for the two RF deflectors in the Combiner Ring.

The block diagram in Figure 11.2 shows the basic circuit of an existing LIL klystron-modulator.

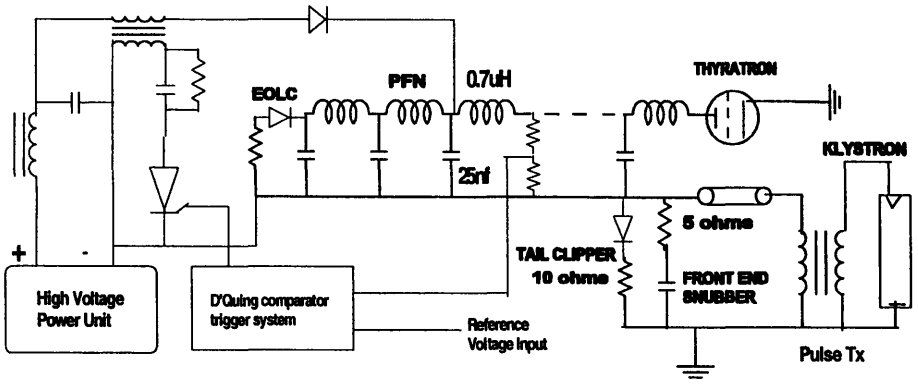

Figure 11.2 LIL klystron-modulator block diagram

All LIL 3 GHz modulators were designed to drive 35 or 37 MW klystrons, consequently some of the modulators will be modified to drive the 45 MW klystrons. These modifications, which consist of using a lower impedance pulse forming network (PFN) to produce a 305 kV (compared to 270 kV) high-voltage pulse at a higher peak current, have already been tested with two modulators in CTF2. The nominal operating parameters at maximum peak output power for both types of klystron-modulator operating at 100 Hz repetition frequency are given in Table 11.1.

Table 11.1 Klystron-Modulator peak operating parameters

Parameters	35 MW klystron-modulator	45 MW klystron-modulator	Units
RF Frequency	2998.55	2998.55	MHz
RF Peak output	35 (37)	45	MW
RF average power	17.5 (18.5)	20	kW
RF power gain	53	54	dB
Klystron efficiency	45	44	%
RF pulse length	4.5	4.5	μs
Klystron voltage	273	305	kV
Klystron current	285	335	A
PFN impedance	5.5	4.4	Ω
Pulse transformer ratio	1:13	1:14.85	
Pulse voltage ripple	±0.15	±0.15	%
Pulse stability	±0.1	±0.1	%

11.1.2 Additional S-band klystron-modulators

The circuit topology for the new modulators is very similar to the existing LIL systems of Figure 11.1 and uses where possible the same component types to maintain common spares. In order to have a more compact design to fit into the available building space, small rack mounting, DC high voltage switched mode power units have been used instead of the larger and more expensive LIL resonant charging systems for the PFN charging. The high-voltage charging capacity for each of the new klystron-modulators (MDK15 and MDK33) will be 30 kJ/s. This will assure 25 Hz operation at the required PFN voltage for maximum peak RF output power. Figure 11.3 shows the calculated charging limit of these switched mode power units at the maximum PFN voltage of ~40 kV and up to 48 Hz repetition frequency. To operate at the maximum PFN voltage and above 48 Hz, extra charging capacity would need to be installed.

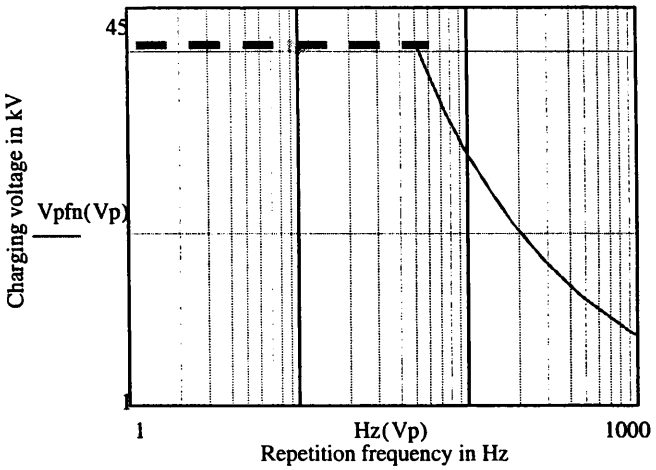

Figure 11.3 Charging voltage versus repetition frequency

The nominal parameters of all CTF3 klystrons are listed in Table 11.2

Table 11.2 Klystron-modulator status for CTF3

Klystron-Modulator	Peak Output Power MW	Frequency MHz	Existing	New	Modify
MDK01	0.5	1500		x	
MDK02	20	1500		x	
MDK03	40	3000	x		x
MDK13	32	3000	x		
MDK15	32	3000		x	
MDK25	32	3000	x		
MDK27	32	3000	x		
MDK29	42	3000	x		x
MDK31	30	3000	x		
MDK33	42	3000	x		x
MDK35	30	3000	x		x
MDK97	40	3000	x		
MDK98	32	3000	x		

11.1.3 S-band Drive-Beam waveguide networks

This waveguide system, connecting the klystron-modulator RF outputs via the pulse compressors to the new accelerating sections will use the modified and extended LIL network. The 35 MW klystron-modulators in the Drive Beam Accelerator will each feed two accelerating sections through 3 dB power splitters. A new long waveguide network, together with a DBA splitter, attenuator and phase shifters will be installed from klystron-modulator MDK33 to the 3 GHz RF deflectors in the Combiner Ring. A new waveguide network will also be installed from the test modulator MDK35 to the Main Beam Accelerator to provide RF power for the probe beam generation.

11.1.4 S-band Injector waveguide network and klystrons

A new waveguide network that combines the outputs of MDK03 and MDK97 to provide RF power to the pre-buncher, buncher and accelerating sections of the CTF3 injector linac will be installed. This operation of two klystrons with their outputs combined via a hybrid power splitter [4] enables efficient phase to amplitude modulation of the summed output RF pulse. It also suppresses flat-top phase ripple created by the high-voltage modulator, and provides a

flat RF phase and amplitude response of the compressed pulse after each LIPS. This combination scheme is shown in Figure 11.4.

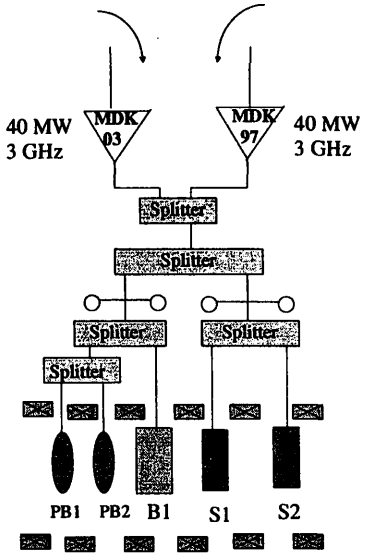

Figure 11.4 Dual klystron drive scheme for CTF3 injectors

11.1.5 L-band klystron-modulators

Two new 1.5 GHz klystron-modulator systems are required (Figure 11.1). One of these systems is used in the sub-harmonic bunching (SHB) scheme and will provide up to 0.5 MW of peak power for the three SHB cavities. The second system is designed to produce a peak output power of ≥20 MW for the two RF deflector cavities in the Delay Loop.

11.1.6 SHB L-band klystron-modulator

The front-end part of the CTF3 injector linac is shown in Figure 11.5. This shows the thermionic gun and the three sub-harmonic cavities SHB1-3 connected to the wide-band, 1.5 GHz klystron. Not shown are the pre-buncher, buncher and the two accelerating cavities, which follow the SHB cavities (see Figure 11.4).

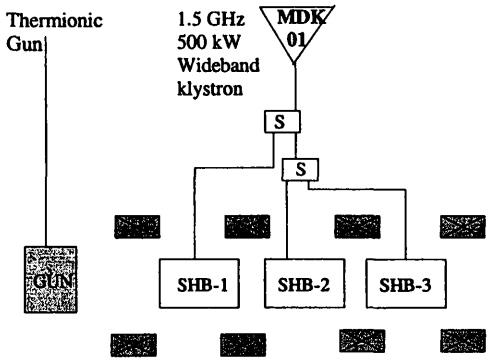

Figure 11.5 Klystron-modulator scheme for the SHB cavities

The parameters of the wide-band 1.5 GHz klystron [5] for the SHB cavities are given in Table 11.3. The klystron will have an efficiency of only ≤ 30% due to the wide bandwidth requirements as shown in Figure 11.6. This bandwidth is needed so that the phase of the klystron can be switched rapidly (<10 ns) through 180° every 140 ns, to produce a train of "phase-coded" pulses within the 2 μs RF pulse.

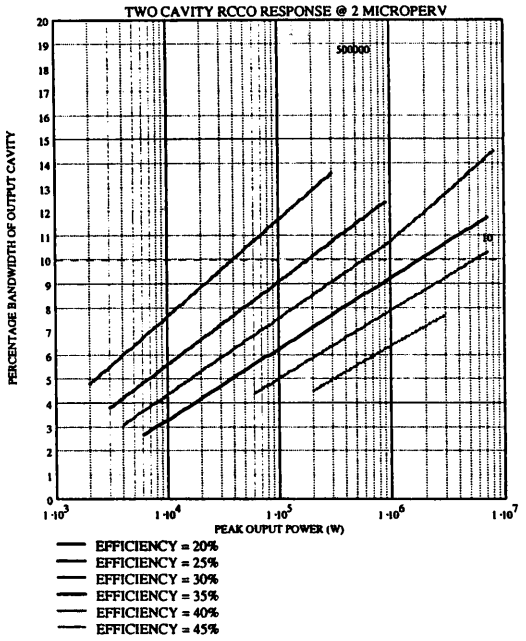

Figure 11.6 Bandwidth-Power-Efficiency parameters of L-band klystron with an extended interaction output cavity RCCO

The bandwidth, power and efficiency parameters for the wideband 1.5 GHz klystron shown in Figure 11.6 refer only to the extended interaction, Resonant Coupled Cavity Output (RCCO) type output cavity of the klystron. The two-cavity RCCO response parameters are calculated for a gun perveance of 2.0 $\mu A/V^{3/2}$ and are lines of constant efficiency. The eight buncher cavities that drive the output section are designed to have a large signal gain of about 40 dB over most of the 150 MHz bandwidth. The nominal working point on these curves for providing power to the three sub-harmonic cavities is indicated at 10% bandwidth and 0.5 MW peak RF output power The output power is taken out through a coaxial window and can connect via a pressurised waveguide transition piece into a standard L-band waveguide WR860.

The wide-band klystron is designed to be grid pulsed but can also be cathode pulsed with a negative voltage in the traditional way. Grid pulsing will improve the rise and fall times of the output RF pulse. An interception grid has been studied because of the low duty cycle involved, although a shadow grid design would enable cathode pulsing with a lower power grid-bias divider. Using a purely grid controlled tube requires a high voltage DC power source with crowbar protection, whereas a pulsed cathode approach can use a more compact modulator. The klystron design enables both methods to be employed.

Table 11.3 Parameters for the 1.5 GHz wide-band klystron

Parameters	Values	Units
Centre frequency	1499.27	MHz
Bandwidth (at -DBA)	≥ 150	MHz
Repetition frequency	10 (operational) 50 (test)	Hz
Peak output power	500 (400 min)	kW
Average power	12.5 (62.5)	W
RF pulse width	≥ 2.0	μs
Klystron beam voltage	69 (63)	kV
Klystron beam current	36 (32)	A
Perveance	2	$\mu A/V^{3/2}$
Focusing field	640	G
Signal gain	≥ 30	dB

A compact modulator circuit is proposed [6] that uses components common to existing high power modulators, but has an Integrated Gate Commutated Thyristor (IGCT) semi-conductor switch array instead of a thyratron. This IGCT device [7] has low switching and on-state losses, requires no snubber components and has an integrated diode and control gate circuitry to reduce the parts count. Unlike the Insulated Gate Bipolar Transistor (IGBT), the IGCT turn-off is not gate-current controlled and its performance is enhanced by the integrated opto-triggered gate-driver, so that it behaves like a true on-off switch. The 91 mm diameter devices chosen have a nominal blocking voltage of 4500 V with a 3500 A turn-on/off current capability. For reliability, a stack of four units is used since the permanent DC voltage that reduces the failure rate due to ambient cosmic radiation at sea level is 2800 V per device. The main parameters of the klystron-modulator are given in Table 11.4.

Table 11.4 SHB modulator main parameters

Parameter	Value	Units
Primary capacitor voltage	5	kV
Peak IGCT pulse current	450	A
Pulse voltage rise time(10-90%)	800	ns
Flat top voltage deviation over 2 μs pulse width	0.3	%
IGCT DC voltage for 100 FIT failure rate	2800	V

The basic electronic circuit of the modulator is given in Figure 11.7 and shows the IGCT device array that discharges an energy storage capacitor network into a step-up pulse transformer. The simulation results of Figure 11.8 show that the circuit produces a good pulse shape with a small amount of droop over the pulse width. A low-inductance capacitor network replaces a PFN that eliminates any flat top voltage ripple, and consequently any phase ripple at the wide-band klystron output.

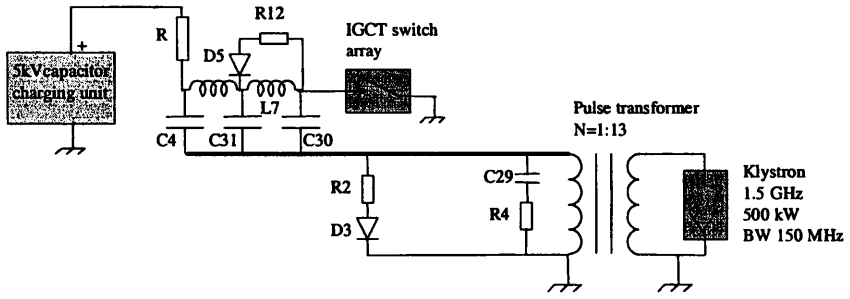

Figure 11.7 Basic SHB klystron-modulator circuit

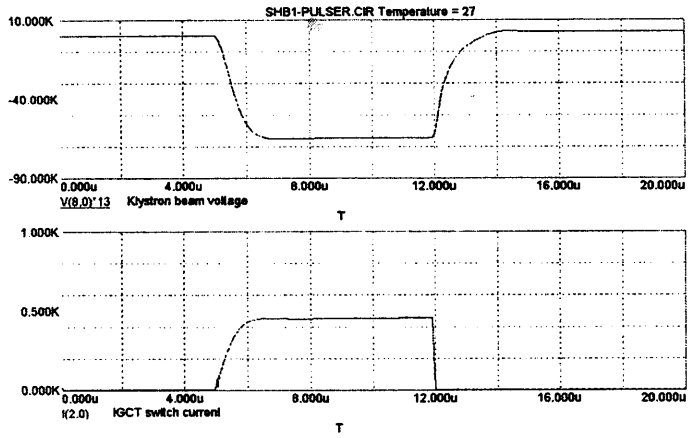

Figure 11.8 Simulation waveforms of SHB klystron-modulator

11.1.7 L-band RF deflector klystron-modulator

The 3 GHz frequency of the Drive Beam Accelerator enables the existing LIL klystron-modulators and pulse compression units to be used for power production. These systems will produce a compressed RF power pulse of 1.4 μs. An L-band klystron-modulator system will provide the 1.5 GHz RF power for the two transverse RF deflecting sections in the Delay Loop. The basic block diagram of this klystron-modulator is given in Figure 11.9. Two types of transverse RF deflecting structures [8] are being studied (travelling wave and standing wave) although the diagram below shows only travelling wave deflectors with their terminating loads. From the klystron and modulator operational perspective, a travelling wave structure will require a shorter RF pulse than a standing wave structure. This implies that the klystron must be capable of providing the desired amount of peak power at the largest pulse width, and the modulator pulse-forming network must be designed accordingly. The 1.5 GHz klystron design will ensure that a pulse width of up to 8 μs at a peak output power is provided at a maximum repetition frequency of 50 Hz to allow for RF conditioning of the structures in a shorter period of time. The klystron parameters are given in Table 11.5.

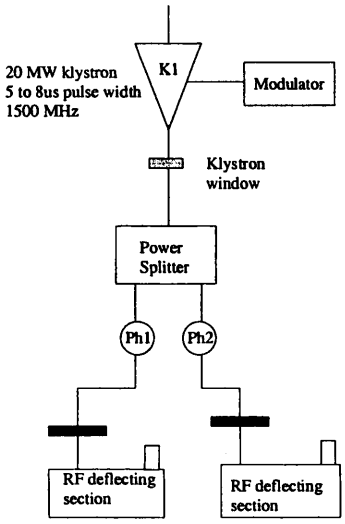

Figure 11.9 Transverse RF deflection klystron-modulator scheme

Table 11.5 General L-band klystron parameters

Parameters	Value	Units
Centre frequency	1500	MHz
Bandwidth (1 dB)	8.5 (min)	MHz
Peak Output Power	20 (min), 25 (max)	MW
Pulse width	5 max at 25 MW, 8 max at 20 MW	μs
Repetition frequency	100 (max)	Hz
Electronic efficiency	42	%
Klystron beam voltage	260 (max)	kV
Klystron beam current	250 (max)	A
Microperveance	1.9 (min) to 2.0 (max)	$\mu A/V^{3/2}$
Heater voltage	28 (max)	V
Heater current	28 (max)	A
Large signal gain	49.5	dB
SF6 pressure on RF window	1.5 (max)	bar
Focal coil voltage	180	V
Focal coil current	70	A
RF window flange	CPR 650F	-

The two different sets of klystron-modulator (MDK) parameters for the 5 and 8 μs RF pulse width generation are given in Table 11.6. These have been calculated for the maximum repetition frequency of 50 Hz and assume a standard line-type modulator configuration with a thyratron switch, as used in the ex-LIL systems. The perveance of the L-band klystron load is put to a minimum of 1.9 and maximum of 2.0 $\mu A/V^{3/2}$ in order to calculate the range of the other modulator parameters. This data shows that a common modulator design can be used for both cases. Only a change in the cell capacitance value (32 to 42.5 nF) and a cell inductance tuning range from about 0.6 to 1.0 μH are needed. The PFN switched-mode charging voltage supply will need to operate between 30 and 35 kV, and the charging power requirements indicated are for operation at a 50 Hz repetition rate.

Table 11.6 RF deflector klystron-modulator parameters

Parameters	TW deflector MDK	SW deflector MDK	Units
Peak output power	25 (max)	20 (max)	MW
RF pulse width	5 (max)	8 (max)	μs
Repetition frequency (max)	100	50	Hz
Klystron perveance	1.9 [2.0]	1.9 [2.0]	$\mu A/V^{3/2}$
Voltage pulse width	6	9	μs
Klystron beam voltage	250 [245]	230 [225]	kV
Klystron beam current	238 (243)	210 [213]	A
PFN impedance	4.5	4.75	Ω
Klystron to PFN mismatch	+5	+5	%
Number of PFN cells	25	25	-
Cell capacitance	32	42.5	nF
Cell inductance	0.7 [0.65]	1.0 [0.87]	μH
PFN operating voltage	34 [33]	31 [30.5]	kV
Pulse transformer ratio	1:14.85	1:14.85	-
Pulse transformer volt-seconds	1.76 [1.73]	2.3 [2.15]	VS
Thyratron peak current	3.67 [3.7]	3.29 [3.4]	kA
Thyratron average current	1.3	1.65	A
PFN charging power	30	30	kW
PFN charging time	15	18	ms

11.2 RF Pulse Compression

11.2.1 Phase programming the LIPS system

RF power pulses of 1.6 msec length are required to accelerate the drive beam. In order to provide sufficient RF power to achieve the nominal accelerating gradient and full beam loading, the RF pulses from the available klystrons have to be compressed in time to achieve a gain in peak RF power of about a factor of two. LPI used the LIPS [9] RF pulse compression system, consisting of two storage cavities coupled via a 3-db hybrid, which produced a pulse shape with high peak power and an exponential decay. CTF3, however, requires a rectangular pulse with a maximum amplitude variation of 0.5 % and a phase modulation of one degree at the flat top.

The required flat pulse can be obtained by using RF amplitude or/and RF phase modulation of the klystron input signal [10]. This gives a RF power gain of about two. The phase / amplitude modulation is optimised for the cavity Q-value and coupling factor, as well as the pulse duration. An additional power gain of about 10 % can be obtained by switching on the RF before the HV pulse reaches klystron saturation. An example of the compressed pulses for two different klystron pulse lengths is shown in Figure 11.10 . The power gain vs. klystron pulse length for the two types of modulation (RF phase or RF amplitude) is shown in Figure 11.11. Here results are given for the actual LIPS system and for a modified system with optimised cavity coupling factors.

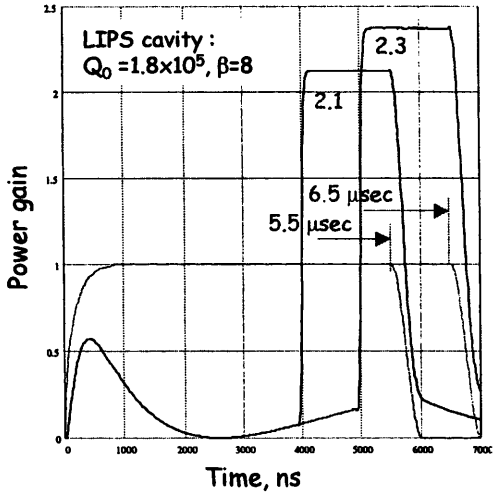

Figure 11.10 Compressed pulses with different klystron pulse length

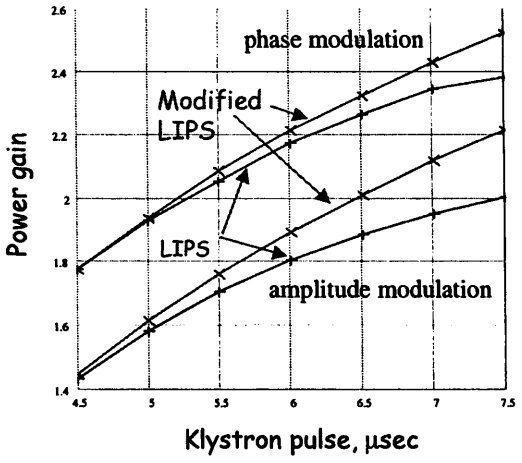

Figure 11.11 Peak power gain as function of klystron pulse length. The upper curves are for phase modulation, the lower ones for amplitude modulation.

Due to the higher power gain, the method using RF phase modulation was adopted. The typical shape of the klystron phase modulation and the phase behaviour of the output pulse are shown in Figure 11.12. To compensate the variation of the output RF phase $\Delta\varphi$, which leads to a modulation of the beam energy, it is foreseen to introduce a slight RF frequency offset $\Delta\omega$. The required detuning is: $\pm\Delta\varphi = \pm\Delta\omega T_{out}$, which in our case it is about 130 kHz. The residual RF phase sag (second order effect) will be compensated by anti-phase operation of alternate klystrons.

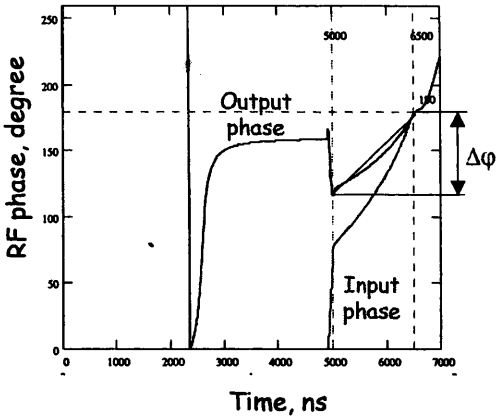

Figure 11.12 Input and output RF phases for the case of the flat compressed pulse

In the following the effect of system imperfections will be analysed.

A ripple of the klystron High Voltage supply causes parasitic amplitude and phase modulation of the klystron output. Since the klystrons operate in saturation, the RF amplitude ripple is generally small. However, parasitic phase ripple distorts the RF pulse dramatically. The resulting amplitude ripple of the compressed pulse due to a 3 ° RF phase modulation of the input pulse is shown in Figure 11.13. The RF amplitude ripple of the compressed vs. klystron RF phase ripple amplitude is shown in Figure 11.14.

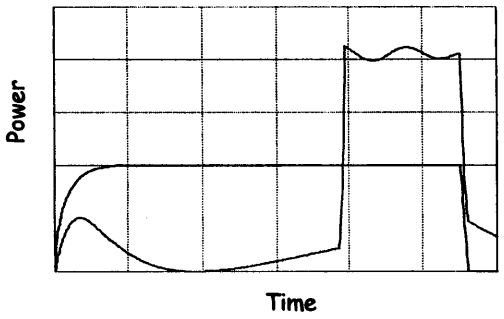

Figure 11.13 Amplitude ripple caused by RF phase ripple

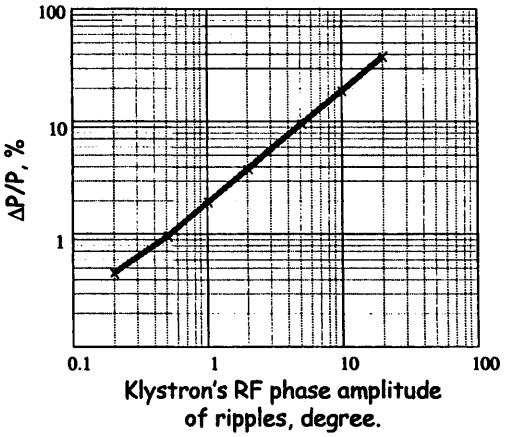

Figure 11.14 Peak-to-peak amplitude ripple as function of RF phase ripple

From this we conclude that less than ± 1° of RF phase ripple from the klystrons is necessary to obtain the required pulse flatness.

Another source of distortion is a tuning error of the storage cavity resonant frequency. This can be a common error of both cavities or a difference between the two cavities of a pair. The distortion of the flat top as a function of cavity detuning is shown in Figure 11.15. The maximum amplitude of this distortion vs. detuning of the cavity central frequency (circles) and vs. the frequency difference between the two cavities (diamonds) is shown in Figure 11.16.

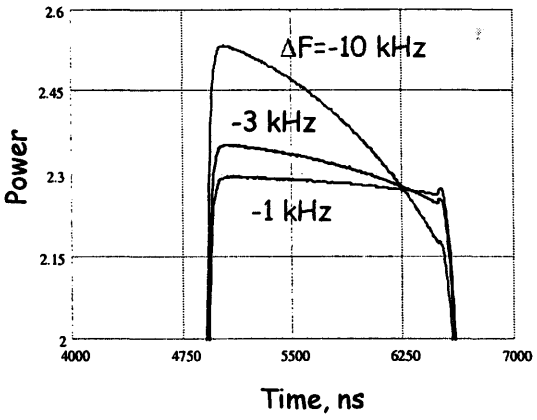

Figure 11.15 Pulse shape distortion for different values of cavity frequency detuning

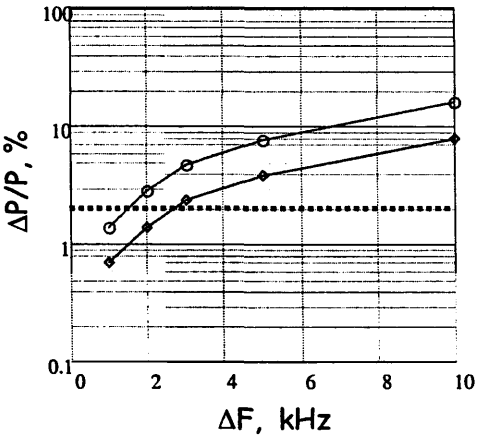

Figure 11.16 Amplitude of pulse distortion vs. frequency detuning

To keep the flatness of the compressed pulse within the specified range, the cavity resonant frequency must be stabilized to better then ±1.5 kHz. This imposes very stringent requirements on the cavity cooling system. The water temperature must be controlled to an accuracy of 0.03 °C. However, this is only required for long-term stability. Short term corrections will be applied with RF phase control [11].

High power tests were carried out to demonstrate the overall performance of the LIPS pulse compression with RF phase modulation [12].

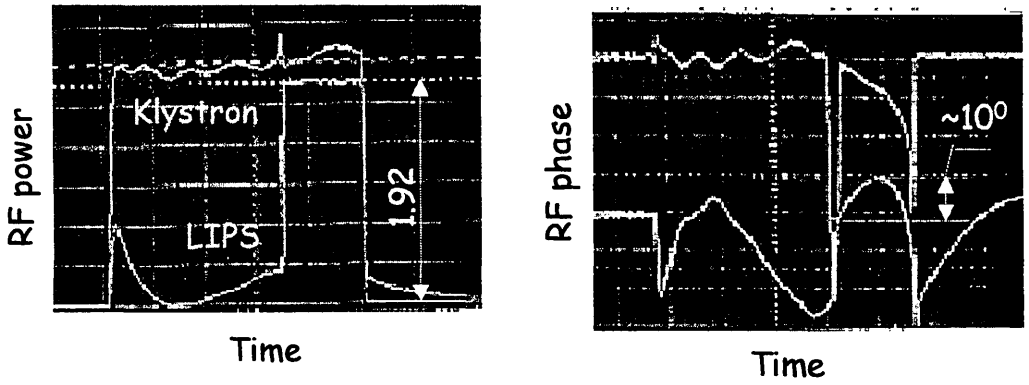

Figure 11.17 RF power and phase of the compressed pulse measured during high power tests

In these tests first the RF phase ripple of the klystron was corrected by RF phase modulation of the klystron input. Second the RF phase modulation programme for the flat top of the compressed pulse was installed. The results of the preliminary tests are shown in Figure 11.17. The flat top deviations were measured to be better than 1 % and the power gain was 1.92, i.e. 95% of the theoretical value. A power gain factor of two seems within reach.

11.2.2 Barrel Open Cavity Pulse Compression System (BOC).

At least nine RF pulse compression systems are required for the 3 GHz Drive Beam Accelerator. Since presently only five reliable LIPS systems are available from LPI, it was decided to develop a different technique for the new systems, based on the Barrel Open Cavity (BOC). This scheme avoids the double-cavity system of LIPS by making use of a single, travelling wave cavity. Such a system (VPM) was developed in Russia for the VLEPP

Linear Collider [13]. An X-band version of VPM was successfully tested at KEK at an RF power level of 150 MW [14].

The BOC is based on a special mode of operation, the "whispering gallery" mode. Here almost all RF energy is concentrated close to the cavity surface. The theory is described in [15].

The elliptical cavity profile (Figure 11.18) is described by:

Cavity profile:

$$z = \sqrt{ar_0\left\{1-\left(\frac{r}{a}\right)^2\right\}}$$

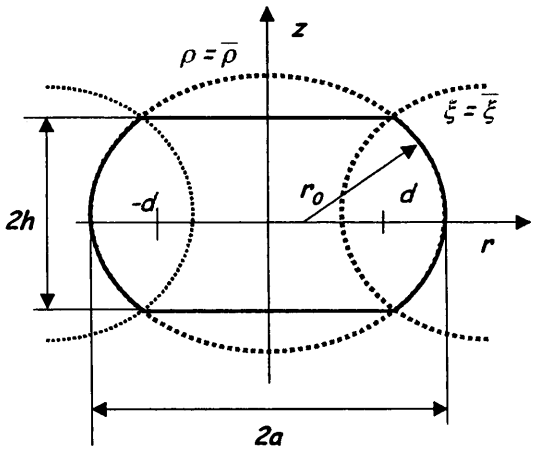

Figure 11.18 BOC profile

The eigen-frequencies of the BOC operating with E_{mnq} modes can be found from :

$$ka = \nu_{mn} + \frac{(q+1/2)a}{\sin\delta},$$

where ν_{mn} is the root of the Bessel function, which can be approximated for big m values as:

$$\nu_{mn} = m - \mu t_n^0 \quad n = 1,2....,$$
$$t_n^0 = [(n-0.25)1.5\pi]^{2/3}, \quad \mu = (m/2)^{1/3}$$

In such a cavity the field decays exponentially towards the z-axis which prevents the operating mode from radiating outside. The optimum cavity wall radius r_0, for which this decay is strongest, is defined as: $r_0 = 2a\sin^2\theta$, where α and θ can be derived from:

$$\sin\alpha = \sqrt{\frac{a}{r_0}}\sin\theta \quad , \quad \cos\theta = \frac{m}{\nu_{mn}}.$$

The Q-factor of the cavity operating with E modes is given simply by:

$$Q_0 = \frac{a}{\sigma},$$

where σ is a skin-depth of the cavity wall material. At 3 GHz the skin-depth for cooper is about 1.2 μm. Therefore a Q-factor of about 200 000 can be achieved in a copper BOC with a radius of about 25 cm.

In order to satisfy the RF pulse compression requirements, the $E_{10,1,1}$ mode was chosen. The theoretical Q-factor for such a cavity computed with HFSS was 190 000. The electric field distributions for some modes of the BOC are shown in Figure 11.19.

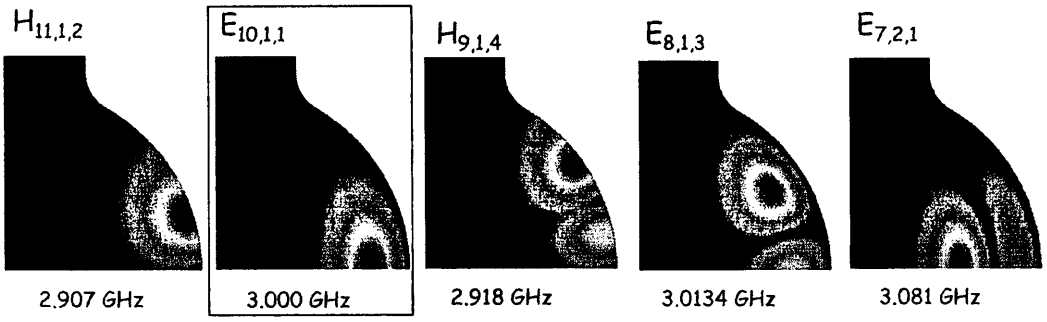

Figure 11.19 Electric fields pattern of the modes in BOC.

Special attention must be attributed to the dense spectrum of cavity modes. The mode separation should be more than the frequency spread due to transient effects in the cavity. In our case this corresponds to about 10 MHz. The neighbour modes of the present design configuration are separated by at least 13 MHz. This is considered a safe margin, therefore no additional damping is foreseen.

The cavity is excited through 40 coupling holes between the cavity and the surrounding waveguide. The waveguide width (w) was chosen to provide synchronism between cavity and waveguide at the resonant frequency with wavelength λ_0:

$$2\pi(a+\Delta+w)/m=\lambda_0/\sqrt{1-\left(\frac{\lambda_0}{2w}\right)^2}$$

where Δ is the thickness of the common wall. The waveguide junctions were designed to provide an overall matching of better than –30 db. This is very important in order to assure a travelling wave regime and to reduce reflections (see Figure 11.20).

The number of coupling holes N is $N = m/4$ (total 40) satisfy travelling wave excitation, with an RF phase shift of $\lambda/4$ between the coupling holes at the resonant frequency. The diameter of the coupling holes was optimised to meet the design loaded Q-factor. The electric field distribution at the BOC median plane operating in a TW-regime is shown in Figure 11.21. The BOC compressor design is shown in Figure 11.22.

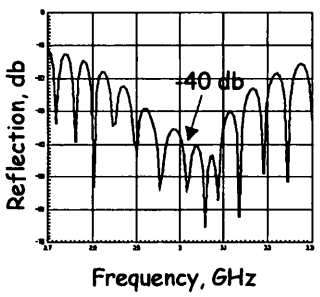

Figure 11.20 Matching of the waveguides

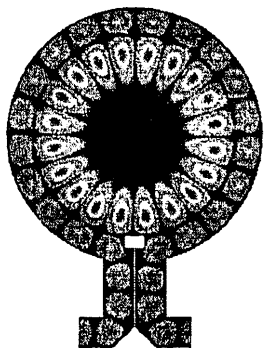

Figure 11.21 . Electric field plot in the BOC median plane.

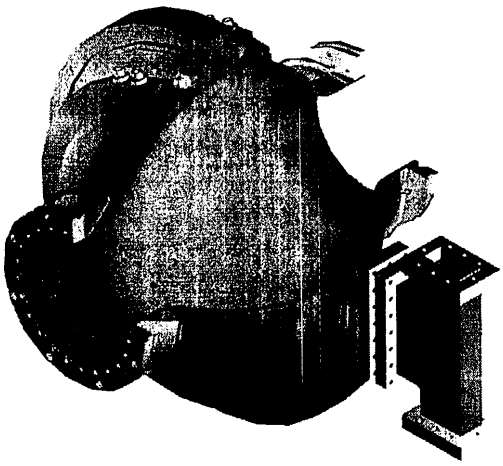

Figure 11.22 The BOC RF pulse compressor

No mechanical tuning of the cavity frequency is foreseen during operation. The required frequency adjustments will be done with the temperature of the cooling water. With ±5 °C temperature variation the frequency tuning will be within ± 0.5 MHz.

11.3 REFERENCES:

[1] P.Pearce, "Towards an RF power source scenario for CTF3 using LIL klystron-modulators". CTF Note 99-27 (August 1999).

[2] P.Pearce, "Specification for a feasibility study of a Broad-Band klystron for the CLIC test facility (CTF3) to operate at a centre frequency of 1.5 GHz". PS/LP Note 2000-003 (Spec) (October 2000).

[3] P.Pearce, "Specification for the supply of a design report and the manufacture of an L-Band klystron operating at 1.5 GHz for the CLIC test facility CTF3". PS/LP Note 2000-004 (Spec) (February 2001).

[4] I.Syratchev, "Possibility of the Pulse Compression application for the CTF3 injector". Private communication (January 2000).

[5] V.R.Nuth and G.Phillips, "A 500kW L-Band Klystron with Broad Bandwidth for Sub-Harmonic Bunching in the CLIC Test Facility". Proceedings of the 5th Klystron-Modulator Workshop, MDK2001 (CERN, Geneva, April 2001).

[6] P.Pearce, "Design proposal for a Compact Solid-State, Low-Power Klystron –Pulser for CTF3". Proceedings of the 5th Klystron-Modulator Workshop, MDK2001 (CERN, Geneva, April 2001), CLIC-Note-479.

[7] H.M.Stillman, "IGCTs-Megawatt power switches for medium-voltage applications". ABB Zurich, Switzerland-ABB Review 3/97.

[8] A.Gallo, D.Alesini, F.Marcellini, R.Corsini, D.Schulte, I.Syratchev, "Studies on the RF deflectors for CTF3". Proceedings of EPAC 2000, Vienna, Austria.

[9] A.Fiebig and R.Hohbach, Study of peak power doublers with spherical resonators, CERN/PS/RF/83-9, published at 1983 Particle Accelerator Conf., Santa Fe, 1983

[10] A.Fiebig and Ch.Schieblich, A SLED type pulse compressor with rectangular pulse shape, CERN/PS 90-13(RF), published at EPAC90, Nice 1990, p.937

[11] I. Syratchev 'RF pulse compression system for CTF3', MDK Workshop, CERN, Geneva, April 2001

[12] R. Bossart 'Flat-Topped RF Pulse Compressor for CTF3-Accelerator', RF Pulse Compression Power Distribution Workshop, SLAC, October 2001.

[13] V. Balakin, in Proceedings of the LC-90 Workshop, Tsukuba, Japan.

[14] Syrachev I.V., "The Results of RF High Power Tests of X-Band Open Cavity RF Pulse Compression System", Proc. Int. Conference Linac-94, Tsukuba, Japan, 1994, pp. 475-477.

[15] Vainshtain L.A., "Barrel-shape open cavities", in High RF Power Electronics, 1964 pp. 170-215 (in Russian).

12. RF LOW POWER

The main RF frequency of 2.99855 GHz is generated in a stable synthesiser (Figure 12.1). The frequency for the sub-harmonic buncher is derived with a divider and with more dividers the timing system is synchronised to the RF frequency. Two more frequencies are generated for the klystrons with pulse compression: a leading frequency, which is applied to the odd numbered klystrons with pulse compression and a lagging one, applied to the even numbered klystrons. The propagation delay of the RF-signals from the centrally located frequency synthesiser to the input of the low level phase control system for each klystron is kept equal for all klystrons by using phase stabilised coaxial cables of equal length. A ½ inch cable from Andrews, the HJ 4 – 50 could be used. The temperature coefficient for this cable is between 3 and 6 ppm/degree C. The coaxial lines are partly installed on cable drums in the accelerator tunnel, where the temperature differences are smaller than 1 degree C. The maximum phase difference between the coaxial distribution lines of 60 m length amounts then to 1.4 deg. at 3 GHz. If the attenuation of this cable (16.2 dB/100 m at 3 GHz) is too high, a similar 7/8 inch cable with an attenuation of 7.9 dB/100 m could be used.

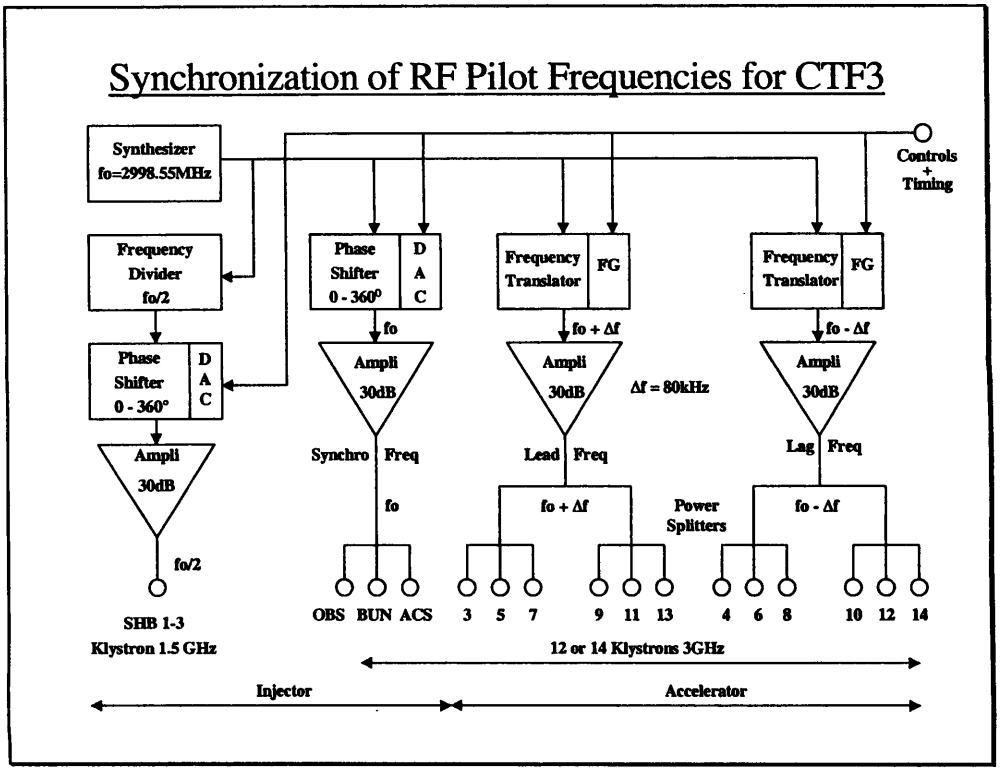

Figure 12.1 Block diagram of the RF distribution system.

12.1 Phase control

A block diagram of the Phase Control system is shown in Figure 12.2. At the input of each 3 GHz amplifier chain a remotely controllable digital 10 bits 360 degree phase shifter is used to adjust the phase of the RF-wave in the accelerating structures. In CTF3 the synchronous RF-phase angle of the beam is about 7 degrees before the crest of the RF wave.

Uncontrollable phase variations in the amplifier chain, especially the klystron and in the waveguide system are compensated with a feed forward loop. The phase between the reference and a signal, taken from a directional coupler in the waveguide close to one of the two accelerating structures is measured with a quadrature mixer during the compressed pulse duration. With a fast data acquisition system which could include a digital signal processor, the phase is measured at intervals of maximum 100 ns during the passage of the bunch train.

The average phase error is then calculated and applied to the digital phase shifter. The sensitivity of the phase detector is directly proportional to the amplitude of the RF signal returned from the waveguide. This can vary by a factor two. By using a quadrature detector the amplitude information is also available and the phase signal can be corrected accordingly. The fast analogue phase shifter is used for the phase programme of the pulse compression system.

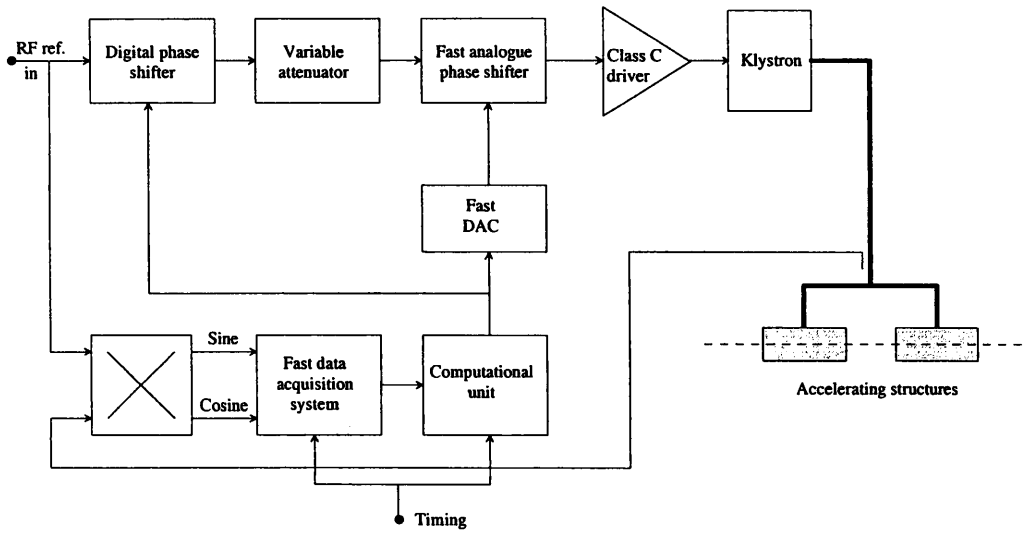

Figure 12.2 Block diagram of the phase control system

12.2 Amplitude control.

At nominal beam current the accelerating sections are fully loaded which means that the field in the last cell is zero. With the same klystron power at very low current the field will then be twice as high. To obtain the same accelerating voltage the klystron output power should be decreased a factor four. This cannot be done by acting on the drive of the klystron because the driver amplifiers are of the class C type working in a strongly non linear regime. Instead, the klystron output power can be varied between 17 and 35 MW by adjusting the modulator voltage.

For beam energy control, the power gain of the compressor can be adjusted with high resolution by changing the timing of the pulse compression and the duration of the RF power production of the klystron. A similar timing adjustment of the pulse compression has been successfully employed during the operation of LIL for adjustment of the beam energy.

13. LONGITUDINAL BEAM DYNAMICS ISSUES

One important problem to be solved in the compressor system of CTF3 [1] is to preserve the beam quality. In particular, energy losses and energy spread are of a great concern for the Combiner Ring design.

A very short bunch length is required after recombination for efficient 30 GHz power production. In order to avoid excessive bunch lengthening, the momentum compaction of the transfer lines, the Delay Loop and the Combiner Ring are kept very small. However, for short bunches the impedance of the Combiner Ring as well as coherent synchrotron radiation effects become important issues, leading to an energy loss and an increase in energy spread. The energy losses give rise to relative phase errors between bunches through non-perfect ring isochronicity, which result in deterioration of the timing between both individual bunches and merging trains. The energy spread, in turn, leads to bunch lengthening and phase space distortion. Thus, both energy spread and energy losses can strongly affect the efficiency of the driving beam interaction with the transfer structures of the Drive Beam Decelerator. In order to minimise these effects, the rms bunch length is increased from its value of 1.3 mm in the linac to a maximum of 2.5 mm in the Delay Loop and Combiner Ring, by using a magnetic chicane placed at the end of the linac. After combination, for efficient power production, the individual bunches are finally compressed in length to about 0.5 mm rms in a magnetic bunch compressor.

In paragraph 13.1 we discuss the energy spread and losses due to the coherent synchrotron radiation (CSR), while in paragraph 13.2 we make an attempt to estimate the Combiner Ring impedance budget and to describe possible design solutions of different vacuum chamber discontinuities, aimed at the reduction of the wake-fields. In paragraph 10.3 we give the results of a longitudinal beam dynamics simulations in CTF3, taking into account the effects described above.

Despite the fact that CSR can be described in terms of coupling impedance like the "conventional" impedance of vacuum chamber discontinuities, we intentionally separate these two impedance contributions in two paragraphs since they have different impact on the vacuum chamber design. The CSR emission can be decreased by reducing the dimensions of the beam pipe. On the contrary, for the reduction of conventional wake-fields bigger beam pipe sizes are preferable. A reasonable compromise between the conflicting requirements needs to be found. According to the design requirements, the maximum bunch energy spread added in the Combiner Ring should not exceed ±1% of the nominal energy and the average energy variation along the bunch train must be less than 1%.

13.1 Coherent Synchrotron Radiation in CTF3 Combiner Ring

Short, high charge bunches deflected by the small radius bending magnets of the CTF3 Combiner Ring can emit CSR at wavelengths longer than the bunch length. This is a potentially dangerous effect leading to energy spread, energy loss and transverse emittance growth.

First analytical evaluations of the effect and numerical simulations in the longitudinal phase [1] have shown that both energy spread and energy loss due to CSR are tolerable for the ring longitudinal acceptance and allow final bunch compression. These estimates rely on the parallel plate (PP) approximation, i.e. considering a bunch rotating on the circular orbit in the mid plane between two infinite parallel plates, while a real accelerator vacuum chamber is more similar to a toroidal cavity. Therefore, the validity of the PP approximation needs to be checked. Moreover, the CSR estimates were done for arc cells of the Combiner Ring containing bending magnets with a radius of curvature of 3.6 m and 1.4 m. Since we are planning to re-use the EPA magnets with a radius of about 1 m the CSR estimates need to be redone.

Contrary to a rather smooth PP impedance (see, for example, [2]), the toroidal chamber (TC) impedance consists of numerous narrow peaks [3]. This means that long lasting TC wake-fields can affect multibunch beam dynamics, specially when taking into account the short bunch separation of 2 cm in CTF3 bunch trains. There are, at least, two points in favour of the PP approximation applicability to the CTF3 ring case:

1) The TC impedance is shown [3] to be very similar to the impedance of a flat pill-box. Asymptotically, by increasing the pill-box radius, its impedance is transformed into the PP impedance [4]. In turn, the PP impedance tends to the free space CSR impedance by increasing the distance between the parallel plates. Thus, one should expect similar wake-fields, at least along the bunch length, in the PP case and for the flat toroidal chamber, when the horizontal chamber size is much larger than the vertical one. Indeed, this has been proven by studying CSR in the Compact Storage Ring [5] with a vacuum chamber cross section of 38×80 mm, which is very similar to that proposed for the CTF3 Combiner Ring, having dimensions of 36×90 mm.

2) A realistic vacuum chamber has a racetrack geometry instead of toroidal, i.e., the bending sections are interleaved with straight sections. For such geometry the resonant condition changes, leading to resonant peak broadening [6]:

$$\Delta n = \frac{2\pi\rho}{w}\frac{\rho}{l}$$

where Δn is the peak bandwidth in terms of revolution harmonics; ρ is the radius of curvature; w is the vacuum chamber width; l is the bending magnet length.

For CTF3 Combiner Ring parameters, the resonant bandwidth is such that the wake-field decays at a distance of 1.2 cm behind the bunch and does not affect the next bunches in the bunch train following at a distance of 2 cm. Figure 13.1 shows for comparison the real part of the PP impedance and that of the toroidal chamber with CTF3 ring cross section (which takes into account the resonant peak broadening). Since the wake potential is the anti-Fourier transform of the impedance weighted by the bunch spectrum, the resulting wake inside the bunch should be very similar for both cases shown in Figure 13.1. The PP model appears therefore to be a good approximation in this respect.

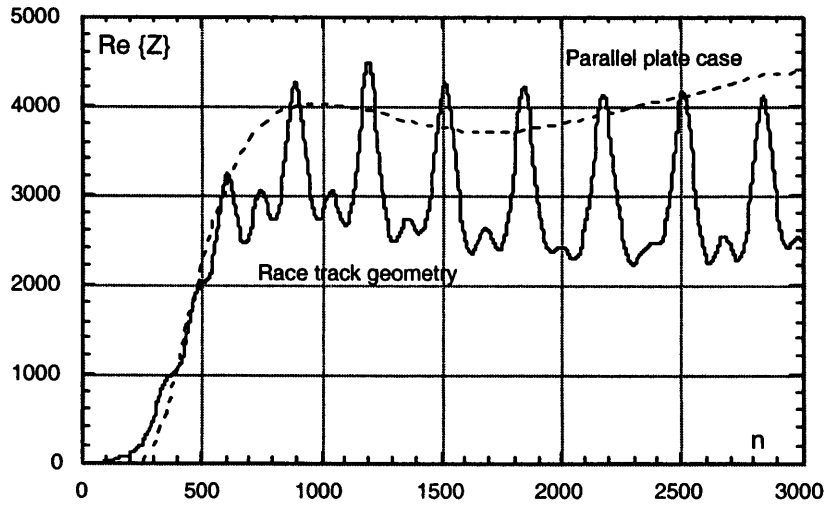

Figure 13.1 Real part of the CSR impedance

Another concern is the fact that both the PP and the TC models are strictly valid for constant length, rigid bunches following a circular orbit. However, in the Combiner Ring the bunches do not have a constant length, nor follow a circular orbit. Therefore, a check has been made using the code TraFiC^4 [7], recently tested successfully against experimental results in CTF2 [8]. A full isochronous cell has been used in the simulation. The rms bunch length oscillates in the cell by about ± 0.3 mm, in good agreement with MAD calculations. Unfortunately, TraFiC^4 does not yet allow the use of sextupoles, so that the second order momentum compaction cannot be corrected, and the final bunch length after one pass in the cell is slightly longer than the initial one. In spite of that, a first evaluation of the longitudinal wake has been obtained by plotting the difference between initial and final energy of the test particles against their initial position in the bunch. The average energy loss and the energy spread are in reasonable agreement with the analytical evaluation of the wake [9].

So, in order to simplify the estimate, one can safely apply the PP approximation to evaluate the energy spread and the energy loss due to CSR. The wake force calculated in eV/m in the PP plate approximation is given by [2]:

$$W(x/\sigma)=\frac{10^{10}}{1.111}\frac{Q}{\left(3\rho|^3\sigma^4\right)^{1/3}}\sqrt{\frac{2}{\pi}}\left[\Phi(x)-\left(\frac{3}{4}\right)^{1/3}\Sigma^{4/3}\int_{-\infty}^{\infty}dyG_2(\Sigma y)\exp\left(-\frac{1}{2}(x-y)^2\right)\right].$$

Here Q is the bunch charge; σ is the bunch length, $G_2(x)$ is a scaling function (see [2]). The parameter characterising the PP CSR shielding effect is defined as:

$$\Sigma=\frac{\sigma}{2h}(\rho/h)^{1/2}$$

with $2h$ being the distance between the parallel plates. The function $\Phi(x)$ describing the free space CSR behaviour along the bunch is given by:

$$\Phi(x)=\Gamma(2/3)\exp\left(-\frac{x^4}{4}\right)D_{1/3}(-x)$$

where $\Gamma(x)$ is the Gamma function and $D_{1/3}(x)$ is the parabolic cylinder function. Figure 13.2 shows the wake force calculated for a bunch length of 1 mm, 2 mm and 3 mm, respectively, considering the EPA magnets with ρ = 1.075 m and the distance between the parallel plates $2h$ = 36 mm.

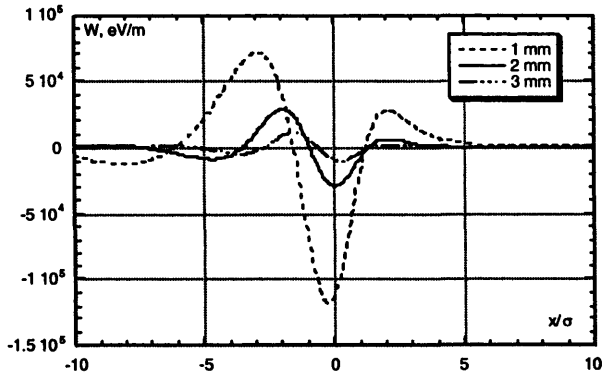

Figure 13.2 CSR wake force in EPA magnets for different bunch lengths.

Let us estimate the energy spread for a bunch with rms length of 2 mm. As is seen in Figure 13.2, the peaks of the wake force have almost the same absolute value of 3×10^4 eV/m. Taking into account that the CTF3 Combiner Ring contains 12 bending magnets each 0.5629 m long and in the worst case the bunches make 4.5 turns, we can immediately

calculate $\Delta E = \pm 0.9$ MeV, or $\Delta E/E \sim \pm 0.5\%$. This means that the energy spread due to CSR is half of that allowable by specifications. Comparing in Figure 13.2 the wakes of 1 mm and 2 mm bunches, we conclude that the energy spread for 1 mm long bunches would exceed the acceptable value. So, bunch stretching before injection into the Combiner Ring up to 2 mm or preferably larger is necessary to minimise the CSR effect and to keep the energy spread within limits.

13.2 Conventional Impedance Budget and Wake-Fields

Besides CSR, the electromagnetic interaction with the vacuum chamber can produce energy spread and energy loss. This interaction is usually described in terms of the frequency dependent impedance or in terms of wake-fields in the time domain [10]. The vacuum chamber has to be carefully designed in order to minimise the impedance and thus to avoid excessive energy loss and spread.

Below we list possible impedance contributing elements in the CTF3 Combiner Ring.

Phenomena (not discontinuities)

1. Coherent synchrotron radiation
2. Resistive walls
3. Space charge

Large objects

1. RF deflectors
2. Extraction kickers
3. BPMs or striplines
4. Synchrotron radiation port
5. Injection port
6. Extraction port
7. RF cavity (if decided to be installed)
8. Other

Small discontinuities

1. Tapers
2. Pumping ports
3. Valves
4. Shielded bellows
5. Flanges
6. Other

Let us evaluate very roughly an acceptable conventional impedance (i.e. excluding the CSR contribution) for the CTF3 Combiner Ring. Assume that the energy spread should be less than ± 1 MeV after 4.5 turns ($\Delta E/E \sim \pm 0.5\%$). Note that this condition also automatically satisfies the project constraint of having the energy spread along the train below 1%.

For the estimation, we assume an inductive impedance that dominates at low frequencies:

$$Z(\omega) = j\omega L; \qquad \frac{Z(\omega)\omega_0}{\omega} = \frac{Z}{n} = j\frac{cL}{R}$$

where ω is the angular frequency, ω_0 the angular revolution frequency, n the harmonic number, c the light velocity, L the vacuum chamber inductance and R the average machine radius.

For such an impedance the minimum and maximum of the wake potential inside the bunch are reached at $-1\ \sigma$ and $+1\ \sigma$, respectively and are given by:

$$W_{\max}\left[\frac{V}{C}\right] = -W_{\min}\left[\frac{V}{C}\right] = \frac{Lc^2}{\sigma^2\sqrt{2\pi e}}$$

In order to satisfy the above-mentioned requirements on the energy spread for a 2 mm long bunch with a charge of 2.33 nC, the vacuum chamber inductance L must be smaller than $1.752 \cdot 10^{-8}$ H and the corresponding normalised impedance $Z/n < 0.4\ \Omega$. However, this estimate can be considered as very approximate. The impedance and the wake potential of vacuum chamber discontinuities can differ a lot from the inductive one, especially for large vacuum chamber objects. Nevertheless, the estimated value compared to the impedance of other accelerator rings (for example, $Z/n \sim 21\ \Omega$ in EPA [11] and $0.6\ \Omega$ in DAΦNE [12]) shows that a very careful design of the CTF3 Combiner Ring vacuum chamber is necessary.

Since bunches make less than 5 turns in the Combiner Ring, it is more convenient to consider directly wake-fields in the time domain.

13.2.1 Resistive walls

In calculating the resistive wall contribution we assume that the Combiner Ring vacuum chamber has a constant cross section with dimensions $2a \times 2b = 90 \times 36$ mm. This is the cross section of the vacuum chamber inside bending magnets. Since, in order to avoid many vacuum chamber discontinuities, we are planning to build a smooth vacuum chamber keeping its cross section as constant as possible, this assumption is correct. The bunch length in the ring is much longer than the characteristic distance s_0 [13]:

$$s_0 = \left(\frac{c\rho b^2}{2\pi}\right)^{1/3}$$

where ρ is the material resistivity. Because of that, the long-range formulae for the resistive wall impedance and the loss factor k_l per unit length can be safely applied:

$$\frac{\partial Z}{\partial l}(\omega) = (1+j)\frac{\omega}{c}\frac{Z_0\delta}{4\pi b}F_0\left(\frac{b}{a}\right)$$

$$\frac{\partial k_l}{\partial l} = \frac{c}{4\pi^2 b\sigma^{3/2}}\sqrt{\frac{Z_0\rho}{2}}\Gamma\left(\frac{3}{4}\right)F_0\left(\frac{b}{a}\right)$$

where δ is the skin-depth:

$$\delta = \sqrt{\frac{2c\rho}{\omega Z_0}}$$

with Z_0 the free space impedance = $120\pi\ \Omega$. F_0 is a form factor equal to 1 for round beam pipes and differs slightly from 1 for rectangular cross sections [14]. The wake potential corresponding to the resistive wall impedance and defining the field distribution inside a bunch is given by:

$$W\left(\frac{s}{\sigma}\right) = Af\left(\frac{s}{\sigma}\right) \quad \text{where}$$

$$f(x) = |x|^{3/2}\exp\left\{-\frac{x^2}{4}\right\}\left[I_{-3/4}\left(\frac{x^2}{4}\right) - I_{1/4}\left(\frac{x^2}{4}\right) \mp I_{-1/4}\left(\frac{x^2}{4}\right) \pm I_{3/4}\left(\frac{x^2}{4}\right)\right]$$

The numerical coefficient A is defined as:

$$A = \frac{1}{16\pi b}\sqrt{\frac{2\rho Z_0 c^2}{\sigma^3}}$$

and the function $-f(x)$, $I_v(z)$ being the modified Bessel function, is shown in Figure 13.3.

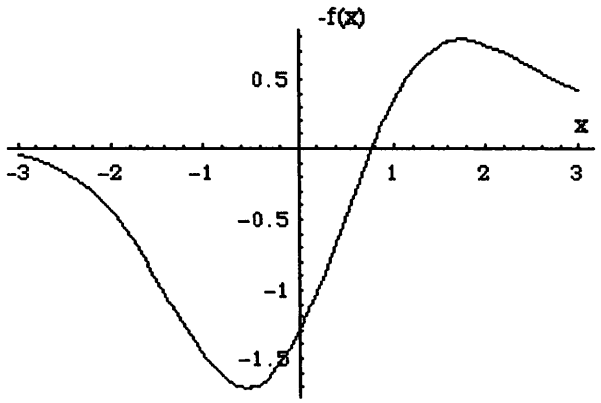

Figure 13.3 Function defining the resistive wall wake potential distribution inside a bunch.

For a numerical estimate we consider b = 18 mm; σ = 2 mm; Q = 2.33 nC; F_0 ~ 1; $\rho = 2.62*10^{-8}$ Ωm (Al). This gives:

$$eQ\frac{k_l}{l} = 29.928\left(\frac{\text{eV}}{\text{m}}\right)$$

$$eQA = 38.363\left(\frac{\text{eV}}{\text{m}}\right)$$

This means that after 4.5 turns in the Combiner Ring, which is 84 m long, the bunch loses 11.312 keV and the energy spread is about 35 keV. These are quite reasonable values. However, if instead of using aluminium one builds a stainless steel vacuum chamber, the losses and the energy spread will increase by about a factor of 6 and will no longer be negligible.

13.2.2 Space Charge Impedance

For simplicity let us consider two point charges travelling along a circular beam pipe on trajectories parallel to the pipe axis. If the distances of the leading charge r_1 and the trailing one r from the axis are much smaller than the pipe radius b, the space charge impedance is dominated by its monopolar term [10]:

$$\frac{\partial Z_{m=0}}{\partial l} = -j\frac{\omega Z_0}{2\pi c(\beta\gamma)^2}\left[K_0(\xi r_1) - \frac{I_0(\xi r_1)}{I_0(\xi b)}K_0(\xi b)\right]K_0(\xi r)$$

where $\xi = k/\beta\gamma$; $k = \omega/\beta c$ and I_0 and K_0 are the modified Bessel functions.

By analysing the behaviour of this term in the frequency domain one can note that in the region $\xi b << 1$, the impedance per unit length grows linearly, and does not depend on the radial position of the trailing charge:

$$\frac{\partial Z_{m=0}}{\partial l} = -j\frac{\omega Z_0}{2\pi c(\beta\gamma)^2}\ln\left(\frac{r_1}{b}\right)$$

For the Combiner Ring the condition $\xi b << 1$ is fulfilled over all the bunch spectrum for bunches with rms sizes of 1 – 3 mm and beam pipe radius of 18 mm. In the literature the

space charge impedance is presented as the space charge monopolar term due to a disk of radius a centred on the pipe axis. Integrating the above expression over the distribution for r_1 between 0 and a for $\xi b << 1$ we get:

$$\frac{\partial Z}{\partial l} = -j\frac{\omega Z_0}{4\pi c(\beta\gamma)^2}\left[1 + 2\ln\left(\frac{b}{a}\right)\right]$$

By substituting the disk radius a by the vertical rms bunch size and taking into account that the geometric aperture is about a factor of 10 larger than the transverse rms beam size, i.e., putting the ratio $b/a \sim 10$, we obtain a rough estimate of the space charge impedance:

$$\frac{Z}{n} \cong -j0.008\ \Omega$$

This value is much smaller than the imposed impedance limit of 0.4 Ω. Moreover, it has the sign opposite to that of purely inductive impedance due to small vacuum chamber discontinuities. Therefore, in the following we can neglect the space charge contribution to the energy loss and spread.

13.2.3 RF deflectors

The transverse RF deflectors are travelling wave iris loaded waveguides whose fundamental mode is a deflecting hybrid mode with $2\pi/3$ phase advance per cell and negative group velocity.

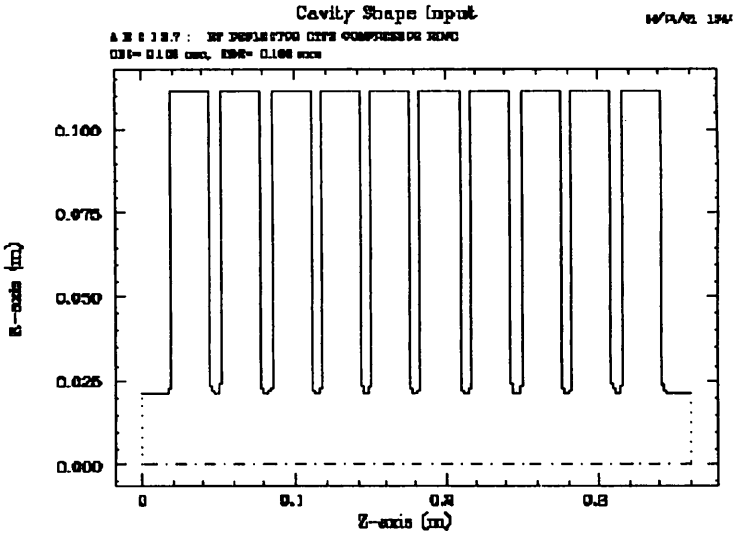

Figure 13.4 ABCI RF deflector input structure

The RF deflector design and detailed analysis of the transverse beam dynamics are given in [15]. Since the deflector structure is azimuthally symmetric except for the output and input couplers, the 2D ABCI code [16] can be used to calculate the energy spread and loss. Figure 13.4 shows the ABCI input structure consisting of 10 cells.

The resulting wake potential calculated for a 2 mm long bunch is shown in Figure 13.5, while Table 13.1 summarises the loss factors and gives the maximum values of the wake potential for different bunch lengths.

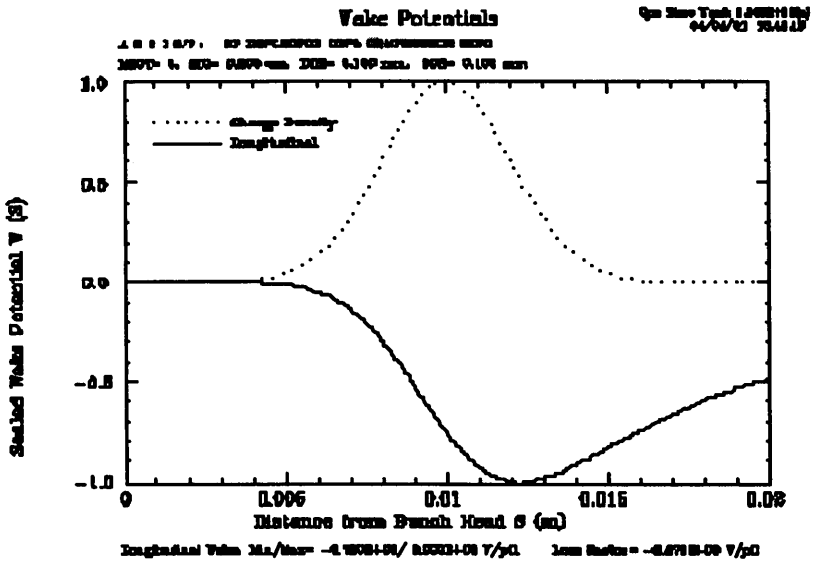

Figure 13.5 Wake potential of a 2 mm bunch in the RF deflector.

Table 13.1 Loss factors and maximum values of the wake potential

σ, mm	k_l, V/pC	$\lvert W_{max}\rvert$, V/pC
0.5	11.66	15.67
1.0	8.532	11.70
2.0	6.585	9.759
3.0	5.665	8.449

The Combiner Ring contains two RF deflectors. Thus, we can calculate that a 2 mm bunch with 2.33 nC charge loses at most 153 keV after 5 turns and gains an energy spread from 0 to –227 keV. From the data of Table 13.1, one can easily scale these data to other bunch lengths.

13.2.4 Extraction kicker

The design and technical parameters of the extraction kicker are discussed in [17]. Here we simulate a 2D model of the kicker with the ABCI code. As shown in Figure 13.6, for this purpose we substituted the two strip lines by one full coverage strip. This is expected to give a slight overestimate of the final result.

The wake potential for a bunch with 2 mm rms size is shown in Figure 13.7 and the loss factors and peaks of the wake potential for different bunch lengths are listed in Table 13.2. Now it is easy to calculate that a 2.33 nC bunch 2 mm long loses 18 keV and accumulates an energy spread of 34 keV due to the extraction kicker after 5 turns in the Combiner Ring. Note that the kicker contribution to the losses is much smaller than that of the RF deflectors.

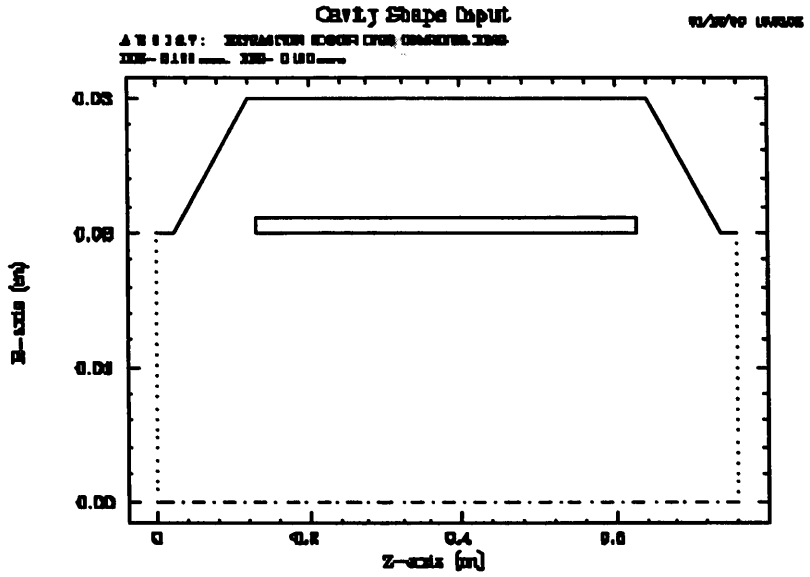

Figure 13.6 ABCI extraction kicker 2D model.

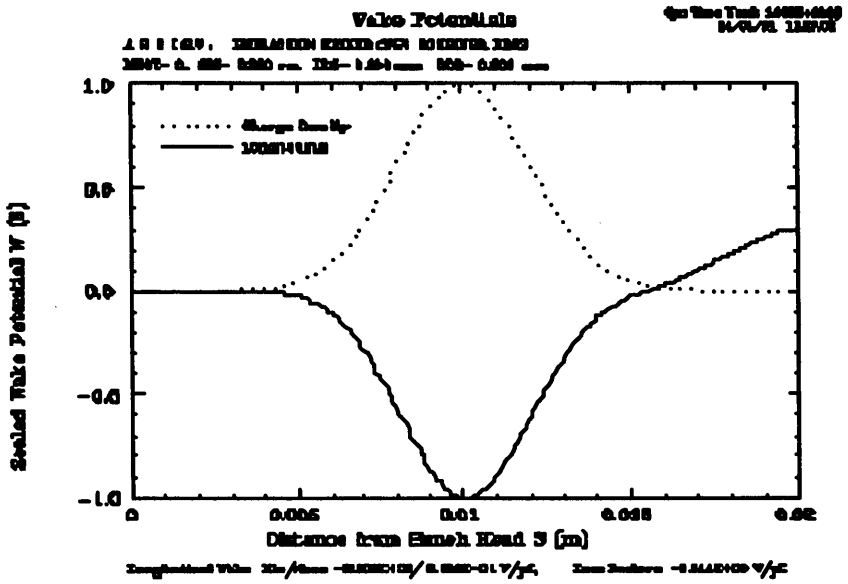

Figure 13.7 Extraction kicker wake potential of 2 mm bunch

Table 13.2 Loss factors, maximum and minimum values of the wake potential

σ, mm	k_p, V/pC	W_{max}, V/pC	W_{min}, V/pC
0.5	5.914	0.567	-9.667
1.0	3.008	0.094	-4.205
2.0	1.544	0.69	-2.215
3.0	0.989	0.79	-1.429

13.2.5 Beam Position Monitors (BPM)

We are planning to employ magnetic pick ups similar to those used for the LEP pre-injector [18] as beam position monitors in the CTF3 compressor rings. Technical performance of such BPMs is described in detail in [19].

The magnetic position monitor consists of a pick up pill-box and the vacuum chamber welded together. A ceramic ring with a resistive metallisation inside is used to prevent charge accumulation. Evaluation of the coupling impedance of such a structure is not a simple task. This is why a number of recent papers have been dedicated to both analytical studies [20] and to impedance measurements [21] of BPMs of that type.

According to bench measurements [22] the maximum value of the normalised impedance Z/n reaches 70 mΩ in the frequency range up to 3 GHz. This high value is a matter of concern since the impedance contribution of 36 BPMs, which are to be installed in the Combiner Ring, can exceed the acceptable impedance budget.

Despite the fact that the maximum impedance value is high, one has to consider the actual frequency behaviour of the impedance in order to calculate correctly the energy loss and the energy spread.

The BPM impedance is measured up to 3 GHz, while the frequency spectrum of 1-3 mm bunches goes beyond some tens of GHz. Generally, the impedance above the beam tube cut off decreases with frequency. Moreover, the ceramic metallisation is expected to screen completely the BPM for higher frequencies. This means that the effective impedance weighted by the bunch spectrum will be much smaller than the maximum value measured at relatively low frequency.

In order to estimate the impedance we will rely here on the results of the impedance measurements described in [22]. We also assume that the impedance beyond 3 GHz vanishes. This assumption can be justified by the fact that we will increase the thickness of the metallisation in order to enhance the screening effect at high frequency.

The measured BPM impedance is well approximated by a sum of two broadband resonances with shunt impedances $R_1 = 26\ \Omega$ and $R_2 = 21\ \Omega$ at the resonant frequencies $f_1 = 1.3$ GHz and $f_2 = 2.3$ GHz, respectively. The resonant modes have poor quality factors of $Q_1 = 2.5$ and $Q_2 = 5$.

The real part of the model impedance (shown in Figure 13.8) is notably similar to the measured one. The imaginary part is slightly lower, but behaves in the same way as the measured quantity. Now, it is easy to calculate the wake-fields corresponding to this resonant impedance applying the standard definitions.

Figure 13.9 shows the energy loss distribution inside a 2 mm long Gaussian bunch with a charge of 2.33 nC in the range of $-5\ \sigma$; $+10\ \sigma$. As we can see, the maximum energy loss is about 2 keV. So, after 4.5 turns inside the Combiner Ring containing 36 BPMs the bunch will gain energy spread of about 330 keV. This energy spread is comparable or even higher than the spread due to the RF deflectors, but still does not exceed the design value. We also hope to significantly reduce this amount by increasing the metallisation thickness

We should note here another important feature of the BPM wake. Despite the BPM resonant impedance being rather broad, the resulting wake lasts much longer than the distance between bunches in the beam (see Figure 13.10). This has to be taken into account when analysing multibunch dynamics.

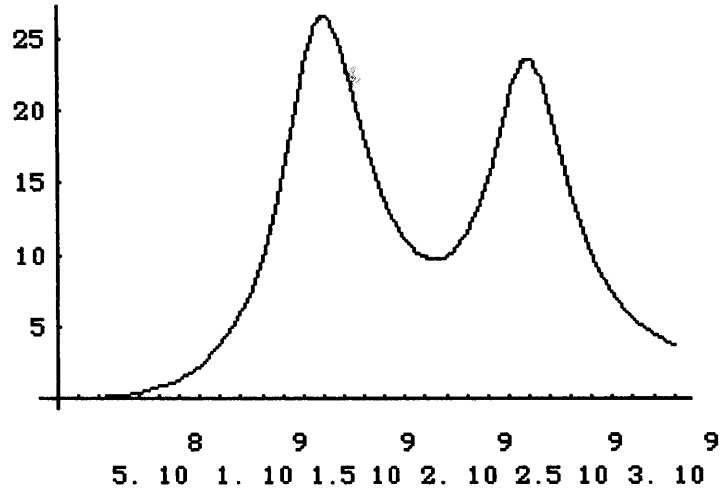

Figure 13.8 Real part of the BPM impedance.

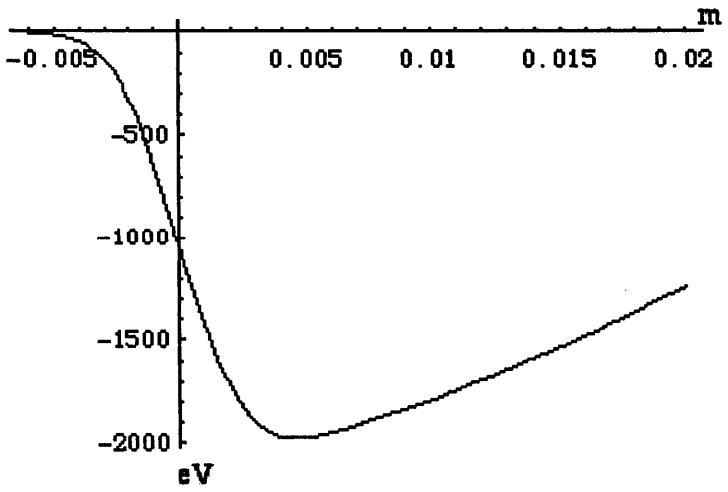

Figure 13.9 Distribution of the energy loss inside 2 mm Gaussian bunch with 2.33 nC charge.

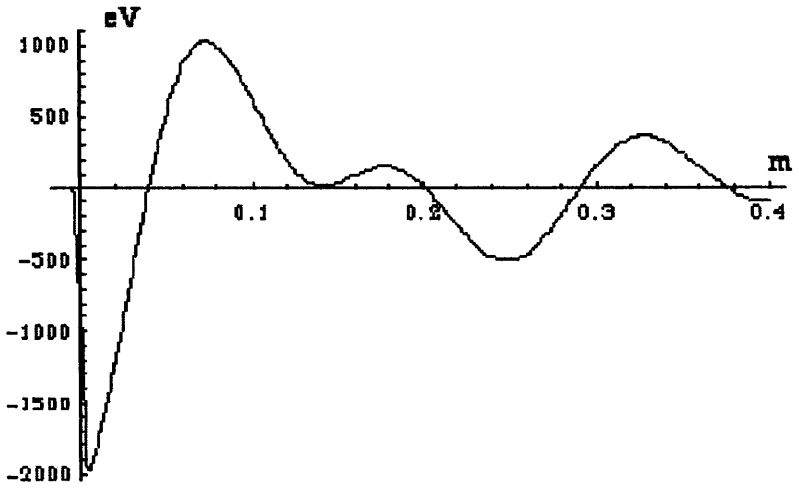

Figure 13.10 Long-range BPM wake-fields.

13.2.6 Vacuum port RF screen

In the design of a vacuum port RF screen we use the idea of hidden slots [23] that has been successfully applied for PEP II [24]. This substantially reduces the coupling impedance (up to some orders of magnitude) and prevents radiation into the pump chamber.

Figure 13.11 shows a sketch of the RF screen. It consists of 38 grooves 72 mm long, 2 mm wide and about 2 mm deep in the rectangular vacuum chamber pipe with 4 mm thickness. Along each groove 25 circular holes with a radius of 1 mm are drilled for pumping purpose. The following features are taken into account in the present design:

1) the impedance of long slots saturates when the slot length exceeds 2-3 slot widths. Thus, it is more convenient to use long slots instead of many holes providing the same pumping speed

2) however, for the long slots, TE mode travelling waves excited in a ring can radiate into the pump chamber and may damage the pumps and also create resonant HOMs beyond the RF screen.

Therefore, the long grooves are used to decrease the impedance, while the holes prevent penetration of the RF fields outside the beam pipe.

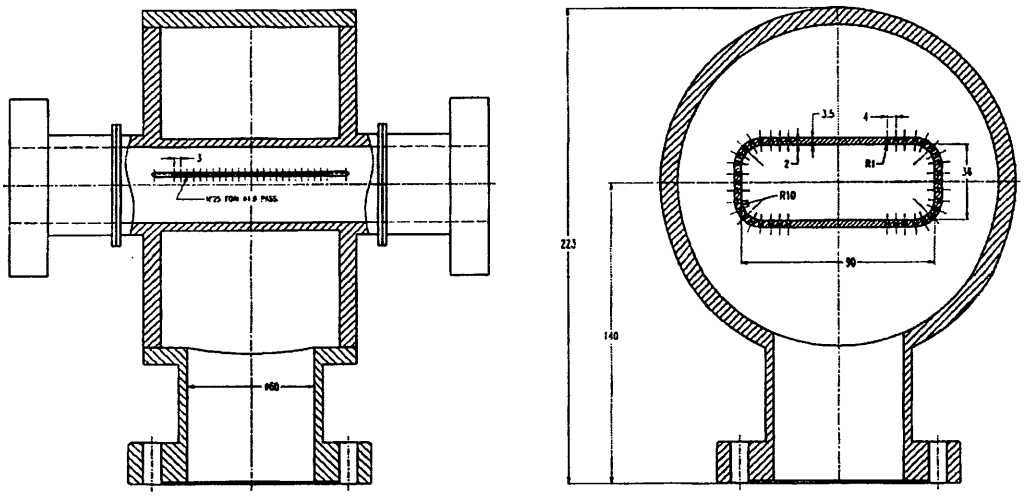

Figure 13.11 Vacuum port sketch.

In order to decrease the coupling impedance further we exploit the properties of the impedance for a rectangular geometry of the beam pipe. The grooves are placed closer to the chamber corners and there are no grooves on the lower and upper sides of the chamber near the symmetry axis.

The impedance of such long narrow slots remains mainly inductive up to rather high frequencies and can be estimated for a rectangular beam pipe as [25]:

$$Z(\omega) = jZ_0 \frac{\omega}{c} \frac{(\alpha_e + \alpha_m)}{b^2} \Sigma^2$$

where the sum of the electric and magnetic polarisabilities for a rectangular slot with length l and width w is given by:

$$\alpha_e + \alpha_m = w^3 \left(0.1814 - 0.0344 \frac{w}{l} \right)$$

Here the geometric factor Σ is defined by the series:

$$\Sigma = \sum_{m=0}^{\infty} \frac{\cos((2m+1)\pi y_h / b)}{\cosh((2m+1)\pi x_h / b)}$$

with b being the vacuum chamber height; x_h and y_h are the hole coordinates.

Calculations of the impedance for the pumping screen shown in Figure 13.11 gives $Z/n = j\ 4.3 \cdot 10^{-6}\ \Omega$ for a single vacuum ports and about $1.4 \cdot 10^{-4}\ \Omega$ for all the 32 vacuum ports of the Combiner Ring. This is a negligible value.

13.2.7 Tapers

In order to minimise the vacuum chamber impedance, the vacuum chamber must be as smooth as possible. All the changes in the vacuum chamber cross section have to be provided with gradual transitions i.e. tapers. The number of these cross section variations of the vacuum chamber must be kept to the very minimum.

The vacuum chamber in the CTF3 Combiner Ring is rectangular, 36×90 mm, with smoothed corners. Since the existing quadrupole magnets to be used have large enough apertures it is possible to keep this cross-section without changes all along the machine arcs. The only variations of the vacuum chamber cross section take place between the arcs and the wiggler sections and between the arcs and the injection/extraction straight sections.

The wiggler vacuum chamber has the same vertical size as the rest of the arc chamber (36 mm), but is much wider in the horizontal direction. Therefore, only horizontal tapering is necessary, allowing a reduction in impedance. Due to the flat rectangular geometry, these horizontal tapers are not expected to give any substantial contribution to the machine impedance. The beam pipe cross section in the straight sections is circular with a diameter equal to the vertical chamber size in the arcs of about 36 mm. Again, only horizontal tapering is needed.

Note that the whole vacuum chamber has a constant vertical size and a limited number of the horizontal tapers. This allows to reduce the taper impedance contribution to a minimum.

13.2.8 Valves

Since the vacuum chamber is expected to be rather smooth without abrupt cross section variations and there are no narrow chamber sections in the ring, the vacuum conductance should be good enough. This gives us the possibility of not using vacuum valves.

13.2.9 Bellows

There will be 16 bellows providing flexibility to the vacuum chamber. We have adopted the so-called sliding finger structure, similar to that used in the KEKB rings, to shield the interior part [26]. These bellows have small, predominantly inductive, impedance [27] and have proven their reliability working at high beam current with bunches of rms length in the millimetre range.

By scaling the impedance of the KEKB bellows to the Combiner Ring vacuum chamber size we get the very small values of about $10^{-6}\ \Omega$ per single bellows and $1.6 \cdot 10^{-5}\ \Omega$ for all the ring bellows, respectively.

13.2.10 Flanges

Another possible source of inductive impedance is constituted by the flanges. The coupling impedance is due to shallow and narrow gaps created between facing flanges. Since the gap sizes can be reduced to fractions of mm [28], which are much smaller than the bunch length, we can safely neglect their impedance contribution.

13.3 Longitudinal Beam Dynamics Evolution

The required rms bunch length in the CTF3 Drive Beam Accelerator is ≤ 1.3 mm. This bunch length is obtained at the end of the injector after the cleaning chicane, where the beam is energy collimated. A head-to-tail energy correlation is introduced in the accelerator through the combined effects of short-range wake-fields and off-crest acceleration. As mentioned in section 13.1, in order to minimise CSR and conventional wake-field effects on the beam, the rms bunch length can be increased to a maximum of 2.5 mm in the Delay Loop and Combiner Ring, by means of a magnetic chicane placed at the end of the linac itself. After combination, the individual bunches are finally compressed in length to about 0.5 mm rms in a magnetic bunch compressor, before being sent to the 30 GHz region for power production.

In order to give an estimate of the final bunch length obtainable in CTF3, a model of the single-bunch longitudinal phase space evolution in the complex, based on the use of macro particles, has been developed. The starting point is the longitudinal phase space distribution at the exit of the injector obtained from PARMELA simulations. In Figure 13.12 and in Figure 13.13 the details of the distribution are given. A total of about 600 macro particles have been used in this example. The distribution assumes a cut of the long low-energy tail generated during the bunching process. About 30% of the initial current is cut by the cleaning chicane collimator. The resulting rms bunch length is 1.2 mm, with an energy spread of about 4 %. However, as can be seen from Figure 13.12, the energy spread is mainly correlated along the bunch, since an off-crest acceleration has been used in the two accelerating sections of the injector in order to facilitate the low-energy tail cut.

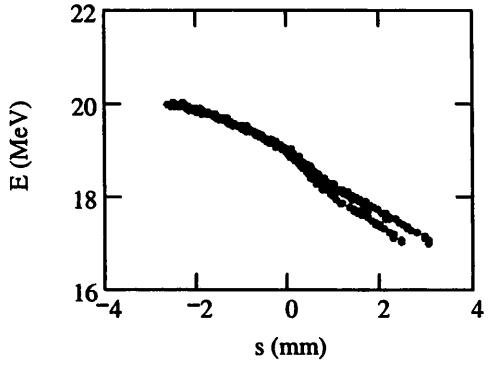

Figure 13.12 Longitudinal phase space distribution of a bunch at the injector exit (PARMELA simulations).

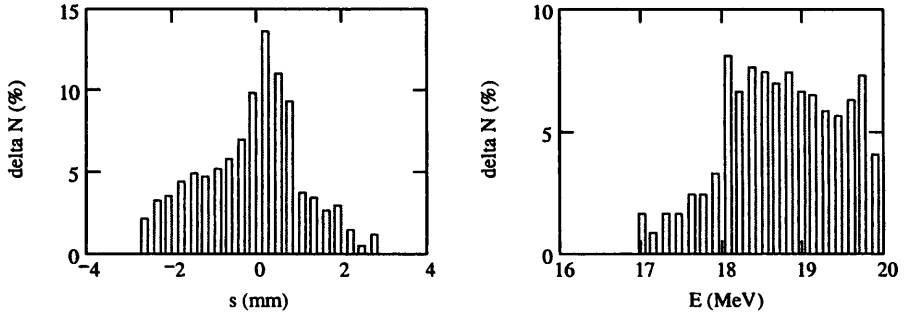

Figure 13.13 Longitudinal profile (left) and energy spectrum (right) for a bunch at the injector exit.

The phase space distribution at the end of the Drive Beam Accelerator is then calculated taking into account the mean RF phase in the drive beam accelerating structures and the longitudinal short-range wake-field. The RF phase is adjusted to 6° in order to maximise the head-tail correlation used for the final bunch compression, while keeping the total energy spread within the total momentum acceptance of the transfer lines, Delay Loop and ring (5%). The short-range wake-fields are modelled by applying to the macro-particle distribution delta wake-fields of the form:

$$W_z = w_1 \exp\left(w_2 \sqrt{z/\mathrm{mm}}\right)$$

The numerical values of the constants w_1 = 177 V/(pC m), w_2 = -0.85, have been obtained by fitting the calculated wake-fields for test macro-particle distribution (Gaussian, 1 to 2 mm rms) to the results of ABCI runs for Gaussian bunches with the same rms values. An additional uncorrelated spread with an rms value of $1 \cdot 10^{-3}$ (Gaussian distribution) has been also included. The longitudinal phase space after acceleration is given in Figure 13.14, where the distributions before and after the bunch stretcher are shown. The maximum bunch length in the Combiner Ring is about 2.5 mm rms, limited by the maximum acceptable phase extension in the RF deflectors. Consistently with the rest of the section and in order to keep a safety margin, here we limit ourselves to stretching the bunch rms length only to 2 mm.

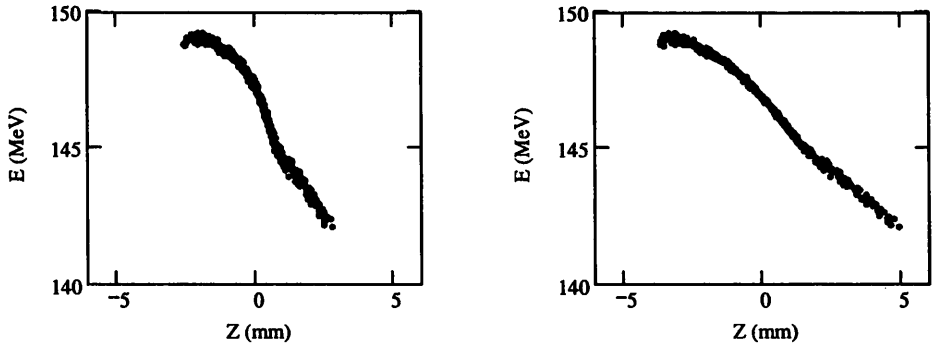

Figure 13.14 Longitudinal phase space distribution after the linac, before (left) and after (right) bunch stretching.

The evolution in the ring has been calculated taking into account CSR, conventional wakes and isochronicity errors. The analytical PP model has been used for CSR, with the approximation of considering a Gaussian longitudinal distribution for the bunches, with the same rms length (see Figure 13.2).

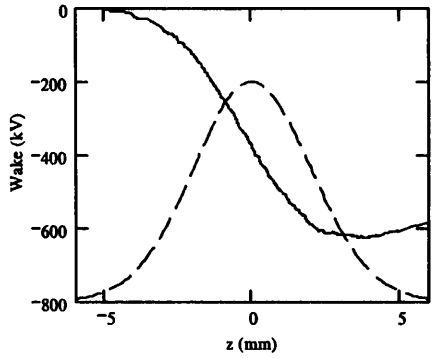

Figure 13.15 Cumulative conventional wake force in the ring, for a Gaussian bunch with 2 mm rms length.

The conventional wake-fields have been treated using a delta wake model similar to the one used in the linac, with w_1 = 0.48 V/(pC m) and w_2 =-0.2. Such values should give a good approximation of the cumulative wake-field, with a peak deceleration of about 620 kV over 4.5 turns for a Gaussian bunch with 2 mm rms length (see Figure 13.15). The main contributions to the impedance (wake-fields from the BPMs, the RF deflectors and the extraction kicker plus the resistive wall effect) have been considered.

A perfect compensation of the first and second order momentum compaction in the ring has been assumed, but a third order contribution, corresponding to a path length variation of ± 1 mm (over 4.5 turns) for particles with ± 2.5 % momentum variation, has been introduced. The longitudinal phase space distortion from CSR, conventional wakes and isochronicity errors in the transfer lines and in the Delay Loop should be small with respect to the distortion taking place in the Combiner Ring and has been neglected. In Figure 13.16 the resulting distribution in the longitudinal phase space is given for a bunch belonging to the first injected train, which makes 4.5 turns in the Combiner Ring.

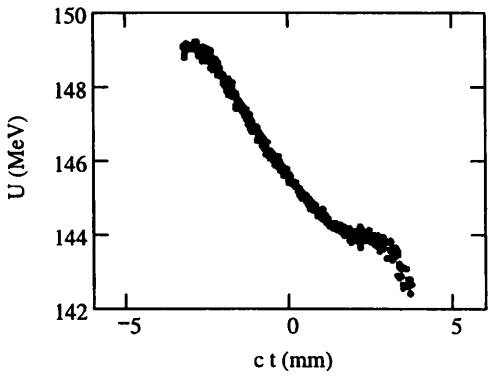

Figure 13.16 Longitudinal phase space distribution after the ring, for a bunch making 4.5 turns.

Since bunches belonging to different trains make a different number of turns in the ring, their phase space distribution at extraction are different. The optimum R_{56} for final compression must be found as a compromise. In Figure 13.17 the bunch length after final compression is given as a function of the bunch compressor R_{56}, for different bunches.

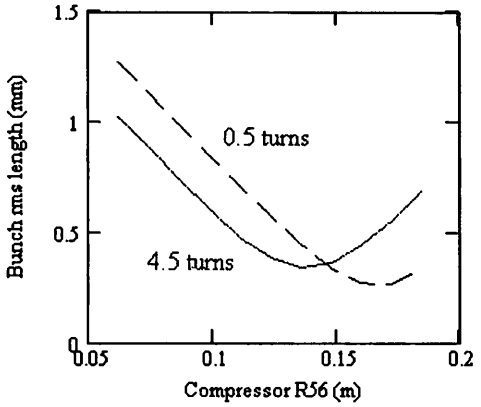

Figure 13.17 Bunch length as a function of the momentum compaction factor R_{56} in the final bunch compression system, for bunches making a different number of turns in the Combiner Ring.

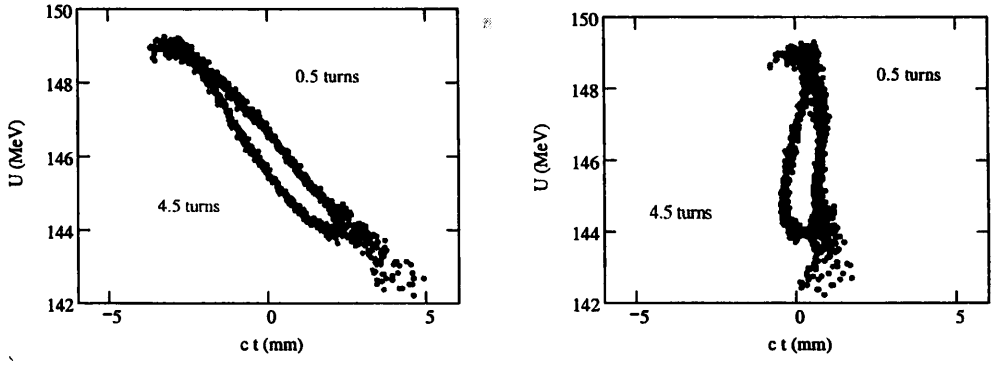

Figure 13.18 Longitudinal phase space distribution after the ring, before (left) and after (right) the final bunch compression, for different bunches.

In Figure 13.18 the phase space distributions before and after compression (with $R_{56} = 0.15$ m) are shown for the first and the last train bunches (making 4.5 and 0.5 turns in the ring, respectively). The final rms length of all the bunches is below the goal of 0.5 mm. A small phase error arises from the different energy loss suffered by the bunches, but the power production factor (30 GHz Fourier component, squared) is still above 91 %.

13.4 Summary

Our preliminary estimates reported in this paper have shown that by careful vacuum chamber design it is possible to keep the energy loss and the energy spread within the design limits. The CSR and the conventional wake-fields are evaluated to give almost equal contributions to the energy spread and losses.

The energy spread due to CSR is $\Delta E = \pm 0.9$ MeV ($\Delta E/E \sim \pm 0.5\%$) for a 2 mm long bunch. It is not reasonable to have bunches shorter than 2 mm in the Combiner Ring since the energy spread grows fast with the inverse of bunch length (faster than $\sim \sigma^{-4/3}$). For a 1 mm long bunch the spread would exceed the acceptable value of $\Delta E/E = \pm 1\%$.

Among vacuum chamber components the 2 RF deflectors and the 36 BPMs give dominant contributions to both energy spread and energy loss. For a 2 mm bunch they are estimated to give about 550 keV of total energy spread for the bunch that performs 4.5 turns in the ring. The wake-fields created by these components last longer than the separation between the bunches in the trains and, because of that, an additional study of the multibunch and multiturn effects is necessary.

The wake-fields induced by the extraction kicker are weaker than those of the deflectors and BPMs: the 2 mm bunch with nominal charge of 2.33 nC loses 18 keV and accumulates 34 keV of energy spread after 5 turns.

The contribution of the resistive wall can be small if the vacuum chamber is made of aluminium. The estimated losses in this case are about 12 keV, while the spread does not exceed 36 keV.

In trying to design a smooth Combiner Ring vacuum chamber, it seems to be possible to keep the vertical chamber size constant and to reduce the number of lateral (horizontal) tapers. At the present stage of the chamber design these tapers are foreseen only between arcs and two straight sections and between the arcs and two wiggler chamber sections.

The experience acquired during vacuum chamber construction of high current colliders (PEP II, KEKB and DAΦNE) can be successfully applied in order to reduce the coupling impedance of some vacuum chamber components to a minimum. In particular, the inductive

impedance of hidden pumping slots, sliding contact bellows, RF screened flanges are expected to be negligible.

A simplified model, based on macro-particle distribution and analytical calculations has been developed to evaluate the evolution of the longitudinal phase space in the CTF3 complex, taking into account CSR and conventional wake-fields. The results show that the desired bunch length and 30 GHz power production efficiency can be obtained after final compression, with the assumptions made above.

13.5 References

[1] "CLIC RF Power Source: a Novel Scheme of Two Beam Acceleration for Electron-Positron Linear Colliders", Yellow Report CERN 99-06. See also "Proceedings of the First CLIC/CTF3 Collaboration Meeting held at CERN, 3-5 May, 1999", CLIC NOTE 401.

[2] J.B.Murphy, S.Krinsky and R.L.Gluckstern, "Longitudinal Wakefield for an Electron Moving on a Circular Orbit", Particle Accelerators, 1997, Vol.57, pp.9-64.

[3] R.L.Warnock and P.Morton, "Fields Excited by a Beam in a Smooth Toroidal Chamber. Part 1: Longitudinal Coupling Impedance.", Particle Accelerators, 1990, Vol.25, pp.113-184.

[4] R.L.Warnock, "Shielded Coherent Synchrotron Radiation and Its Effect on Very Short Bunches", SLAC-PUB-5375, Nov. 1990.

[5] R.L.Warnock and K.Bane, "Coherent Synchrotron Radiation and Stability of a Short Bunch in a Compact Storage Ring", SLAC-PUB-95-6837, May 1995.

[6] A.V.Burov and E.A.Perevedentsev, "Coherent Synchrotron Radiation and Its Effect on Bunch Lengthening", in Proceedings of High Energy Accelerator Conference, Hamburg 1992, Vol.2, pp.1112-1114.

[7] A.Kabel, M.Dohlus, T.Limberg, "Using TraFiC4 to Calculate and Minimize Emittance Growth due to Coherent Synchrotron Radiation", to be published in NIM A.

[8] H.H.Braun, R.Corsini, L.Groening, F.Zhou, A.Kabel, T.O.Raubenheimer, T.Limberg, "Emittance Growth and Energy Loss due to Coherent Synchrotron Radiation in the Bunch Compressor of the CLIC Test Facility (CTF 2), CERN/PS 2000-056 (AE), Proceedings of the XX International Linac Conference, 21-25 August 2000, Monterey, California, USA and CLIC Note 458 (2000).

[9] C.Biscari, A.Ghigo, F.Marcellini, C.Sanelli, F.Sannibale, M.Serio, F.Sgamma, G.Vignola, M.Zobov, R.Corsini, T.E.D'Amico, L.Groening, G.Guignard, "CTF3 -Design of Driving Beam Combiner Ring", Proceedings of the 7th European Particle Accelerator Conference, 26-30 June 2000, Vienna, Austria and CLIC Note 471 (2001).

[10] L.Palumbo, V.Vaccaro and M.Zobov, "Wake-Fields and Impedance", Lecture given at *CAS Advanced Accelerator School*, 20 September - 1 October, Rhodes, Greece, 1993, CERN 95 - 06, 22 November 1995, V.1, pp. 331- 390. See also LNF-94/041 (P), 5 September 1994.

[11] S.Bartalucci et.al., "Measurements and Analysis of Collective Effects in the LEP Electron Positron Accumulator (EPA)", in Proceedings of European Particle Accelerator Conference EPAC88, Rome, June 7 – 11, 1988, Vol.1, pp. 672 – 674.

[12] M.Zobov et.al., "Bunch Lengthening and Microwave Instability in the DAΦNE Positron Ring", DAΦNE Technical Note: BM-3, Frascati, June 7, 1998.

[13] K.Bane and M.Sands, "The Short-Range Resistive Wall Wakefields", SLAC-PUB-95-7074, December 1995.

[14] R.L.Gluckstern, J.van Zeijts and B.Zotter, "Coupling Impedance of Beam Pipes of General Cross Section", CERN SL/AP 92-25 (1992).

[15] D.Alesini et al., "The RF Deflectors for CTF3", CTFF3 Technical Note-003, Frascati, April 18, 2001.

[16] Y.H.Chin, User's Guide for ABCI Version 8.8, LBL-35258, UC-414, February 1994.

[17] D.Alesini, R.Boni, A.Gallo, F.Marcellini, "The RF Deflectors for CTF3",CTFF3 Note 023, June 2001.

[18] S.Battisti et al., "Magnetic Beam Position Monitors for LEP Pre-Injector", Proceedings of the 1987 IEEE Particle Accelerator Conference, Washington, March 16-19, 1987, pp. 605 – 607.

[19] CTTF3 Technical Note, to be published.

[20] R.Gluckstern and B.Zotter, "Analysis of Shielding of Charge Particle Beams by Thin Conductors", published in Phys.Rev.ST Accel.Beams 4:024402,2001.

[21] D.Brandt et al., "Experimental Evaluation of the RF Shielding Properties of a Thin Resistive Layer in a Ceramic Chamber", Proceedings of EPAC 2000, Vienna, Austria, 2000, pp. 1417 – 1419.

[22] S.Battisti, F.Caspers and D.J.Williams, "Mesure de L' Impedance Longitudinale du Prototype no 2 du Capteur de Position Magnetique", PS/LPI/Note/85-04, 1 March 1985.

[23] T.Weiland, "Low Impedance Vacuum Chambers", PEP-II Technical Note No. 59, 1994.

[24] C.K.Ng and T.Weiland, "Impedance of the PEP-II DIP Screen", SLAC-PUB-95-7005, September 1995.

[25] S.S.Kurennoy, "Beam – Chamber Interaction in Accelerators. Methods for Calculating Coupling Impedances ", IFVE-91-158 (Serpukhov, IHEP), Oct 1991. 63pp (in Russian).

[26] Y.Chin and K.Oide, "Impedance and Collective Effects in the KEKB", KEK Proceedings 96-6, August 1995, pp. 1 – 22.

[27] Y.Suetsugu, "Bellows Design and Testing", KEK Proceedings 96-6, August 1995, pp. 189-194.

[28] V. Lollo, INFN-LNF, private communication.

14. DELAY LOOP

The bunch compression is obtained in two steps; a factor two in the Delay Loop (DL) and a factor five in the Combiner Ring (CR) [1,2].

The separation between the bunches at the linac output is 20 cm (twice the linac RF wavelength) so that the macro bunch time structure alternately presents empty and filled buckets. Moreover the macro bunch consists of alternate sequences 140 ns long of *even* and *odd* buckets, the difference in phase between them being one RF wavelength. The linac is connected to the DL by a transfer line, where a 1.5 GHz RF deflector, see Figure 14.1, deviates only the odd bunch sequences into the DL.

The DL length is 140 ns times c so that after the DL the odd sequence will be recombined with the incoming even sequence in such a way as to fill the interleaved empty 3 GHz buckets. The resulting macro bunch structure, at the DL output, presents 140 ns long trains of bunches separated now by 10 cm, followed by 140 ns long voids.

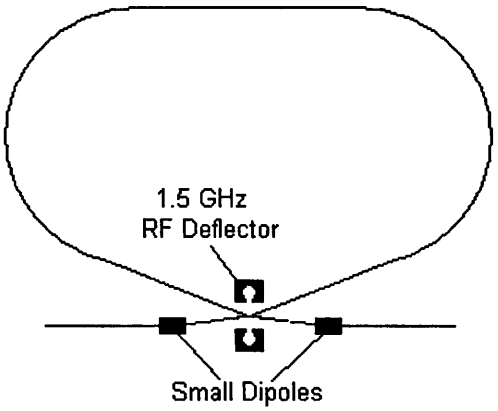

Figure 14.1 Delay Loop Injection Scheme.

The general characteristics of the DL and the described recombination scheme with the single RF deflector were first presented in [1]. Table 14.1 shows a summary of the main requirements and constraints that the DL must fulfil.

Table 14.1 Delay Loop Main Requirements and Constraints.

Length [m]	42
Energy [MeV]	150 ~ 300
Maximum Charge/Bunch [nC]	2.3
Isochronicity	$\lvert\alpha_p\rvert \leq$ 5e-4
Momentum Acceptance (total)	$\Delta p/p = 5\%$
Path Length Tuning [mm]	± 0.5

14.1 Delay Loop Description

Figure 14.2 shows the DL layout while Table 14.1 and Table 14.2 report the DL main parameters. According to the CTF3 philosophy of reusing, wherever possible, existing hardware, design material and documentation, most of the DL magnetic components, (see Table 14.2), are copies of already existing magnets. In fact, the bending magnets are the 22.5° rectangular dipoles (HR.BHZij) of EPA [3] now used as 30° magnets, while the 2° DC septa magnets, the quadrupoles and the sextupoles are copies of magnets of the DAΦNE Accumulator Ring [4, 5, 6]. The 27.14° DC septa are a modified version of the 34° DAΦNE Accumulator septa. New elements are the single period wiggler used for tuning the DL length

(same as the ones used in the CTF3 Combiner Ring [2]) and the very small 5 mrad dipoles used in the injection region.

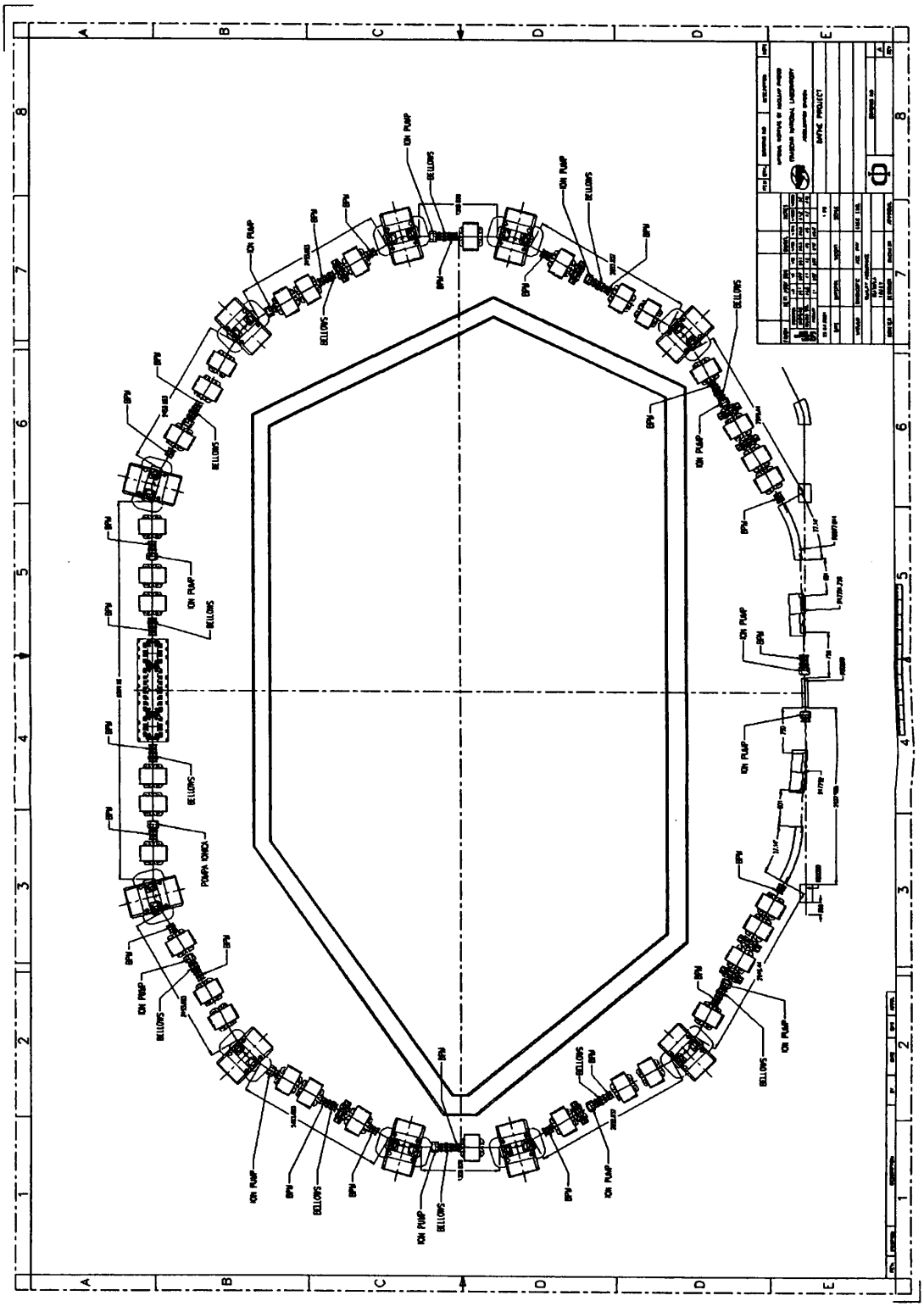

Figure 14.2 Delay Loop Layout.

Table 14.2 Delay Loop Magnetic Elements.

A)	Number of Dipoles (EPA-like)	10
	Dipole Bending Radius [m]	1.079
	Dipole Bending Angle [deg]	30
	Dipole Field [T] (150/300 MeV)	0.46/.93
	Integrated Quadrupole Coeff. in Dipoles [T] (150/300 MeV)	0.18/0.37
B)	Number of Quadrupoles (DAΦNE Accumulator-like)	34
	Max. Integrated Gradient [T] (150/300 MeV)	1.2/2.4
	Quadrupole Families (minimum/preferred)	14/18
C)	Number of Sextupoles (DAΦNE Accumulator-like)	10
	Max Integrated Gradient [T/m] (150/300 MeV)	9.5/19
	Sextupole Families	5
D)	Number of Path Length Tuning Wiggler	1
E)	Number of 2° Septa (DAΦNE Accumulator-like)	2
F)	Number of 27°.14 Septa (DAΦNE Accumulator-like)	2
G)	Injection Dipoles Number	2
	Injection Dipoles Bending Angle [mrad]	5

14.1.1 Lattice

In designing the DL an important constraint is the isochronicity of the lattice. This condition must be carefully fulfilled in order to preserve the longitudinal structure of the bunch along the loop [7]. To first order, the particle longitudinal position in the bunch is given by:

$$ct = (ct)_0 + R_{56}\frac{\Delta p}{p} \tag{1}$$

where c is the speed of light, $\Delta p/p$ the momentum deviation and R_{56} is the momentum related term of the DL first order transfer matrix. Isochronicity is obtained when such a term vanishes:

$$R_{56} = \int \frac{D_x}{\rho} ds = 0 \tag{2}$$

According to expression (2) the horizontal dispersion D_x must be properly arranged inside the DL dipoles where the trajectory curvature radius ρ assumes a finite value. At the same time the very large momentum acceptance requires small dispersion values all over the loop for containing beam envelopes.

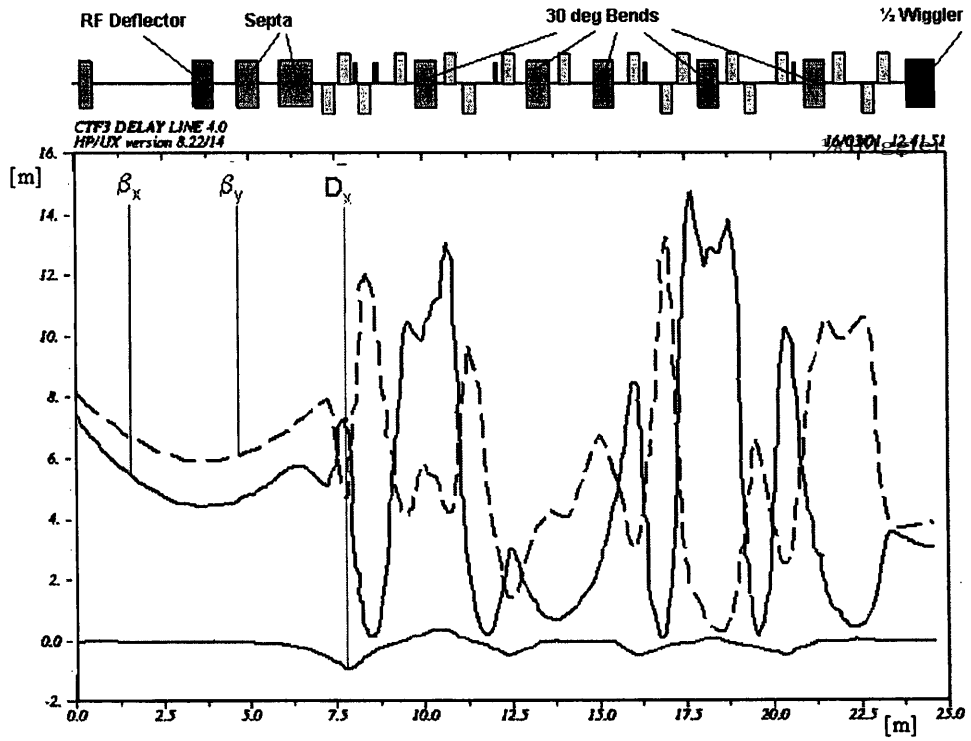

Figure 14.3 Delay Loop Optical Functions. Half Loop.

Figure 14.3 shows the optical functions of half the DL, as calculated by MAD8. The second half is exactly symmetric. The half machine can be divided in quarters, each with a triple bend arc with the sign of dispersion alternated in the dipoles. Dispersion and dispersion derivative are zero at the end and at the output of each quarter and the isochronicity condition (2) is obtained in half the machine. In the quarter including the injection, the role of the first bend in the arc is performed by the couple of septa magnets. Horizontal and vertical functions are well separated in the entire loop and in particular the vertical beta assumes small values inside the dipoles and the wiggler where the reduced "stay clear" requires small beam sizes.

Figure 14.4 shows the 14 quadrupole families. It must be remembered that the dipoles have a quadrupole component and that the model used for the bends is the one based on the magnetic measurements reported in [8].

In order to facilitate the matching between the DL and the downstream transfer line, the number of quadrupole families could be increased to 17 or 18 by making the 3 or 4 quadrupoles before the output septa independent.

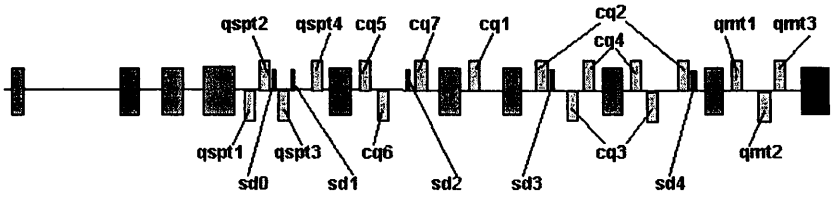

Figure 14.4 Quadrupole and Sextupole Families.

The isochronicity requirement for the momentum compaction is $|\alpha_P| \leq 5 \cdot 10^{-4}$ (see Table 14.1). As the DL is 42 m long, this means $|R_{56}| \leq 2.1 * 10^{-2}$ m. The R_{56} variation must be done maintaining the matching at the DL output and preferably without generating strong modifications in the optical functions. The best way for achieving such a situation is by performing small variations on the strength of all the DL loop quadrupole families.

14.1.2 Second Order Isochronicity

Figure 14.5 shows a MAD8 tracking output (TRANSPORT mode). Off-energy particles within $\Delta p/p = \pm 2.5 \cdot 10^{-2}$ are tracked from the DL input (crosses) up to the output (dots) and the related longitudinal positions inside the bunch are shown in the ordinate (for all the particles $x_0 = x_0' = y_0 = y_0' = 0$). In the DL transfer matrix, isochronicity is corrected only to the first order ($R_{56} = 0$ m). The large displacement of the off-energy particles indicates that a higher order correction is necessary. To the second order:

$$ct = (ct)_{0+} R_{56} \frac{\Delta p}{p} + T_{516}\, x_0 \frac{\Delta p}{p} + T_{526}\, x_0' \frac{\Delta p}{p} + T_{536}\, y_0 \frac{\Delta p}{p} +$$

$$+ T_{546}\, y_0' \frac{\Delta p}{p} + T_{556}\, (ct)_0 \frac{\Delta p}{p} + T_{566} \left(\frac{\Delta p}{p} \right)^2 \qquad (3)$$

where T_{ijk} are elements of the second order transfer matrix. Isochronicity is achieved when:

$$T_{5i6} = 0 \qquad \forall\, i \qquad (4)$$

Five families of sextupoles were added in the DL layout in order to obtain condition (4), see Figure 14.3 and Figure 14.4.

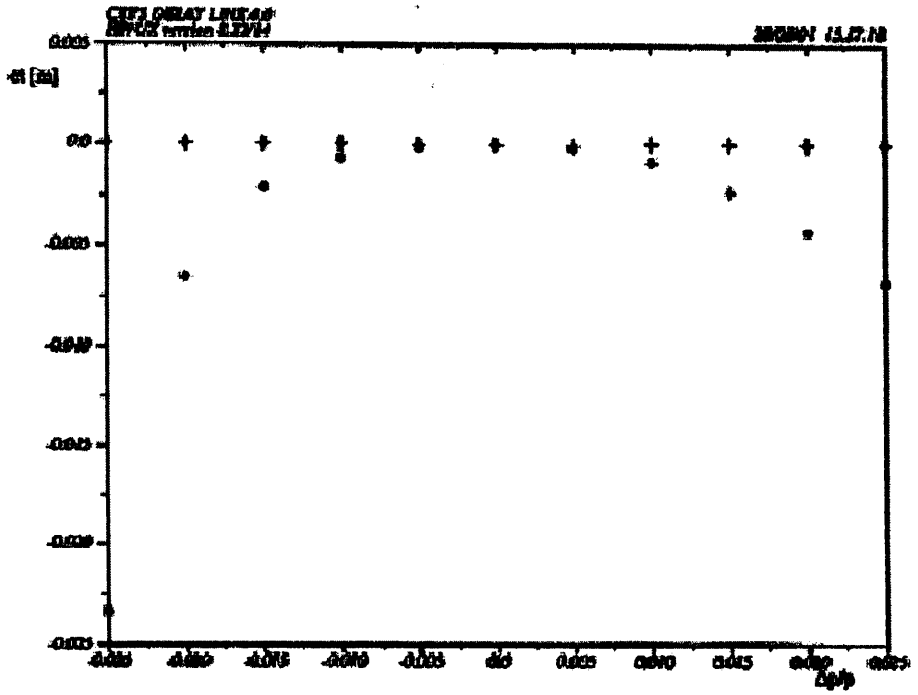

Figure 14.5 Off-energy Particles Longitudinal Position at DL Input (Crosses) and Output (Dots) First Order Correction

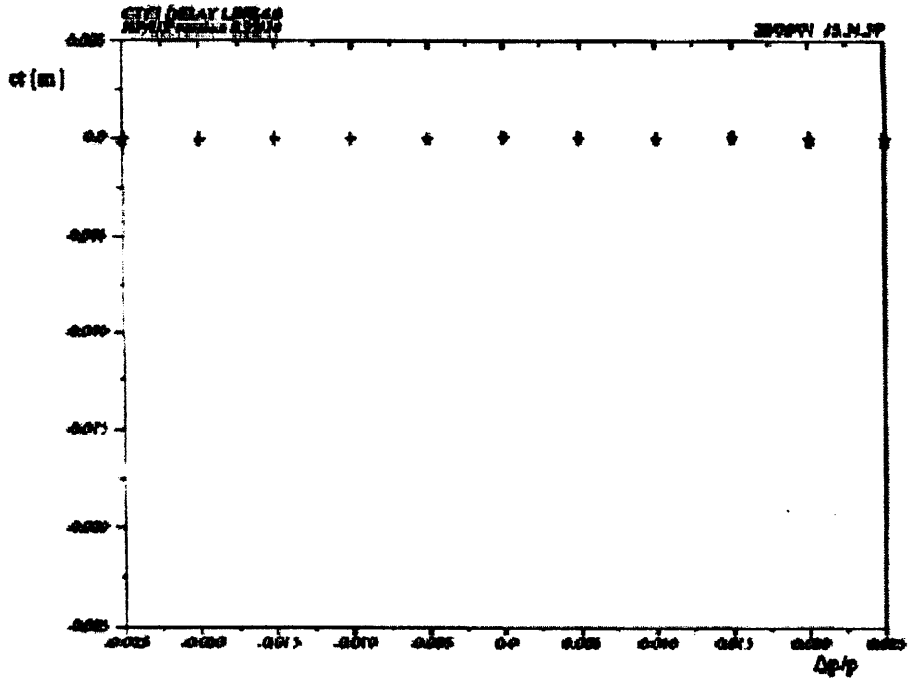

Figure 14.6 Off-energy Particles Longitudinal Position at DL Input (Crosses) and Output (Dots) First and Second Order Correction.

Figure 14.6 shows the tracking result with the second order correction applied. Condition (4) is fulfilled using only 4 of the 5 families. The extra family has been added in order to give some additional capability in tuning the second order matrix terms. In fact, other second order terms not depending on the energy deviation affect the position of the particle inside the

bunch and must be controlled. Moreover, the terms affecting the particle transverse position along the DL must be controlled as well to avoid particle losses. The second order correction presented here must be considered preliminary and extensive six-dimension particle tracking is required in order to fully understand the second order behaviour of the DL matrix.

14.1.3 Path Length Tuning

The wiggler magnet placed in the half machine straight section performs the DL length tuning. This compact device, already presented in reference [2], is a single period wiggler with two half end poles and a central pole independently powered. The tuning characteristics of the wiggler are described in paragraph 15.1.3.

It is worth remarking that the overall length of the DL is a very critical parameter. The tuning capability is limited to ~ ± 3.0 mm so that an accurate estimate of the trajectory length inside elements such as dipoles and wiggler must be done. Simulations based on magnetic measurements and focused on the definition of the 'real' trajectories are required. Moreover an installation strategy for placing the elements with the required precision must be studied.

14.1.4 Injection Region

The injection scheme, briefly described in the introduction, is based on a 1.5 GHz RF deflector exerting a kick of θ_k = 10 mrad on the odd bunches and $-\theta_k$ on the even ones. Figure 14.1 indicates also the presence of two small dipoles with bending angles of $\theta_k/2 = 5$ mrad, necessary for making the injection-extraction scheme symmetric. The matching with the DL is completed by the two pairs of septa of 2° and 27.14°. It is worth noting that the odd bunches receive a second kick of θ_k from he deflector when leaving the DL. The net deflection at the output of the DL injection region is 2π for the odd bunches and 0 for the even ones, so that both bunches are recombined in the same trajectory.

14.1.5 Even Bunches Line Matching

Figure 14.7 shows the optical functions that the sequences of even bunches will see through the DL injection region. Dispersion is self-matched and beta functions and derivatives present the same values as the ones seen by the odd bunches at the end of the DL. The isochronicity condition is not completely fulfilled but the very small value of R_{56} at the line output (0.2 mm) does not require a correction.

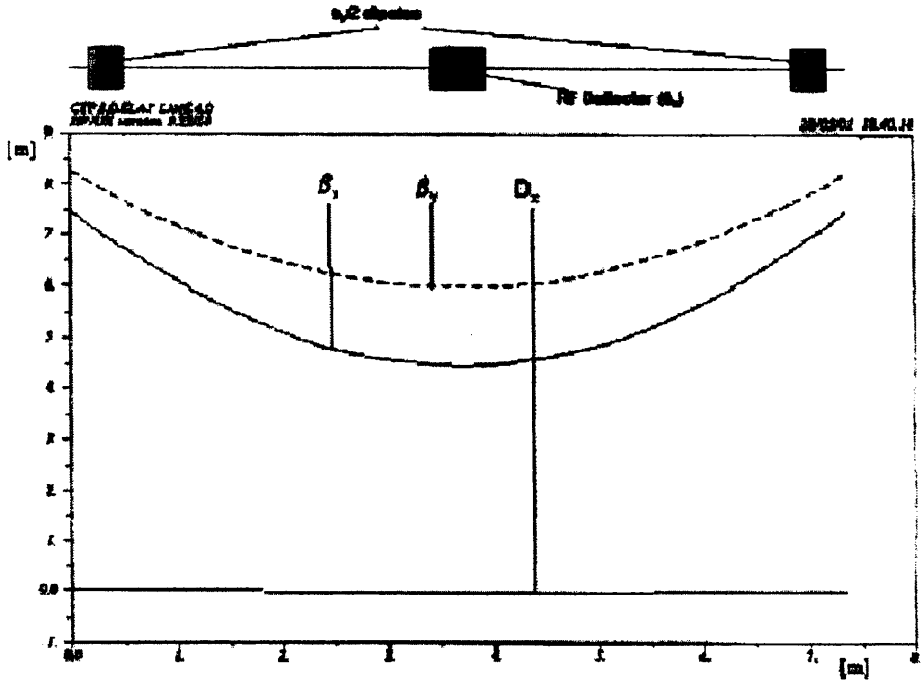

Figure 14.7 Even Bunches Line Optical Functions.

14.2 Stay Clear Requirements

14.2.1 Beam Envelope and Stay Clear Requirements

Table 14.3 shows the stay clear apertures of the DL elements. In the case of the Injection Dipoles and of the RF Deflector, the only elements not yet designed, the stay clear apertures are suggested.

Table 14.3 Delay Loop Elements Stay Clear.

Element	Horizontal [mm] (total)	Vertical [mm] (total)
Dipoles	136	42
Quadrupoles	100 (Ø)	100 (Ø)
Sextupoles	100 (Ø)	100 (Ø)
Wiggler	100	40
2° Septa	20 (Ø)	20 (Ø)
27°.14 Septa	20 (Ø)	20 (Ø)
Injection Dipoles *	> 35	> 35
RF Deflector *	> 35	> 35

* Suggested stay clear apertures.

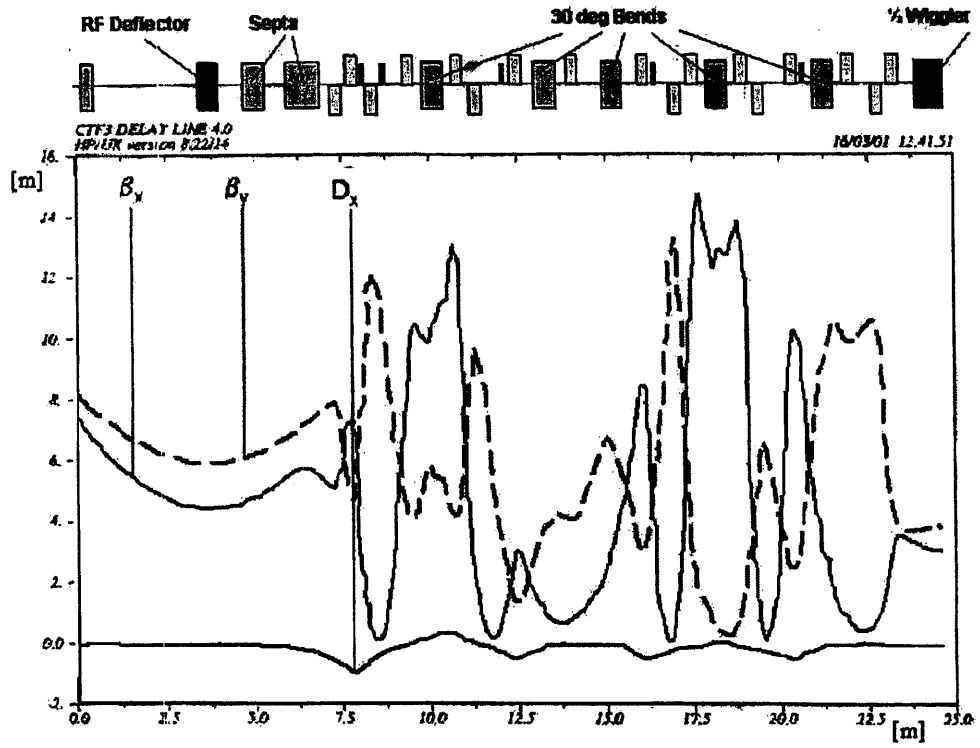

Figure 14.8 Delay Loop Beam Envelopes (rms values).

Figure 14.8 shows the rms beam envelopes in half the DL. Envelopes have been calculated according to:

$$\sigma_w = \sqrt{\beta_w \varepsilon_w + (D_w \Delta p / p)^2} \qquad w = x, y \tag{5}$$

where ε_w are the transverse emittances. The values used were $\varepsilon_x = \varepsilon_y = 10^{-6}$ m and $\Delta p / p = 0.833$ % (value consistent with the total momentum acceptance of 5 %).

The criterion of defining the vacuum chamber stay clear greater than ten times the rms beam envelope will be used. From Figure 14.8, the total apertures that the vacuum chamber must have all along the DL are at least 80 mm and 35 mm in the horizontal and vertical planes respectively. This condition can be fulfilled in the entire loop except the injection region. In particular the vacuum chamber inside both septa is a cylinder with 20 mm inner diameter. In the 2° septum this implies a stay clear 8 times the beam envelope, which is still a reasonable value. In the 27.14° septum horizontal plane the beam envelope increases from the beginning to the end in such a way that the stay clear passes from 7.7 to 5.4 times the beam envelope. In that point the beam size is dominated by the horizontal dispersion due to the septa magnets that cannot be reduced. The situation seems to indicate that the design of a new vacuum chamber for the 27.14° septum (and maybe of a new septum as well) is required. The suggested total stay clear for the new element could be 30 mm for both the planes.

14.2.2 Considerations on Orbit Correction.

The DL orbit must be corrected in order to minimise path length orbit modulation and the effects of non-linearities on the isochronicity. A very conservative solution should include one beam position monitor (BPM) per quadrupole, 34 in the DL case, while a reasonable compromise could have four BPM's per betatron period, which means in the DL about 24 BPMs. Of course, the decision about the number of BPMs must take into account also the maximum impedance that the vacuum chamber can present to the beam.

As far as the number of corrector magnets is concerned, at least one horizontal corrector downstream each of the bending magnets, the wiggler and the 27.14° septa should be foreseen (12-13 correctors). The vertical plane is less demanding (no dipoles; small vertical tune) and one vertical corrector every two horizontal ones should ensure an effective orbit correction.

14.3 References

[1] CLIC Study Team, Proposal for Future CLIC Studies and a New CLIC Test Facility (CTF3), CERN/PS 99-047 (LP) and CLIC Note 402 (1999).

[2]C.Biscari et al., CTF3: Design of Driving Beam Combiner Ring, 7th European Particle Accelerator Conference, Vienna 26-30 June 2000.

[3] LEP Preinjector Parameter List (EPA part), PS/LPI Note 88-02, March 1988 (rev.).

[4] B.Bolli et al., The Injection/extraction 2 deg Septum Magnets of the DAΦNE Accumulator, DAΦNE Technical Note MM-7, June 7, 1995.

[5] B.Bolli et al., Measurements on Tesla Quadrupole Prototype for the DAΦNE Accumulator and Main Rings, DAΦNE Technical Note MM-4, December 2, 1994.

[6] B.Bolli et al., The DAΦNE Accumulator Sextupoles, DAΦNE Technical Note MM-6, May 10, 1995.

[7] E.T.D'Amico, G. Guignard, A new Family of Isochronous Arc, CERN/SL 95-24 (AP),

[8] R.Chritin and D. Cornuet, SL-Note-2000-031 MS (2000).

15. COMBINER RING

The Combiner Ring multiplies the driving beam bunch repetition frequency and peak current by a factor five. After the passage in the Delay Loop the 1.4 μs train from the Linac is subdivided in five 140 ns pulses, in which the bunch spacing is 10 cm, interleaved by 140 ns gaps. The Combiner Ring combines the five pulses, reducing the bunch spacing to 2 cm. The final beam consists of 140 ns long pulses, with peak currents 10 times larger than the initial one, at a repetition frequency of 5 Hz (nomial).

The basic principle of the recombination, based on two RF deflectors working at 3 GHz, is described in chapter 3.3 and Figure 3.4.

Each group of 5 pulses does n+1/2 turns inside the ring, with n=0,1,2,3,4, after which they are extracted by a kicker, with a flat top of at least 140 ns.

The main requirements on the ring are the necessity of preserving the beam emittance and the longitudinal correlation during the recombination process, in order that bunches making a different number of turns maintain the same characteristics.

The lattice has been designed such that, wherever possible, EPA magnets and beam diagnostics equipment can be used. Comparison of the existing magnet characteristic [1] and design constraints [2] have shown that both EPA dipoles and quadrupoles fit the requirements, while EPA sextupoles are too large and will be replaced by sextupoles of the same type as DAΦNE [3].

Although not necessary for the recombination, the possibility of inserting an rf cavity in order to store the beam for diagnostic purposes, (lattice modelling, orbit length definition, closed orbit correction...), is not excluded. The necessary space has been allocated in the extraction section.

15.1 Combiner Ring Lattice and Magnetic Layout

The ring consists of four isochronous arcs, two short sections housing the path length tuning device and two symmetric, opposite long sections for injection and extraction. Quadrupole doublets around the arcs are used for matching. The layout of the ring is shown in Figure 15.1 and the main parameters are listed in Table 15.1.

Table 15.2 refers to the magnets (dipoles, quadrupoles and sextupoles) used in the design, specifying their number, maximum gradients and EPA reference type [1]. The requirement of reaching energies of 300 MeV prevents the use of the smaller type of EPA quadrupoles (type 4.8.1), whose maximum integrated gradient is only 0.5 T. The twelve available quadrupoles of type 4.8.2 are used, two per arc and two in each wiggler section. All the other quadrupoles are of type 5.3. The compatibility with the buildings and general layout has been checked. The compatibility with correctors and diagnostics must still be verified. Due to the large dimensions of the type 5.3 quadrupoles it might be necessary to change some of them for smaller quadrupoles of the same type as the DAΦNE Accumulator [4]. The two family numbers listed in the table correspond to two conditions. The minimum number corresponds to the exact 4-fold symmetry, which needs only 9 families. The preferred configuration corresponds to the possibility of separating the injection from the extraction section (4 more families added) and the two wiggler sections (two more families), still maintaining all the arcs equal. The sextupoles are of the same type as the DAΦNE accumulator [3].

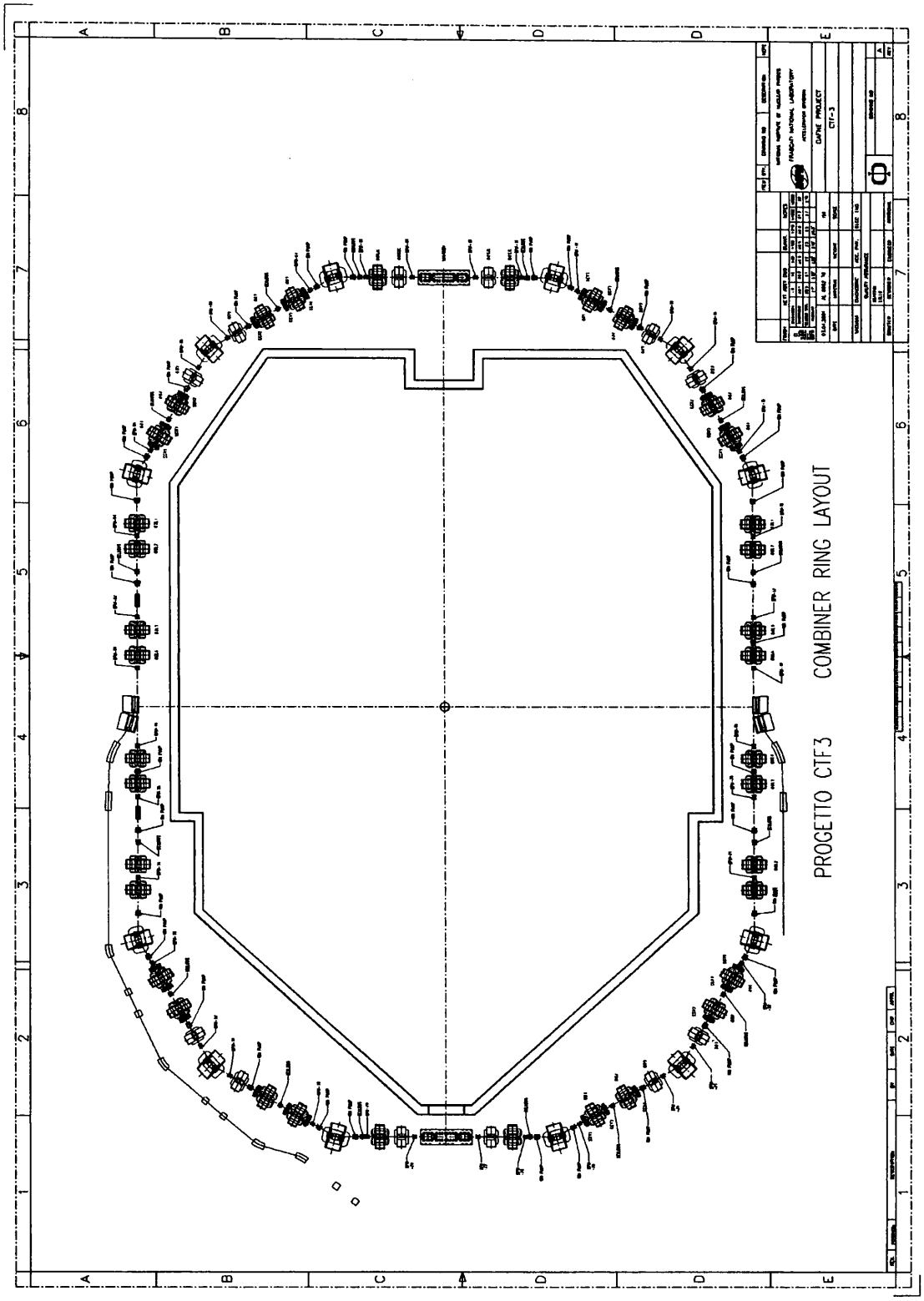

Figure 15.1 Combiner Ring layout

Table 15.1 CR main parameters

Energy (MeV)	150/300
Bρ (T m)	0.5/1.0
Circumference (m)	84
No. Cells	4
Max. beta (m) (H/V)	11.1/11.1
Max. Dispersion (m)	.72
Betatron Tune (H/V)	7.23/4.14
Chromaticity (H/V)	-12.0/ -8.8
Momentum compaction	$<10^{-4}$
Horizontal emittance (mm mrad)	1/0.5
Vertical emittance (mm mrad)	1/0.5
Energy spread (%)	±1
Energy acceptance (%)	±2.5

Table 15.2 CR magnets

A) N. of Dipoles (type 4.7)	12
Dipole Field (T)	0.46/.85
Dipole Bending Radius [m]	1.09
Pole width [mm]	230
Gap height [mm]	45
B) N. of Quadrupoles	48
Quadrupole families (minimum/preferred)	*9/15*
N. of Quadrupoles -type 4.8.2	*12*
Magnetic length [m]	*0.38*
Maximum K_1 [m^{-2}]	*2.24*
Maximum gradient [T/m]	*0.43/0.85*
Pole width [mm]	*140*
Available aperture [mm]	200
N. of Quadrupoles type 5.3	*36*
Magnetic length [m]	*0.38*
Maximum K_1 [m^{-2}]	*3.54*
Maximum Integrated Gradient [T]	*0.67/1.34*
Pole width [mm]	*134*
Available aperture [mm]	*184*
C) N. of sextupoles	*24*
Magnetic length [m]	*0.10*
Maximum K_2 [m^{-3}]	*100*
Max Integrated Gradient [T/m]	*5/10*
Sextupole families	*3*
Available aperture [mm]	*108*
D) N. of Path Length Tuning Wigglers	*2*
Pole width [mm]	*150*
Gap height [mm]	40

15.1.1 Isochronous Arc

The arcs are triple bend achromats [5], with negative dispersion in the central dipole, therefore the term R_{56} of the first order transport matrix relating path length with energy vanishes:

$$R_{56} = \int \frac{D_x}{\rho} ds = 0$$

where D_x is the dispersion and ρ the bending radius.

Three quadrupoles in each half arc allow tunability of betatron functions and tunes. Tuning two of the arc quadrupoles by a few percent is the simple knob which varies the momentum compaction α_c around zero. The value of the dispersion in the mid point of the central dipole in each arc (D_o) is related to the value of the momentum compaction α_c by:

$$D_o\,(\mathrm{m}) = 40.218\ \alpha_c - 0.10278$$

Figure 15.2 shows the amount of variation of α_c obtained by changing the gradient of the outer focusing quadrupoles by ±7%, and the defocusing ones by less than 2%. In this range the rest of the ring can be easily matched to keep tunes and betatron functions similar to the design ones.

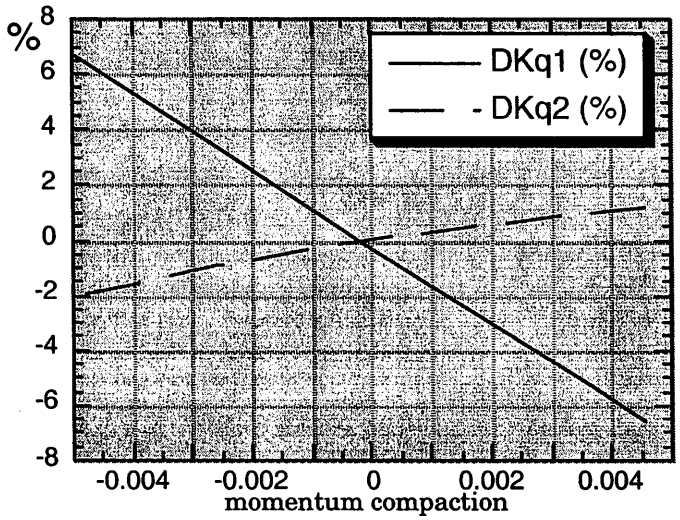

Figure 15.2 Relative change in the gradients of two arc quadrupole families to tune α_c.

15.1.2 Injection and Extraction

Identical structures are designed for the injection and extraction regions, which have similar requirements, thus doubling the ring periodicity. Injection and extraction septa are placed symmetrically (see Figure 15.1) in the middle of a straight section 3.08 m long. The rf deflectors and the extraction kickers are placed in a free zone, 2.32 m long. The π phase advance in between the two injection kickers is created by four quadrupoles arranged symmetrically around the septum. In the extraction region this assures the necessary $\pi/2$ phase advance between the extraction kicker and the septum. The space corresponding to the second kicker can be used to house an rf cavity in the hypothesis of storing the beam for diagnostic purposes.

A critical issue is the value of the horizontal betatron function, β_{xk}, at the fast rf injection kickers, effecting the amount of beam loading of the successive turns (see section 17).

Values of β_{xk} ~ 1.0 m and α_{xk} ~ 0 correspond to minimum beam loading. The design allows the necessary tunability. The optical functions in the injection/extraction section are shown in Figure 15.3.

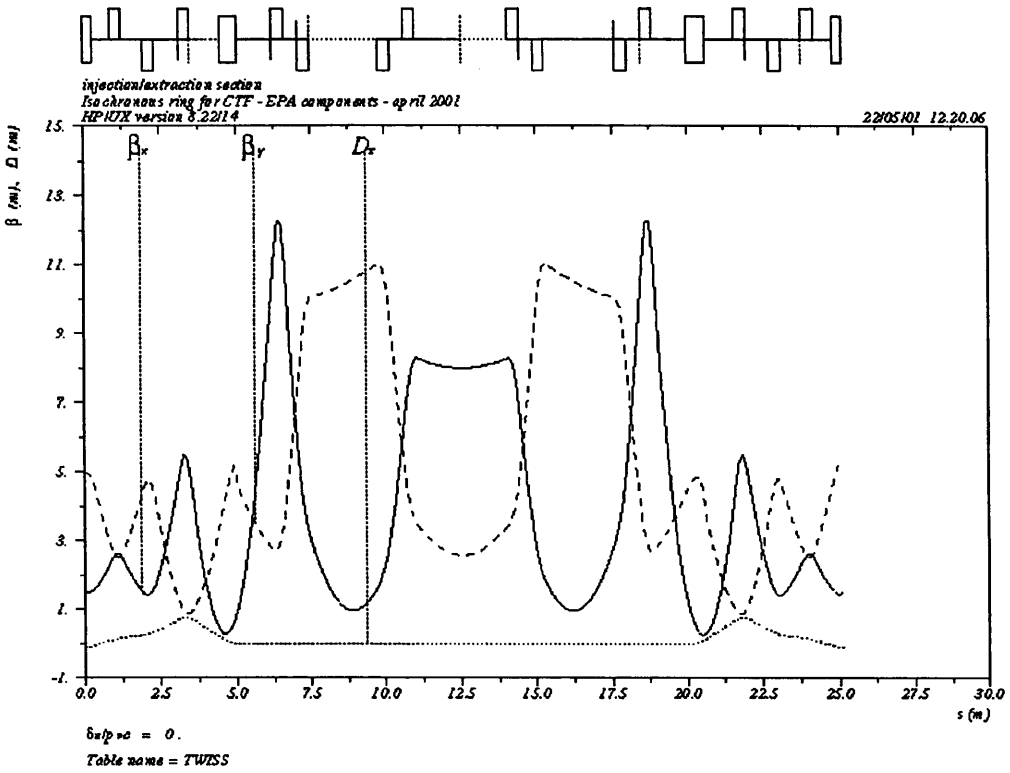

Figure 15.3 Optical functions of injection/extraction from midpoints of adjacent arcs.

15.1.3 Path-length tuning section

The tuning of the relative phase of injected and circulating bunches and the compensation of orbit variations is needed twice in the ring, to adjust independently each bunch train. The path-length tuning devices are variable field, one period, wiggler magnets, housed in the short straight sections. With respect to a magnetic chicane, the wiggler offers the advantage of compactness, a larger tuning range and a lower contribution to the R_{56} term. It has two half end poles and a central one, independently powered, with bending angles –7°, 14°, –7° and total length 1.6 m. The dispersion function introduced by the wiggler is self matched and the contribution to the momentum compaction, $-5 \cdot 10^{-3}$ per wiggler, is compensated inside the arcs.

Changing the field by ±6% gives a path length variation of ± 0.5 mm, which is the original requirement [1]. The tunability of the wiggler is an order of magnitude higher: the path length variation from the wigglers off to a field value 50% higher than the nominal one corresponds to –4 / +5 mm per wiggler. Figure 15.4 shows the path length variation as a function of the wiggler field and the corresponding value of the maximum horizontal displacement of the orbit from the ring axis. It is clear that if the whole range of the wiggler tunability is to be used, the horizontal aperture requirements increase. The change in the betatron tunes and momentum compaction of the whole ring for a single wiggler field variation are shown in Figure 15.5, together with the corresponding change in the wiggler section quadrupole families. The isochronicity condition can be in any case recovered by tuning the arc R_{56} (see Figure 15.2).

The optical functions from the arc centre to the wiggler centre are shown in Figure 15.7 for the nominal case.

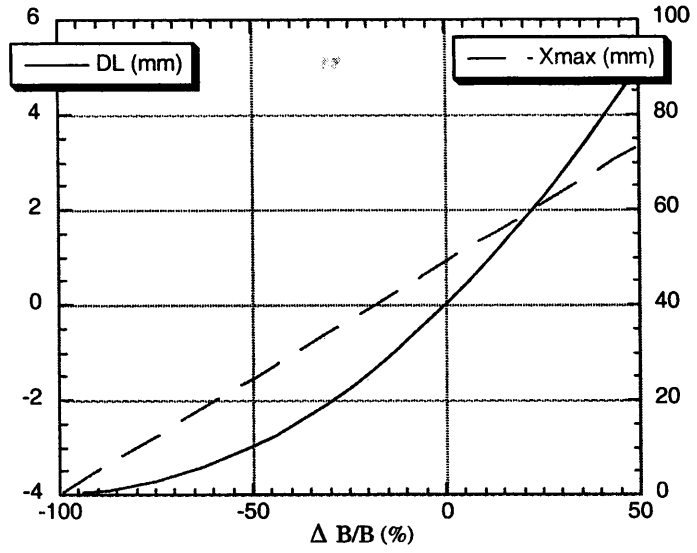

Figure 15.4 Path length variation (full line) as a function of wiggler field and maximum transverse displacement of the trajectory (dashed line).

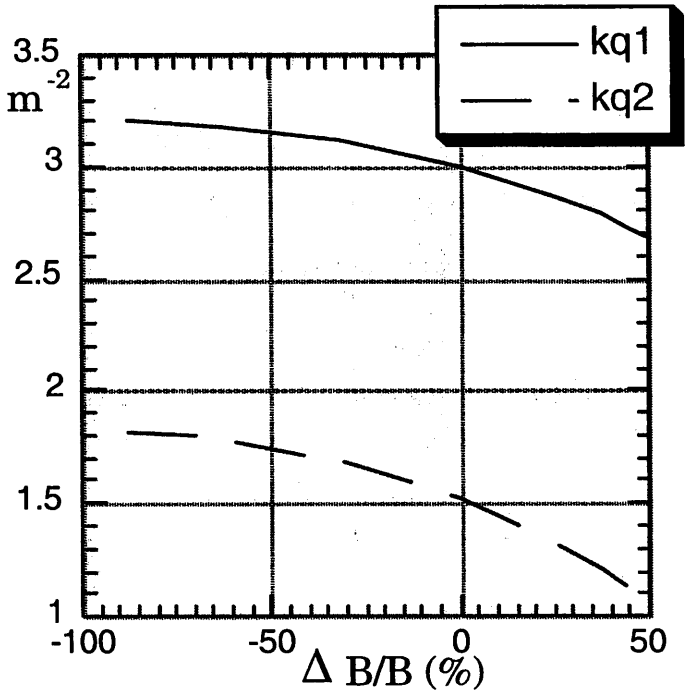

Figure 15.5 Strength of the wiggler section quadrupoles which match transverse betatron waists at the wiggler centre as a function of wiggler field.

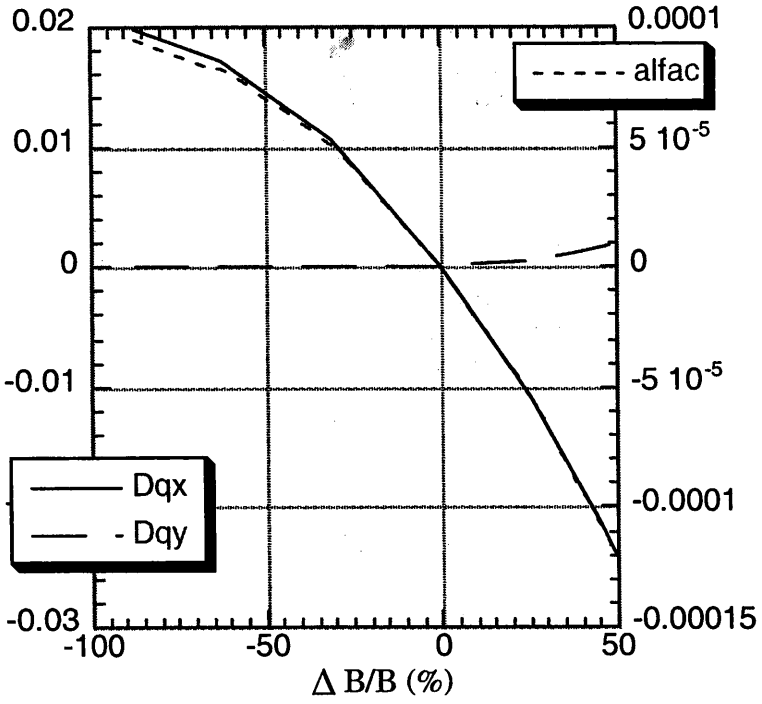

Figure 15.6 Momentum compaction and change in betatron tunes as a function of wiggler field.

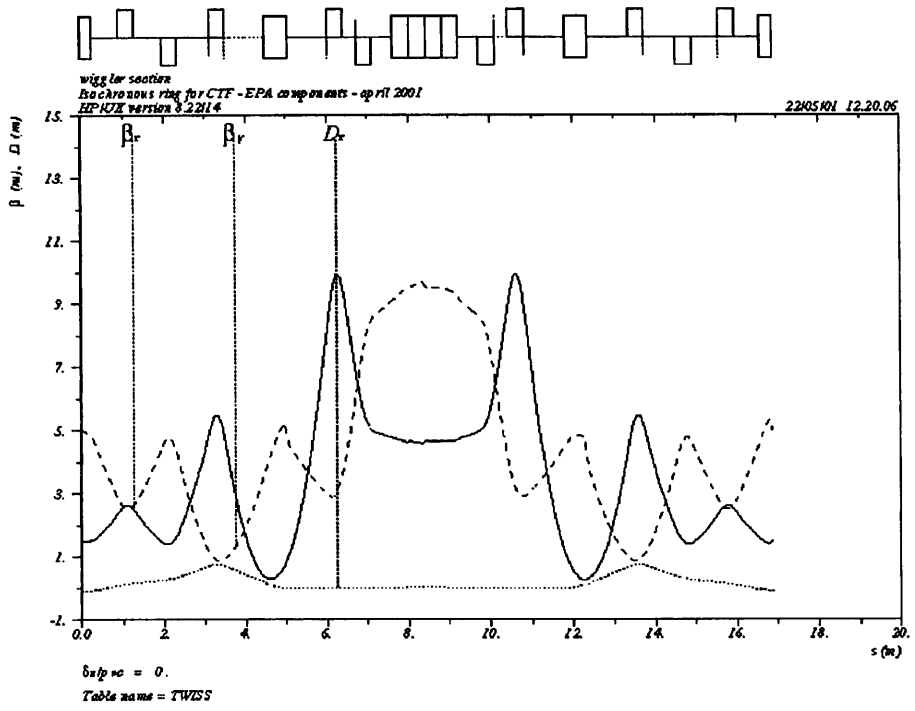

Figure 15.7 Optical functions of wiggler section from midpoints of adjacent arcs.

15.2 Beam size and apertures

The beam size along the ring has been computed with the parameters corresponding to the lowest energy (ε_x = ε_y = 1 mm mrad), which are more demanding. Figure 15.8 shows the behaviour in one quarter of the ring of the horizontal beam envelope $\sigma_x = \sqrt{\beta_x \varepsilon_x}$ (full line), the horizontal beam envelope term $D_x \Delta p/p$ due to 1% energy spread (dots) and the vertical envelope $\sigma_y = \sqrt{\beta_y \varepsilon_y}$ (dashed lines).

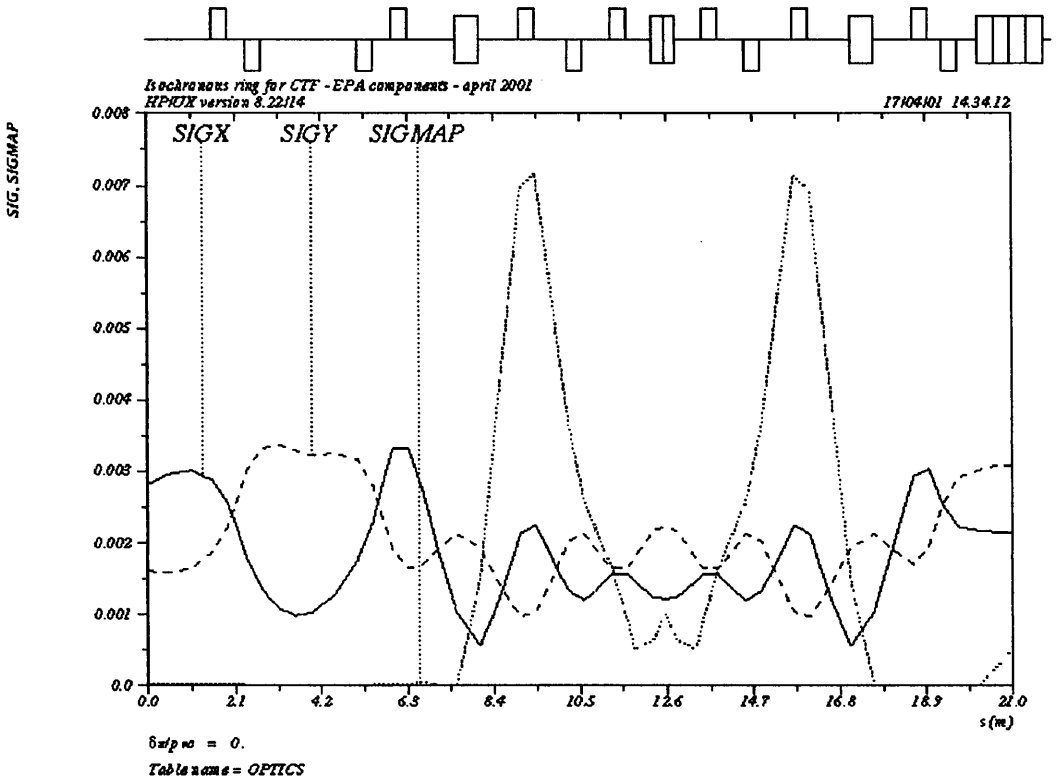

Figure 15.8 Beam size (one sigma) in a quarter of the ring.

The proposed vacuum chamber aperture is 90 x 36 mm^2 (H x V) all around the ring, except in the injection/extraction sections where it has a round cross section (40 mm diameter). In the wiggler section the horizontal aperture is still being defined, since it depends on how much the wiggler tunability can be exploited. Figure 15.9 and Figure 15.10 show that the aperture acceptance of the ring is $\pm 6\sigma_{x,y}$ and ± 4% of energy spread.

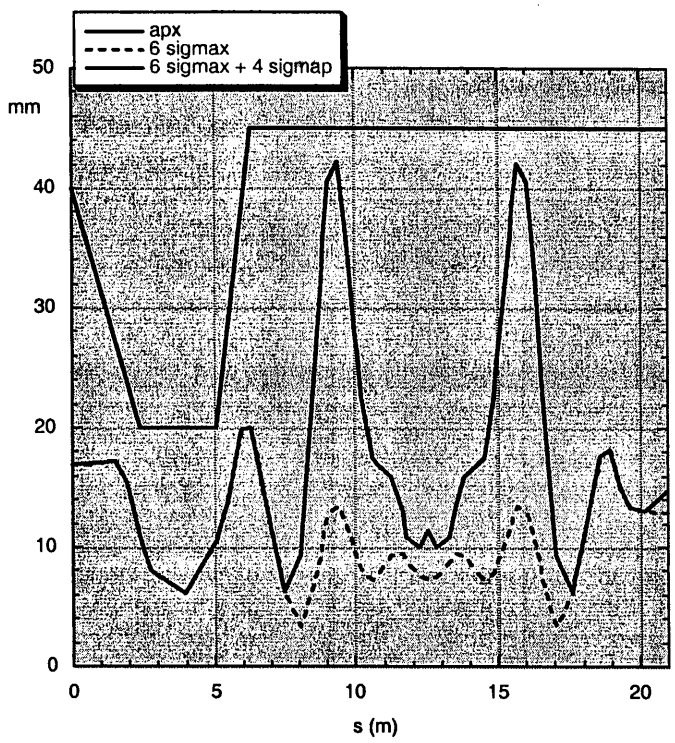

Figure 15.9 Horizontal beam size (six sigmas), momentum spread (4%) and horizontal aperture in a quarter of the ring.

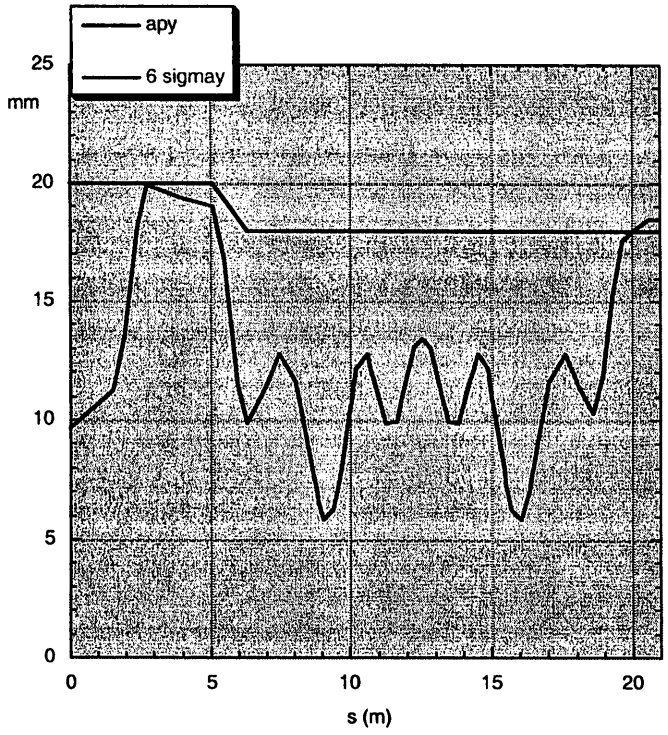

Figure 15.10 Beam size (six sigma) and vertical aperture in a quarter of the ring.

15.3 Isochronicity

The path length variation with energy is given up to the second order by:

$$c\Delta t = R_{56}\frac{\Delta p}{p} + T_{566}\left(\frac{\Delta p}{p}\right)^2 + \ldots$$

where T_{566} is the element of the second-order transfer matrix.

Isochronicity to the first order is assured by the zero integral of the dispersion function in each arc of the ring. Particles with energy deviations ±2.5% and with zero transverse initial invariant change their path length by up to 2.5 cm, with a clear second order dependence (see Figure 15.11); even going to α_c values of a few 10^{-2}, the second order term is still dominant.

The cancellation of the second order term is done by sextupoles. A focusing sextupole in each arc can do the job, but this solution increasing the negative vertical chromaticity, leads to isochronicity loss in the presence of vertical oscillations. The best solution is a compromise between the T_{566} cancellation and the chromaticity correction. A possible solution, which can still be improved, is the use of three sextupoles in each half arc, which give T_{566} = 0.00 and chromaticity of –0.9, -9.8 in the horizontal and vertical plane respectively.

Tracking has been performed for particles with energy deviations up to ±2.5%. Figure 15.11 shows the longitudinal and the horizontal phase planes of particles tracked for five turns in the case of no sextupoles in the ring. The top row corresponds to particles with zero transverse invariant, the second row to particles with horizontal invariant $W_x = 1\ \sigma_x$, the third row to $W_x = 3\ \sigma_x$ and the bottom row to $W_x = 6\ \sigma_x$. The scales in the longitudinal phase plots are the same in the four cases, the scales in the first two cases of the horizontal phase plane plots are equal and multiplied by 3 and in the last two cases by 6. The corresponding vertical plane is always zero in all cases. We observe that the neat 2nd order dependence of path length with energy deviation for particles with no transverse invariant is distorted and increased as the particle oscillates in the horizontal plane.

Figure 15.12 corresponds to the same particles in the case with sextupoles on. The 2nd order isochronicity is corrected. The distortion in the longitudinal phase space is still present, but smaller than before. It should be noticed that the horizontal scale of the longitudinal phase plane plots is lowered by a factor ~2 with respect to Figure 15.9, while the other scales are unchanged.

Figure 15.13 corresponds to particles with vertical invariants (0, $\sigma_{y,}$, 3 σ_y, 6 σ_y). The behaviour of the longitudinal phase plane is different from the one seen in the previous figure, and it can be modified by tuning the sextupole configuration.

With this configuration particles within ± 1% of energy deviation and within $3\sigma_x$ are inside 1 mm of path length difference and those within 3 σ_y inside 2 mm.

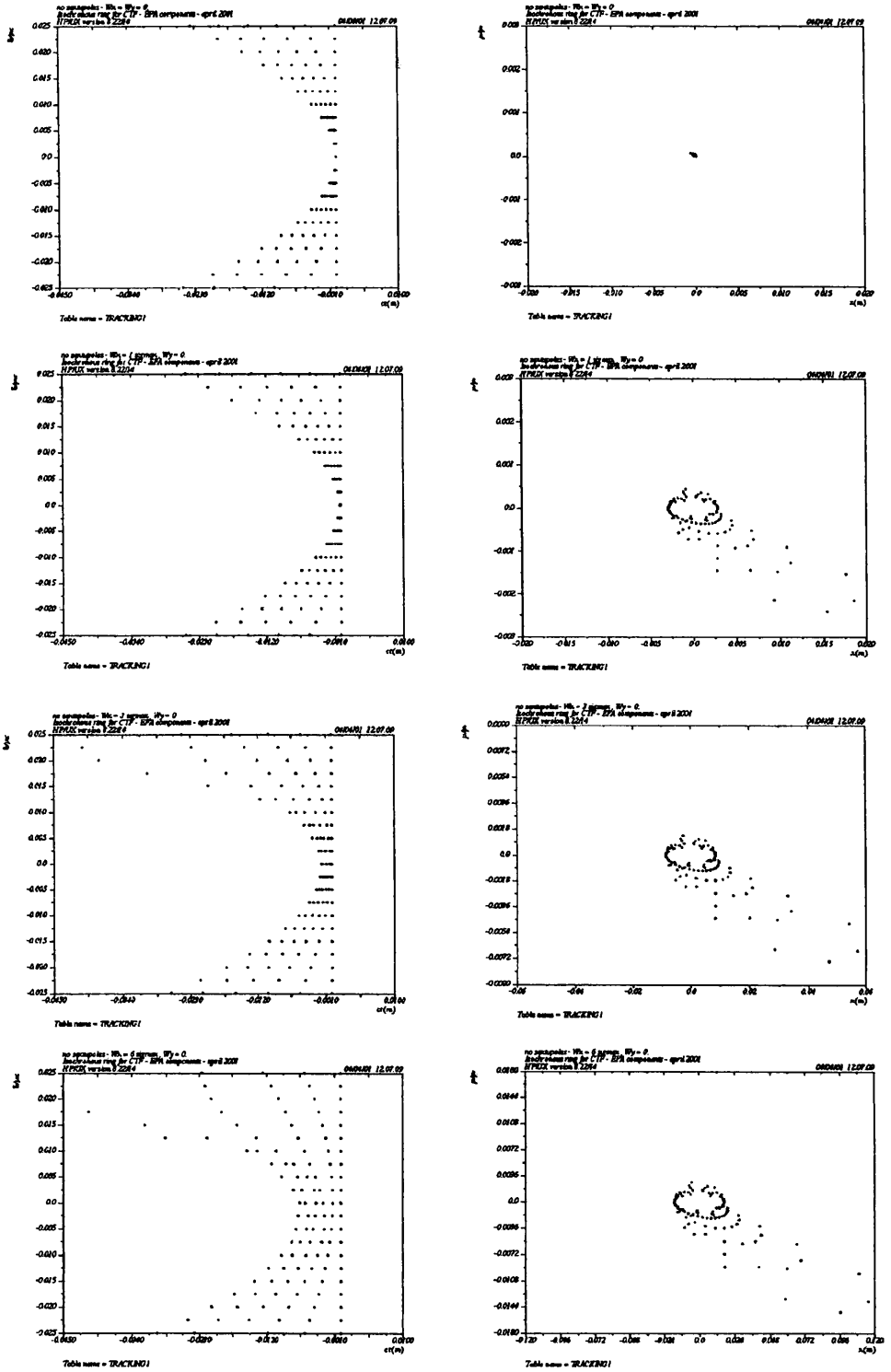

Figure 15.11 Path length with energy deviation (left) and horizontal phase plane (right) for sextupoles off.

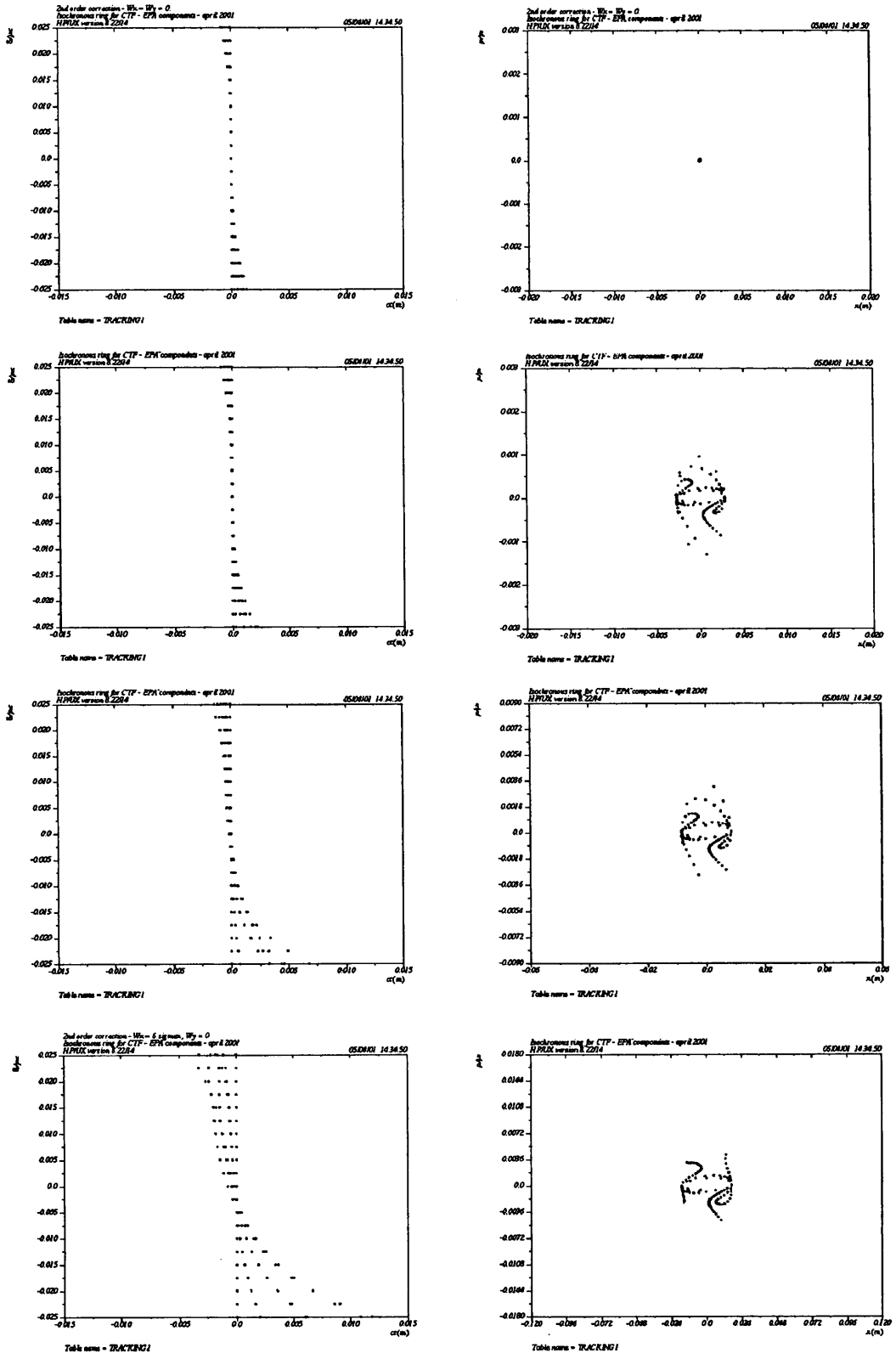

Figure 15.12 Path length with energy deviation and horizontal phase plane for sextupoles on.

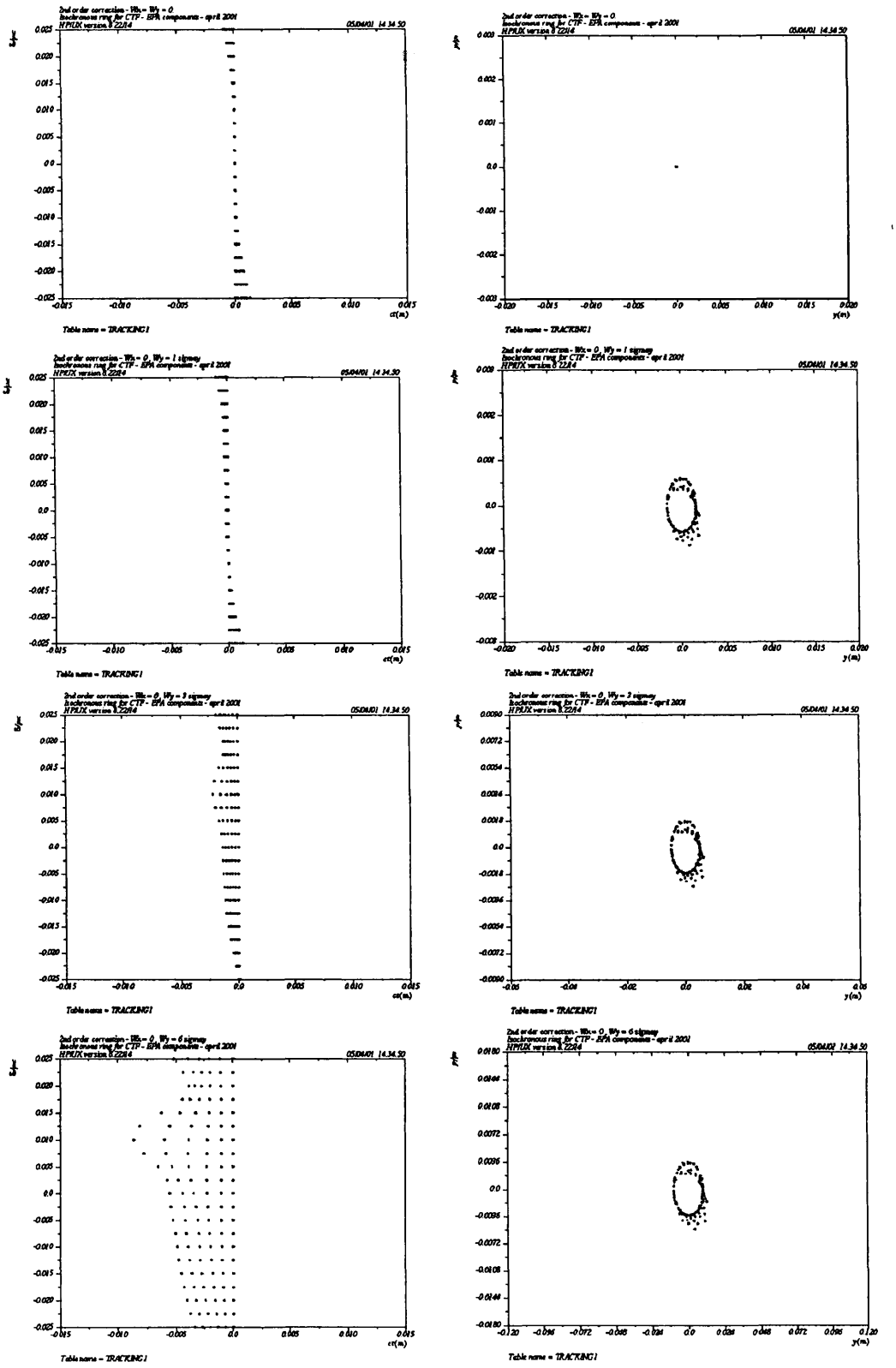

Figure 15.13 Path length with energy deviation and vertical phase plane for sextupoles on.

15.4 Orbit and trajectory correction

The first simulations show that closed orbit corrections of the Combiner Ring used as a storage ring also correct the trajectory when the Combiner Ring is used for the recombination. The trajectory during the first five turns oscillates around the corrected closed orbit with amplitudes determined by the injection offset.

These simulations have been done assuming misalignments in the quadrupoles of 200 μm in the horizontal plane, 100 μm in the vertical plane and tilts around the longitudinal direction of 0.02 mrad.

A preliminary correction scheme, with 20 correctors and 20 monitors per plane has been applied, which corrected the orbit better than one tenth of millimetre. Ten different random uniform distributions of errors were simulated. The closed orbit amplification factors [6] are almost equal in both planes as shown also by the results of the closed orbit values with no correction. The closed orbit characteristics (maximum and rms values) averaged over the ten simulations are listed in the Table 15.3 for both planes (no errors in monitors have been included). The peak and rms values of the closed orbit, before and after the correction, are shown for the ten machines in Figure 15.14 and Figure 15.15. The maximum corrector kick is always less than 1 mrad.

Table 15.3. CLosed orbit characteristics

	before correction	after correction
x_{max} (mm)	3.8 ± 1.0	0.08 ± 0.04
x_{rms} (mm)	1.9 ± 0.5	0.04 ± 0.02
y_{max} (mm)	2.8 ± 1.3	0.11 ± 0.07
y_{rms} (mm)	1.5 ± 0.7	0.06 ± 0.04

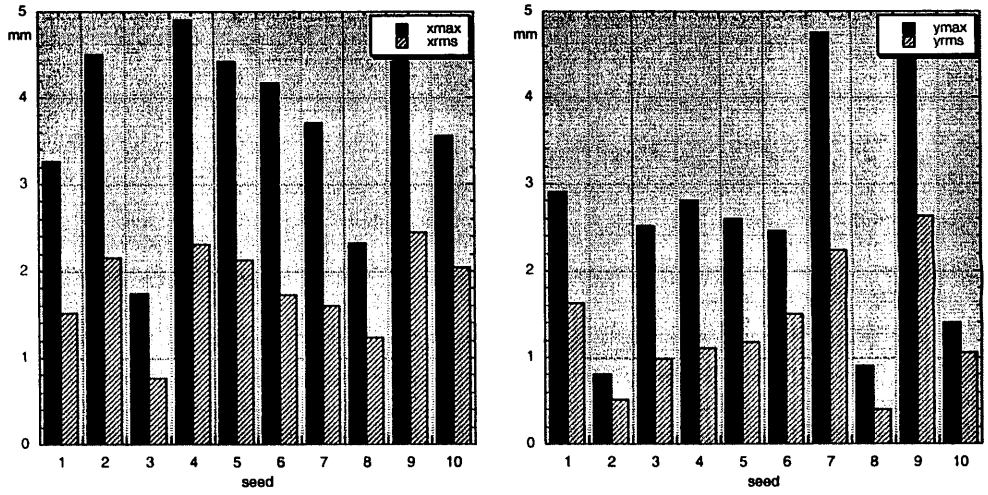

Figure 15.14 Closed orbit (horizontal and vertical) before correction

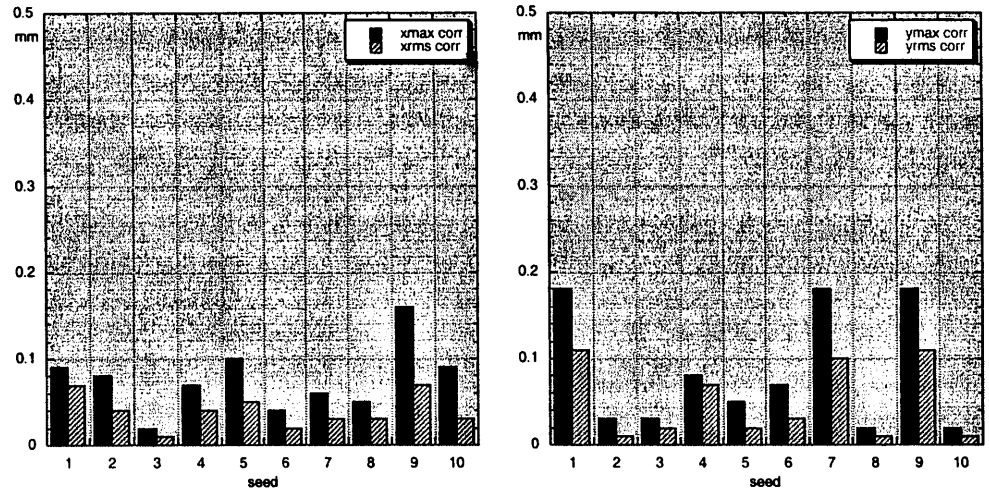

Figure 15.15 Closed orbit (horizontal and vertical) after correction (the vertical scale is one tenth of previous figure)

The definition of the corrector dimensions and consequent positioning in the ring, the positioning of the monitors, the analysis of other kinds of errors (dipole misalignments, dipole and quadrupole field errors, monitor errors,...) are still in progress. The trajectory correction in the Combiner Ring without the option of storing the beam has not been studied yet.

15.5 References

[1] LEP Preinjector Parameter List (EPA part), CERN PS/LPI Note 88-02.

[2] C.Biscari et al, CTF3: Design of Driving Beam Combiner Ring, 7th EPAC, Vienna 26-30 June 2000.

[3] B.Bolli et al., The DAΦNE Accumulator Sextupoles, DAΦNE Technical Note MM-6, May 10.

[4] B.Bolli et at., Measurements on Tesla Quadrupole Prototype for the DAFNE Accumulator and Main Rings, DAFNE Technical Note MM-4, December 2, 1994.

[5] E.T.D'Amico, G.Guignard,'First-Order design of a new type of Isochronous Arc', CERN SL/95-120 (AP), 1995.

[6] E.Keil, Single particle dynamics – linear machine imperfections, CERN 77/13, CERN, 19771995.

16. TRANSFER LINES

Linac, Delay Loop and Combiner Ring are joined together by 60 m of Transfer Lines which also must be isochronous.

The transfer lines are made up of several well-defined sections, meeting the spatial requirements imposed by housing the complex in existing buildings. They have been designed assuming that the beam from the Linac has an energy in the range 150–300 MeV.

The beam from the Linac passes through a four-bend magnetic achromat where the bunch length can be modified over a wide range, then a section provides the necessary matching with the Delay Loop betatron function, allowing beam injection and extraction. A s-shape line drives the beam around the Combiner Ring where a dispersion free section provides the proper betatron functions for injection.

The general Transfer Line layout [1] is shown in Figure 16.1, Figure 16.2 presents the betatron functions along the line.

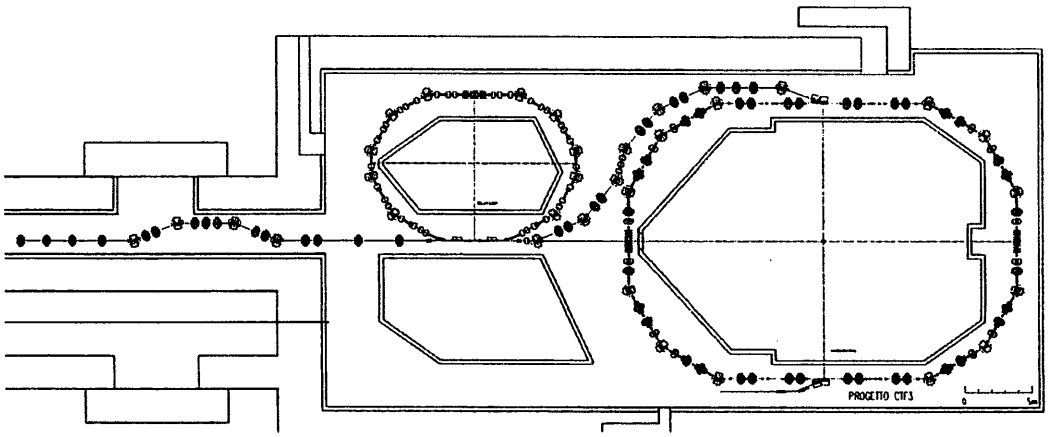

Figure 16.1 CTF3 Layout

A special effort has been put into reusing wherever possible the magnets from the decommissioned EPA ring. It has been possible to use all the bending magnets and a few quadrupoles, those preceding the four-bends achromat insertion. In fact space limitation in the zone between the Delay Loop and Combiner Ring required smaller quadrupoles. For this reason the 0.3 m long quadrupoles [2], designed for the DAΦNE complex, have been used. The maximum strength of the DAΦNE type quadrupoles is:

K_{MAX} = 5.76 (2.88) [m^{-1}] at 150 (300) [MeV]

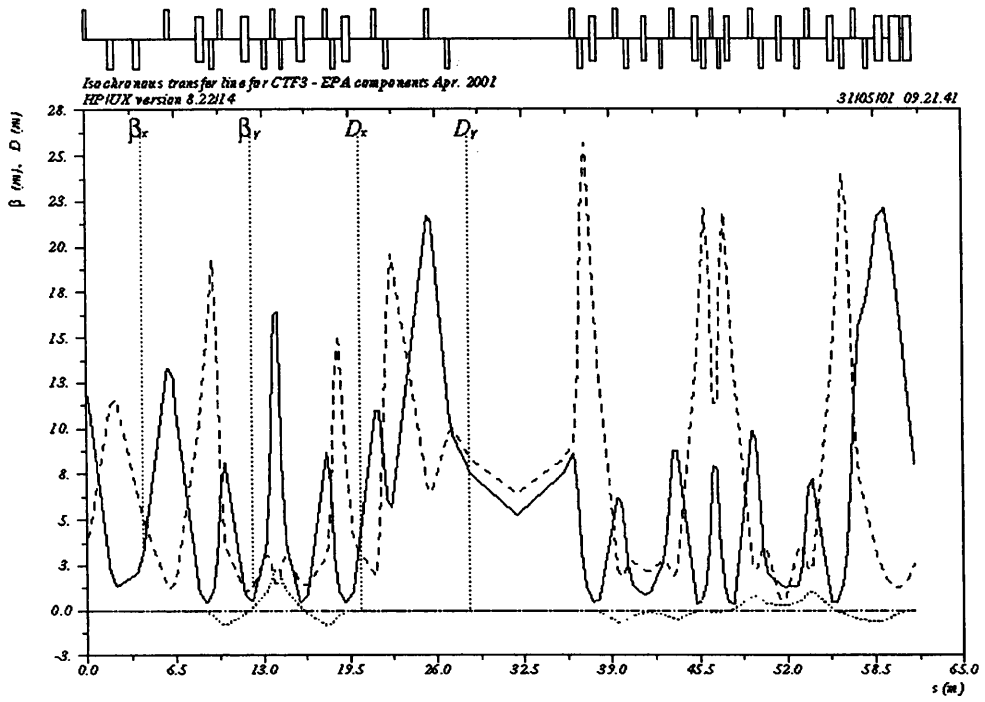

Figure 16.2 Transfer Lines Optical Functions

The 0.505 m long EPA quadrupoles have a smaller focusing strength since their maximum K_1 value is:

$$K_1 = 0.96\ [\mathrm{m}^{-1}] \text{ at } 300\ [\mathrm{MeV}]$$

16.1 Four Bend Magnets achromat

The four bends achromat is an insertion designed to modify the bunch length in order to provide a wide set of different experimental condition during operation. In first order approximation the bunch length variation is proportional to the R_{56} matrix element:

$$\Delta l = -R_{56}\frac{\Delta p}{p}$$

By varying the horizontal dispersion and, as a consequence R_{56}, the bunch length can be tuned.

In Figure 16.3 a schematic layout of this zone is presented. The quadrupole doublets just after the first dipole and before the last dipole allow full control of the horizontal dispersion derivative at the ends of the insertion, while the quadrupole triplet is used to make the betatron function symmetric over the section and to vary the positive peak value of the horizontal dispersion in order to tune the R_{56} factor.

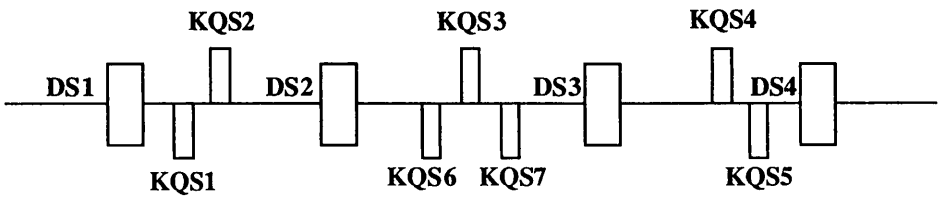

Figure 16.3 Four-bend achromat schematic layout

The betatron functions relative to the four bends achromat are shown in Figure 16.4. The horizontal dispersion and its derivative are obviously equal to zero at both ends of this section.

Table 16.1 gives the available excursion range for the R_{56} coefficient; it can be varied over a wide range including zero, when the bunch length is completely unaffected, keeping the quadrupole strengths reasonably low.

Assuming an energy deviation $\Delta p/p = 0.8\%$ the R_{56} values in Table 16.1 allow a bunch length excursion $\Delta l_b = \pm 2.5$ mm.

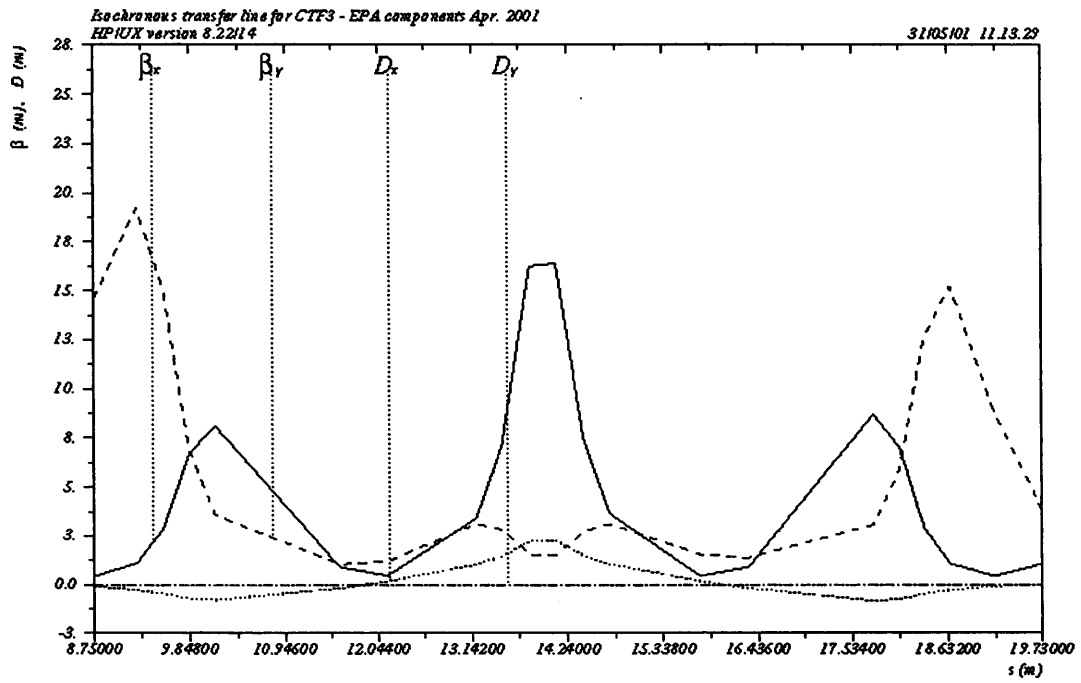

Figure 16.4 Four Bends Achromat Optical Functions

Table 16.1 Quadrupole strengths for different R_{56} in the four-bends achromat

	R_{56} = -.3 [m]	R_{56} = 0 [m]	R_{56} = .3 [m]
KQS1 K2 [m-1]	-1.5366	-1.5204	-1.3902
KQS2	1.9737	1.6451	1.3294
KQS3	1.7941	1.7990	2.0690
KQS4	1.9137	1.6373	1.3662
KQS5	-1.6246	-1.2820	-1.2530
KQS6	-0.9722	-0.9625	-1.2699
KQS7	-1.1477	-0.86532	-0.70083

16.2 Delay Loop Insertion

The Delay Loop insertion includes six quadrupoles. They are used to match the betatron functions in the 6.5 m long straight section shared with the ring, see Figure 16.5.

The betatron values at both ends (points A and C) and at the centre (point B) of the shared line are given in Table 16.2. They are symmetric with respect to the point B where they match the Delay Loop design requirements [3].

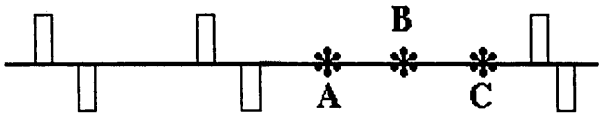

Figure 16.5 Delay Loop insertion schematic layout, A B and C are the symmetry points of the shared line

Table 16.2 Betatron functions at the A, B and C symmetry points

	A	B	C
β_x [m]	7.47	5.23	7.49
β_y [m]	8.254	6.418	8.248
α_x	.654	0.00	-.657
α_y	.535	0.00	-.534

16.3 S-Shape Section

The s-shape section transports the beam over a distance of 11 m to the Combiner Ring injection septa. Due to the narrow passage between the Delay Loop and the Combiner Ring the s-shape is mandatory. It has been designed using two triple bend isochronous modules of the same kind as those proposed at CERN [4]. The betatron functions between the two modules are matched by a quadrupole triplet.

16.4 Combiner Ring Insertion

The injection line into the Combiner Ring includes a dipole transporting the beam to the entrance of the first septum where the beam trajectory is bent 19.64 °. A further deflection of 2 ° is provided by the final septum. The matching of the betatron functions required for injection is obtained by a quadrupole triplet.

The septa used are the ones designed for the accumulator of the DAΦNE complex [5] having a thickness of 1.5 mm and a very low stray field.

16.5 Beam Envelope

The beam envelopes have been computed assuming for emittance and momentum deviation the nominal values:

$\varepsilon_x = \varepsilon_y = 10^{-6}$ [m rad]
$\sigma_e = .8\ \%$

The rms beam envelopes are shown in Figure 16.6.

$$\sigma_x = \sqrt{\varepsilon_x \beta_x + (\sigma_e \eta_x)^2}$$

$$\sigma_y = \sqrt{\varepsilon_y \beta_y} \qquad (4)$$

The horizontal beam size has a significant contribution coming from the energy spread related term in the four-bend achromat section.

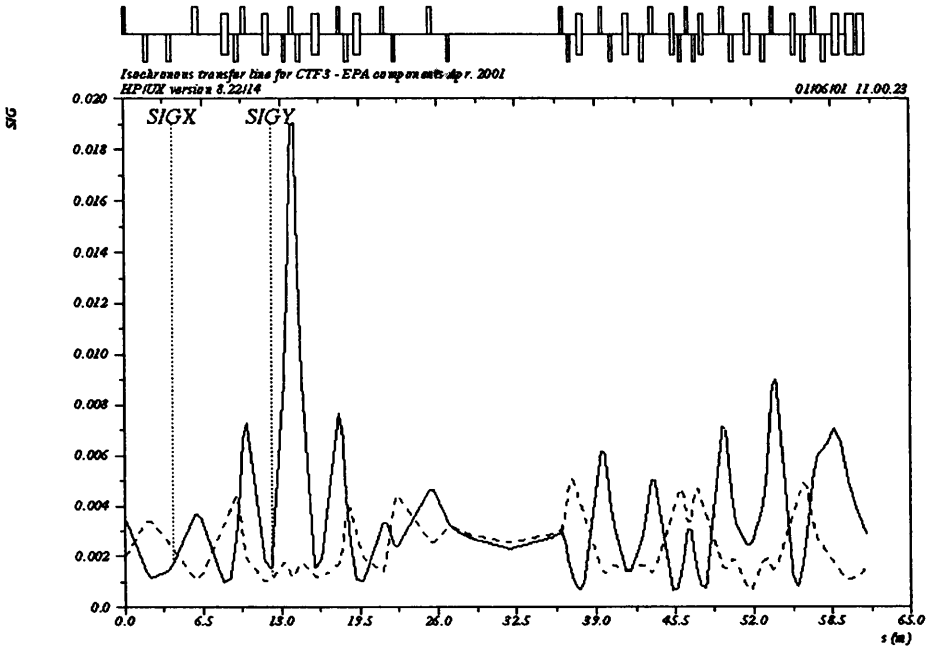

Figure 16.6 Transfer Lines Beam Envelopes (rms values)

16.6 Combiner Ring Extraction Line

The Combiner Ring extraction line has not yet been defined in detail, since its shape depends on the positioning of the RF Power Extractor. However, some general consideration about its design can still be made.

Due to the symmetry in the Combiner Ring, the extraction line can be derived by mirroring the injection line. The necessary bunch compression can be provided by exploiting the flexibility of a four bend achromat in tuning the bunch length. So the only parts which will have to be designed are the straight sections, matching the Combiner Ring extraction line, the four bend achromat and the RF Power Extractor.

16.7 References

[1] F.Sgamma, A. Beatrici, Transfer Line Layout, in preparation.

[2] B.Bolli et al., Measurements on Tesla Quadrupole Prototype for the DAΦNE Accumulator, DAΦNE Technical Note, MM-2, December 2, 1994.

[3] F.Sannibale, Driving Beam Delay Loop Design for CTF3, CTFF3 Technical Note, CTFF3-001, April 2001.

[4] E.T.D'Amico, G.Guignard, Tunable Achromats and CLIC Application, 7th European Particle Accelerator Conference, 26-30 June 2000, Vienna, Austria and CERN/PS/2000-027 (AE),

[5] B.Bolli et al., The Injection/extraction 2 deg. Septum Magnets of the DAΦNE Accumulator, DAΦNE Technical Note, MM-7, June 7, 1995.

17. RF DEFLECTORS

The bunch train compression scheme for the CLIC Test Facility CTF3 relies on the use of fast RF deflectors. The most demanding issues in the deflector design are those related to the beam dynamics, including the beam loading effects on the fundamental deflecting mode. The CTF3 efficiency parameters can be easily met by scaling already existing travelling wave (TW) or standing wave (SW) structures.

The injection and the closed bump orbit allowing the multi-turn circulation in the Combiner Ring require a pair of RF deflectors working at f_{DB}, the Drive Beam (DB) linac frequency, while the injection/extraction in the delay line requires a RF deflector working at $f_{DB}/2$.

Table 17.1 CTF3 RF Deflector Parameters

	Delay line		Combiner Ring	
	TW	SW	TW	SW
nom. Energy E_n [MeV]	150		150	
max. Energy E_{max} [MeV]	300		300	
frequency f [MHz]	1499.28		2998.55	
number of cells N_c	10	1	10	1
De-phasing/cell	$2\pi/3$	---	$2\pi/3$	---
total length L [cm]	67	8	33	4
group velocity v_g/c	-.0244	0	-.0244	0
phase velocity v_{ph}/c	1	∞	1	∞
filling time τ_{F_0} [ns]	90	2500	46	900
Shunt impedance $R_s = (E\phi)^2/2P_{RF}$ [MΩ]	0.275	1.2	0.19	0.85
Deflection ϕ [mrad]	10		5	
max RF Power P_{RF} [MW]	22	5.1	8	1.8

The main parameters of the CTF3 RF deflectors are summarised in Table 17.1, comparing the characteristics of travelling wave (TW) and standing wave (SW) structures.

A disk-loaded backward waveguide working in the EH_{11} hybrid mode (RF separator or Lengeler structure) [1] already optimised for beam deflection has been considered as a possible TW solution, while a single-cell cavity working in the deflecting TM110 mode, obtained by scaling existing designs of crab-crossing cavities, has been taken as a possible SW candidate [2]. In the last case, the shunt impedance values reported in Table 17.1 have been specified at the optimal coupling between the SW cavity and the external RF power source. The filling time is $\tau_{F_0} = Q_0/\omega$ in this case. In order to match the pulse length of the existing RF source, the filling time τ_F can be shortened by overcoupling the cavity input.

In the latter case the effective shunt impedance is decreased by the factor $(\tau_F/\tau_{F_0})\cdot(2-\tau_F/\tau_{F_0})$ and the RF power dissipation is increased by the same factor.

Both types of structure meet the CTF3 efficiency requirements. They can provide the required deflection with a reasonable amount of RF power. A TW structure is more promising considering only beam dynamics issues, since wakefields leave the structure faster, due to the shorter filling time, but a rigorous computation of the wake is not trivial. In the following, we report on the study of the wake generated by the interaction of the beam with the deflector operating mode (beam loading) and analyse the problem of the single-passage wake in the TW structure considered in Table 17.1 (RF separator). The results of a multi-

passage tracking based on the simplest formulation of the single-passage wake are also reported.

17.1 Beam Loading in RF Deflectors

The beam loading in transverse, deflecting structures may be described by two mechanisms:

- The transverse component of the bunch velocity couples with the deflecting E-field, and the energy exchange creates a deflection gradient along the train;

- The longitudinal component of the bunch velocity couples with the longitudinal E-field, which is non-zero off axis, and the energy exchange generates an out-of-phase component of the deflecting field.

The first contribution is very similar to the loading of a linac accelerating section or to that of a storage ring RF cavity crossed by a truncated bunch train. The deflection spread along the train can be estimated and in the case of CTF3 the value is quite small.

The second contribution is of more concern, because in the Combiner Ring the bunch pattern is such that at a certain time the deflector will be crossed by bunch trains with a phase separation of only $2\pi/5$ ($= 72°$), generating a mutual perturbation mainly through the out-of-phase wake. Turn-by-turn the perturbation propagates with the one-turn transport matrix of the ring, and the overall effect may lead to a magnification of the injection errors.

To study this process for a TW structure we have worked out models of the single-passage wake for a Lengeler structure and implemented then in a tracking code. We can then analyse the multi-passage effects taking into account the role of the one-turn transport matrix, i.e. of the ring optics.

17.1.1 Single-passage wake

We considered three approaches in determining the single passage wake generated by the iris-loaded waveguide EH11 mode excited by an off-axis travelling bunch [3]:

Complete: detailed dispersion curve of the iris-loaded waveguide is considered. The solution is a superposition of the field distributions at any frequency in the dispersion curve band-pass;

Partial: the dispersion curve is linearised over the band. Only the field distribution at resonant frequency ω^* ($v_{ph} = \omega^* / \beta(\omega^*) = c$) is considered;

Simplified: the dispersion curve is linearised over an unlimited frequency range. The local excitation is proportional to the leading charge offset. A rigid wave profile results in this case, which moves backward with the group velocity.

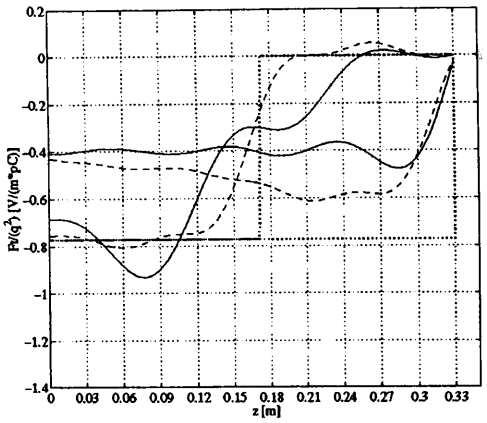

Figure 17.1 Single passage wakes

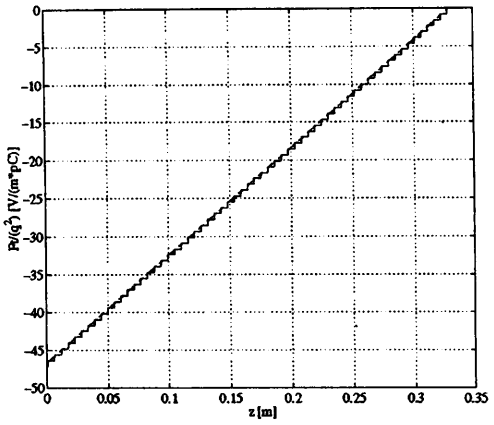

Figure 17.2 Multi-bunch wakes

The transverse wake excited by a leading charge travelling 1 mm off-axis as probed by particles injected out-of-phase with a delay of $T/4$ and $T/4 + \tau_F/2$ is shown in Figure 17.1 (complete solution = solid lines, partial solution = dashed lines, simplified solution = dotted lines). In spite of the fact that the basic assumptions are far less physical, the amplitude of the simplified wake is not too different to the other cases.

17.1.2 Multi-passage tracking

We have considered the effects of the multibunch wake for the bunch pattern of the CTF3 Combiner Ring. The multibunch wake is obtained by simply adding up the single passage wakes taking into account the bunch pattern. After one filling time the multibunch wake converges to a steady-state regime solution. It is noticeable that the three different single passage wakes of Figure 17.1 produce steady-state multibunch wakes that are almost identical, as shown in Figure 17.2. The explanation is that the multibunch regime solution is the response to an almost monochromatic excitation, and therefore the details of the dispersion curve out of resonance are not relevant in this case. Therefore the simplest model of single passage wake (corresponding to the dotted line plot of Figure 17.1) has been assumed for studies of the multibunch beam loading in the Combiner Ring deflectors. On this basis, a simple tracking program has been written to simulate the behaviour of the design bunch pattern.

The tracking scheme is sketched in Figure 17.3. Each bunch, represented as a macro particle, enters either deflector with some horizontal initial conditions (x_{in}, x'_{in}). It then interacts with the main RF deflecting field and the wake left by the bunches ahead, contributes to the wake and exits the deflector with some new horizontal conditions (x_{out}, x'_{out}). Then the bunch is transported to the other deflector by one of the two transport matrices (M_{12} or M_{21}), interacts with the RF fields before leaving it, and so on up to the extraction.

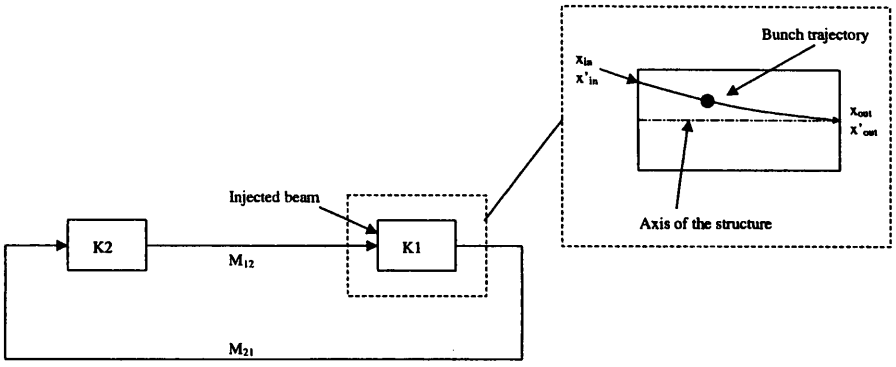

Figure 17.3 Ring schematics for multi-bunch tracking

At the end of the merging process each macro particle ends up with certain horizontal conditions (x_o, x_o') corresponding to a certain value of the Courant-Snyder invariant $I_o = \gamma\ x_o^2 + 2\alpha\ x_o x_o' + \beta\ x_o'^2$ associated with the motion of the bunch centre of mass. The tracking is aimed at studying the distribution of the final values of the Courant-Snyder invariant for all bunches, and its dependence on the deflector wakes, the injection errors and the ring tunes.

17.1.3 Perfect injection of the 5 trains

We consider first the case of bunch trains injected with the initial conditions that perfectly match the main deflecting field of the deflectors, so that if there were no wake, all the bunches would end up on the combiner design orbit. The 1st train makes the first revolution alone, and there are no bunches interacting with its out-of-phase wake.

During the second revolution, there is the presence of both the 1st and 2nd trains, which cross the deflectors with some horizontal displacement. The two trains are interleaved with a separation of 72° RF phase and their bunches interact through the out-of-phase wake. This generates a first perturbation that deviates the bunches from their ideal trajectories. Similar processes take place during the next interleaving phases, and when the five trains are finally merged into one, the bunches are spread by a certain extent in the horizontal phase space.

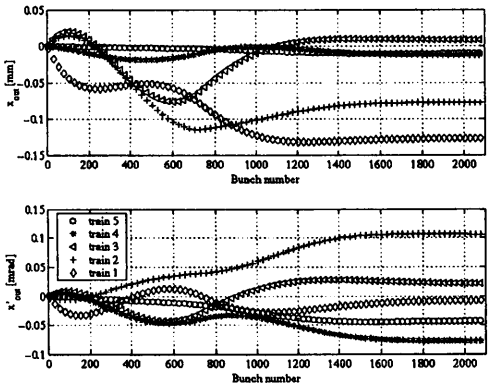

Figure 17.4 Position and angle of the bunches of the merged trains

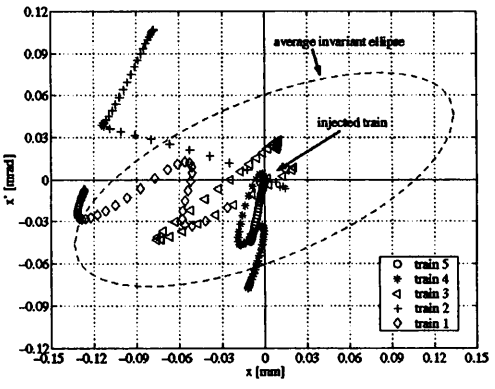

Figure 17.5 Phase space footprint of the bunch centres-of -mass of the merged trains

A plot of the position and angle of the bunches with respect to the nominal orbit at the first kicker output after the merging process is shown in Figure 17.4, while the corresponding

plot of the bunch phase space is shown in Figure 17.5. In this case we are considering a 10-cell TW Lengeler structure as a RF deflector, and the transport matrices M_{12} and M_{21} are given by the nominal Combiner Ring optics [4] (Qx = 7.229). Figure 17.4 and Figure 17.5 represent the "systematic effect" since it is not driven by initial injection errors. The average value and the maximum value of the Courant-Snyder invariant distribution in these figures are respectively $I_{o\_ave} \approx 8 \cdot 10^{-3}$ mm mrad and $I_{o\_max} \approx 4.2 \cdot 10^{-2}$ mm mrad.

The spread of the macro particle invariant values caused by the systematic effect is therefore a small fraction of the CTF3 bunch design emittance ($\varepsilon \approx 0.5$ mm mrad at 150 MeV).

17.1.4 Errors in the injection of the trains

We considered the case of an equal injection error for all the bunches in a linac pulse, i.e. equal for all the five incoming trains. This is true, if one assumes that the error can fluctuate only from pulse to pulse due to some jitter in the beam transport. The build-up mechanism for the final invariant spread is driven by such an initial error.

It may be seen that, in general, the maximum value I_{o_max}, the average value I_{o_ave} and the standard deviation σ_{I_o} of the final distributions are not constant for a given initial value I_{in} of the invariant but, due to the nature of the wake, depend also on the betatron phase of the bunch train at the injection. If we consider all the possible betatron phases for a given I_{in}, and calculate the maximum and average values for the corresponding final distributions, we obtain the 3D plots of Figure 17.6. For any given initial I_{in} value, there are some betatron phases giving the largest I_{o_max} value ($\hat{I}_{o\_max}$), and the largest I_{o_ave} value ($\hat{I}_{o\_ave}$).

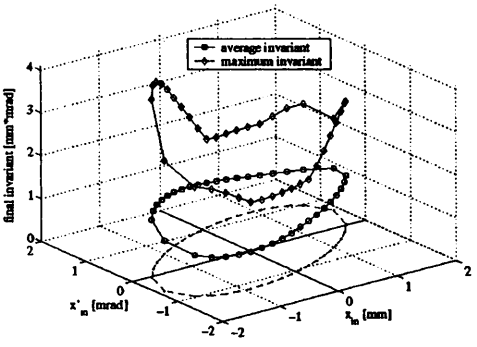

Figure 17.6 I_{o_max} and I_{o_ave} for a given I_{in} for various betatron phases

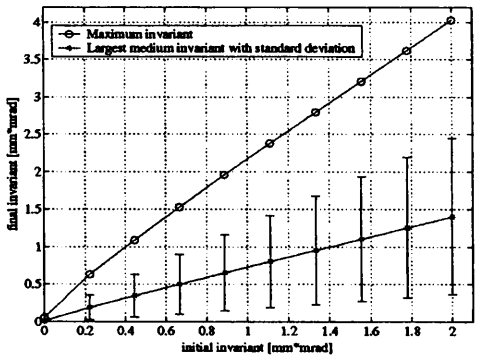

Figure 17.7 $\hat{I}_{o\_max}$ and $\hat{I}_{o\_ave}$ as function of the injection Courant-Snyder invariant

The plots of $\hat{I}_{o\_max}$ and $\hat{I}_{o\_ave}$ (this last includes the ± 1 standard deviation bar) for I_{in} ranging from 0 to 2 mm mrad are shown in Figure 17.7. It may be seen that, for the optics parameters considered and with the exception of the $I_{in} \approx 0$ case, it is always $\hat{I}_{o\_ave} < I_{in}$, which means that, on the average, the deflector wake gives a sort of "cooling" of the Courant-Snyder invariant of the bunch centre-of-mass. On the other hand from Figure 17.7 one has $\hat{I}_{o\_max} / I_{in} \leq 2.6$, which means that, in the worst case and for the worst bunch, the magnification of the injection error is a factor $\leq \sqrt{2.6} \approx 1.6$. The magnification factor is reduced to $\leq \sqrt{1.5} = 1.23$ for all bunches staying within +1 standard deviation above the average (≈70% of the bunches).

The minimisation of these magnification factors is one of the criteria for the choice of the ring horizontal tune. Different tunes may result in very different magnification factors. For example, we report in Figure 17.8 the ratio I_{o_ave}/I_{in} and I_{o_max}/I_{in} in the case of an injection error caused by a pure displacement of 1 mm for various values of the betatron phase advance in the M_{21} matrix. Our nominal tune corresponds to a phase advance of 262°, which is close to the minimum. Modifications of the phase advance in the range of ±10° (corresponding to variations of the tune value of ≈ ± .03) does not significantly change the scenario. Anyway, some tunes outside the range shown in Figure 17.8 may give magnification factors larger than 10 [3].

Studies of the beam loading effects based on tracking simulations will continue to investigate other aspects. The most important items to be analysed are:

Contribution of the RF structure modes different from the operational one to the final quality of the merged train. In particular, the vertical polarity of the operational mode which is detuned by some asymmetry in the cells, has to be taken into account, since the vertical tune of the ring may be far from optimum.

Different injection conditions for "odd" and "even" bunches in each incoming train due to the "memory" of the different paths in the Delay Loop.

Beam loading effects due to off-time injection and finite bunch length.

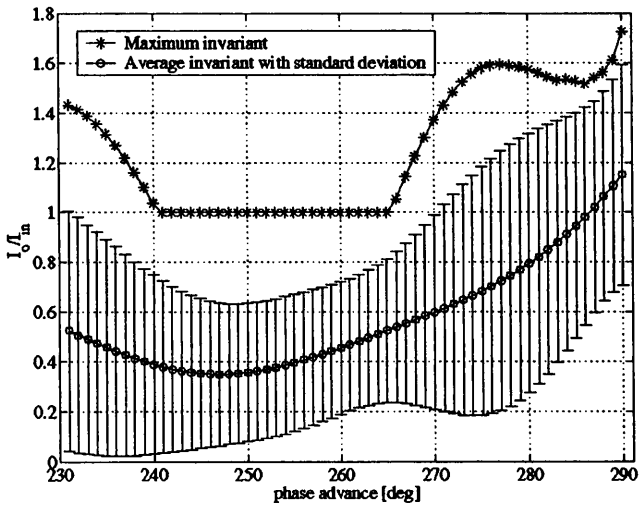

Figure 17.8 Tune dependence of the Courant-Snyder invariant magnification for an injection offset of 1 mm

17.2 The Delay Loop RF Deflector

The dynamics implications of the RF deflector for the Delay Loop are less demanding, and this is mainly due to the bunch pattern in the deflector since there are no bunches probing the out-of-phase wake in this case.

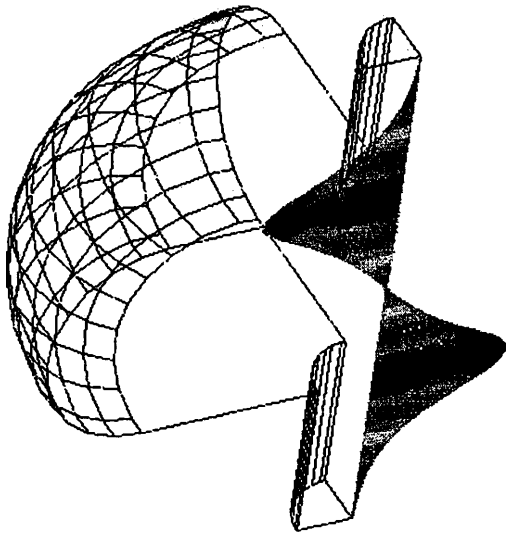

Figure 17.9 HFSS model of a SW single-cell cavity

The operating frequency of this device will be 1.5 GHz. Since there are no RF power sources available to drive these devices, the power level and the pulse duration is still a free parameter.

An obvious possibility is that of scaling a Lengeler structure to 1.5 GHz. In this case the expected behaviour for the beam dynamics is excellent, but the size of the structure is quite large. Since the beam loading requirement are relaxed for the Delay Loop deflector with respect to the Combiner Ring ones, we can in principle consider other options, such as standing wave cavities that are more compact and efficient (see Table 17.1). In this case a longer RF pulse could be required to fill the cavity with the best efficiency. The filling time can be shortened by properly over-coupling the cavity input, at the expense of the reduction of the efficiency. A possible standing wave RF deflector could be designed starting from the proposed geometry for crab-cross cavities or standing wave separators. An HFSS model of a single cell, standing wave deflecting cavity is shown in Figure 17.9.

17.3 Combiner Ring RF Deflectors

The simulation results reported in the previous section indicate that a proper choice of the Combiner Ring horizontal tune keeps under control the beam loading effects of a pair of Lengler structures.

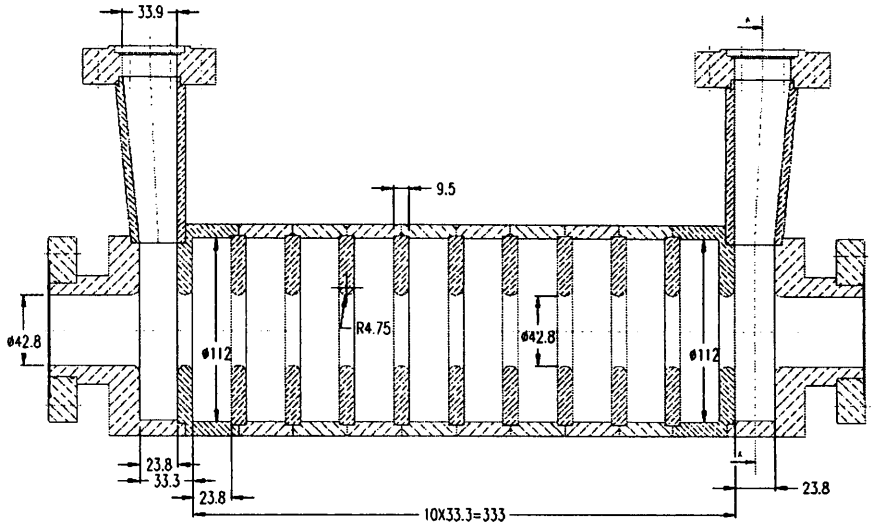

Figure 17.10 Mechanical sketch of a 3 GHz, 10 cells Lengeler structure

For that reason a design activity aimed at constructing two RF deflectors of this type in less than one year has been started. Mechanical drawings of such a RF structure scaled to 3 GHz frequency have been almost completed and a sketch is shown in Figure 17.10. Some details, like the geometry of the of the two terminal cells, are still under study.

The study of the structure is mainly addressed by the fundamental papers and it is based on 3D simulations that make use of the well known MAFIA and HFSS codes. Although the codes are very powerful, some aspects of the design need to be experimentally confirmed. For that reason it has been decided to construct an aluminium prototype suitable for laboratory measurements and flexible enough to allow the experimental characterisation of different options

17.4 References

[1] P.Bernard et al., CERN 68-30, 1968

[2] K.Akai et al., SLAC-0400,1992, p.181

[3] A.Gallo et al., Proc. of the EPAC 2000 conf., p. 465.

[4] C.Biscari et al., Proc. of the EPAC 2000 conf., p. 450.

18. EXTRACTION KICKER

A pulsed kicker is used to extract the bunch train from the Combiner Ring. The flat top duration is slightly longer than the entire CR bunch train length (143 ns) in order to deflect all bunches with the same angle into the extraction septum vacuum chamber. The rise time is shorter than the distance of the kicker from the injection septum (~140 ns) to allow the injection and extraction of the last linac pulse in the same turn.

18.1 Electromagnetic design

The kicker is based on stripline pair design (see Figure 18.1), where each electrode forms with the vacuum pipe a transmission line of $Z_0 = 50\ \Omega$ characteristic impedance.

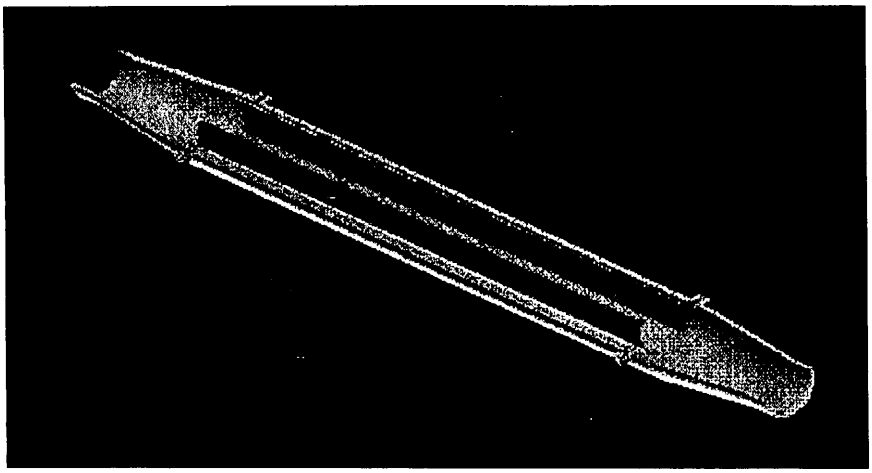

Figure 18.1 Extraction kicker inner structure

Each electrode is 50 cm long. The kicker has been designed using HFSS electromagnetic 3D code [1]. A prototype has been built to measure the efficiency and to study and damp the high order modes trapped in the structure. The stay clear full aperture is 40 mm, and the vacuum chamber diameter in the kicker section is 60 mm. The strip thickness is 1 mm. Tapers at both ends of the structure join the kicker to the adjacent 40 mm diameter beam pipe.

From computer simulations, a 90° stripline coverage angle has been found to correspond to 50 Ω characteristic impedance. The coaxial feedthroughs connect the electrode ends to the power pulser at one end and to the external load on the other end. Two long tapers, joining the kicker vacuum chamber with the rest of the beam pipe, are also needed in order to minimise the losses.

In order to use this device as a transverse kicker, two high voltage pulsers, with voltage of opposite polarity, drive the ports located downstream the beam direction. The combined magnetic and electric field along the axis structure gives a net deflecting Lorentz force in the horizontal plane.

Figure 18.2 shows the electric field in a transverse section with the downstream ports driven in the differential mode (180 degrees out of phase).

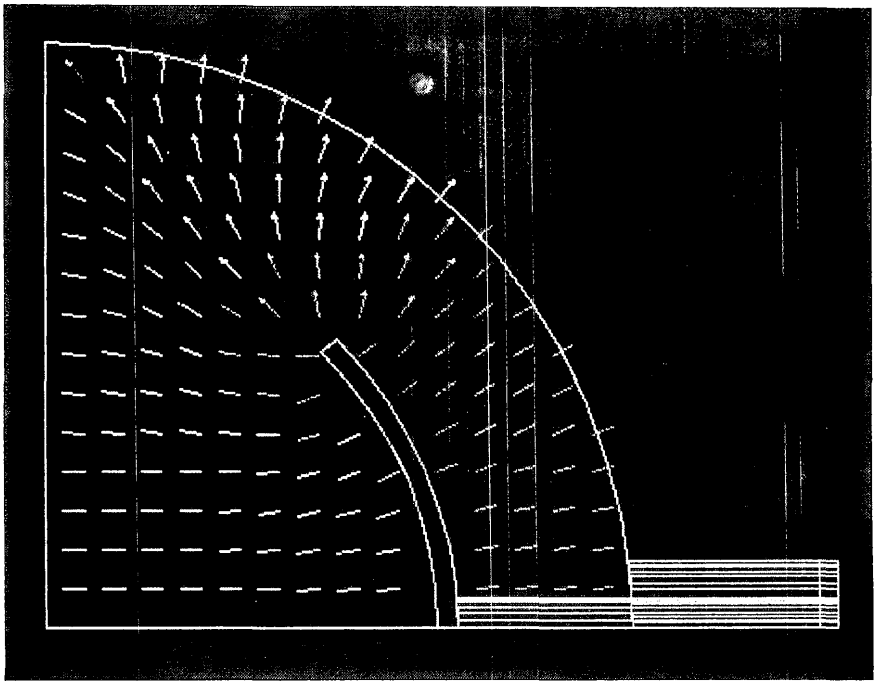

Figure 18.2 E-field distribution on a middle transverse plane in case of differential mode excitation.

Figure 18.3 shows the magnetic field in the same transverse plane: the contributions of the electric and magnetic fields to the deflecting force $F = q\ (E + v \times B)$ add up when the beam and the kicker e.m. wave travel in opposite directions.

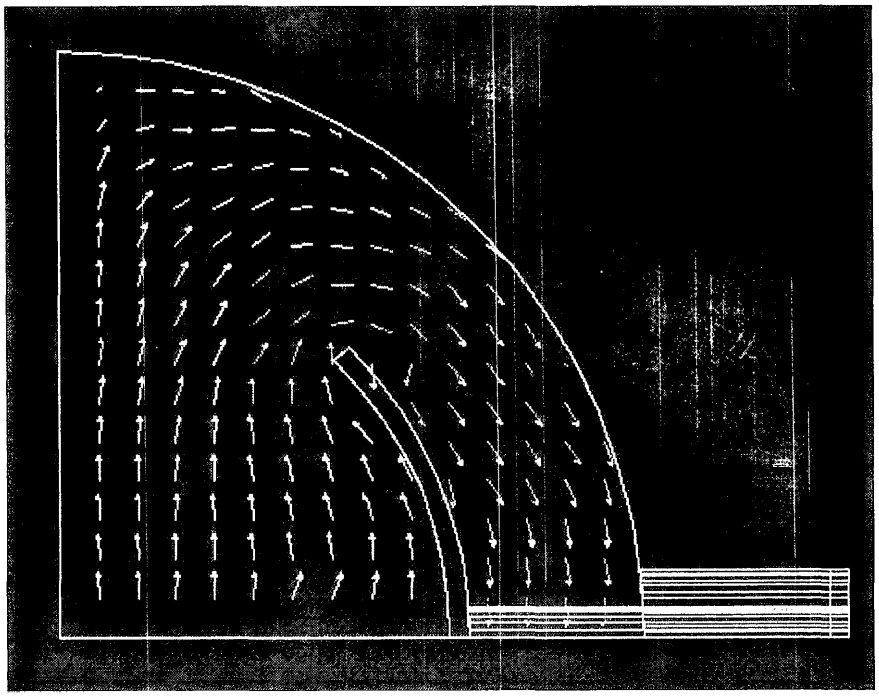

Figure 18.3 B-field distribution on a middle transverse plane in case of differential mode excitation.

If the particle and the wave propagation velocities are equal, from TEM wave theory it turns out that:

$$|E| = |v \times B|$$

so that the transverse force is $F = 2qE$ when the kicker is driven from the downstream ports, while the electric and magnetic deflection forces cancel out if the excitation is applied to the upstream ports.

18.2 Simulations

18.2.1 Strip line characteristic impedance matching

The design parameter has been carried out by means of the HFSS code. In order to optimise the amplifier power transfer to the load, it is necessary to match each strip line to the 50 Ω external transmission lines in the working frequency range. Since the deflecting electrode diameter is equal to that of the straight section stay clear (40 mm), matching has been obtained by enlarging the vacuum chamber diameter to 60 mm in the kicker region and setting the electrode coverage angle to 90^{o}.

The reflection to the amplifier has been also minimised by optimising the position of the transitions from the stripline to the coaxial input/output lines.

Figure 18.4 shows the reflection coefficient (S_{11} parameter) vs. frequency at the input ports: the reflected power is less than 1% of the forward one in the operating bandwidth.

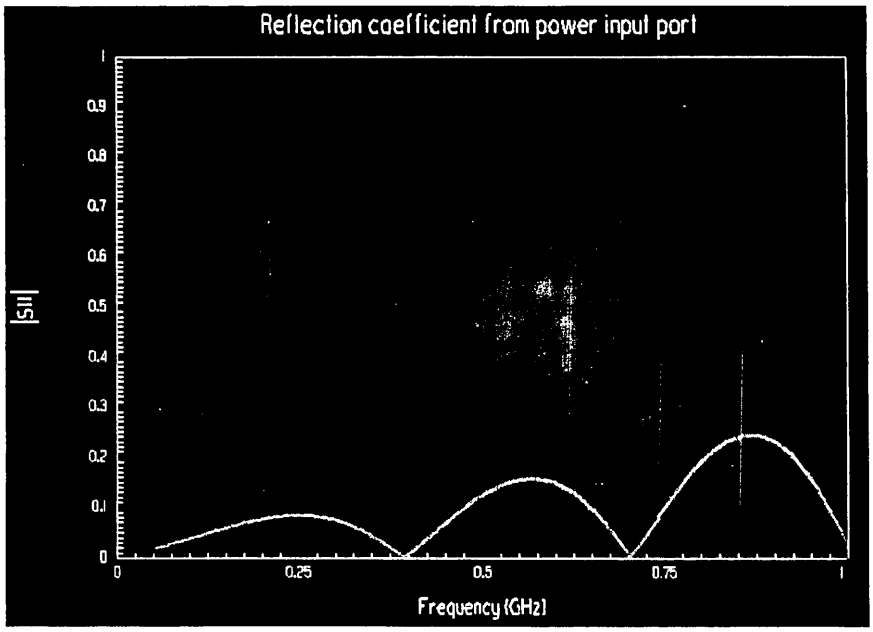

Figure 18.4 Reflection frequency response at the input ports (driven in the differential mode).

18.2.2 Trapped resonant modes

Good matching between striplines and input/output coaxial lines is important not only in the very low working frequency range, but at much higher frequencies too, up to the vacuum chamber cut off. In fact, in case of some mismatching, the e.m. power delivered by the beam on the striplines cannot leave the structure to be dissipated on external loads, and a standing

wave field develops along the electrodes. Figure 18.5 shows the transmission frequency response between the stripline and the connected coaxial line.

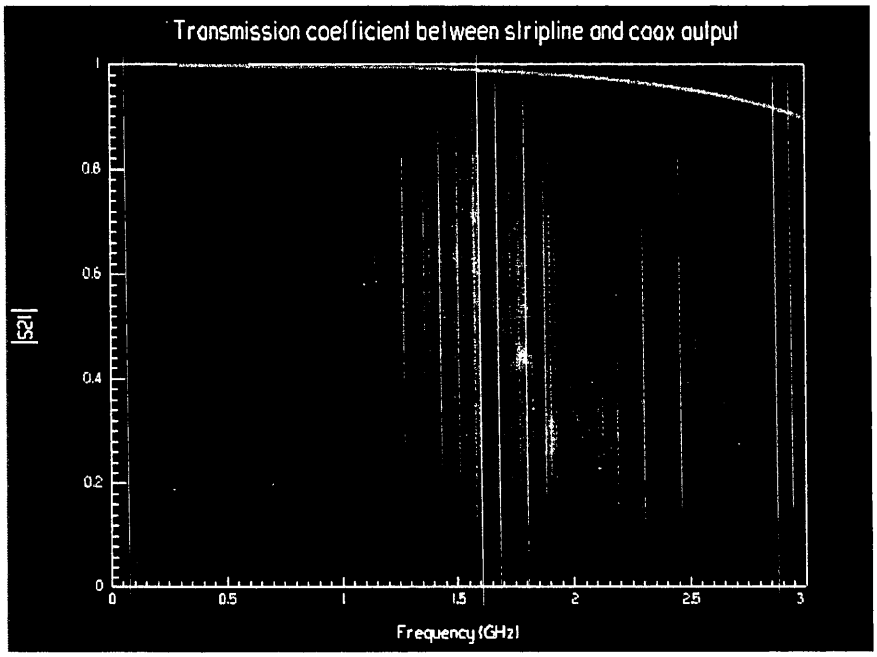

Figure 18.5 Transmission stripline-coaxial line

Moreover some resonances could be trapped in the taper region. In order to damp these modes some coupling device (loop or antenna) will be inserted inside the structure and connected to external loads. A design of these dampers is not yet developed.

18.3 Transverse Shunt Impedance

The kicker efficiency is described by the transverse shunt impedance parameter R_s', defined as the ratio between the square of the transverse voltage $V_\perp$ and twice the forward power P_{fw} at the kicker inputs:

$$R_s' = \frac{V_\perp{}^2}{2P_{fw}}$$

where the transverse voltage $V_\perp$ is defined as the integral of the transverse component of the Lorentz force per unit charge along the beam axis:

$$V_\perp = \int_0^l \left(\overline{E} + v \times \overline{B}\right)_\perp dz$$

For a stripline transverse kicker driven in the differential mode, the transverse shunt impedance can be calculated according to the following formula [2]:

$$R_s' = 2Z_c \left(\frac{g_{trans}}{kh}\right)^2 \sin^2(kl)$$

where Z_C is the characteristic impedance (~50 Ω) of the transmission line having each electrode and the vacuum chamber as inner and outer conductors, g_{trans} is the coverage factor (g_{trans}~1), $k=\omega/c$, h is the stay clear radius (20 mm) and l the electrode length (~50 cm).

The results given by the previous formula can be compared to those obtained from the integration along the kicker axis of the electric and magnetic fields as computed by the simulation code. The agreement between analytical and numerical results is very good and in the working frequency range the kicker shunt impedance is more than 60 kΩ.

18.4 References

[1] Hewlett&Packard Co, "HFSS, The High Frequency Structure Simulator HP85180A™"

[2] Goldberg-Lambertson, "Dynamic Dvices: A Primer on Pickups and Kickers", LBL-31664. ESG-160.

19. BEAM INSTRUMENTATION

19.1 Overview

The beam instrumentation for CTF3 requires special developments due to the quite unusual beam characteristics. The drive beam parameters in different parts of CTF3 are summarised in Table 19.1. The long macro-pulse length of 1.54 μs in the drive beam linac requires a low frequency cut-off ≤ 1 kHz for current and position monitors. But simultaneously a high frequency cut-off ≥ 200 MHz is needed for these devices to observe fast transients in the beam as generated for example by the fast phase switch of the sub-harmonic bunchers or the short fill time of the accelerating structures. The high beam currents suggest monitors of low impedance, to avoid excessive voltages in the acquisition electronics and detrimental wakefield effects on the beam. The desire of a not too large diversity of beam monitors and a coherent instrumentation implies the use of similar instruments in the different parts of the accelerator.

Observation of beam profiles is difficult, because intercepting devices like optical transition radiation (OTR) screens or secondary emission monitors (SEM) can be damaged by the high beam power. Multiple scattering introduced by these intercepting devices can lead to distributed beam losses in downstream parts of the accelerator and subsequent radiation problems.

Table 19.1 Beam parameters at different locations in CTF3

location in drive beam	Beam current (averaged over bunch spacing)	micro bunch repetition frequency	macro pulse length	r.m.s. micro bunch length
gun	7 A	-	1540 ns	-
accelerator	3.5 A	1.5 or 3 GHz	1540 ns	1.5 mm
Combiner Ring extraction	35 A	15 GHz	140 ns	0.4 mm

19.2 Beam current measurement

To get consistent measurements of beam current, pulse charge and transmission in different parts of the machine it is desirable to use the same type of current monitor everywhere. For this purpose we foresee to use wall current monitors (WCM) with a design based on the WCMs which had been developed for CTF2 [1]. These WCMs have demonstrated in CTF2 [2] good and reliable performance for a very wide range of currents (up to beam currents of more than 50 A averaged over one 3 GHz RF period). The high frequency capability of these monitors allows capturing the temporal structure of a current pulse with the highest real time bandwidth available with modern oscilloscopes (≈4 GHz). This permits for example to measure in detail the reaction of the beam to the fast phase switch of the sub-harmonic bunching system. However, a drawback of the present design is the relatively high value of the low frequency cut-off ν_L. Without modifications this leads to a non-acceptable droop of the signal during the pulse. This is in particular true for the drive beam linac, where the pulse length is longest. Increasing the inductance of the WCM lowers ν_L. This is achieved by combining ferrites of microwave absorber type with ferrites of high magnetic permeability, and a moderate increase of the device length (the present CTF2 WCMs use only ferrites of microwave absorber type). We foresee a design with a ν_L of about 100 kHz and an active baseline restoration electronics to compensate for the still considerable signal droop. The raw signal, before baseline restoration, as expected from this WCM for a 1.54 μs long linac pulse is shown in Figure 19.1. The baseline restoration reduces of course the high frequency capability, however, by splitting the signal the baseline restoration circuit can be bypassed for

applications like the fast transient or beam phase measurement. Another important feature of our WCM design is the capability to bake out the monitor up to 200 °C. This allows its use in parts of CTF3 with UHV requirements. The parameters of the wall current monitor are summarised in Table 19.2.

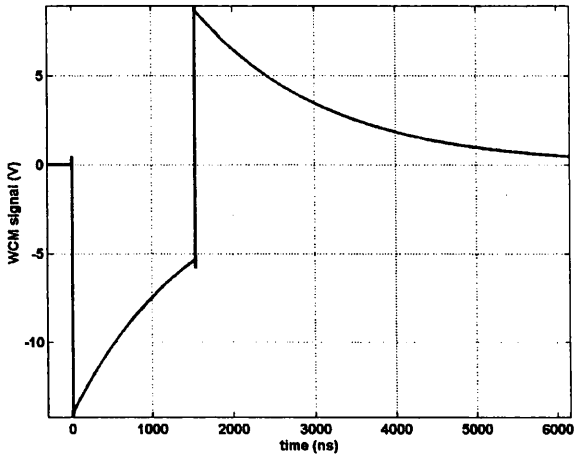

Figure 19.1 Expected raw signal (before baseline restoration) for WCM in CTF3 drive beam linac running with nominal parameters

Table 19.2 Parameters of WCM

impedance	4 Ω
low frequency limit ν_L	0.1 MHz
high frequency limit ν_H	10 GHz
number of feed-through	8
gap length	2 mm
beam aperture diameter	40 mm
length	150 mm
flange type	DN63CF
max. temperature for bake-out	200^0 C

19.3 Transverse beam position measurement

Beam dynamics requires a measurement of transverse position with a precision of ≤ 0.1 mm in CTF3. The short bunch spacing ranging from 20 cm in the linac to 2 cm at Combiner Ring extraction makes the use of strip line or button type beam position monitors (BPM) difficult. The use of RF cavity monitors seems to be inappropriate as well, since their high sensitivity together with high beam currents would lead to excessive signal levels. In consequence, BPMs of the magnetic transformer type have been chosen for CTF3. Their design is a derivative of the BPMs, that had been developed for the LEP pre-injector [3]. To cope with the drive beam linac pulse-length of 1.54 μs the electrical parameters have to be adapted to reduce the low frequency cut-off. The four signals from the BPM are combined in a hybrid to give one sum signal and the horizontal and vertical difference signals. The main parameters of the system are given in Table 19.3.

Table 19.3 Parameters of BPMs

type	A	B
locations	linac, straight sections of Combiner Ring, 30 GHz test stand, dispersion free section of transfer lines	Delay Loop, Combiner Ring arcs, transfer lines, dispersive sections of transfer lines
beam aperture	round ø 40 mm	rectangular 30 x 90 mm
low frequency limit ν_L	25 kHz	
high frequency limit ν_H	150 MHz	
signal (sum at hybrid)	0.15 V/A	

19.4 Data acquisition for WCMs and BPMs

The analogue signals from WCMs and BPMs are sent with cables to the electronics crates for data acquisition. These crates will be located in a utility room next to the control room, thus making selected signals available in the control room for direct observation at full bandwidth. A schematic layout of the data acquisition system is shown in Figure 19.2. This configuration permits to read out all monitors on a single machine pulse. The variable integration gate allows to read either the average position of the beam macro-pulse or the value for a selected time-slice in the pulse. A drawback of this system is that only one of the four turns in the Combiner Rings can be digitised per accelerator pulse. However, a turn to turn readout can be performed by observing the analogue BPM signal with an oscilloscope or an appropriate waveform digitiser.

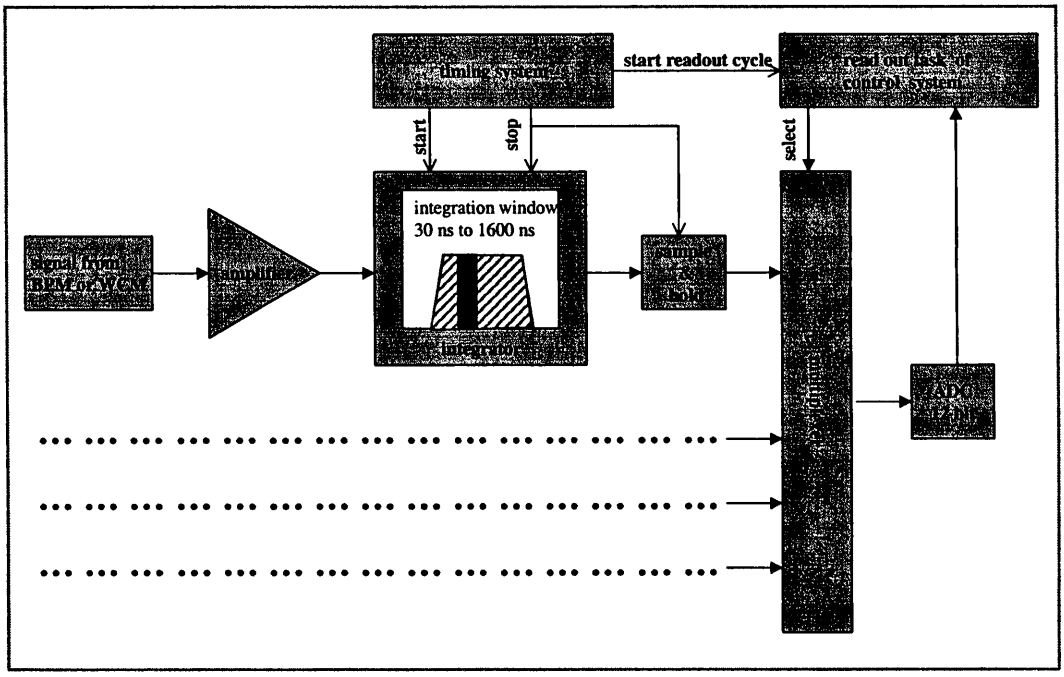

Figure 19.2 Data acquisition for BPM and WCM signals

19.5 Profile monitors

For the measurement of transverse beam profiles three different methods will be used:

- Optical transition radiation (OTR) screens
- Synchrotron radiation (SR) monitors
- Secondary emission strip monitors (SEM)

OTR screens have been already used in CTF1 and CTF2 [4]. In CTF3 they are foreseen for measurements at the end of the drive beam injector and at the end of the linac. However, their use has to be limited to operating conditions with reduced beam pulse-length and/or beam density, since the thermal limits of the OTR screens will be exceeded for the nominal drive beam [5]. Synchrotron radiation from bending magnets is used in the Delay Loop, transfer lines and the Combiner Ring. The light from the OTR screens as well as from SR will be observed with CCD cameras for transverse profiles. Longitudinal micro-bunch profiles and variations along the bunch trains will be done with OTR and SR with two streak cameras, which were used before in CTF2 and LEP. SEM monitors will be used in the magnet spectrometers and the ends of the injector and linac to get pulse by pulse measurements of the beam energy distribution. The vertical beam size on the SEM monitors has to be kept large to avoid excessive heating. R&D is continuing to study the possibilities of using non-interceptive techniques for transverse profile measurements at full intensity.

19.6 Injector instrumentation

The standard monitors as described in sections 19.2 and 19.3 cannot be used in those parts of the injector which are immersed in a solenoid field, because the ferrites used in these devices would disturb the beam focusing. Therefore some special devices are foreseen for the injector. A capacitive pick-up electrode will measure the beam current from the gun. A scintillating screen will be used to detect the beam position and size before entering the 3 GHz pre-buncher. Between the buncher cavity and the accelerating structure a four button BPM with detection electronics tuned to 3 GHz will measure the transverse beam position and the beam RF phase relative to the 3 GHz reference line. The design of this button BPM is very similar to those used in CTF2 using the same vacuum feedthroughs and 1.57 mm ϕ buttons, but the beam aperture diameter is reduced to 34 mm.

19.7 Beam Position Monitor System for Combiner Ring and Delay Loop

For the determination of the trajectory at least 4 beam position monitors (BPM) per betatron wavelenght are generally required. Keeping in mind this constraint, 36 and 24 BPM respectively will be equally distributed with respect to betatron phase advance around the ring circumference in the Combiner Ring (CR) and Delay Loop.

The BPM system must be able to detect the average position of the train of bunches in the single pass mode with a 0.1 mm resolution and a dynamic range that starts with 10% of the nominal beam current. The nominal beam in the CTF3 Combiner Ring is constituted by trains of bunches with a total length of 140 ns performing 1 to 5 turns before extraction, although, in the Initial Phase, a beam (indicated in Table 19.4 with "CR optics") with a different internal time structure, a lower peak current and performing a thousand of turns will be injected to allow measurements of the optical properties of the ring.

Table 19.4 Beam Parameters

	CR optics	CR nominal	
total charge	120	2100	nC
time structure	333ps/3GHz	15GHz/66ps	GHz
number of bunches	90	2100	
Current	4	35	A
train length	30	140	ns
number of trains	1	1	
bunch spacing	10	2	cm
bunch length (σ)	0.5-2.5	0.5-2.5	mm

The measurement of the average position of the whole bunch train can be based on a pickup working in the lower part of the beam power spectrum. To this purpose the use of pickups (UMA) developed for the linac, and resembling the ones installed in the EPA ring, have been taken into consideration [6,7].

This kind of pickup works in the 500 KHz-200 MHz frequency range and offers an appropriate response to the CTF3 beam both from the sensibility and dynamic range point of view as well as a reduced longitudinal size (~9 cm). The proposed pickup is in principle a transformer excited by the beam (representing a single turn primary loop) whose 4 secondary windings, placed symmetrically with respect to the horizontal and vertical planes, surround a ferrite core placed in correspondence of a vacuum chamber ceramic gap.

The ceramic gap, which allows the propagation of the beam electromagnetic field outside the vacuum chamber, represents a discontinuity for the image currents flowing on the beam pipe that can be dangerous to the beam itself. It is possible to reduce the effective coupling impedance presented to the beam by coating the internal side of the ceramic with a conductive film which has a thickness such that only the lower frequency component of the electromagnetic beam spectrum can penetrate to be picked-up by the BPM, the higher frequency component sensing a continuous metal boundary.

The beam current acts as a winding that drives magnetic flux in the core, inducing a voltage signal in the secondary windings whose amplitude is beam position dependent.

Interactions of the beam transformer with external electromagnetic fields are reduced by placing the secondary windings and the ferrite core in a metal shield.

Each monitor provides, using hybrid circuits, the difference signals $\Delta x, \Delta y$ and the sum signal Σ of the pulse induced by the beam on each secondary winding.

For a UMA-like pickup working in the frequency range 500 KHz-200 MHz excited with the CR nominal beam, the typical low pass filtered output reported in Figure 19.3 is obtained (hybrid losses and cable attenuation are not taken into account).

As expected. every detail of the internal time structure of the beam disappeared, allowing only an average position measurement of the position of the bunch train. Beam signals from the pickup are transmitted through independent coaxial cable to the acquisition electronics.

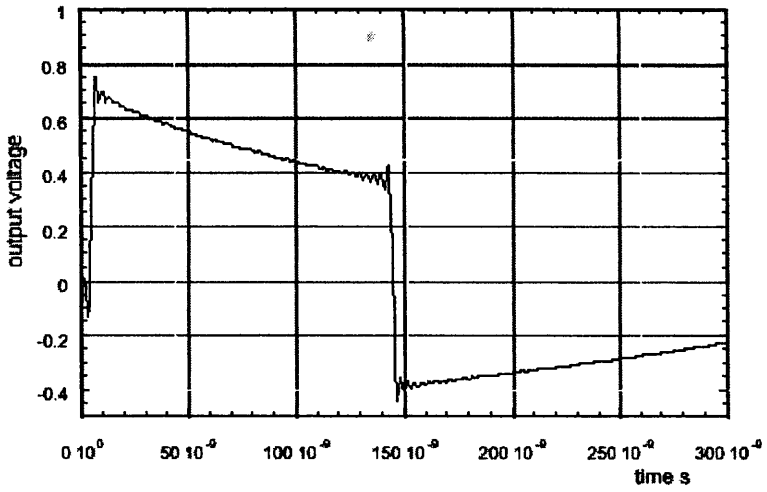

Figure 19.3 Expected response (sum) of the UMA pickup to the CR beam (I_b=1.5A)

Externally triggered digitisers with a minimum sampling rate of 10 Ms/s, 12 bit resolution and analogue bandwidth of 500 MHz are suitable for fast acquisition of the peaks of difference and sum signals for each beam turn in the CR.

Normalisation of the horizontal and vertical signals to the sum signals is achieved by software to get an intensity independent measurement from which the beam position (x,y) can be deduced. To first order and in the vicinity of the axis of the beam pipe, we get:

$$x \cong \frac{1}{S_x}\frac{\Delta x}{\Sigma} \qquad y \cong \frac{1}{S_y}\frac{\Delta y}{\Sigma}$$

where S_x and S_y are the sensitivity, dependent on the electromagnetic pickup and vacuum chamber geometry. For large offset of the beam from the vacuum chamber axis, the previous approximation is no longer valid because of the non-linear response of such monitors. In order to reconstruct accurately the beam position, the acquired data need to be corrected by using a non-linear fitting function.

To this purpose a polynomial fitting function can be used. Implicit fitting functions:

$$x = K_x(x,y)\cdot\frac{\Delta x}{\Sigma} \qquad y = K_y(x,y)\cdot\frac{\Delta y}{\Sigma}$$

or explicit fitting functions:

$$x = P_x\left(\frac{\Delta x}{\Sigma},\frac{\Delta y}{\Sigma}\right) \qquad y = P_y\left(\frac{\Delta x}{\Sigma},\frac{\Delta y}{\Sigma}\right)$$

can be used, where K_x, K_y, P_x, and P_x are polynomial functions whose coefficients are deduced through a bench calibration procedure of the pickup and will be stored in the acquisition system for use during measurements.

19.8 mm-wave spectrometer

A mm-wave spectrometer for the frequency range from 27-90 GHz has been developed for non-intercepting bunch length measurements in CTF2 [8]. This instrument allows spectral analysis of beam induced signals in a waveguide pick-up connected to the beam-pipe. Apart from bunch length this instrument can also determine errors of bunch spacing and bunch intensity [9]. This spectrometer will be used in CTF3 in the Combiner Ring and after bunch

compression. In the Combiner Ring it will allow a continuous monitoring of train build up from turn to turn (see Figure 19.4). Downstream of the bunch compressor it will be used to adjust the bunch length used for 30 GHzpower production with PETS structures.

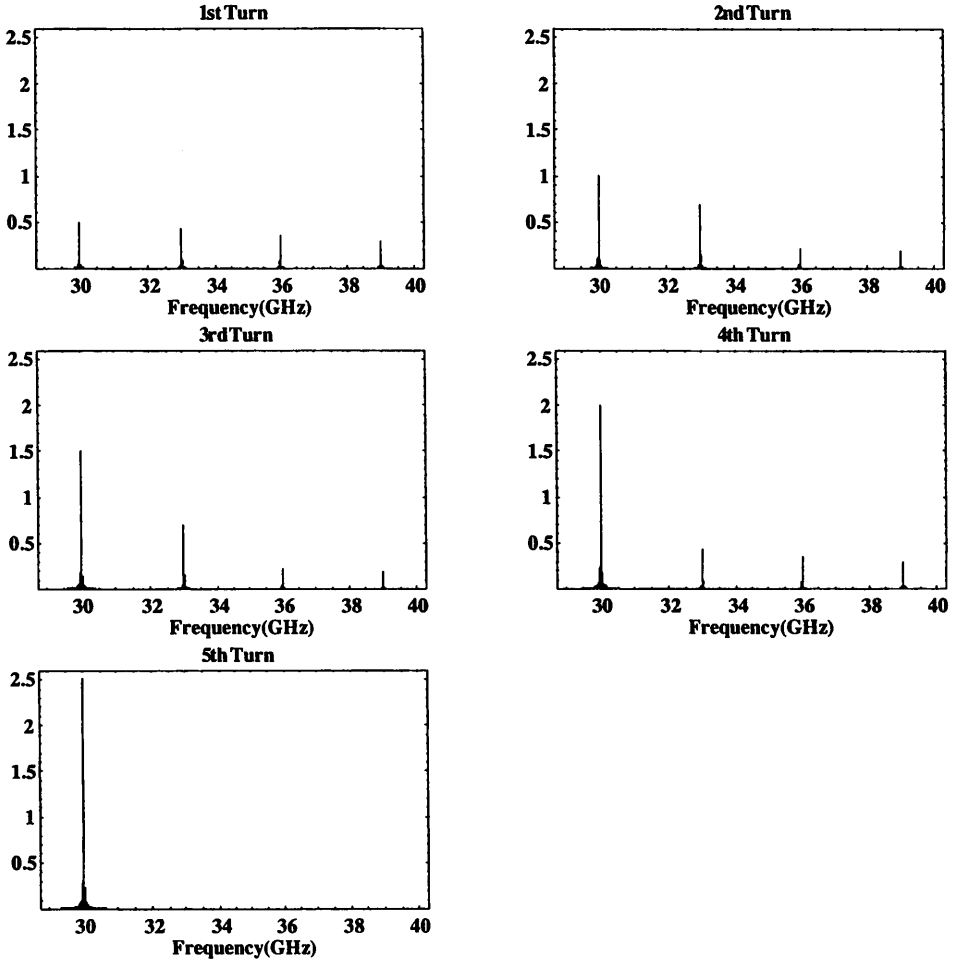

Figure 19.4 Spectra expected from mm-wave monitor in 29-40 GHz window for nominal train build-up in Combiner Ring

19.9 References

[1] J.Durand, T.Tardy, M.Wurgel, "A 10 GHz Wall Current Monitor," PS/LP/Note 95-09 (Tech)

[2] J.Durand, H.H. Braun, "Wall Current Monitors for CTF3," CTF3 Note 14

[3] S.Battisti, M.Le Gras, J.M.Roux, B.Szeless and D.J.Williams, "Magnetic Beam Position Monitors for LEP Pre-Injector," proc. Part. Accel. Conf., Washington, 1987

[4] S.Battisti, "Measurement of the short Bunch-length in the CLIC Test Facility," CERN/PS 93-40 (BD) and CLIC Note 211

[5] E.Bravin, "Thermal Analysis of OTR Screens for CTF3," CTF3 Note 19

[6] S.Battisti et al: "Magnetic Beam Position Monitors for the LEP Pre-Injector"

[7] S.Battisti: "Measure de Position du Faisceau dans EPA", CERN PS/LPI/Note 83-8

[8] C.Martinez, H.H.Braun, "Non-Intercepting Bunch Length Monitor for Picosecond Electron Bunches," proc. of Europ. Part. Acc. Conf., Stockholm, 1998

[9] N.Reurink, "Influence of Bunch Train Errors on mm Wave Spectra," CTF2 Note 99-28

20. PROBE BEAM

The CTF3 probe beam will provide per machine pulse either a single bunch or a train of up to 32 micro-bunches with a bunch spacing of 0.667 ns and a micro-bunch charge of 0.6 nC.

The single bunch mode will allow to:

- Test acceleration in 30 GHz accelerating structures prototypes
- Cross check the calibration of the 30 GHz RF measurement system
- Measure synchronous frequency of accelerating structure prototypes
- Measure higher order mode frequencies of accelerating structure prototypes
- Test CLIC main beam instrumentation prototypes

The multi bunch mode will in addition permit to

- Test the CLIC beam loading compensation scheme
- Test damping of HOM's in accelerating structure prototypes
- Test multibunch properties of CLIC main beam instrumentation

Table 20.1 shows the requirements for the 3 GHz probe beam injector. The bunch charge and spacing correspond to the nominal CLIC main beam values. The number of bunches is a compromise to allow measurements of the transient part of the multi-bunch beam-loading in the CLIC accelerating structures without imposing too severe constraints on the beam loading in the injector and the laser. The beam energy of 190 MeV makes the beam sufficiently rigid to pass a 30 GHz accelerating structure for different accelerating fields without the need of retuning the beam optics. This retuning would be needed at lower energies because of the strong RF focusing field at the entry and the defocusing fields at the exit of these structures. The short bunch length is required for precision measurements of acceleration in the 30 GHz structures. The beam emittance will allow for a beam passage through the 30 GHz structures with at least 4 σ beam clearance.

Table 20.1 Probe beam parameters after pre-acceleration

Bunch charge	0.6 nC
Number of bunches	1-32
Bunch length (r.m.s.)	0.75 ps
Timing jitters relative to drive beam	< 1 ps
Bunch spacing	0.667 ns
Energy	190 MeV
Emittance (r.m.s., norm.)	< 50 π mm mrad
Energy spread (total)	< 4%
Rep. Rate	5 Hz

For the probe beam particle source we have, as for the drive beam injector, two options: a thermionic gun with RF buncher or an RF photo-injector. Since the injector of the probe beam is in many respects less demanding than the one of the drive beam, the final choice for the probe beam will depend on the choice for the drive beam.

20.1 Thermionic gun option

For the thermionic gun option (see Figure 20.1) we will reuse the 90 kV gun and the S-band buncher of the CTF3 Preliminary Phase [1]. However, to produce the required number of

bunches and bunch spacing, the gun pulser will be modified and a 1.5 GHz sub harmonic (SHB) buncher will be added. Since this SHB does not need the fast phase switching of the drive beam SHBs, the Q can be high and the required 200 W of 1.5 GHz power can be supplied by a solid-state amplifier.

Acceleration to 190 MeV will be done with two of the existing 4.5 m long LIL accelerating structures running at a mean accelerating field of 20.5 MV/m. Since the required bunch length cannot be produced directly by the bunching system, a bunch compressor chicane will be used in between these two structures.

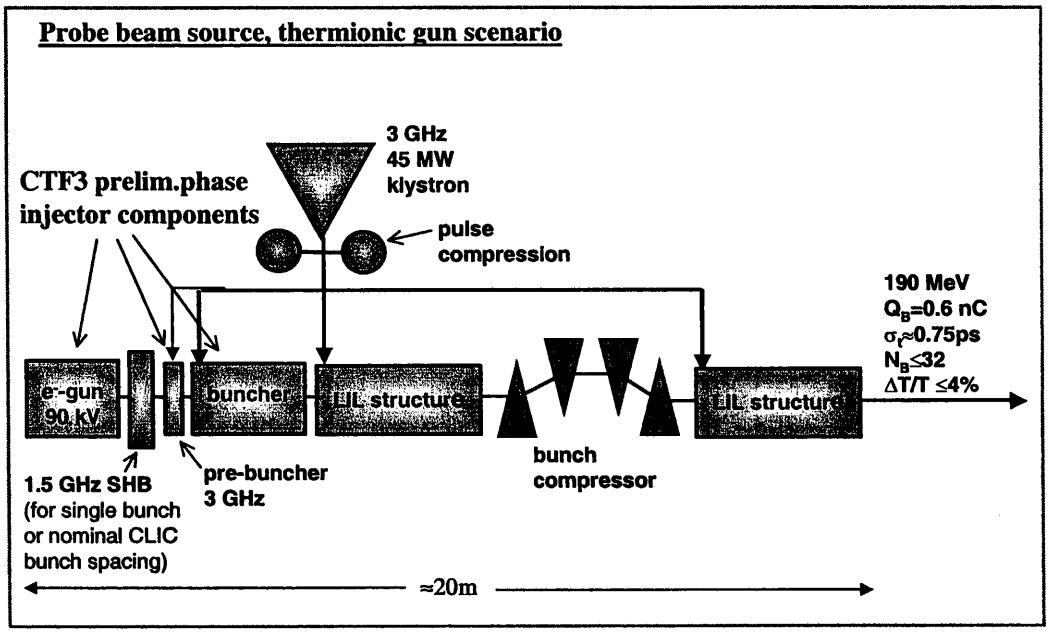

Figure 20.1 Layout of probe beam injector / thermionic gun version

20.2 RF Photo injector option

For the photo-injector, shown in Figure 20.2, the existing 1½ cell RF gun of the CTF2 probe beam together with its cathode preparation chamber can be used [2]. The laser system is based on the same all diode pumped technology as for the drive beam photo injector. However, due the much lower bunch charge and bunch number the probe beam laser system is considerably less demanding. Acceleration to 190 MeV will be done in the same way as for the thermionic option, with two of the existing 4.5 m long LIL accelerating structures and a bunch compressor chicane between these two structures. With a more sophisticated design of the RF gun a considerably smaller emittance than quoted in Table 20.1 could be obtained. Such a small emittance would be particular useful for CLIC beam diagnostic developments.

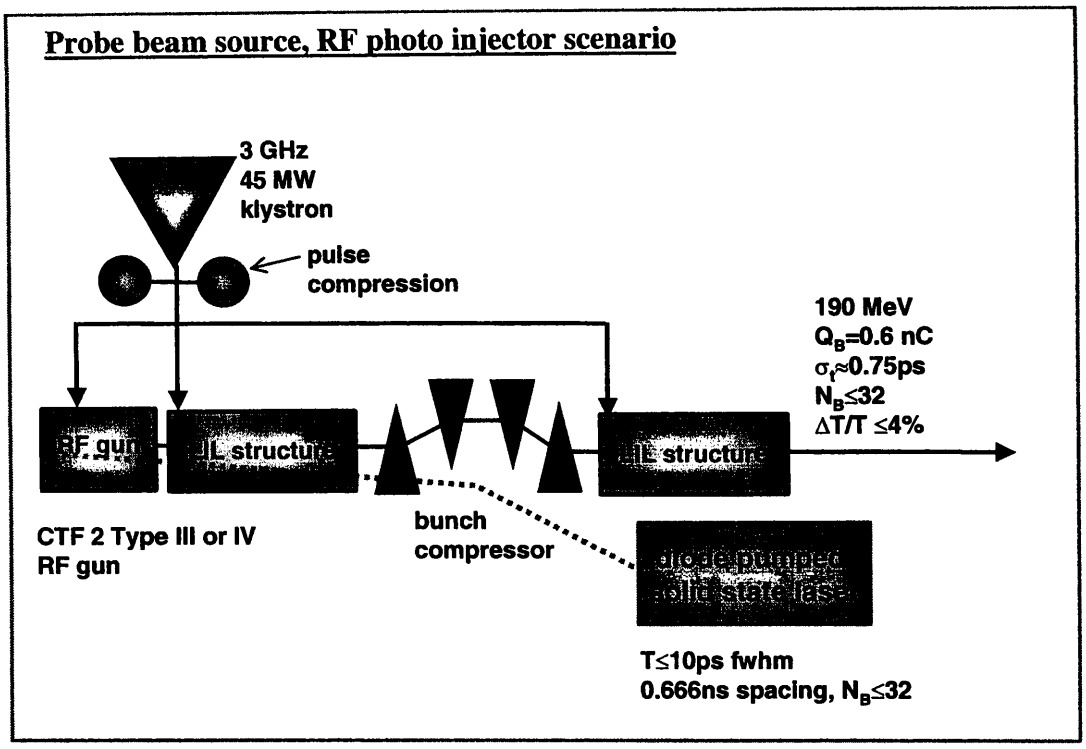

Figure 20.2 Layout of probe beam injector / RF gun version

20.3 References

[1] "CTF3 Design Report, Preliminary Phase," CERN/PS 2001-072 (RF) and CTF3-Note 039, 2001

[2] "CTF2 design report, a two-beam test accelerator for linear collider studies," CLIC-Note 304, 1996

21. 30 GHZ POWER PRODUCTION AND TESTING IN CTF3

21.1 Introduction

In addition to its role in demonstrating the feasibility of the drive beam generation scheme, CTF3 will be an important source of intense bunched electron beams and 30 GHz power for the development and testing of drive and main linac components. CLIC design parameters [1] specify that components must operate at very high powers and fields (above 250 MW and 170 MV/m accelerating gradient respectively) for pulse lengths of 130 ns. A high-power 30 GHz testing program at CTF3 is planned, where such powers and fields are produced using the CTF3 beam in special test stands. The test stands in their standard configuration will consist of a transfer structure, which powers a single accelerating structure.

The high power tests and experiments made in the CTF3 test stands will be an integral part of the CLIC main and drive linac structure design process, an opportunity to develop new ideas, materials and processes to achieve high gradients and an opportunity to gain insight into the physical processes involved in breakdown. RF processing and lifetime tests are however probably not feasible due to the relatively low, 5 to 25 Hz, repetition rate of CTF3. The design of the test stands and their experimental programs draw heavily on similar work in CTF1 and CTF2 [2].

The structures to be studied in the test stands include transfer structures, accelerating structures and waveguide components. A number of distinct types of tests will be made:

- Direct high-power test of transfer structures powered by beam.
- High-power tests of accelerating structures, specialised cavity and waveguide components with 30 GHz power generated in a transfer structure.
- High-power beam-driven tests of specialised cavities.

The majority of these tests will be made in the *'main test stand'* which is fed by the beam exiting the combining ring and final bunch length compressor and is located in the new hall which will be constructed next to the existing LIL building. In addition a second, simplified, *'end of linac test stand'* will be constructed in the EPA building. This test stand will be fed directly by the beam exiting the drive linac, so that testing can begin as soon as the first high power beams become available. The test stand areas will be shielded from radiation generated in the rest of CTF3 in order allow preparation of experiments while other CTF3 work is ongoing.

The main test stand is designed to produce power levels of the order of 300 MW to allow testing of CLIC components above design values. The end of linac test stand will only be able to deliver power of up to about 50 MW at the accelerating structure input, but nonetheless a rich program of testing of special structures, standing wave and small aperture travelling wave, of materials and of processing is possible. Testing with very long pulse lengths can also be made. Finally, experiments on the frequency dependence of breakdown are possible. Since the driving beam has a bunch repetition frequency of 3 GHz, it has large Fourier components at harmonics of 3 GHz limited ultimately only by the bunch length. The power associated with the harmonics can be exploited with a series of scaled structures.

The test stands will be equipped with magnets to focus the drive beam through installed power-generating structures and with diagnostics for RF conditioning and breakdown experiments. The main test stand will also be equipped with a low charge drive beam to verify achieved field levels and to make specialised RF/beam interaction measurements. The control system of CTF3 will accept input from the test stand so that, for example, automated conditioning of structures can be implemented.

21.2 RF power generation

The starting point for the design of a high power test stand is the structure, which is used to extract energy from the driving beam in the form of RF power. In order to produce a desired power, the impedance of the structure must be adapted to the current of the driving beam. Ignoring losses, the relation between RF power P, beam current I and decelerating voltage V is,

$$P = IV$$

The nominal beam current exiting the Combiner Ring and final bunch compressor is 35 A while the Drive Beam Accelerator linac will produce a current of 5 A (a special mode of operation is envisaged for operation above the normal 3.5 A). Thus more than 8.5 MeV of deceleration are required to produce 300 MW in the main test stand and more than 10 MeV are required to produce 50 MW in the end of linac test stand. The relation of output power and driving current expressed as a function of the beam and RF structure parameters is [3,4],

$$P = \frac{\omega(R'/Q)}{4}\frac{I^2 l^2}{v_g}\alpha^2$$

R'/Q=shunt impedance(linac convention)
ω=RF frequency,
l=structure length
v_g=group velocity

α^2 is the power form factor due to bunch length - a value of 0.95 is assumed in the discussion, which follows. RF losses have not been included in order to simplify the discussion. Real structures will have to compensate for losses with some combination of increased R'/Q and l and decreased v_g - and also with an increased voltage drop of the driving beam. A survey of possible candidate transfer structures for both the main and end of linac test stands are presented in section 21.4.

In addition to providing the desired power level, the structures must also have an aperture sufficient to accept the beam and have low enough transverse wakefields to allow transmission of the drive beam. Finally surface electric fields inside the structure must be limited to values well below those in the structure being high power tested. Currently a factor of two is being used as a design criterion. Recirculation of RF power can reduce the effect of these limits.

It should be noted that a pulse compression system would give a substantial and desired relaxation of power generating structure design criteria. A shift of 5 mm of bunch position during the drive train would however be required.

21.3 Test Stand Layout

The test stand consists of hardware associated with the electron beams and hardware associated with the RF structures. In the case of the main test stand, it also consists of hardware associated with the power generating beam and hardware associated with the probe beam. The layout of the main test stand is shown in Figure 21.1. The layout of the end of linac test stand is the same except that there will not be a probe beam. A short description of some of the main elements follows below:

- The focusing magnets to create a waist in the beam for transmission through the structures under test and for continued transmission downstream of the structure.
- Wall current monitors will allow both optimisation of transmission and observation of currents produced in structures during high power operation (dark currents and breakdown currents).

- A streak camera with beam profile screens before and after the structures under test is used to optimise transmission and to observe, for example, the effects of transverse wakefields on the beam.
- Steering magnet pairs to allow independent displacement and angular sweep of the beam through the structures under test.
- The beam position monitors before and after the structures are used to steer the beam through the structures. The beam position monitors must be mechanically referenced to the structures under test.
- Spectrometer magnets are used to measure beam energy before and after the structures under test. The beam lines through which the beam passes when the spectrometer is powered end in beam dumps. The spectrometers will also be used to measure the dark current energy spectrum.
- RF structures include transfer structures, accelerating structures, standing wave cavities and beam position monitors.
- A multi-frequency receiver system will allow fast (sub ns resolution) shot-by-shot capture of RF signals produced in the structures. This includes for example both high power signals and transverse mode excitations.
- An on-line low-power RF system will provide a measurement of attenuation and phase shift across the structure to diagnose damage of structures.
- Light generated in structures during high power operation will be imaged and also measured for spectrum and time response.
- An extensive system of vacuum pumping and detection will be installed around the test stand area. The vacuum of the test are must be easily separated from the rest of the machine in order to allow fast replacement and bake out of structures under test.

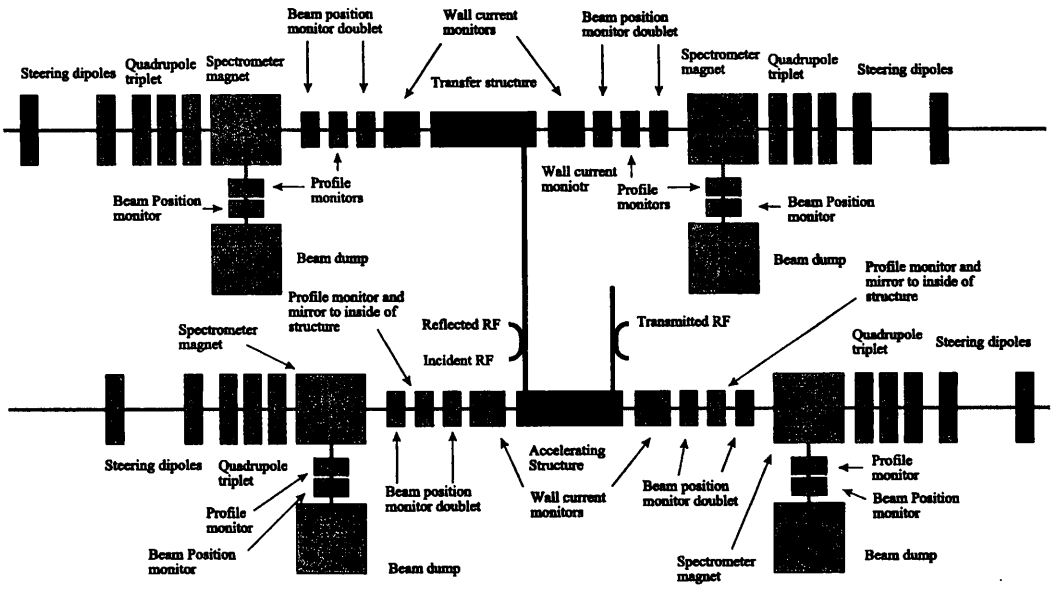

Figure 21.1.: Layout of Main Test Stand

21.4 30 GHz Power extraction Structures

21.4.1 Transfer Structures (PETS) for 30 GHz power production in CTF3

The geometry of the four-waveguide PETS [5] envisaged for CLIC is shown in Figure 21.2. It has a beam aperture diameter 24 mm and main RF parameters of R'/Q= 52 Ω/m (circuit convention) and β_g = 0.40 normalised group velocity of $2\pi/3$ mode. Used in the main test stand, it would deliver 47 MW power, neglecting losses (about 15%). It clearly has too low an impedance for high power generation in CTF3.

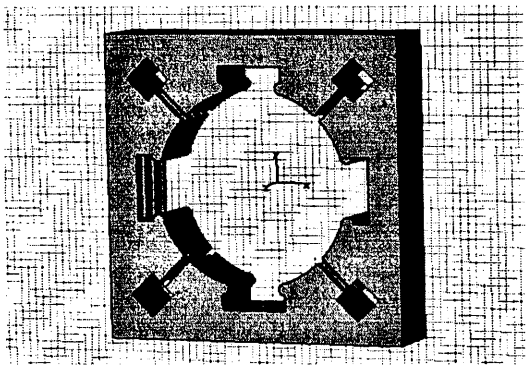

Figure 21.2 Waveguide PETS, 3 cells simulation

The four waveguide PETS that has been used for power production in CTF2 is shown in Figure 21.3. It has an aperture of 15 mm, an R'/Q= 540 Ω/m (circuit convention) and a length of 1.0 m. It would produce 370 MW power with a 35 A beam current (neglecting losses). This structure has been built and tested in CTF2 where it has produced power up to 270 MW/m for a pulse length of 16 ns.

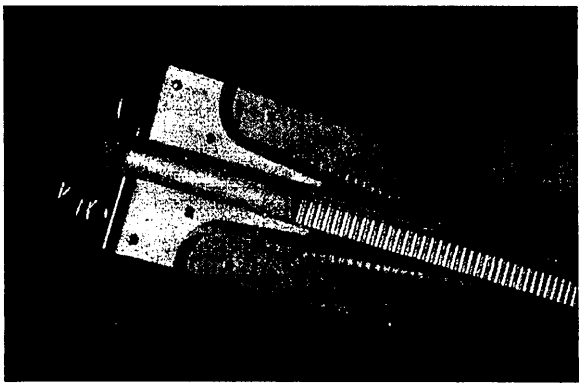

Figure 21.3 Open section of 15 mm aperture PETS

For the end of linac test stand, the impedance of the PETS must be increased further by reducing the beam aperture. For the four-waveguide geometry, the lower aperture limit is about 10 mm because of the width of the waveguides. A structure with this aperture would have an R'/Q= 1763 Ω/m (circuit) and β_g = 0.46. For 1.0 m length it would produce 28 MW power for 5 A beam current with the same assumptions as above. This type of structure can be built using the same construction and assembly methods as the existing four-waveguide 15 mm aperture PETS.

21.4.2 Cylindrical PETS with reduced aperture.

A higher impedance for the same beam aperture is possible using a circularly symmetric geometry. Such a structure with beam aperture diameter 10 mm has the following RF parameters: R'/Q = 2190 Ω/m (circuit) and β_g=0.46 . It would give 35 MW in the end of linac test stand. The output couplers are of a novel design and are shown in Figure 21.4.

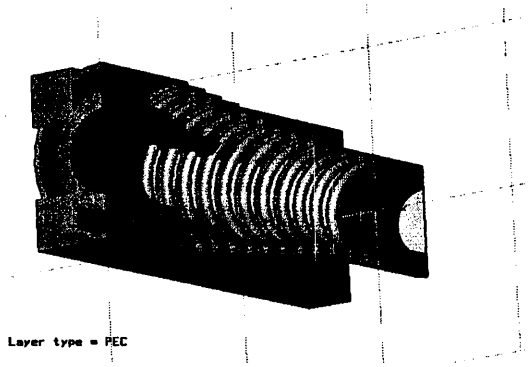

Figure 21.4 Cylindrical PETS output coupler simulation

It is of course possible to further increase the normalised impedance of the cylindrical structure by reducing its aperture below 10 mm, however the problem of beam stability must be addressed before proposing this solution.

21.4.3 Possible configuration of the 30 GHz PETS for the end of linac test stand

In order to achieve a sufficiently high impedance, small aperture, low group velocitiy and high R'/Q values are required, leading to high surface fields in the end of linac test stand PETS.

Using the fact that along the structure the power flow is highest at the downstream end, we can alleviate these extreme surface fields through tapering: a low group velocity at the beginning and a high group velocity at the end (Tapered-Out Structure).

For the structure geometry this simply means an aperture increase between the beginning and the end. Moreover such an approach could be useful from the beam dynamics point of view; the structure aperture would in principle follow the beam envelope increase caused by deceleration.

Simulation results are shown in Figure 21.5 and Figure 21.6. The parameters are given in Table 21.1.

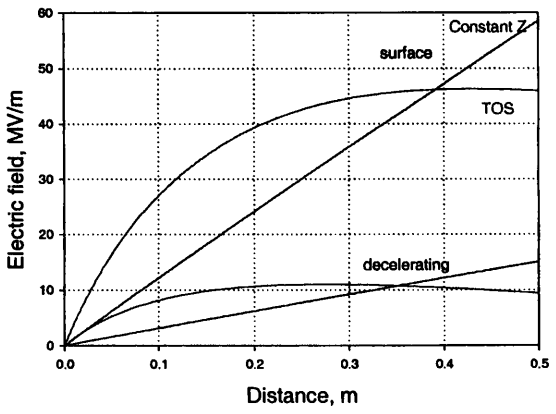

Figure 21.5 Comparison for the 0.5 m structure and 3.5 A current.

Table 21.1 Comparison TOS/Constant Z PETS for 0.5 m structure length.

	Aperture, mm	β_g, %c	Max. surf. field, MV/m	Power, MW
Constant Z	7.5	31.5	58.5	12.54
TOS	5->10	15-48	46.0	14.87

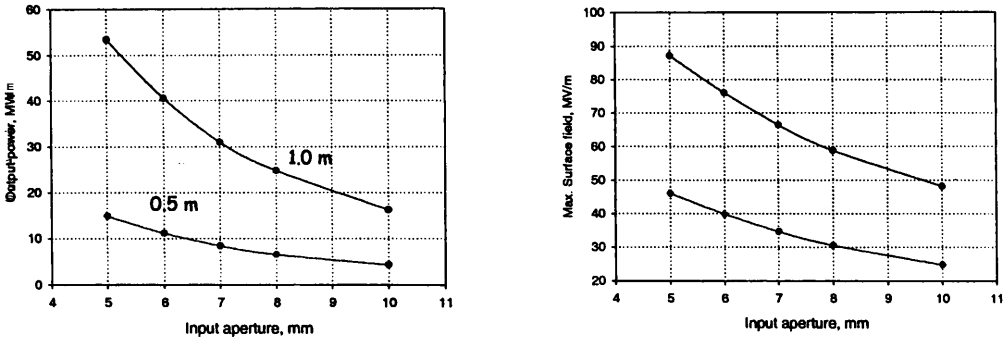

Figure 21.6 The RF power production and electric surface field in TOS with 3.5 A current vs. input aperture (the TOS output aperture is 10 mm.).

21.5 References

[1] R.W.Assmann, et. al., "A 3 TeV e^+e^- Linear Collider Based on CLIC Technology", CERN Publication CERN 2000 – 008, July 28.

[2] H.H. Braun et. al., Status of CLIC High-Gradient Studies, CLIC note 489, CERN/PS2001-045, PAC 2001

[3] W.Wuensch, I.Wilson, Beam Loading Voltage Profile of an Accelerating Section with a Linearly Varying Group Velocity, CLIC note 399.

[4] A.Millich, L.Thorndahl, 'PETS Output Power and Drive Beam Deceleration for finite Q-Value and Tune Errors' CLIC Note 407, July 1999.

[5] G.Carron, A.Millich, L.Thorndahl 'The 30 GHz Transfer Structure for the CLIC Study', ICAP98 Monterey, September 1998 and CLIC Note 365,

22. TIMING

22.1 INTRODUCTION

For reasons of klystron output stability, CTF3 must be synchronised to the zero-crossings of the 50 Hz network. In fact, for RF synchronisation, timing signals must be referenced from the nearest tick after the network zero-crossing of a clock derived from the RF. For the Preliminary Phase [1], this clock will either be the EPA 19 MHz or a 19.2 MHz signal derived from the LIL frequency. The former will be used for accumulation and the latter for the combination test. For the later phases of CTF3, only the 3 GHz-derived clock will be required (unless the Combiner Ring contains a RF cavity for beam storage).

In the present proposal, the central timing system will also be synchronised to the 50 Hz network zero-crossings. This is in contrast to the rest of CERN's central timing, which is synchronised to the GPS network. CTF3 will therefore require an independent Master Timing Generator (MTG) [2,3]. Synchronisation with the electric power grid will both simplify and enhance the performance of the central timing and, consequently, the CTF3 control system.

Timing pulses (for modulators, klystrons etc.) will be provided by the counters incorporated in the CERN standard Tg8 timing modules [2,3]. These will provide the majority of the timing signals. However, for more precise timing, an ECL system running at higher frequency is being developed.

22.2 RF SYNCHRONISATION

A block diagram of the proposed RF synchronisation scheme is shown in Figure 22.1. The master source will be a 3 GHz synthesiser and all other frequencies will be produced by division and, for the 4.5 GHz (if required), by multiplication. The 250 MHz will be used as a clock for ECL precision delay counters (Chapter 22.4). The 19.2 MHz will clock the Tg8 modules of the central timing system as described in Section 22.3.

To ensure good phase stability, the RF synchronisation equipment will have to be located in temperature controlled racks.

22.3 CENTRAL TIMING

22.3.1 Shortcomings of present system

There are several reasons why the LIL/EPA timing architecture is not suitable for CTF3. They arise because of the different operational constraints, the age of the present equipment and the need for a more versatile timing system for a test accelerator that will constantly evolve.

As LPI injected into the PS, there is, at present, a dependency on the PS timing composed of the 1.2 s basic period and the 1 kHz C-Train clock, both of which are derived from a very stable GPS-piloted clock. This greatly complicates and limits the control of a machine that must also be synchronised to the 100 Hz network zero-crossings (the NZC signal). For example, the present production/dummy selection scheme is very rigid and there is no possibility to use the machine timing system to tag zero-crossings for, say, beam measurements. In addition, most of the hardware is composed of obsolete CAMAC modules.

For the start of CTF3 Preliminary Phase, the existing LIL/EPA system will be used with the addition of special modules for gun and streak camera timing [1]. However, during the 2001/2002 shutdown, the entire central timing will be replaced by a more powerful system that will permit operation of CTF3 then and in future phases of the project.

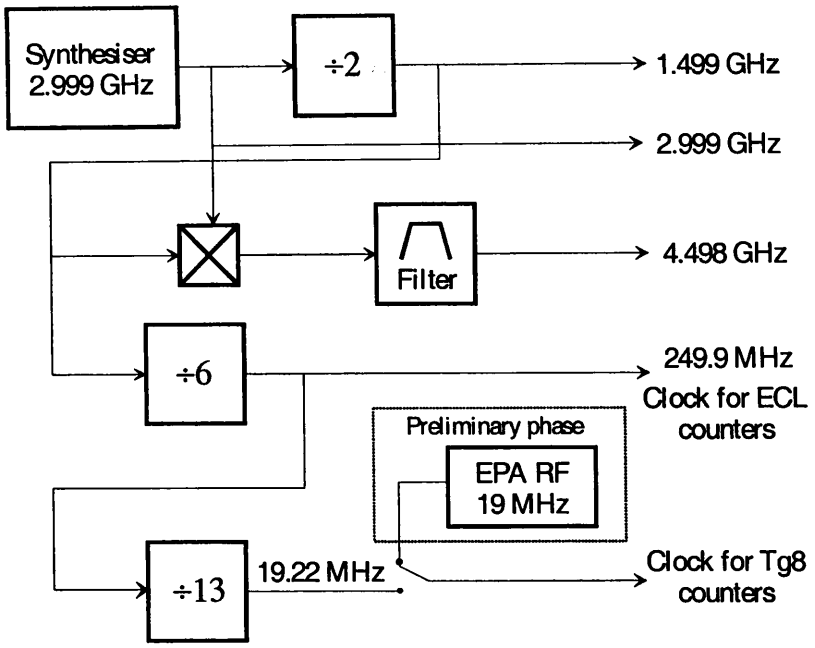

Figure 22.1.: Proposed frequency generation scheme for CTF3.

22.3.2 Proposal for new timing system

At the core of this proposal is the need to reconcile the requirements for a machine synchronised to the 50 Hz network with the wish to exploit existing PS investments in the 1.2 s cycling and pulse to pulse modulation mechanism (PPM, [2]).

The CTF3 central timing will be completely de-coupled from the PS. It will have its own MTG piloted from a 1 kHz clock (termed CTF-C-Train) synchronised to the 100 Hz network zero-crossings. A 1.2 s Basic Period (CTF-BP, 120 zero-crossings) will be derived from this clock. The control system PPM will run at 1.2 s and 100 Hz. Two CTF3 telegrams will be defined and sent over the MTG cable to the Tg8 timing modules, a fast CTF3 telegram (FCT) running at 10 ms and a slow one (SCT) running at 1.2 s.

The SCT will contain USER values organising a collection of 120 NZC periods into operational modes. Simple examples could be called "5 Hz", "10 Hz", others could pulse different groups of equipment at different frequencies. CTF3 could be run with an endless repetition of a USER or with more than one USER where there is some operational structure needed in the timing. USERS are places where acquisition values could be stored in the equipment module data tables, they could be used by application programs on work stations to select acquisition values, and they would remove the need for applications to remain synchronous with the much faster NZC period by grouping data. Most standard applications controlling power supplies, reading instruments, providing displays and accessing equipment modules will be PPM on SCT USER, and this will allow a huge amount of standard software to be used directly, without any modifications. The FCT telegram will contain only information which may change every NZC period, and will control the selection of production, dummy or null timings, the choice of EPA bucket to be filled, and the NZC period number.

A block diagram of the proposed hardware is given in Figure 22.2. It is applicable to the Preliminary Phase where accumulation is required. If, later, this is no longer required, it could be simplified. The timing event Start RUN is for initialising the system. A chain of three standard Tg8 modules is used to generate the signal General Start. The first of the three generates the revolution frequency from the RF clock. The second, clocked by the revolution frequency and started by each 100 Hz zero-crossing, produces an output 1.5 ms before the

next zero-crossing. The third delays this pulse between 0 and 7 RF periods to allow filling of the desired bucket. The first and last of these modules are only useful in accumulation mode. The General Start is used to start all Tg8 counters controlling individual pieces of equipment (klystrons, modulators etc.). They cover the range from 1.5 ms before to 1.5 ms after the network zero-crossing. Each one is followed by a fine delay module that increases the delay resolution to 1/256th of a clock period. Two Tg8's are used with an internal clock to produce the 1 kHz CTF-C-TRAIN. Although this results in 0.5 μs jitter between NZC and the timing events, it ensures that the central timing does not stop if there is a fault with the RF reference. The CTF-BP is produced by division of the CTF-C-TRAIN.

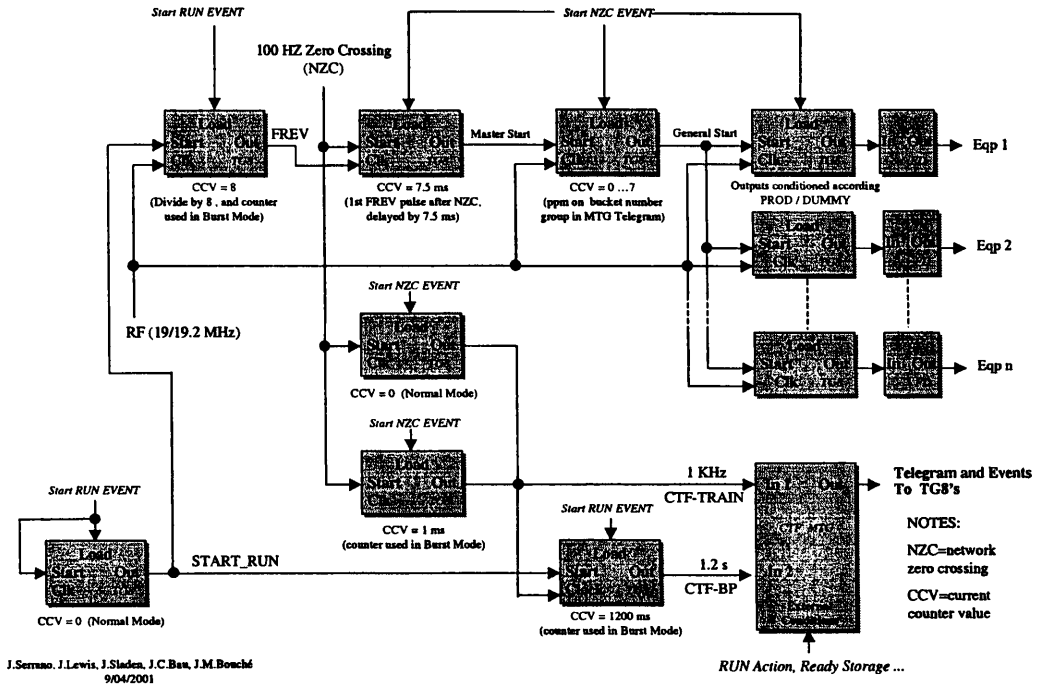

Figure 22.2.: Proposal for central timing for CTF3.

22.4 ECL COUNTERS

The combination of the Tg8 counter and fine delay unit described above have an output jitter in the order of 1 ns. For equipment requiring a more precise trigger, a 250 MHz ECL system is being developed. It will consist of 24 bit counters followed by a vernier delay covering the 2 ns clock period in 20 ps steps. Short term stability, which can only be measured after a prototype is completed, is expected to be in the ps range. For applications requiring very good long term stability, the counter chassis will need to be housed in a temperature controlled environment.

Each of these counters will receive its start from a corresponding Tg8 counter. The trigger rate (5 Hz, 10 Hz etc) of each individual ECL counter is therefore controlled in the standard way by the central timing. The delay setting will be via a parallel interface to the control system.

22.5 REFERENCES

[1] CTF3 Preliminary Phase design report.

[2] J.Lewis, V. Sikolenko, "The new CERN PS timing system", ICALEPCS93 conference, 1993.

[3] J.C.Bau, G.Daems, J.Lewis, J.Philippe, "Managing the Real-time Behaviour of a Particle Beam Factory: The CERN Proton Synchrotron Complex and its Timing System Principles", RT97 conference, 1997.

23. MAGNETS

23.1 Beam path length in short bending magnets

The dipoles of the EPA damping ring (combined functions) and its transfer lines (pure dipoles) will be used for the Combiner Ring, the Delay Loop and the transfer lines of CTF3. Magnetic measurements have been performed on both kinds of dipoles [1,2] at field values corresponding to beam energy in EPA above 500 MeV. Recently, the EPA dipole has been measured again [3] in a wider field range, down to 200 MeV.

The beam trajectory inside bending magnets where the gap height is a non negligible fraction of the magnetic length, namely where the fringe field extension is of the same order as+ the magnetic length, tends to deviate from the "nominal" trajectory in the rectangular model where the particles follow a straight line, a circular arc of fixed radius and a straight line again. The typical effect is to bend the particles towards the inside of the ring before the edge of the magnet in such a way that the total length of the trajectory is shorter than the nominal one. This effect should be taken into account in both the combiner and Delay Loop layouts, where the orbit length is a crucial item.

The trajectory followed by the particles in the dipole can be easily calculated with a simple integration of the equations of motion by interpolating the vertical component of the field measured on a mesh in the horizontal symmetry plane of the magnet. Given a measured field map, the energy of the particle is used as a free parameter to match the nominal bending angle. This procedure has been used to adjust the thickness of the removable end caps in the DAΦNE damping ring dipoles to reach a good compromise between peak field and beam position inside the good field region. The knowledge of the beam trajectory length inside the dipoles was also crucial for the synchronisation with the DAΦNE Main Rings [4].

A preliminary estimate of the path length has been performed for the EPA dipole by using the data presented in [3], where the field was measured on the magnet axis and along two lines parallel to it at a distance of ± 50 mm spanning in the longitudinal direction from -475 mm to -175 mm from the magnet centre. The field has been interpolated linearly in both the horizontal and longitudinal directions and assumed constant and equal to the values at -175 mm from this point to the magnet centre. Figure 23.1 shows the distance in the horizontal plane between the path followed by the particles and the nominal trajectory in half a dipole (the other half is symmetric). The calculation has been performed for the nominal EPA dipole bending angle of 22.5° (16 magnets) and for the same dipole used in the CTF3 Combiner Ring, where the deflection is 30° (12 magnets). The beam energy matching the nominal bending angle with the measured field map comes out to be 397.1 MeV in the case of EPA and 298.8 MeV in the case of the Combiner Ring. In the first case the orbit shortens by 5.5 mm in the whole ring, in the second one by 7.7 mm.

This effect is much larger than the foreseen tuning range of 1 mm provided by the wiggler, and therefore must be taken into account in the design of the ring layout. Being the preliminary estimate based on rather rough approximations to the field, a new set of measurements at the field foreseen for the Combiner Ring would be useful for a more reliable calculation. The same should be done for the dipoles foreseen for the Delay Loop. An additional benefit from these measurements would be the estimate of the sextupole terms at the correct field.

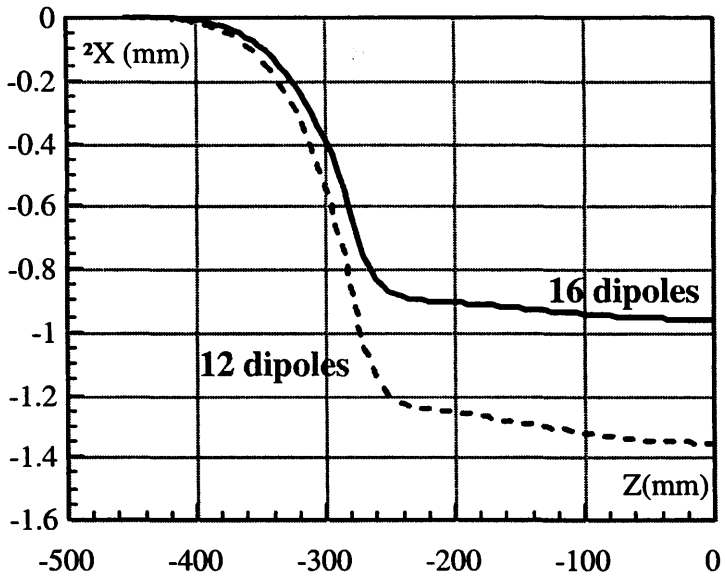

Figure 23.1 Distance between the path followed by the beam and the nominal trajectory in half EPA type dipole (full line = 22.5° bending angle, dotted line = 30°).

23.2 Reference

[1] G.Suberlucq, M.Tardy, "Mesures magnetiques des dipoles EPA type I" - PS/PSR/Note 86-6, 30/5/1986.

[2] G.Suberlucq, M.Tardy, "Mesures magnetiques des dipoles EPA type II" - PS/PSR/Note 85-7, 24/6/1985.

[3] R.Chritin, "Mesures magnetiques complementaires de l'aimant principal prototype EPA" - SL-Note-2000-031 MS.

[4] A.Battisti, B.Bolli, F.Iungo, F.Losciale, M.Paris, M.Preger, C.Sanelli, F.Sardone, F.Sgamma, M.Troiani, S.Vescovi, "Measurement and tuning of DAFNE Accumulator dipoles" - DAFNE Technical Note MM-9 (29/8/1995)

24. VACUUM ISSUES

24.1 Injector and Linac

The Vacuum system layout is presently under design. The basic design will follow closely the LPI system, the level required being in the region of 10^{-7} mbar.

24.2 Vacuum System of the Delay Loop and Combiner Ring

The Combiner Ring (CR) and the Delay Loop (DL) need Ultra High Vacuum conditions ($P < 10^{-8}$ mbar). The vacuum system has been designed in order to achieve a dynamic mean pressure inside the CR and DL vacuum chamber in the range of 10^{-9} mbar, taking into account the beam parameters, the machine requirements and the vacuum chamber feasibility.

24.3 Residual gas sources

The residual gas inside the vacuum chamber of a particle accelerator is a contribution of two sources: thermal out gassing and synchrotron radiation photo desorption.

The thermal out gassing contribution is proportional to the inner surface of the vacuum chamber and it strongly depends on the surface condition and on the whole history of the surface treatments. The factors that contribute to a good vacuum performance are: the choice of the material, a good vacuum design, machining, cleaning, assembling, welding, testing, handling, storing and mounting. If all the procedures are followed, it is possible to reach a specific thermal gas load value better than 10^{-12} mbar l s^{-1} cm^{-2} at room temperature for a very well cleaned and low roughness surface after bake out.

The synchrotron radiation photo desorption contribution is proportional to the photon flux emitted by the particle beam and is a decreasing function of the beam dose, so that after about 1 Ah of beam conditioning (one month of operation) it is reasonable to consider a photo desorption coefficient in the range of 1×10^{-3} molecules per photon.

The total gas load is the sum of thermal and photo desorption contributions:

Thermal	1×10^{-6} mbar l/s
Synchrotron Radiation	1.5×10^{-8} mbar l/s

In this case, the main contribution to the gas load arises from the thermal out gassing, and this is the value used for the dimensioning of the pumping system.

24.4 Vacuum chamber

Our approach is to choose for the vacuum chamber only all-metal components (the sole exception are the ceramic feedtrough and ceramic insulators). The material that will be used for the vacuum chamber is mainly aluminium alloy, although some components will be made of stainless steel and some others of copper.

Due to the short length and the shape of the vacuum chamber, extrusion is not economical. More convenient and more performing is a vacuum chamber manufactured from plates of aluminium alloy, with well-defined metallurgical properties, machined under controlled environment conditions.

Figure 24.1 shows the typical cross section of the DL and CR vacuum chamber. This vacuum chamber can be easily obtained starting with two aluminium plates machined and then welded together along the equatorial plane.

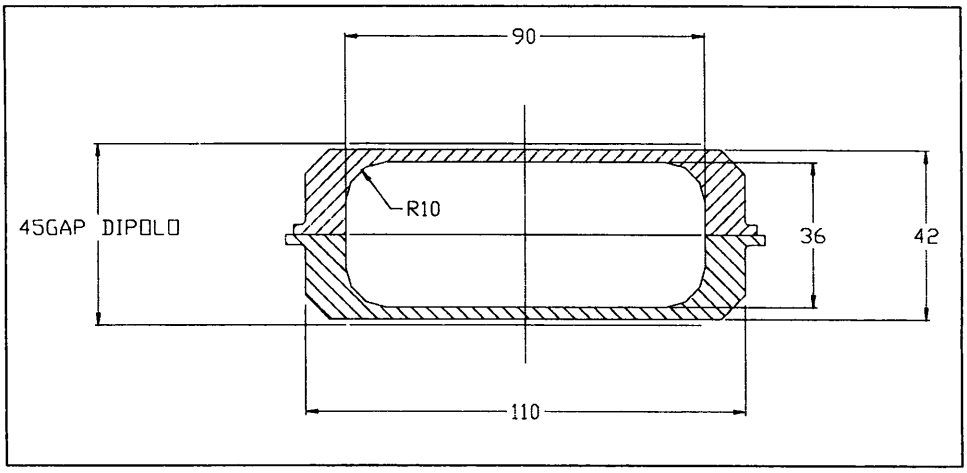

Figure 24.1 Typical cross section of the vacuum chamber, dimensions in mm.

Due to the very low impedance budget, the cross section of the vacuum chamber must be as uniform as possible, any joint must have its own RF contact and pumping ports must be properly screened.

24.5 Vacuum pumps

To cope with the gas load and to satisfy the 10^{-9} mbar range mean pressure requirements, it is necessary to install 32 vacuum pumps along the vacuum chamber of the CR and 16 on the DL. All the pumps are 70 l/s Sputter Ion Pumps.

Each vacuum pump is connected to the chamber by means of a special RF screened connection, as shown in Figure 24.2. Some of these sections are provided with additional flanges to connect the vacuum gauges and the valves for fore vacuum.

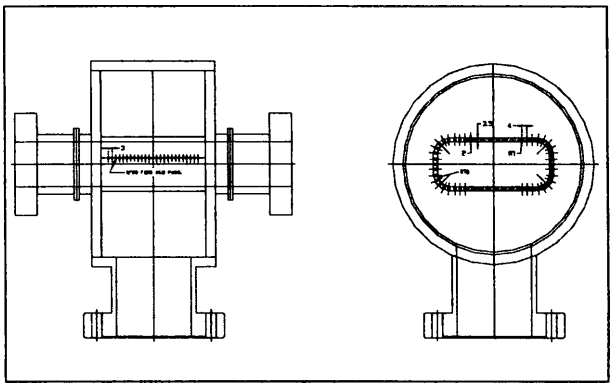

Figure 24.2 Typical pumping port with RF shield.

Figure 24.3 shows a simulation of the pressure profile along the vacuum chamber of the CR. Because of symmetry reasons, only one quadrant is shown, starting from the septum magnet up to the wiggler. The mean dynamic pressure is about 1.5×10^{-9} mbar.

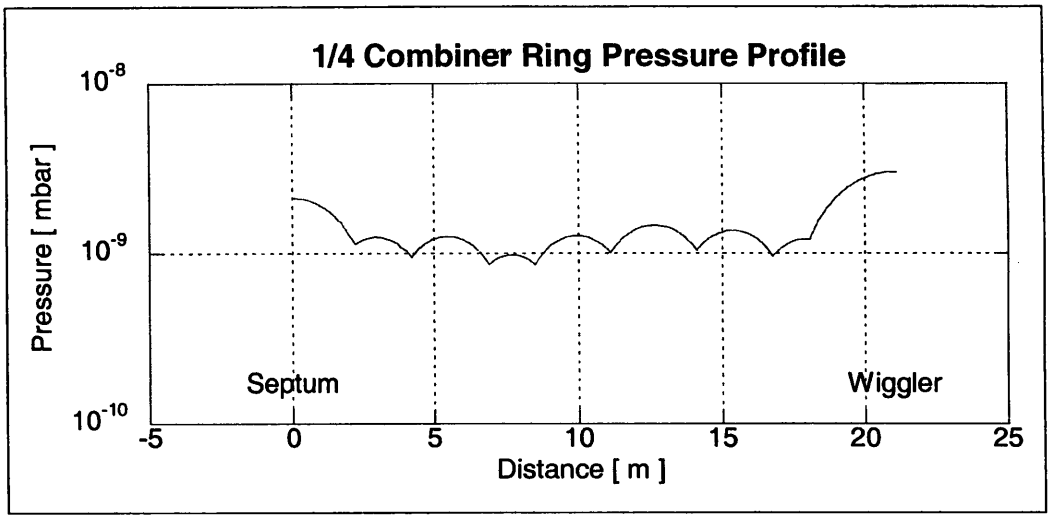

Figure 24.3 Pressure profile of one quadrant of the Combiner Ring

24.6 Bellows

The vacuum chamber of any particle accelerator foresees a certain number of flexible connections, needed for the assembling procedure and for compensating the thermal expansion of the chamber itself under operation. For these reasons, 22 bellows are installed on the DL vacuum chamber, and 36 bellows are installed on the CR vacuum chamber.

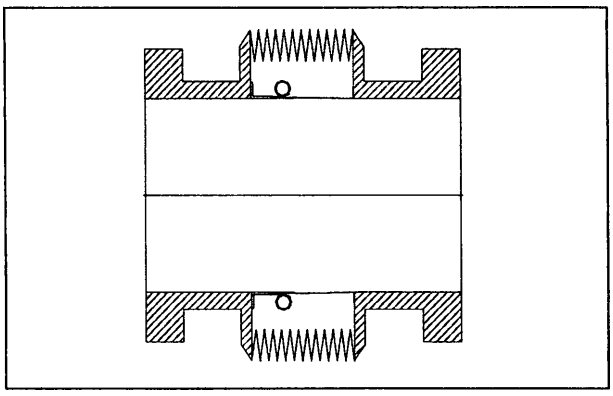

Figure 24.4 RF screened bellow.

Each bellow is provided with a proper sliding contact RF screen, as shown in Figure 24.4.

24.7 Vacuum diagnostic

Due to the small size of the two rings, it is possible to install a limited number of UHV vacuum gauges: 8 on the DL and 16 on the CR. Moreover, two gauges for rough vacuum are foreseen for each ring.

25. SAFETY

25.1 Shielding Design

In order to estimate the required shielding for the controlled radiation areas in CTF3, (CLEX, Klystron Galleries), an annual dose equivalent target has been set: personnel working in these areas should not be exposed to more than 2 mSv/year from CTF3 operation. The value represents twice the effective dose limit for the public or a tenth of the effective dose limit for radiation workers and is reasonably strict for the design of a new facility. Occupancy times have been estimated for the Klystron Galleries and for CLEX. Together with the annual dose equivalent target, they determine target values for hourly dose rate in the case of beam losses. They are summarised in Table 25.1.

Table 25.1 Estimated occupancy times and target dose rates derived from the annual dose target of 2 mSv. Two alternatives are given for every area.

Area	max. dose rate for annual occupancy time of ...		
	200 h	500 h	1000 h
Klystron Galleries	10 μSv h^{-1}	4 μSv h^{-1}	
CLEX		4 μSv h^{-1}	2 μSv h^{-1}

The maximal attainable dose rate for the public areas (streets, parkings and passageways around the CTF3 complex) is taken from recent Swiss legislation [1]. Because these areas are not permanently occupied, a dose rate of up to 2.5 μSv h^{-1} can be tolerated.

The stray radiation originates from beam losses and it is necessary to assume a conservative estimate for such losses. CTF3 is an experimental facility and the present study assumes the pessimistic figure of 5 % (P_{loss}=250 W). Furthermore, for the shielding estimates, losses are assumed to occur in one single point. This assumption yields more conservative shielding requirements than losses distributed over some length. It must be stressed that the present shielding estimates are valid only if a full beam loss (P_{loss}=5 kW) can be strictly limited in time. The CTF3 design foresees beam loss monitors which can shut off the beam.

The dose equivalent H at a distance r meters from a beam loss point and after the radiation has passed through a thickness d of shielding is represented by [2]

$$H = \frac{H_0}{r^2}\exp(-d/\lambda). \qquad \{1\}$$

H_0 is the so-called source-term which is the dose equivalent under condition of secondary particle equilibrium per kW of lost beam power at one metre distance from the loss point and zero shielding depth and λ is the radiation attenuation length (mean free path). With exception of the most simple situations, H is usually the sum of contributions from different types of radiation, and for every radiation type there will be a source term H, and for every combination of radiation type and shielding material there will be a specific attenuation length λ.

In this study, the source terms and attenuation lengths published by Sullivan [2] for the design of the original LIL/EPA complex [3] are used. Only the source term for neutrons with an energy less than 25 MeV (and having typically energies of 1 – 2 MeV, [4]) has been increased by 11.5% to reflect recent changes in fluence-to-dose rate conversion factors [5]. Lateral shielding – walls and roofs – is determined by source terms for radiation emerging from the loss point at 90° with respect to the beam axis. They are assumed to be independent of beam energy in [2,3]. Table 25.2 summarises the source terms for four different types of radiation and the corresponding attenuation lengths for the materials iron and concrete. It

must be stressed that these parameters are very coarse estimates and justify the considerable conservatism in the operation parameters of the facility.

Table 25.2 Source terms H_0 and attenuation lengths λ for the four types of stray radiation provoked by beam losses of electrons. Source terms for neutrons with energies from 25 MeV onwards have been read from Fig. 23 in [3] or Fig. 3.2 in [2].

Radiation type	Source term ($Sv\ h^{-1}\ kW^{-1}$)	Attenuation length (cm) for	
		Concrete	Iron
Gamma rays	50	21	4.7
neutrons, $E < 25$ MeV	11.5	18	16
neutrons, $25 < E < 100$ MeV	0.3	28	-
neutrons, $E > 100$ MeV	$4\ 10^{-3}$	43	18

Table 25.3 summarises the shielding thickness required to limit the dose equivalent rate to the target figures from Table 25.1 for each of the areas. The shielding model {1} and the parameters from Table 25.2 were used throughout. For each shielding, the estimated dose equivalent rates attained during a full beam loss are indicated. For more detailed results the reader is referred to [6], containing a complete discussion.

Table 25.3 Required thickness of shielding or additional shielding, dose equivalent rate H attained during continuous loss of 5 % and during full loss.

Shielding Wall	Material, Thickness	H at 5% loss ($\mu Sv\ h^{-1}$)	H at full loss ($\mu Sv\ h^{-1}$)
3.1 DBA-CLEX	concrete, 280 cm	≤ 1.8	35
3.2. DBA roof	additional iron, up to 20 cm*	< 4	< 80
3.3 CLEX roof	concrete, 260 cm	3.4	70
4.1. Side walls	concrete, 270 cm	1.5	30
4.2 Combiner roof	additional concrete, 90 cm	< 2.5**	< 50**

* see reference [6] for details

** due to sky shine on ground 10 m from the facility

25.2 References

[1] Le département fédéral de l'intérieur, Ordonnance sur l'utilisation des sources radioactives non scellées du 21 novembre 1997, annexe 2

[2] A.H.Sullivan, A Guide to Radiation and Radioactivity Levels near High Energy Particle Accelerators, Nuclear technology Publishing, Ashford, England, 1992

[3] A.Fassò, K.Goebel, M.Höfert, G.Rau, H.Schönbacher, G.R.Stevenson, A.H.Sullivan, W.P.Swanson and J.W.N.Tuyn, Radiation Problems in the Design of the Large Electron-Positron Collider (LEP), CERN 84-02, Technical Inspection and Safety Commission, 5 March 1984

[4] W.P.Swanson, Radiological Safety Aspects of the Operation of Electron Linear Accelerators, Technical Report Series No. 188, IAEA, Wien 1979

[5] International Commission on Radiological Protection, ICRP Publication 74, Conversion Coefficients for use in Radiological Protection against External Radiation, Annals of the ICRP, Vol. 26 (3-4) p. 1-205 (1996)

[6] T.Otto, Lateral Shielding Estimates for the CTF3-Facility, Terchnical Memorandum CERN-TIS-RP-TM-2001-24 (2001)

26. PLANNING

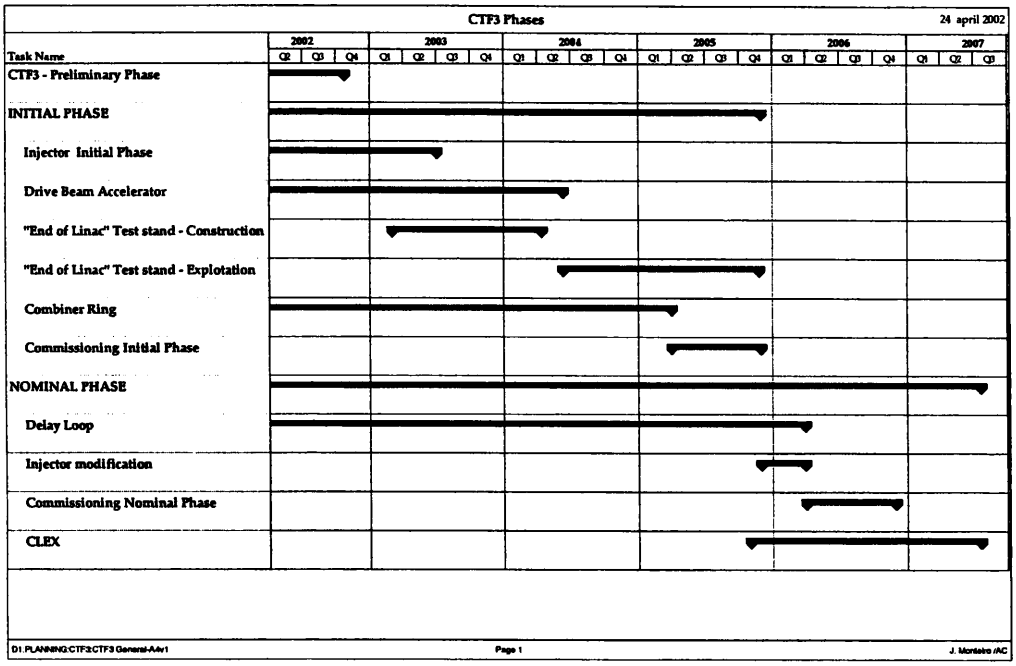
CTF3 Phases
24 april 2002
Task Name
2002
2003
2004
2005
2006
2007
Q2 Q3 Q4 Q1 Q2 Q3 Q4 Q1 Q2 Q3 Q4 Q1 Q2 Q3 Q4 Q1 Q2 Q3 Q4 Q1 Q2 Q3
CTF3 - Preliminary Phase
INITIAL PHASE
Injector Initial Phase
Drive Beam Accelerator
"End of Linac" Test stand - Construction
"End of Linac" Test stand - Explotation
Combiner Ring
Commissioning Initial Phase
NOMINAL PHASE
Delay Loop
Injector modification
Commissioning Nominal Phase
CLEX
D1:PLANNING\CTF3\CTF3 General-A4v1
Page 1
J. Mortaise /AC